Molecular Shocks in the Interstellar Medium

Author

Rosie O Sumpter

Submitted in accordance with the requirements for the degree of Doctor of Philosophy

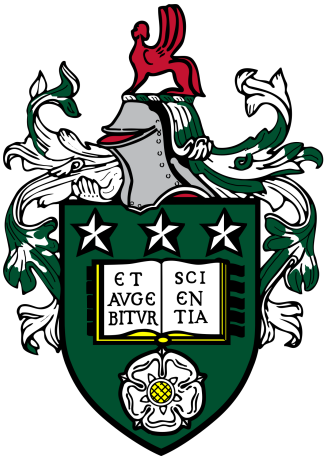

The University of leeds
School of Physics and Astronomy

May 2021

Declaration of Authorship

The candidate confirms that the work submitted is her own, except where work which has formed part of jointly authored publications has been included. The contribution of the candidate and the other authors to this work has been explicitly indicated below. The candidate confirms that appropriate credit has been given within the thesis where reference has been made to the work of others.

Abstract

Shocks in the interstellar medium occur as a result of a variety of phenomena, e.g. protostellar outflows, supernovae and cloud-cloud collisions. In these dense, molecular environments the ionisation fraction of the plasma is low and the magnetic fields threading the clouds can be significant. This results in the shocks from the bipolar outflows of young stellar objects being C-type, meaning there is a smoothing effect on the discontinuities in the fluid parameters through the shock. These shocks are important for the generation of molecules such as SiO which are otherwise heavily depleted from the gas phase as they are condensed into dust grains in these regions. Observations of SiO rotational lines in star-forming regions make SiO a reliable tracer for the shocks which propagate due to the outflows from young stellar objects. The presence of gas-phase SiO suggests that the dust grains undergo destructive processes. The destruction of dust grains in C-type shocks can occur due to both gas-grain sputtering and grain-grain collisions.

The aim of this thesis is to extend the treatment of dust grains in the model used by Van Loo et al. (2013) and Ashmore (2011) for simulations of oblique C-type shocks. The ability of numerical models such as these to accurately evolve dust grain-size distributions is important, as changes to the distribution have implications for the shock structure and dynamics which, in turn, impact the chemistry of the region.

A novel approach for evolving grain size-distributions is presented, which, when tested against piecewise-constant and -linear approaches which appear in the literature, is shown to be both accurate and computationally viable. This new method adopts a power-law discretisation and uses both the grain mass and number densities in each size bin to determine the power law parameters. In sputtering tests the relative error in the total grain mass remains below 0.01 per cent for all numbers of bins $N \geq 8$, while other methods only achieve this for $N > 50$. Likewise, shattering tests show that the method produces small relative errors in the total grain numbers while conserving mass. Not only does the power-law method conserve the global distribution properties, it also preserves the inter-bin characteristics so that the shape of the distribution is recovered to a high degree.

This new method has been implemented into the original time-dependent, multifluid MHD code and is used to evolve an initial MRN grain-size distribution in C-type shocks. Results are compared with those for multiple single-sized grain fluids and it is shown that 2 bins are sufficient to accurately model the shock structure and dynamics when destructive processes are neglected, in contrast to 16 single-sized grain fluids. When sputtering is applied, 8 bins are required to accurately describe the fraction of Si removed from the grains, and to reliably produce the shape of the downstream distribution function. This is due to the size dependency of the sputter rate, which is best captured when enough bins are used to correctly model the region in which the grains transition from moving with the charged particles to moving with the neutrals.

Grain-grain collisions have the potential to both alter the grain-size distribution, due to shattering, and contribute to the abundance of gas phase SiO, due to vaporisation. Expressions for the source terms for the number and mass densities of grains are formulated in a more accurate way than has been seen before in the literature. In particular, the fragments and remnants which result from grain-grain collisions are distributed into the appropriate size bins without the use of average values. The implementation of this routine is tested for a gas density of 10^5 cm^{-3}, where it is shown that the fraction of Si removed from the grains by a combination of sputtering and grain-grain collisions is accurate for 8 bins. However, the grain-grain relative velocities are not sufficient for vaporisation to occur at this density. Simulations for higher density models (10^6 cm^{-3}) prove to have a much greater impact on the downstream grain-size distribution, and vaporisation dominates over sputtering for the production of gas-phase SiO. Shattering increases the total number density of grains in the distribution by a factor of 3, due to the abundance of small fragments which are created. This causes the shocks to have a width $\sim 30\%$ narrower than those which neglect grain-grain processing.

The development of the original multifluid MHD model through this thesis allows physical dust grain processes occurring in C-type shocks to be simulated in a more accurate way than has been seen previously in the literature. A new approach for modelling grain-size distributions, which works particularly well for power-law distributions, allows the evolution of grain sizes to be followed in a way that is both accurate and computationally viable. An improved routine for calculating changes to the numbers and mass of grains due to grain-grain collisions means that the grain-size distribution can be evolved using just a few necessary assumptions. Grain-grain

collisions may be pertinent in explaining the enhanced abundances of SiO observed in shocked regions of molecular clouds, and our simulations have shown that for a pre-shock density of 10^6 cm^{-3}, the amount of Si released from grains is increased by grain-grain processing.

Acknowledgements

I would firstly like to thank Prof Tom Hartquist for encouraging me to apply for this PhD, and then for spending time discussing physics with me and funding trips to the fluids lab. You are an inspiration. I would also like to thank Dr Sven Van Loo for supervising this project. Not only have you have been incredibly patient and supportive, but I have also learned so much from you and for that I am grateful. Thank you to everyone else who has been part of my many years at Leeds, with a special mention to the S.Cs (to whom I owe most of my undergraduate success).

Next, I would like to thank my family and friends. To everyone in the Warren/-Sumpter clan - thank you for the enjoyable Zoom calls. I'm sure I won't be the last in what is now a whole line of family physicists. Particular thanks goes to my Grandparents, who have always taken an interest in what I do. Thanks to my Mum, who is possibly the most supportive human on the planet. Thanks to my Dad who, when I wanted to change undergraduate degree courses, believed I would succeed, and then enabled me to begin my physics journey. Thanks to Podge for the many, many... many FaceTimes. Thanks to Tom and Tilly for the entertaining calls and videos, and to Denise for fuelling my feminism. Thanks to all the Meggitts for the much-needed trips to Cornwall. Thank you to The Greatest Team, who understood the struggles of doing a PhD and made sure the fun (and empty pockets) continued through the years. Thank you to The Girls - you are the best, most supportive friends anyone could hope to have.

Finally, thank you to Dr J. W. R. Meggitt who, for more than 10 years, has been my fellow cheesebag. From funding my lapsang souchong habit to supporting me at my first proper conference talk, you have been there for me through it all. Since I genuinely couldn't have done this without you, 49% of the credit for this thesis goes to you.

Contents

List of Figures

List of Tables

Author Publications

Chapter 4 is made up of work published in the following paper:

"Evolving grain-size distributions embedded in gas flows", Sumpter. R., & Van Loo, S. 2020, *MNRAS*, 494:2147-2157.

Dr Sven Van Loo provided the initial idea, guided me through the work and gave comments on the written paper. I conducted the work, including running the simulations and writing the paper.

The contents of Chapters 5 and 6 will be written up for publication after the submission of this thesis.

1

Introduction

This chapter presents an introduction to C-type shocks and their presence in dense clouds due to the molecular outflows from young stellar objects. The features of star formation concerned with outflows are covered. Dense clouds are modelled as weakly-ionised plasmas, so the presence of a magnetic field is vital to the formation of C-type shocks. The MHD fluid equations are presented, with a particular focus on chemistry and dust grains. The literature concerning the research area of C-type shocks and dust grains is reviewed, and the remaining structure of the thesis is outlined.

Contents

1.1 Star formation

Curiosity in the nature and evolution of space has led to huge advancements in our understanding of the universe over the last few hundred years, with the light from stars being a fundamental diagnostic tool. It is therefore of significant interest to understand how and why stars form, not only from an observational perspective, but also from a theoretical one; computational models give clarity to physical processes that observations alone cannot. Current theories of star formation place the origin of

stars in dark interstellar clouds of gas and dust. Observational surveys of molecular gas in galaxies show that it is concentrated into regions spanning 100 pc in the case of giant molecular clouds (GMCs) (Lada, 2005). These clouds contain multiple density inhomogeneities, such as filaments and clumps, with the densest regions being known as dense clouds or cores which have densities $\gtrsim 10^4\,\mathrm{cm}^{-3}$ (Stahler and Palla, 2004). It is these smaller regions, on scales of the order of 0.1 pc, where protostars are born.

1.1.1 Molecular clouds

Star formation is associated with molecular gas. The densest, and coldest, regions of the ISM are dominated by molecular hydrogen, H_2, with the next most abundant gas-phase molecule being CO (Combes, 1991). Despite H_2 being the most abundant molecule in the universe, it is difficult to observe directly. This is because the low temperatures in molecular clouds ($T = 10 - 20$ K) are not sufficient to excite even the lowest rotational transition of the H_2 molecule. Conversely, CO is readily observed via both emission and absorption, and it is known that the $J = 1 \rightarrow 0$ transition line intensity of ^{12}CO is correlated with the column density of molecular hydrogen in these clouds (Dame et al., 2001). The densest regions of space appear to us as dark against the bright background of stars because the interstellar dust present there is a very efficient absorber of visible light from the distant stars behind it. First described as a 'hole' in space by Herschel in the 18th century (Steinicke, 2016), Barnard 68, rather than being an absence of material, is a dense cloud of gas and dust. It appears as a dark hole because of interstellar extinction; the scattering and absorption of starlight due to dust grains. Dense clouds are known to be sites of star formation and extensive research has been carried out across both radio and infrared wavelengths in order to characterise the structure and composition of these small clouds (Larson, 2003).

For a star to form, the dense cloud must be gravitationally unstable. The conditions for the stability of a gas which is subjected to density perturbations was considered by Jeans (1902). It was shown that perturbations exceeding a critical size, the Jeans length, will cause the gas to become unstable to gravitational collapse. The Jeans length can be derived via analysis of the self-gravitating fluid equations. In 1-D, the coordinates are time t and distance x, and the continuity equation for the cloud with density ρ is

$$\frac{\partial \rho}{\partial t} + \frac{\partial}{\partial x}(\rho u) = 0 \tag{1.1}$$

where u is the fluid velocity. The momentum equation is

$$\frac{\partial}{\partial t}(\rho u) + \frac{\partial}{\partial x}(\rho u^2) = -\frac{\partial P}{\partial x} - \rho\frac{\partial \Phi}{\partial x} \tag{1.2}$$

where P is pressure, and $-\partial\Phi/\partial x$ is the acceleration due to gravity where Φ is the gravitational potential. Φ is given by Poisson's equation,

$$\frac{\partial^2 \Phi}{\partial x^2} = 4\pi G\rho \tag{1.3}$$

where G is the gravitational constant. The energy equation is given by the isothermal equation of state,

$$P = c_s^2 \rho \tag{1.4}$$

where c_s is the isothermal sound speed. For the initial constant cloud properties ρ_0, P_0, Φ_0 and $u_0 = 0$, small perturbations are applied so that

$$\rho = \rho_0 + \rho_1, \tag{1.5}$$

$$P = P_0 + P_1, \tag{1.6}$$

$$u = u_1, \tag{1.7}$$

and

$$\Phi = \Phi_0 + \Phi_1 \tag{1.8}$$

where the perturbations are small compared with the initial quantities and

$$P_1 = c_s^2 \rho_1 \tag{1.9}$$

since c_s is unchanged given the assumption of isothermal perturbations. Substituting Eqs. 1.5 - 1.9 into Eqs. 1.1 - 1.4 and neglecting non-linear terms, we obtain

$$\frac{\partial \rho_1}{\partial t} + \rho_0 \frac{\partial u_1}{\partial x} = 0, \tag{1.10}$$

$$\frac{\partial u_1}{\partial t} = -\frac{\partial \Phi_1}{\partial x} - \frac{c_s^2}{\rho_0}\frac{\partial \rho_1}{\partial x}, \tag{1.11}$$

and

$$\frac{\partial \Phi_1^2}{\partial x^2} = 4\pi G\rho_1. \tag{1.12}$$

As these equations are now linear, every solution can be constructed from plane-wave contributions, hence solutions for ρ_1, u_1 and Φ_1 proportional to $\exp[\mathrm{i}(\mathrm{kx}-\omega\mathrm{t})]$ are assumed. Then, $\partial/\partial x = ik$ and $\partial/\partial t = i\omega$ (where k is the wavenumber and ω is the angular frequency) and we arrive at

$$\omega\rho_1 + k\rho_0 u_1 = 0, \tag{1.13}$$

$$\frac{kc_s^2}{\rho_0}\rho_1 + \omega u_1 + k\Phi_1 = 0, \tag{1.14}$$

and

$$4\pi G\rho_1 + k^2\Phi_1 = 0. \tag{1.15}$$

This homogenous linear system of equations only has non-trivial solutions for

$$\omega^2 = k^2c_s^2 - 4\pi G\rho_0. \tag{1.16}$$

If k is sufficiently large, then $k^2c_s^2 - 4\pi G\rho_0 > 0$ and ω is real. This means that the perturbation varies periodically, and the equilibrium is stable; the amplitude does not increase with time. However, if $k^2c_s^2 - 4\pi G\rho_0 < 0$ then ω has the form $i\zeta$ where ζ is real; there exist perturbations where the equilibrium is unstable and the amplitude grows exponentially with time. The critical wavenumber separating these two regimes is then $k_J = (4\pi G\rho_0/c_s^2)^{1/2}$. Use of the relation $k = 2\pi/\lambda$ allows the critical wavelength, the Jeans length, to be determined as

$$\lambda_J = \left(\frac{\pi c_s^2}{G\rho_0}\right)^{\frac{1}{2}}, \tag{1.17}$$

Perturbations with $\lambda > \lambda_J$ are unstable, known as the Jeans criterion. This derivation, although neat, is flawed. Eq. 1.12 tells us that $\partial^2\phi_0/\partial x^2 = 0$, but from Poisson's equation it is required that $\partial^2\phi_0/\partial x^2 = 4\pi G\rho_0$. The only way these can both be satisfied is if $\rho_0 = 0$, hence why Binney and Tremaine (2008) referred to this description as the "Jeans swindle". Although this is a clear limitation of the analysis, it gives the correct instability criteria.

The mass which corresponds to the Jeans length is called the Jeans Mass and is given by

$$M_J = \rho_0\left(\frac{\lambda_J}{2}\right)^3. \tag{1.18}$$

Use of the equation of state for ideal gases allows the isothermal sound speed to be defined as

$$c_s = \left(\frac{k_B T_0}{\mu m_u}\right)^{\frac{1}{2}} \tag{1.19}$$

where k_B is the Boltzmann constant, T_0 is the gas temperature, μ is the mean molecular weight and m_u is the atomic mass unit. Therefore the Jeans mass can be rewritten as

$$M_J = \rho_0 \left(\frac{\pi k_B T_0}{4\mu m_u G \rho_0}\right)^{\frac{3}{2}}, \tag{1.20}$$

so $M_J \propto T_0^{3/2} \rho_0^{-1/2}$. This means that if a cloud of gas with an initial temperature T_0 and density ρ_0 has a mass larger than M_J then it is unstable and will eventually collapse under self-gravity. This simplified model neglects mechanisms such as turbulence and magnetic fields which work to stabilise the cloud, so the Jeans mass can be considered to be a lower bound on the stable cloud mass. As cloud collapse begins, the gas initially remains isothermal if it is optically thin and the energy transfer by radiation is efficient. The Jeans mass of the cloud therefore depends only on the density; as the cloud density increases the Jeans mass decreases. This therefore allows small regions of the cloud to become unstable, resulting in fragmentation. With increasing density comes increasing opacity. The collapsing fragments can no longer efficiently radiate away energy and the gas heats up. An increase in temperature causes the Jeans mass to increase, halting further fragmentation.

The typical timescale for the collapse of a cloud is the free-fall time. To derive an expression for the free-fall time, we consider a uniform, homogenous and spherically symmetric cloud with mass M and radius R in free-fall (i.e. pressureless). The gravitational force is $\approx GM/R^2$ and

$$\left|\frac{1}{\rho}\frac{\partial P}{\partial R}\right| \approx \frac{P}{\rho R} \approx \frac{k_B T}{\mu m_u R} \tag{1.21}$$

is the pressure term in the momentum equation. The ratio of the gravity term to the pressure term is proportional to $M/(RT)$, which increases during the isothermal collapse phase (as R decreases). We consider a spherical shell of mass with radius r in a Lagrangian reference frame. From Newton's second law, the equation of motion for a test particle at the edge of the cloud is

$$\frac{d^2 r}{dt^2} = -\frac{Gm}{r^2} \tag{1.22}$$

where m is the mass contained within the radius r. The velocity of the shell is

$$u(r(t)) = \frac{dr}{dt} \tag{1.23}$$

so

$$\frac{d^2r}{dt^2} = \frac{du}{dt} = \frac{dr}{dt}\frac{du}{dr} = u\frac{du}{dr} = \frac{1}{2}\frac{du^2}{dr} \tag{1.24}$$

and Eq. 1.22 becomes

$$\frac{1}{2}du^2 = -\frac{Gm}{r^2}dr. \tag{1.25}$$

Integration yields

$$u^2 = 2GM\left(\frac{1}{r} - \frac{1}{R}\right) \tag{1.26}$$

where $-2GM/R$ is the constant of integration determined using the initial conditions $u = 0, r = R$ and $m = M$. Therefore,

$$\frac{dr}{dt} = \pm\left[2GM\left(\frac{1}{r} - \frac{1}{R}\right)\right]^{\frac{1}{2}} \tag{1.27}$$

and, for $u < 0$ (i.e. infall),

$$dt = -\frac{dr}{\left(\frac{2GM}{R}\right)^{1/2}\left(\frac{R}{r} - 1\right)^{1/2}}\ . \tag{1.28}$$

Use of $M = 4/3\pi\rho_0 R^3$ for a spherical cloud, and the substitutions

$$\xi = \frac{r}{R} \tag{1.29}$$

and

$$d\xi = \frac{dr}{R} \tag{1.30}$$

give

$$dt = -\left(\frac{8\pi G\rho_0}{3}\right)^{-\frac{1}{2}}\left(\frac{\xi}{1-\xi}\right)^{\frac{1}{2}}d\xi. \tag{1.31}$$

The right-hand side is integrated from $r = R$ to $r = 0$, so $\xi = 1$ to $\xi = 0$, to give the total free-fall time

$$t_{ff} = \left(\frac{3\pi}{32G\rho_0}\right)^{\frac{1}{2}}. \tag{1.32}$$

It is notable that the free-fall timescale depends only on the cloud's density, not its radius. The inner-most, densest regions of the cloud collapse fastest, resulting in so-called inside-out collapse. Typical densities in GMCs are $n \sim 100$ cm^{-3}, which

corresponds to $\rho \sim nm_H \sim 2 \times 10^{-22}$ g cm^{-3}, and gives a free-fall time of $t_{ff} \sim 5$ Myr. The total mass of molecular gas in the Milky Way is approximately 10^9 $M_\odot$ (Bhat et al., 1985), therefore the galaxy would be expected to have a star formation rate of

$$\dot{M} \sim \frac{10^9 \ M_\odot}{5 \text{ Myr}} \sim 200 \ M_\odot \text{ yr}^{-1}. \tag{1.33}$$

However, the observed star formation rate is approximately 100 times smaller than this (e.g. McKee and Williams, 1997). It is thought that mechanisms exist to inhibit star formation, such as winds and radiation from young massive stars (Dale and Bonnell, 2008), which disrupt their parent cloud and limit further star formation.

After the initial isothermal collapse, when the cloud core begins to heat up, an equilibrium is obtained between gravity and the gas pressure and the newly forming star is called a hydrostatic core (Larson, 2003). The hydrostatic core continues to rise in temperature, eventually causing the dissociation of H_2 molecules at temperatures of the order 10^3 K. The process of dissociation removes energy that would otherwise cause a pressure gradient and means that the core no longer sustains hydrostatic equilibrium. The second phase of collapse involves a continued increase in gas temperature and opacity since the hydrogen atoms become ionised. This process continues until a second hydrostatic core is established at a size of $\sim 1R_\odot$. At this point the protostar contains only a small fraction of its final stellar mass (~ 1 % for a final mass of $1M_\odot$). The rest of the mass is gained through the main accretion phase. This phase lasts $\sim 10^5$ years and ends when the star becomes visible on the 'birthline' on the Hertzsprung-Russell diagram, which is the line along which young, pre-main sequence stars start to become visible at optical wavelengths. When the accreting protostar reaches a mass of $\sim 0.2M_\odot$, deuterium begins to burn in its centre. This is a significant source of thermal energy which prevents the collapse of the central protostar whilst it continues to accrete material.

These infall models are limited since they do not include the effects of rotation, nor magnetic fields. Consideration of even a slowly rotating cloud leads to the angular momentum problem; the amount of angular momentum in a star-forming core is amplified to levels which would not allow star formation to occur (Hartmann and Stauffer, 1989). This means that there must be mechanisms as play which act to remove the excess angular momentum. Possibilities for such mechanisms include:

- The transfer of the initial angular momentum into orbital motion of the stars in a cluster or binary system (Bodenheimer, 1978).

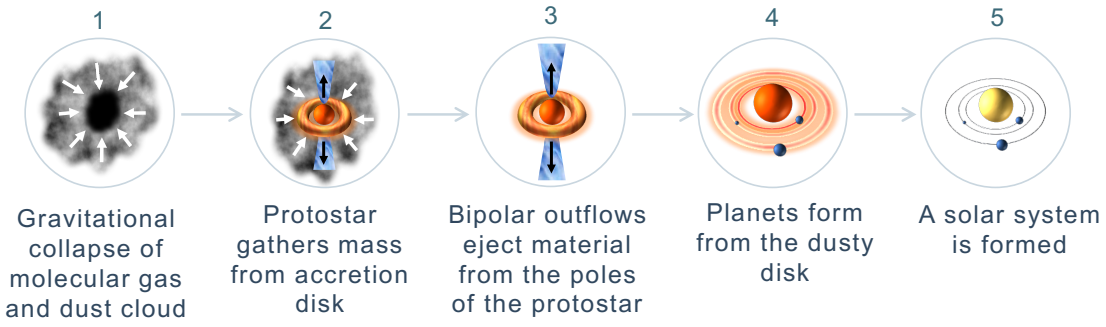

Figure 1.1: Diagram showing the general star formation process. Bipolar outflows are present intermittently for the first 10^5 to 10^6 years of a newly forming star, and occur simultaneously with accretion.

- Magnetic braking of the star occurring in the early, low density phases of cloud evolution when charged particles in the gas are strongly coupled to the magnetic field so resist the motion (Mouschovias and Paleologou, 1980).
- Periods of mass-loss occurring through molecular outflows in which the lost mass carries away excess angular momentum (Königl and Pudritz, 2000).

The influence of the rotation of the parent cloud is that conservation of momentum requires that accreting material forms a circumstellar disk around the protostar from which it spirals inwards onto the stellar surface (Machida and Matsumoto, 2011). Accretion from the disk continues and in doing so depletes matter from the surrounding circumstellar envelope. The opaque region contracts, allowing the spectrum of emitted radiation to shift to high energies. Eventually both visible and infrared components of the central star can be observed and the pre-main sequence star arrives on the birthline (Stahler, 1983). Fig. 1.1 depicts the over-arching star formation process. Stage 1 shows the gravitational collapse of a dense core in a molecular cloud. Stage 2 shows the formation of a protostar, which is accreting material from a surrounding accretion disk. The accretion process powers bipolar outflows which carry away material and angular momentum. The outflows occur periodically, lasting for the first $10^5 - 10^6$ years of a newly forming star, shown in stages 2 and 3 (outflows are explored in greater detail in §1.1.3). Planets form from the dusty protoplanetary disk, eventually forming a solar system, shown in stages 4 and 5.

1.1.2 Classification of young stellar objects

Defining the evolutionary stages of a forming star is not always clear. One way in which a YSO can be classified throughout the period in which accretion is considered important is as follows (Seale and Looney, 2008):

- ***Class 0*** The phase when the protostar accretes rapidly, building up the majority of its final mass and resulting in a final mass of $\sim 1 M_{\odot}$ in a time of $\sim 10^5$ years (Pudritz et al., 1996). This is a relatively short phase, so observations of class 0 protostars are rare. The envelope is optically thick at shorter wavelengths, but (sub)mm wavelengths are able to escape so observed emission is predominantly in this range. This stage is characterised by dense infalling envelopes and highly collimated outflows (Arce and Sargent, 2006).

- ***Class I*** This phase is dominated by near- to far-infrared emissions. These protostars are more commonly seen than class 0, most likely because they spend a larger amount of time in this accretion phase. The outflows tend to be wider, potentially made up of a broad protostellar wind driven by an underlying jet (Arce and Sargent, 2006). The surrounding envelope is depleted by accretion onto the protostar and by mass pushed out by the outflows. It is in the class 0 and class 1 stages when the protostar can begin to fuse deuterium due to the high protostellar core temperatures (Ray, 2007a).

- ***Class II*** This phase sees emission in the near-infrared and the presence of a T Tauri star, which are variable stars seen as the pre-cursors to solar-type stars, surrounded by a large amount of circumstellar dust. The outflow may have widened to the point where its structure is no longer clearly defined (Bachiller, 1996).

- ***Class III*** An individual T Tauri star, where the circumstellar dust is mostly gone and emission is in the optical range (Lada, 1987). Following this phase, the star begins to move from the birthline to the main sequence of the H-R diagram after some tens of millions of years of contraction, until the core temperatures reach those at which hydrogen fusion can commence.

The description here has been of low and intermediate mass star formation. High mass star formation ($> 10\ M_{\odot}$) involves more complex processes and is an active area of current research. However, stars of all masses produce outflows for the first

$10^5 - 10^6$ years of their lives, making outflows an important and distinctive feature of star formation (Frank et al., 2014).

1.1.3 Molecular outflows

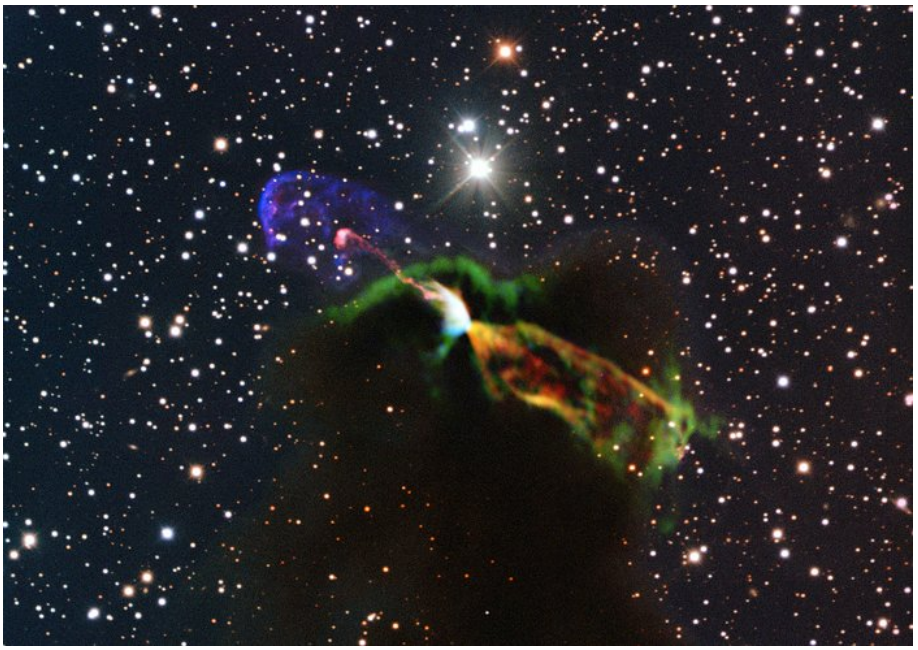

Figure 1.2: Outflow from Herbig-Haro object HH 46/47. Radio observations from ALMA are combined with visible observations from NTT. ESO/ALMA (ESO/NAOJ/NRAO)/H. Arce. Acknowledgements: Bo Reipurth.

Around 1000 Herbig-Haro objects and protostellar outflows have been imaged with atomic (e.g. Hα, SII) and molecular (e.g. CO, SiO) line emission and catalogued by Reipurth (1999) and Wu et al. (2004). Observations of outflows show that they are associated with star formation across the full stellar mass spectrum, from type-O YSOs (e.g. Caratti o Garatti et al., 2017) down to brown dwarfs (e.g. Whelan et al., 2005). As a ubiquitous feature of star formation, the feedback of which is likely important in star-formation regulation, the subject of understanding outflows has continued to receive interest for a number of decades. Observations of YSOs in dense clouds reveal the presence of high energy, cold outflows of molecular gas. Often these outflows are bipolar in nature, extending outwards from the magnetic poles of the protostar. Herbig-Haro (HH) objects are small areas of nebulosity with characteristic optical emission spectra which are found in star-forming regions. First observed independently by Herbig (1950, 1951) and Haro (1952, 1953), emission from HH objects is now known to be the result of post-shock cooling from jets and outflows. Observations of YSOs at mm wavelengths, for example the distinctive 2.6 mm rotational emission from CO molecules, show that on scales $\sim 10^{16}$ m

molecular outflows extend from the magnetic poles of protostars, perpendicular to their circumstellar disks. An example of a protostellar outflow is seen in Fig. 1.2, which shows Herbig-Haro object HH 46/47. The origin of the outflow is a low-mass Class I source, located in Bok globule ESO 216-6A, on the outer regions of the Gum Nebula approximately 450 pc away from us (Zhang et al., 2019).

1.1.3.1 Morphologies

Young stellar objects drive high-velocity jets which are surrounded by wide-angle winds in an outflow lobe. The majority of outflows exhibit bipolar structure, with redshifted gas located on one side of the source and blueshifted gas on the other in an hourglass shape (Bally, 2016). An example of such morphology is demonstrated in Fig. 1.3 where the red- and blueshifted lobes of the HH 46/47 outflow are clearly defined (Arce et al., 2013). The actual morphology of an outflow is determined by the tracer used for observations, and properties of the YSO from which it is produced. It is observed that outflows around younger protostars have narrower cavities whilst more evolved sources show wider-angle cavities, which suggests that outflow cavities expand with time (Seale and Looney, 2008). This change to the opening angle with age could be a result of mass loss in the core and a reduction in the amount of energy in the outflow over time (Hsieh et al., 2017).

In general, jets are launched and collimated from close to the central protostar, and can range in velocities from $\sim 10^2 - 10^3$ km s^{-1}. The jet entrains and shocks the surrounding material, carving out wide-angle cavities to form lower-velocity outflows, with velocities in the range $\sim 1 - 50$ km s^{-1}. This forms the shell-like structure of the molecular outflows which surround jets. The outflow cavity walls are made up of ambient material swept up by the jet bow shocks. Fig. 1.4 shows a diagram from Bally (2016) which outlines the notable features of an outflow. The outflow is launched from the region of the circumstellar disk by MHD processes involving the magnetosphere. Close to the star, in the earlier stages of evolution, the outflow is traced by molecules such as CO, H_2O and H_2 (shown in blue, green and yellow) as the outflow impacts the dense envelope. As the jet moves outwards from the source, at variable speeds, a chain of shocks and knots is formed in the central region. The cavity wall outlines the wide-angle morphology of the outflow as it expands outwards over time, where expansion of the shell produces additional low-velocity shocks.

The mass-loss rates, ejection velocity and collimation of outflows vary over time according to the evolutionary stage of the source. Class 0 sources are heavily embedded

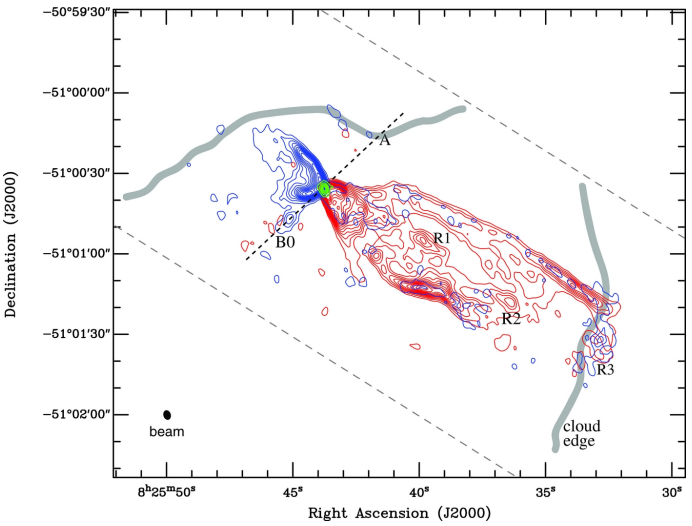

Figure 1.3: Integrated intensity map of the HH 46/47 CO(1-0) outflow, with blue contours representing the blueshifted lobe and the red contours showing the redshifted lobe (Arce et al., 2013).

and jets are launched close to the protostar, so observation of the jet origin location requires high resolution (down to sub-milliarcseconds, corresponding to sub-AU scales), but can be identified through radio continuum emission (e.g. Lee et al., 2014) which is able to penetrate the dust, and H_2O masers (e.g. Claussen et al., 2005). In this early stage of evolution jets are mainly molecular, much less than 1 pc in length and are observed in near-IR H_2 emission as well as in other molecules, such as CO, SO and SiO at (sub)-mm wavelengths as the high-speed jet shocks the gas (Frank et al., 2014). As the jet propagates into the surrounding medium, knots and bow shocks are formed which can be observed via shock tracers such as H_2 and SiO (e.g. Podio et al., 2016). In some jets, these knots and bow shocks show approximately equal spacing, suggesting some periodical variation in ejection velocity; a shock is formed as the fast jet material catches up with the slow jet material (Lee, 2020). The number and separation of such HH objects can be determined from Hα and SII optical images (e.g. Raga et al., 2002). The material which has been swept up moves outwards more slowly, creating a wide-angle cavity which makes up the outflow.

Outflows were first discovered in the L1551 dark cloud of Taurus-Auriga in 1980 by CO observations of the dense shell of swept-up material (Snell et al., 1980). The cavity walls are traced using SiO and low-velocity CO. Additionally, H_2O may be released from icy grain mantles in the cavity walls by photons which reach grain surfaces through the cavity-ISM interface, which reacts with CO^+ to form HCO^+. Shocks are traced by SiO both in the outflow and the cavity walls. The outflow velocity increases as the stellar mass increases, so when the source is in the Class I

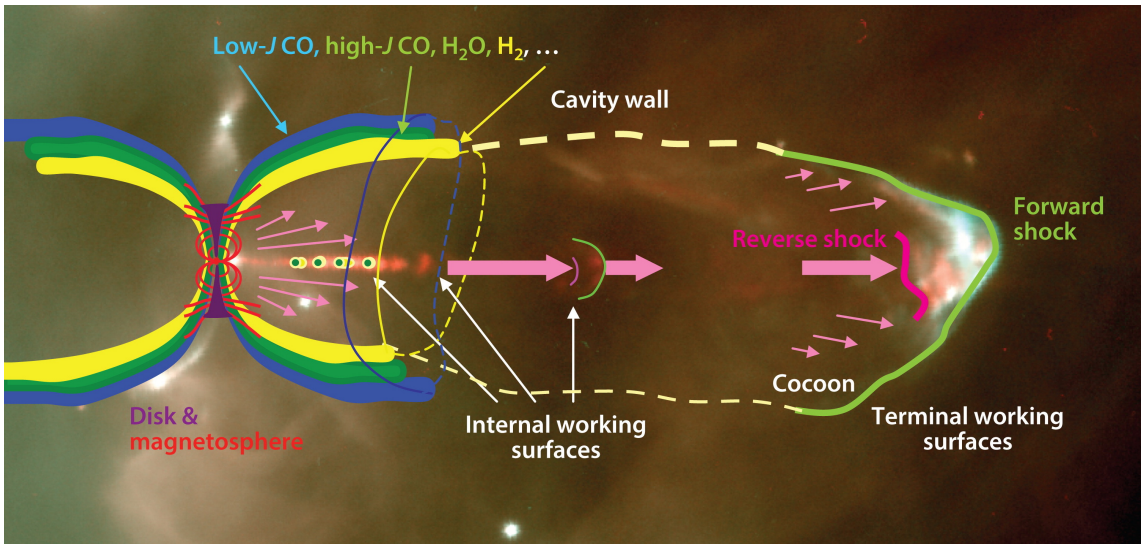

Figure 1.4: The features of a protostellar ouflow lobe, from Bally (2016). The circumstellar disk is shown in purple, along with the poloidal component of the disk and the protostar's magnetic fields are in red. Molecules such as CO, H_2O, H_2 etc. trace the cavity walls (outlined by the dashed yellow line) close to the YSO. The thick yellow, green and blue bands denote the cavity shocks and UV-heated gas, where blue is low-J CO, yellow is shocked H_2 and green is high-J CO, and the yellow/blue/green spots indicate shocks along the jet.

and II stages the jets are detected in atomic and ionised gas, such as O, Hα and SII in the optical and infrared wavebands (e.g. Reipurth and Bally, 2001). The jet quickly emerges from the envelope into the ISM beyond, extending to parsec scales (e.g. Bally et al., 2012) to become a giant outflow. Fig. 1.4 shows that at the head of the jet is a forward bow shock (between the jet and the ambient material) and a reverse shock (between the internal jet and the back of the bow shock), which together make up a 'terminal working surface'. The compression of the gas at the working surface causes it to heat up to temperatures high enough to allow dissociation and therefore can be observed via ionised or atomic species. Additionally, UV radiation from the source produces molecules such as OH via the dissociation of H_2O. An example of such a morphology is that of the jet HH 111, which originates from the YSO IRAS 05491+0247 in the L1617 cloud in Orion at a distance of 460 pc. The protostar is deeply embedded in the dense core from which it is forming and HH 111 extends a few parsecs away from it, consisting of a blue-shifted lobe with a chain of knots, visible in the optical wavelengths, terminating in a bow shock at its head (Podio et al., 2009).

1.1.3.2 Driving mechanisms

The precise mechanism which drives jets from YSOs is a current topic of debate. It is thought that jets are launched from a region less than 1 AU in diameter, making observations of these regions difficult (Ray, 2007b). However, observations associate them with rotating, magnetised accretion disks, which is suggestive that their origin lies in an MHD process in the rotating and accreting star-disk system, where the system undergoes both accretion and ejection. Blandford and Payne (1982) put forward the idea of a centrifugally driven outflow which removes energy and angular momentum from Keplerian disks which are threaded by magnetic field lines. They demonstrated that matter infalling from a disk could be magnetocentrifugally driven outwards, provided the poloidal field line components are bent outwards (away from the disk rotation axis) by more than 30°. This was suggested as the origin of protostellar jets by Pudritz and Norman (1983). There are two current theories based on this model; the disk wind model (D-wind), and the X-wind model (both depicted in Fig. 1.5). The aim of these theories is to determine the magnetic field configurations that are able to centrifugally accelerate matter along the magnetic field lines threading through the protostellar disk. In the disk wind model, large-scale, open magnetic field lines are anchored in the disk and outflows have the form of centrifugally driven winds which eject infalling material from every annulus of the disk surface, i.e. from multiple radii in the disk (Königl and Pudritz, 2000; Ferreira et al., 2006). In contrast, in the X-wind model the magnetic field lines are anchored close to the inner disk radius, at the stellar magnetosphere-disk interface (Shu et al., 1994, 2000). Both models are able to explain how excess angular momentum is removed from the star-disk system. The X-wind model removes most of the Keplerian angular momentum from the inner edge of the disk, whereas the D-wind model allows angular momentum transport at each annulus. Disk-winds are slower, less well-collimated and expected to eject $\sim 10\%$ of accreting material, compared to $\sim 30\%$ with the X-wind model. High-resolution ALMA observations find both a wide-angle component and a well-collimated, episodic component (Zhang et al., 2016, 2019) which suggests both mechanisms could be working simultaneously.

The angular momentum which can be contained in a single star is orders of magnitude less than the angular momentum of the core from which it is formed, suggestive of the fact that there is a mechanism at play by which angular momentum is lost or redistributed during the accretion phase of the protostar (Larson, 2003). As a

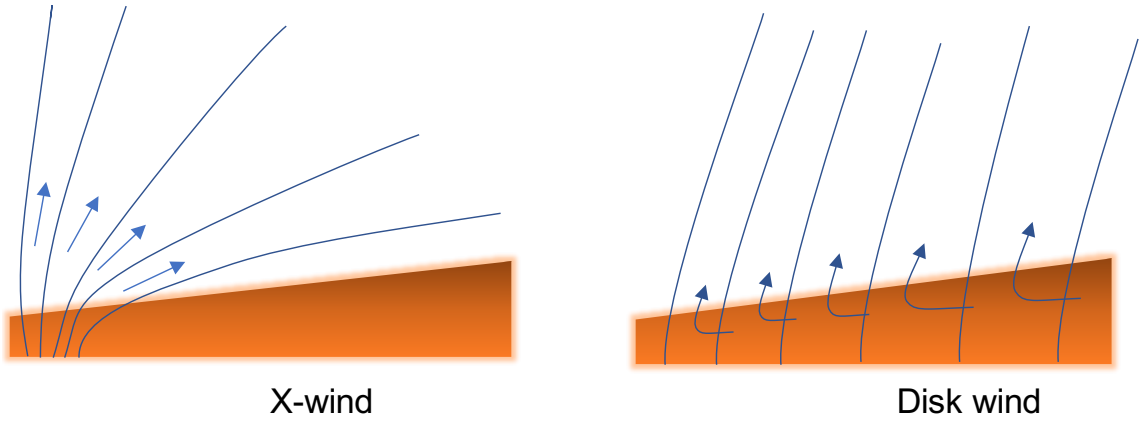

Figure 1.5: Comparison of X-wind (left) and disk wind (right) jet launching mechanisms. The orange plane represents the accretion disk which belongs to a central protostar, the blue lines represent the magnetic field lines which thread through the disk, and the arrows show the paths of the material which is launched from the disk. In the X-wind theory, the entirety of the stellar magnetic flux initially threading the disk is trapped inside a narrow annulus at the inner edge of the disk (Shu et al., 2000). In contrast, in the extended disk wind theory the magnetic field threads the disk at a range of annuli (Königl and Pudritz, 2000).

result of driving winds, rotating stars experience magnetic braking. The magnetic field lines threading through the protostar enforce co-rotation of the disk with the star at the Alfvén radius, where the outflow speed corresponds to the Alfvén speed, given by

$$v_A = \frac{B}{(4\pi\rho)^{1/2}} \tag{1.34}$$

where B is the magnetic field strength and ρ is the cloud core density. If the magnetic field through a collapsing core becomes sufficiently twisted, so that the magnetic field strength becomes very large, then v_A will become correspondingly large. As there is a strong coupling between the magnetic field and the charged particles, and ambipolar diffusion is too slow to take effect, some amount of the infalling material will be taken along with the Alfvén waves and angular momentum is extracted from the rotating body by the outflow (Pudritz and Ray, 2019).

1.1.3.3 Feedback

The feedback from magnetically-launched outflows has a number of important implications. Outflows interact with the surrounding medium, causing cavities in their parent cloud. The opening angles of outflows increase with evolutionary stage of the protostar (Cantó et al., 2008). The clearing out of material imposes a limit on the accretion rate of the source star as infall of material onto the protostar is suppressed, in turn determining its final mass (Cunningham et al., 2018; Matzner and McKee,

2000). At distances beyond the dense core radius (~ 0.04 pc) outflows disturb the medium, injecting momentum and, provided they are not highly-collimated (Banerjee et al., 2007), driving large-scale turbulence. This has the effect of reducing the global star formation efficiency, which has been confirmed by simulations (Federrath et al., 2016). This could help to explain why the observed star formation rate is much lower than would be expected given the amount of gravitationally bound gas which is available (Kuiper et al., 2000; Offner and Arce, 2014).

Shocks caused by outflows heat the gas, allowing chemical reactions to proceed which are usually inhibited in cold, dense clouds. HH knots in the outflows generate UV radiation, stimulating photochemistry in the gas. Finally, dust grains in the parent cloud lock up elements such as Fe, Mg and Si as they make up the silicates and oxides which condense to form grains in the cold cloud. Furthermore, shocks driven by outflows cause destruction of dust grains, which releases these elements back into the gas phase (Richer et al., 2000).

1.2 Magnetohydrodynamic shocks

Shocks are a prominent feature of star-forming regions, with emission tracing bow shocks due to outflows from YSOs being an important diagnostic. Molecular clouds can be treated as a plasma, which is an electrically conducting fluid. They are also threaded by, often significant, magnetic fields, so modelling the shocks in these regions requires an MHD description. Based on works by Hartquist (2017), Schnack (2009), Kulsrud (2009) and Boyd and Sanderson (2003), this section will introduce shocks in such regions.

A plasma occurs when electrons are able to detach from atoms, resulting in a fluid with free electrons and positively charged ions. It can be fully ionised (no neutral particles present), or partially ionised (including neutral particles). A fluid description of matter requires that it is sufficiently collisional, so that the mean free path between collisions is short compared with the distance over which the fluid parameters vary. In this case, the fluid can be described by its mass density, ρ, mean velocity $\mathbf{v}$ and temperature T. To derive the equations which govern how these fluid properties change, we consider an infinitesimal volume element dV. There are then two possible approaches:

1. **Eulerian** - the volume element is fixed in space, and the fluid parameters are functions of space and time.

2. **Langrangian** - the surface of the volume element is co-moving with the fluid, and the fluid parameters are functions of time only.

The Eulerian description is adopted in this thesis.

The full set of MHD equations consist of those which describe the conservation of mass, momentum, energy and magnetic flux[1],

$$\frac{\partial p}{\partial t} + \nabla \cdot (\rho \mathbf{v}) = 0, \tag{1.35}$$

$$\frac{\partial (\rho \mathbf{v})}{\partial t} + \nabla \cdot (\rho \mathbf{v})\mathbf{v} + \nabla p = \frac{1}{\mu_0} (\nabla \times \mathbf{B}) \times \mathbf{B}, \tag{1.36}$$

$$\frac{\partial}{\partial t} \left(\frac{1}{2}\rho v^2 + \frac{p}{\gamma - 1} + \frac{B^2}{2\mu_0} \right) + \nabla \cdot \left\{ \left[\frac{1}{2}\rho v^2 + \frac{p\gamma}{\gamma - 1} \right] \mathbf{v} + \frac{1}{\mu_0} \mathbf{B} \times (\mathbf{v} \times \mathbf{B}) \right\} = 0, \tag{1.37}$$

and

$$\frac{\partial \mathbf{B}}{\partial t} = \nabla \times (\mathbf{v} \times \mathbf{B}) + \frac{\eta}{\mu_0} \nabla^2 \mathbf{B} \tag{1.38}$$

where p is the pressure, ρ is the density, $\mathbf{v}$ is the velocity, $\mathbf{B}$ is the magnetic field strength, μ_0 is the permeability of free space, η is the resistivity and γ is the ratio of specific heat capacities.

MHD waves are the perturbations of the fundamental fluid quantities from smooth motion. The wave solutions determined after perturbations are applied to the MHD equations allude to three wave modes; fast, intermediate and slow. Intermediate (or shear Alfvén) waves are purely transverse, and propagate in the direction of the magnetic field. Conversely, slow and fast mode (termed magnetosonic) waves are compressional and involve perturbations of both the magnetic field and the hydrodynamic fluid parameters. The speeds corresponding to each wave mode are found from the roots of the dispersion relation for the plasma. The Alfvén speed, v_A, is given in Eq. 1.34. The fast and slow magnetosonic speeds are

$$v_{\pm} = \left\{ \frac{1}{2} \left[v_A^2 + c_s^2 \pm \sqrt{\left(v_A^2 + c_s^2\right)^2 - 4 v_A^2 c_s^2 \cos^2 \theta} \right] \right\}^{1/2} \tag{1.39}$$

[1]Note that the MHD equations are not used in this form for the numerical model used in this Thesis. See Chapter 2 for a full description of the MHD equations used.

where c_s is the sound speed and θ is the angle between the magnetic field and the direction of propagation of the wave. Note that $v_+ \geq v_-$, where v_+ is the fast mode speed and v_- is the slow mode speed.

1.2.1 Single fluid MHD shocks

A flow that is supersonic will generate a shock wave. For a purely neutral fluid, the resulting compression will travel through the medium at the sound speed c_s. If the source of the compression travels faster than c_s it overtakes the wavefront, and the state of the fluid changes in a sudden manner. In conducting fluids with a magnetic field, the fluid is able to support additional wave modes and there are three wave speeds; fast magnetosonic, intermediate, and slow magnetosonic. Intermediate waves do not steepen to form shock waves. The fast and slow magnetosonic waves contain longitudinal components in addition the transverse ones so can result in shocks. If all the components of the flow can be considered to travel with the same velocity, a shock in the fluid can be treated as a single-fluid MHD shock.

For simplicity, we assume that the shock wave is plane-parallel, propagating in the x-direction, and take the magnetic field to lie in the $x-y$ plane. Additionally, we take the reference frame to be the rest frame of the shock, so the upstream velocity is $v_x = \mathbf{v} - v_s$ where v_s is the shock speed. The relations between the upstream (identified by the subscript 1) and downstream (subscript 2) fluid parameters can be determined by considering the steady-state (i.e. time-independent) MHD equations, and are given by

$$\rho_2 v_{x,2} = \rho_1 v_{x,1}, \tag{1.40}$$

$$\rho_2 v_{x,2}^2 + p_2 + \frac{B_{y,2}^2}{\mu_0} = \rho_1 v_{x,1}^2 + p_1 + \frac{B_{y,1}^2}{\mu_0}, \tag{1.41}$$

$$\rho_2 v_{x,2} v_{y,2} + \frac{B_{x,2} B_{y,2}}{\mu_0} = \frac{B_{x,1} B_{y,1}}{\mu_0}, \tag{1.42}$$

$$\begin{aligned} \frac{1}{2}\rho_2 v_{x,2}\left(v_{x,2}^2 + v_{y,2}^2\right) + \frac{\gamma p_2 v_{x,2}}{\gamma - 1} + \frac{1}{\mu_0}\left(v_{x,2} B_{y,2}^2 - v_{y,2} B_{x,2} B_{y,2}\right) = \\ \frac{1}{2}\rho_1 v_{x,1}^3 + \frac{\gamma p_1 v_{x,1}}{\gamma - 1} + \frac{v_{x,1} B_{y,1}^2}{\mu_0}, \end{aligned} \tag{1.43}$$

and

$$v_{x,2} B_{y,2} - v_{y,2} B_{x,2} = v_{x,1} B_{y,1}. \tag{1.44}$$

In addition, from $\nabla \cdot \mathbf{B} = 0$ it follows that

$$B_{x,2} = B_{x,1}. \tag{1.45}$$

Eqs. 1.40 - 1.45 are the MHD Rankine-Hugoniot jump conditions.

1.2.1.1 Perpendicular shocks

In the case of perpendicular shocks, the magnetic field makes an angle $\theta = \pi/2$ with the shock propagation direction. In this case, take the upstream magnetic field to be in the y-direction, so that $B_{x,1} = 0$ and therefore, by Eq. 1.45, $B_{x,2} = 0$. Then, the jump conditions are simplified and can be combined to form a cubic equation for the compression ratio ρ_2/ρ_1. It can be shown that one solution to this equation is $\rho_2/\rho_1 = 1$ (Williams et al., 2017), so dividing by $\rho_2/\rho_1 - 1$ results in the quadratic equation

$$\begin{aligned} 2(2-\gamma)\left(\frac{\rho_2}{\rho_1}\right)^2 + \left[2\gamma\left(2\mu_0\frac{P_1}{B_{y,1}^2} + 1\right) + 2\mu_0\frac{p_1}{B_{y,1}^2}\gamma(\gamma-1)M_1^2\right]\frac{\rho_2}{\rho_1} \\ - 2\mu_0\frac{p_1}{B_{y,1}^2}\gamma(\gamma+1)M_1^2 = 0 \end{aligned} \tag{1.46}$$

where $M_1 = v_s/c_{s,1}$ is the Mach number (remembering that $v_s = v_{x,1}$). For $\gamma < 2$ this equation has one positive root,

$$\frac{\rho_2}{\rho_1} = \frac{2(\gamma+1)}{D + \left[D^2 + 4(\gamma+1)(2-\gamma)M_A^{-2}\right]^{1/2}} \tag{1.47}$$

where

$$D = (\gamma - 1) + \left(2M_1^{-2} + \gamma M_A^{-2}\right) \tag{1.48}$$

and $M_A = v_s/v_{A,1}$ (where $v_{A,1} = B_{y,1}/(\mu_0\rho_1)^{1/2}$) is the Alfvénic Mach number. The only possible shock is then determined by $v_s^2 > c_{s1}^2 + v_{A,1}^2$, and is therefore a fast mode shock since the shock speed must be greater than the fast magnetosonic sound speed.

1.2.1.2 Oblique shocks

Oblique shocks occur when the magnetic field lies at an arbitrary angle $0 < \theta < \pi/2$ to the shock propagation direction. In this case, there are a number of solutions for the compression ratio and the shocks, analogously to the MHD wave modes, can be categorised as fast and slow shocks. For fast shocks, the transverse component

of the magnetic field increases across the shock, whereas the opposite is true for slow shocks. For sufficiently strong shocks ($M_1 \gg 1$ and $M_{a,1} \gg 1$) and for a value of $\gamma = 5/3$, the compression ratio has a limit of $\rho_2/\rho_1 = 4$. The solution then corresponds to a fast shock, implying that intermediate and slow shocks do not exist for shocks above a certain strength.

1.2.2 Multifluid MHD shocks

The molecular clouds where stars form have a very low fractional ionisation, on the order of 10^{-7} or less. The magnetic field affects the charged species present in the medium, but not the neutral particles. The result of this is that the different species no longer necessarily travel with the same velocity, and therefore must be treated as distinct fluids. Ambipolar diffusion occurs, since the charged particles move relative to the neutrals due to the action of the magnetic field, and the ion-neutral collisional coupling is small due to the small mass density of ions. A disturbance propagating through the plasma at a velocity $v_s > c_{s,1}$ will cause a shock. However, the structure of the shock is strongly dependent on the whether the shock is faster or slower than the fast magnetosonic speed of waves supported by the charged fluid.

1.2.2.1 C-type and J-type shocks

When the shock speed is less than the ion magnetosonic speed (or, equivalently, when the magnetic field is sufficiently strong), information can propagate upstream of the shock in the charged fluid. The charged fluid parameters no longer experience a discontinuity, but rather vary continuously through the shock. The magnetosonic waves which travel ahead of the neutral shock front compress the magnetic field, in which case it is said that the shock has a magnetic precursor. Ion-neutral collisions heat and accelerate the neutral fluid ahead of the shock as well and, providing radiative cooling is sufficient that neutral fluid remains supersonic everywhere, the neutral fluid will also experience a continuous change in its fluid parameters. Such a shock is known as a C-type shock (Draine, 1980).

A J-type shock may exist with or without a magnetic precursor. A shock speed that exceeds the magnetosonic speed of the charged fluid, which usually indicates the presence of a small, or non-existent, upstream magnetic field, results in a J-type shock front without a precursor. In this case there is a discontinuous jump in the fluid parameters of both the neutral and charged fluids. However, there is also a

case where the shock speed is smaller than the charged magnetosonic speed, but the transverse component of the magnetic field is smaller than some critical value. Then, the momentum and energy transferred to the neutral fluid ahead of the shock is not sufficient to cause a smooth variation in the neutral fluid, despite the charged fluid varying continuously. This is a J-type shock with a magnetic precursor.

The different shock structures are shown in Fig. 1.6. The shock waves due to low-velocity ($\lesssim 50$ km s^{-1}) YSO outflows in molecular clouds are expected to be C-type, due to presence of substantial magnetic fields and a low fractional ionisation. This means that a multifluid model is required to describe the structure of the molecular shocks in star-forming regions. A further consideration to make is the presence of dust grains, since they are known to carry charge and can therefore have significant effects on the dynamics of C-type shocks. Additionally, the grain-neutral relative velocity, which results from grains being charged, allows grain destruction by sputtering, and the relative velocity between different sizes of grains leads to grain-grain collisions. Hence, dust grains are an essential consideration in the modelling of C-type shocks.

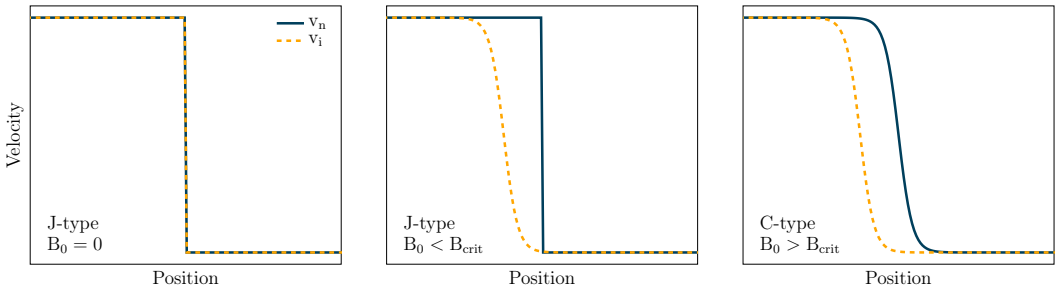

Figure 1.6: Schematic of the different shock types. B_0 is the transverse magnetic field, and v_n and v_i are the neutral and ion fluid velocities, respectively. In the leftmost plot there is no transverse magnetic field and the shock speed is greater than the fast magnetosonic speed. No magnetosonic waves can travel ahead of the shock, there is a discontinuity in the neutral and ion velocities and the shock is J-type without a magnetic precursor. The centre plot is similar, but with a small magnetic field so the ion velocity differs slightly from the neutral velocity due to the difference in the compression ratios of the fluids. There is a magnetic precursor present and the ion velocity varies continuously, but since $B_0 < B_{crit}$ the effect is not transferred to the neutral fluid. In the rightmost plot the shock speed is less than the fast magnetosonic speed and the magnetic field exceeds the critical value required for a C-type shock to occur. The velocities of both the neutrals and charged particles vary continuously with position in the shock.

1.3 Interstellar dust grains

Dust grains make up a relatively modest amount of the mass of the ISM, where there is a gas-to-dust mass ratio of 100:1. Despite this, dust grains are very effective at absorbing and scattering starlight; it is estimated that upwards of 30% of the starlight emitted by the galaxy is re-emitted by dust at infrared wavelengths (Bernstein et al., 2002). It is not just this extinction effect that has important astrophysical implications. Dust grains have dynamical, thermal and chemical influences on the ISM, which in turn lead to changes in the composition and emission signatures of the gas. The first suggestion of material causing the obscuration of light from stars reaching us was by William Herschel in the late 18^{th} century, who noted a 'hole' in the sky and speculated that this was not due to the absence of stars in this region, but could be due to the presence of some material between us and the stars. Following this, in the 19^{th} century, Struve noted that the number of stars seemed to decrease with distance from Earth, hinting at a more general extinction of starlight in the ISM. More recently, in the 20^{th} century, Trumpler made observations of globular clusters which confirmed this general extinction, and in addition showed that this extinction varied with colour; blue light was more heavily obscured than red. Stebbins et al. explained in 1939 that this wavelength-dependent extinction could be caused by dust with sizes comparable to those wavelengths which are extinguished (Williams and Cecchi-Pestellini, 2019).

Since the discovery of dust and its ubiquitous nature, its astrophysical significance has gradually been unveiled. The emission features of dust tell us that their cores are likely composed of graphite and silicate-based materials, which leads to depletion in the ISM of heavy elements such as Mg, Fe and Si. Observations of enhanced abundances of these materials in the gas, for example SiO in star-forming regions, therefore suggest destruction of grains occurs in interstellar shocks. In regions where UV light is present, dust grains can dominate the heating of the gas via the emission of photoelectrons. The surfaces of dust grains are an important location for chemical reactions and molecule formation; they are a catalyst for the formation of H_2, the most abundant molecule in the universe. Finally, dust grains play a role in the formation of stars and planets. It is evident that to model events in the ISM, particularly in the star-forming regions we are interested in here, the impact of

dust grains on the dynamics, chemistry and composition of the gas, as well as the evolution of the dust itself, must be an important consideration.

1.3.1 Extinction

Evidence for the existence of interstellar dust includes the extinction, reddening and polarisation of starlight. Extinction is the sum of absorption and scattering, and the fact that extinction is greater for blue light than for red light means this extinction is referred to as reddening. In regions where there is more reddening, there is also a greater degree of polarisation of the starlight, indicating that dust is the cause of this polarisation. Extinction due to dust alters the apparent magnitude of a star as a function of wavelength according to

$$m(\lambda) = M(\lambda) + 5\,\log(d) + A_\lambda \tag{1.49}$$

where M is the absolute magnitude, d is the distance to the star and A_λ is the extinction due to dust at a particular wavelength. It is found that the amount of extinction increases inversely with wavelength through the optical range. The extinction curve is obtained by comparing the apparent magnitude of a reddened star with that of a star with the same spectral type, but negligible amounts of obscuring dust (so attenuation is due only to the inverse square law). This gives a difference in apparent magnitude between the two stars of

$$\Delta m(\lambda) = 5\,\log\left(\frac{d_1}{d_2}\right) + A_\lambda. \tag{1.50}$$

The difference between the difference in apparent magnitude as measured at two different wavelengths is known as the colour excess. A commonly used colour excess is between the B photometric band (at 4405 Å) and the V band (at 5470 Å), so that

$$E(B-V) = A_B - A_V \tag{1.51}$$

is the amount of reddening. The shape of the extinction curve depends on the line-of-sight of the observations. A way of characterising the shape is to use a dimensionless parameter R_v which describes the slope of the extinction curve through the optical wavelengths and is given by

$$R_V = \frac{A_V}{A_B - A_V} = \frac{A_V}{E(B-V)}. \tag{1.52}$$

The range of observed R_V values is about 2 to 6, but it is commonly accepted to use the average value of $R_v \approx 3.1$ for diffuse ISM regions, and a value of $R_v \approx 5$ for dense clouds. The extinction curve for a range of R_V values as presented by Draine (2004) is shown in Figure 1.7.

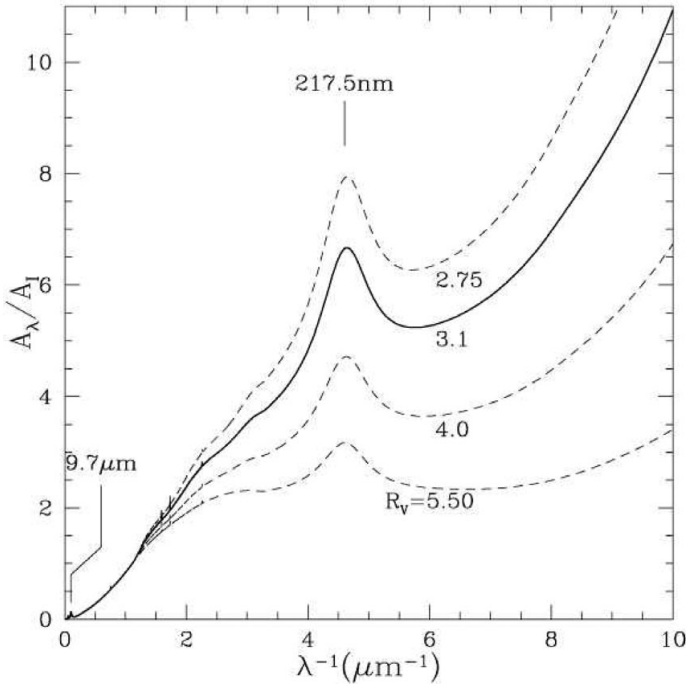

Figure 1.7: The ratio of the extinction at a wavelength λ to the extinction at I = 0.9 μm for a range of R_V values. The silicate feature at 9.7 μm is labelled, as is the graphite feature at 0.1275 μm.(Draine, 2004)

The wavelength dependence of the extinction is influenced by both the composition and the size distribution of the dust grains. We see that for wavelengths between 0.1 μm and 10 μm, the extinction is dominated by absorption and is consistent with Rayleigh scattering. Rayleigh scattering occurs in the regime in which the sizes of the dust grains are much smaller than the wavelength of light, so comparison of the circumference of the grains with the wavelength is $2\pi a/\lambda \ll 1$ where a is the grain radius. Additionally, towards the shortest UV wavelengths, we do not see a flattening of the extinction curve, which suggests that the Rayleigh scattering regime is maintained at these wavelengths, hence there must be a significant population of dust grains smaller than about 0.015 μm.

1.3.2 Composition and size distribution

The Milky Way extinction curve is heavily constrained by the composition and size distribution of dust grains. As we have seen, the fact that the extinction is wavelength-dependent across a broad range of wavelengths must mean that dust grains exist in a broad range of sizes; from $a \lesssim 0.01$ μm to $a \gtrsim 0.2$ μm. Additionally, spectroscopic features indicate the possible range of compositions. The feature at $\lambda = 2175$ Å, which can be seen in Figure 1.7, is the strongest UV-visible signature of dust, and is in the same position for all lines of sight (i.e. all R_V values) as well as appearing to be comparable in strength for both diffuse and dense clouds. The strength of the feature indicates it is due to an abundant element, so is likely to be oxygen- or carbon-rich, and is well-fitted by a Drude profile, which tends to describe metals or semi-metals, like graphite. The graphite hypothesis appears to match the observational constraints well and suggests that the feature can be reproduced using small, spherical graphite grains (Draine, 1989). Another notable feature seen in Figure 1.7 is the one at 9.7 μm. This feature is well-matched to the Si-O stretching mode and is therefore strongly suggestive of silicate materials. Further evidence of silicates is that the corresponding 10 μm emission feature is observed in the outflows from oxygen-rich stars, but not in those of carbon-rich stars. A feature which only appears when the line of sight is not confined to diffuse clouds is at a wavelength of 3.1 μm and is consistent with the O-H stretching mode in H_2O ice. This suggests that in dense clouds icy mantles are present on the dust grains.

The extinction curve indicates that there are many more small grains than there are large grains. Mathis et al. (1977) introduced a model consisting of a mixture of graphite and silicate-based grains with sizes from 0.005 μm to 1 μm distributed in a power-law according to

$$\frac{\mathrm{d}n(a)}{\mathrm{d}a} \propto a^{-3.5} \tag{1.53}$$

where $\mathrm{d}n(a)/\mathrm{d}a \times \mathrm{d}a$ is the number density of grains in the size interval $(a, a + \mathrm{d}a)$. This is known as the MRN distribution, and remains an often-used tool for modelling dust grains in the ISM.

1.3.3 Physical processes

As we have seen, the size distribution of dust grains in the ISM is, at least approximately, power-law in nature. Locally, this size distribution is affected by physical

processes. The processes are depicted in Figure 1.8 and can be broadly divided into two categories; mass-conserving or number-conserving. Mass-conserving processes, such as grain-grain shattering and coagulation, conserve the total mass of grain material in the distribution, but cause a change to the total number of grains. Conversely, number-conserving processes, such as gas-grain sputtering, vaporisation in grain-grain collisions, and growth by accretion, conserve the total number of grains in the distribution, but change the mass. Dust grains predominantly grow by mantle accretion (e.g. Whittet et al., 2013) and coagulation (e.g. Stepnik et al., 2003), which occur in quiescent, dense molecular clouds. On the other hand, grain destruction occurs, for example, in supernovae remnants (e.g. Arendt et al., 2010), due to the shocks caused by outflows from YSOs (e.g. Van Loo et al., 2013), and due to fragmentation in protoplanetary disks (e.g. Birnstiel et al., 2010).

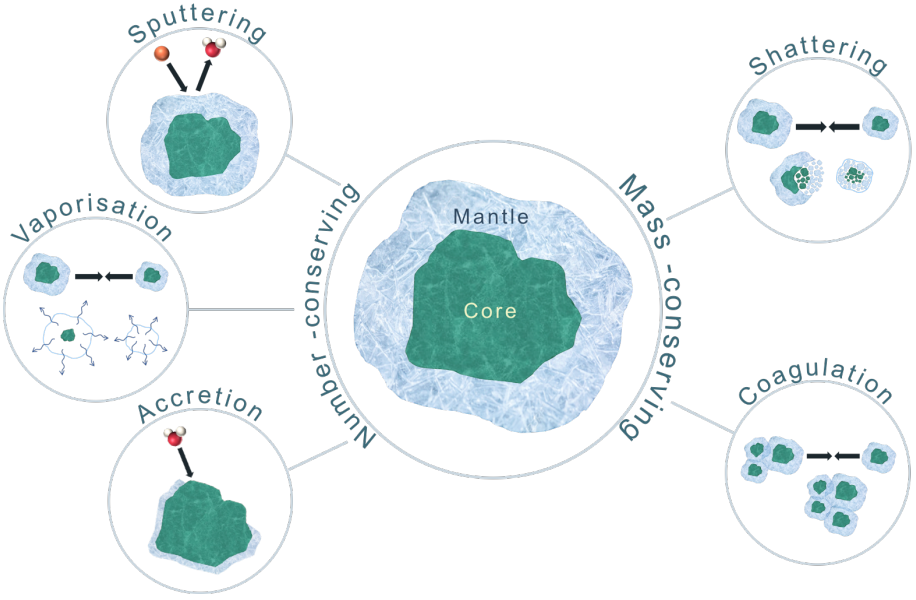

Figure 1.8: The physical processes which affect dust grains in the ISM and cause their size distribution to evolve. Dust grains can be modelled as a core (made up of olivine, for example) and an icy mantle. The processes can be broadly categorised into those that are number-conserving and those that are mass-conserving.

1.4 Research context and literature review

The interstellar medium can be a violent place, owing to high-energy phenomena such as supernovae, cloud-cloud collisions and protostellar outflows. Over the last four decades, this has motivated researchers to develop theoretical models to progress our understanding of the effects these events have on the ISM. Of particular interest

here are the shocks that these phenomena produce, which inject energy and momentum into the material that they propagate through, affecting the physical conditions and chemistry occurring in these regions. The emission lines resulting from shocks provide important tracers, such as CO, SiO, H_2 and H_2O, which allow observers to image and diagnose the sites where shocks occur (e.g. Tafalla and Bachiller, 2011). A number of elements, for example Si, Fe and Mg, are usually depleted from the gas into dust grain material in molecular clouds. These elements experience substantial increases in abundances due to the destruction of grains in shocks (Reipurth and Bally, 2001), hence the need to include dust grain processes into theoretical shock models is clear. This thesis has a focus on C-type shocks in dense clouds due to protostellar outflows, so the review that follows is mainly restricted to this field, with the intention of making clear the progression of relevant models over the years, and the areas which remain to be developed.

Early MHD models of interstellar shocks include those by Field et al. (1968) and Mullan (1971). The model of Field et al. (1968) focuses on shocks in HI regions and involves added magnetic terms to the Rankine-Hugoniot jump conditions to obtain postshock profiles of the gas temperature, density, pressure and magnetic pressure. The magnetic field is assumed to be "frozen" into the gas, and the field strength increases as the field lines are compressed by the shock. Mullan (1971) recognised, however, that in regions of low fractional ionisaton the frozen field assumption may no longer hold, and the charged and neutral particles should be described by the hydrodynamical equations, with their velocities and temperatures allowed to vary from one another. This makes it one of the first multifluid MHD shock descriptions. Draine (1980) expanded on the idea of a multifluid model by analysing steady, radiative, transverse shocks in a weakly-ionised gas, and introduced the concept of a magnetic precursor. Draine (1980) showed that, under particular conditions, the charged fluid can be compressed and accelerated ahead of the shock front since the magnetosonic speed of waves propagating in the charge fluid is greater than the shock speed. If the magnetic field is large enough, collisions between the charged fluid and the neutrals in the precursor heats the neutrals ahead of the shock and the fluid parameters vary continuously, resulting in a C-type shock rather than a J-type one (see §1.2.2.1). In addition, Draine (1980) includes charged grain dynamics in the model, along with chemistry involving important coolants such as H_2, CO, OH and H_2O. The subsequent work by Draine et al. (1983) continued the analysis of C-type shocks, suggesting that in dense, molecular clouds C-type shocks would in

fact be the norm, due to the high magnetic fields and low fractional ionisation which characterise dense clouds.

Until the oblique model by Wardle and Draine (1987), most previous models examined transverse shocks, where the magnetic field lies perpendicular to the shock propagation direction (e.g. Draine, 1980; Draine et al., 1983; Seab and Shull, 1983; McKee et al., 1987). This is a special case which allows the fluid equations to be simplified. However, as noted noted by Wardle and Draine (1987), a randomly oriented magnetic field makes a median angle of $\theta = 60^o$ with the shock propagation direction, so transverse shocks should not necessarily be the default case. They found that the C-type shock structure in diffuse media is weakly dependent on the angle θ, with shocks becoming stronger with decreasing angle. However, the model of Wardle and Draine (1987) did not include dust grains. Dust grains are thought to have important implications for shock models since they carry charge and can affect the ionisation and thermal structure. In addition, grain destruction and disruption provide a means of returning depleted elements such as Si, Fe and Mg to the gas phase where they take part in chemical reactions and provide important observational tracers (e.g. Jura, 1976; Schilke et al., 1997).

A steady-state oblique shock model presented by Pilipp and Hartquist (1994) found that collisions between grains and neutral particles can cause rotation of the magnetic field around the direction of propagation of C-type shocks. Their shock model is set up as follows. Take the shock to be plane parallel, and propagating in the x-direction. For the shock to be oblique, the magnetic field makes some angle θ with the x-axis, and it is assumed that the magnetic field initially lies in the $x - y$ plane (i.e. it has no z-component). When grain-neutral collisions are significant, there can exist a non-zero component of the Hall current (which arises when there are electric currents transverse to the magnetic field) in the direction of propagation of the shock. There must therefore be a current parallel to the magnetic field which has a component in the x-direction to cancel out the Hall current. Ampere's law demonstrates that this current parallel to the magnetic field generates a component of the magnetic field in the z-direction, i.e. out of the plane of the shock. However, due to their method of integrating the MHD equations in a downstream direction, Pilipp and Hartquist (1994) were unable to find steady-state fast mode shock solutions. The work by Wardle (1998) argued that this method is ineffective

since integrating in a downstream direction yields a downstream solution which is a saddle point, and in fact fast mode solutions can be found by instead integrating in an upstream direction.

Integration in the upstream direction is valid under the condition that equilibrium values hold at every point in the shock. This is not often the case, for example the abundances of chemical species can vary from steady state for substantial amounts of time. Therefore, a time-dependent approach is required, such as that developed by Falle (2003). Van Loo et al. (2009) use the formulation of Falle (2003) to model time-dependent oblique shocks and confirmed that for preshock densities $> 10^4$ cm^{-3} there is significant rotation of the magnetic field. In these models grain-neutral collisions dominate the drag force on the neutrals, and substantial charge separation causes a sizeable Hall conductivity. The degree of rotation increases as the angle θ decreases, whereas the shock width decreases. However, this was for the inclusion of a single grain fluid, where all the grains had a radius of 4×10^{-5} cm. The inclusion of a second, smaller-sized grain fluid causes depletion of electrons, since the small grains are much more abundant than the large grains. The small grains are therefore much better coupled to the magnetic field, reducing the Hall conductivity and therefore minimising the magnetic field rotation.

The effect of including an MRN dust grain-size distribution, as opposed to single-sized grain fluids, is explored by Chapman and Wardle (2006) in their oblique, C-type shock models. It was determined that whilst small grains are well-coupled to the magnetic field, large grains become partially decoupled from the field due to collisions. There is an increase in the overall grain charge through the shock due to electrons sticking to the grain surfaces, thus increasing the coupling of large grains to the magnetic field. This therefore suppresses the rotation of the field out of the plane of the shock. The maximum peak in the component of the field out of the shock plane is reduced when using an MRN distribution compared with single-sized grains. This is because although larger grains are less well coupled to the field, smaller grains have a much higher abundance, so minimise the field rotation.

Apart from the effect of grain dynamics on the shock structure, grains also undergo destructive processes which release heavy elements into the gas phase and influence the chemistry in shocked regions. Early models to include dust grain processes are those of Cowie (1978), Shull (1977) and Shull (1978). The model by Cowie (1978) attempts to describe the observations of increased Si abundance in high-velocity gas by considering gas-grain sputtering and grain-grain collisions in MHD

shocks through an analytic formulation. The model by Shull (1977, 1978) is a time-dependent code which incorporates ionisation processes, radiative cooling and an examination of dust grain destruction for five different grain materials. Here, the grains are all of initial size a = 10^{-5} cm, and the shocks have velocities in the range $50 - 120$ km s^{-1} so are not representative of C-type shocks. The model by Pilipp et al. (1990) includes dust grains as a distinct fluid in their 4-fluid perpendicular C-type shock code. The model provides a more complex treatment of the ionisation balance, grain charging and dynamics than previous ones, and includes a number of chemical reactions. In comparing their results with those achieved from following the method of Draine et al. (1983), Pilipp et al. (1990) conclude that the more accurate dust grain treatment leads to a higher and narrower peak in the gas temperature, due to the fact that the gas-grain relative speed is increased. However, one limitation of their model is that grains are single-sized. A number of subsequent works also incorporated dust grains as single-sized fluids (e.g. Flower and des Forêts, 1994, 1995; Flower et al., 1996; Schilke et al., 1997; Caselli et al., 1997; May et al., 2000; Ciolek et al., 2004), the majority of which focused on perpendicular shocks.

The effect of gas-grain sputtering is explored by Flower and des Forêts (1994, 1995) who include the effect of ice mantle sputtering of single-sized grains on the chemistry and thermal shock profile. They found that a 10 km s^{-1} shock propagating through a medium with a preshock density of 10^4 cm^{-3} is sufficient to cause total mantle removal, with the degree of sputtering determined by the shock speed. Schilke et al. (1997) study the production of SiO through sputtering of silicate grain cores with Si-bearing mantles, finding that the best agreement with observed gas phase SiO abundances occurs for a 25 km s^{-1} shock propagating through a medium of preshock density 10^5 cm^{-3}. May et al. (2000) use the model of Field et al. (2004) but with newly determined sputtering yields. For perpendicular, C-type shocks through densities from $10^4 - 10^6$ cm^{-3} their calculated Si and SiO column densities best agree with observations for shock speeds in the narrow range of $25 - 30$ km s^{-1}, regardless of the preshock density.

As time has progressed, shock models have become increasingly comprehensive, working towards codes which self-consistently solve the shock and dust grain dynamics, along with the ionisation structure, chemistry, thermal structure and physical processes. Additionally, since observations suggest that interstellar dust exists in a distribution of sizes, with many more smaller grains than larger grains (see §1.3),

there has been work focusing on including grain-size distributions into C-type shock models. The recent work by Guillet et al. (2007), Guillet et al. (2011) and Anderl et al. (2013) utilise a self-consistent model for transverse, C-type shocks, including an extensive chemical network of over 90 chemical species and ~ 1000 reactions, as well as using a distribution of grain sizes which is evolved due to sputtering and grain-grain collisions.

While these may be some of the most comprehensive models to date, the description of the grain-size distribution involves a piecewise-constant discretisation, where each discrete size bin is characterised by average or mid-point values. Additionally, these models describe either the mass *or* number density of grains in each bin. The formulation by McKinnon et al. (2018) follows both grain properties in each bin, allowing the distribution to be described in a piecewise-linear manner (i.e. a higher-order approximation than piecewise-constant). There is clearly scope for developing methods which are more accurately able to follow the evolution of the dust grain-size distribution through C-type shocks in molecular clouds, in particular for power-law distributions like the MRN distribution, since these require the use of many bins in order to be well-approximated by a piecewise-constant approach. Furthermore, Guillet et al. (2007), Guillet et al. (2011) and Anderl et al. (2013) focus on transverse shocks. We have already seen the potential importance of taking into account varying magnetic field angles in terms of determining shock structures.

The effect of including more than one size of grain when incorporating dust grain destruction into oblique C-type shock models was explored by Van Loo et al. (2013). They applied gas-grain sputtering to two single-sized grain fluids where the grains were coated by a H_2O ice mantle and found that, due to the larger grain-neutral drift speeds, the smaller grains experience more efficient sputtering than larger grains. It was determined that while complete mantle erosion occurs for shocks speeds of $20 - 25$ km s^{-1}, core grain material still remains even up to the so-called critical shock speed (where the shock transitions from C-type to J-type). Additionally, it was found that the magnetic field angle can have a significant impact on the degree of sputtering, particularly for drift speeds close to the sputtering threshold, with higher abundances of gas-phase SiO calculated for smaller angles. However, whilst the importance of the magnetic field angle is clearly demonstrated, the effect of grain-grain collisions has been ignored.

The models by Guillet et al. (2011) and Anderl et al. (2013) include shattering and vaporisation due to grain-grain collisions in perpendicular C-type shocks. They find

that shattering has important consequences for both the dust grain-size distribution, and for the shock dynamics. In particular, for preshock densities $> 10^4$ cm^{-3}, the production of many small grain fragments causes shocks which are hotter and narrower due to enhanced collisional coupling between charged particles and neutrals. They also find that vaporisation of grains due to grain-grain collisions is negligible for preshock densities $< 10^5$ cm^{-3}, but can dominate over sputtering at higher densities. Whilst these models make progress in understanding the impact grain-grain collisions have on the grain-size distribution and structure of C-type shocks, work remains to be done in including shattering and vaporisation into self-consistent oblique shock models.

Despite the fact that there has been a number of studies which include grain mantles, there has been little attempt so far in addressing the issue of evolving grain mantles in shocks where grain-grain shattering occurs. As Guillet et al. (2007, 2011) point out, this becomes a difficult task, which they solve by making the assumption that grain mantles have a constant thickness, regardless of the grain core size, at each timestep in the code, with the justification that the grains mostly follow the ion motion. It is also assumed that processing of grain mantles and cores happen in distinct regions of the shock, allowing the effect of shattering and vaporisation on the mantles to be neglected. However, this simplification relies on the fact that the dust grains are well-coupled to the magnetic field, and therefore the grain-neutral relative speed is independent of grain size, which doesn't hold for large grains. Models remain to be developed which are able to overcome this issue.

1.5 Summary and thesis structure

In this section the background theory to C-type shocks in star-forming regions has been introduced. The use of a multifluid approach for modelling these shocks is clearly a necessity, as is the careful consideration of dust grains, which affect both the dynamics of the shock and the chemical composition of the local gas phase. Computational models in the literature tend to focus on perpendicular shocks, which are a particular case of fast mode shock, and often use simplified grain descriptions. There is work to be done in forming more comprehensive descriptions, in the hope of

better understanding the role that grains have to play in shocks and the importance of feedback mechanisms on the fate of star-forming clouds.

The remainder of this thesis is structured as follows. Chapter 2 provides a description of the initial computational model, forming the basis of this work. Chapter 3 presents a number of improvements which were made to the code described in Chapter 2. Chapter 4 consists of work published in Sumpter and Van Loo (2020), and describes a new method for evolving power-law grain-size distributions due to number- and mass-conserving processes. Chapter 5 details the implementation of the method into the updated numerical model (this section is also published in Sumpter and Van Loo (2020)). Furthermore, the implementation is validated through test simulations with and without dust grain sputtering. Chapter 6 presents an improved method for evolving the grain-size distribution due to grain-grain collisions, and presents results for grain-grain collisions in combination with sputtering. Parts of Chapters 5 and 6 are currently in the process of being submitted for publication. Finally, Chapter 7 provides concluding remarks and details potential future work.

2

Computational method

This chapter presents the governing multifluid equations and details the computational method which is employed to solve them. The chemical reactions, source terms and dust grain treatment are also described for the case of C-type shocks in weakly-ionised plasmas.

Contents

In the dense, molecular clouds where stars form the fractional ionisation is $\lesssim 10^{-7}$ and the gas can be modelled as a weakly-ionised plasma. A magnetic field affects only the charged particles and not the neutrals, resulting in relative motion between the charged and neutral species. Collisions between neutrals and charged particles couple the neutrals to the magnetic field. The different species are described as distinct fluids, governed by their own set of equations. A numerical scheme for solving the multifluid MHD equations governing plane-parallel flow in 1-D is presented by Falle (2003) and it is this scheme that makes up the initial computational method in this thesis. In this chapter, the governing equations are presented and the chemistry, source terms and dust grain treatment are described as they were implemented in the model of Van Loo et al. (2013).

2.1 Governing equations

In dense, molecular clouds the plasma consists of N distinct fluids; neutrals, electrons, ions, and a number of dust grain fluids. The general equations of the time-dependent plane-parallel flow in 1-D[1] are

$$\frac{\partial \rho_j}{\partial t} + \frac{\partial}{\partial x}\left(\rho_j u_{xj}\right) = \sum_{k \neq j}^{N} s_{jk}, \tag{2.1}$$

$$\frac{\partial \rho_j \mathbf{v}_j}{\partial t} + \frac{\partial}{\partial x}\left(\rho_j u_{xj}\mathbf{v}_j + p_j \hat{I}\right) = \alpha_j \rho_j \left(\mathbf{E} + \mathbf{v}_j \times \mathbf{B}\right) + \sum_{k \neq j}^{N} \mathbf{f}_{jk} \tag{2.2}$$

$$\frac{\partial e_j}{\partial t} + \frac{\partial}{\partial x}\left[u_{xj}\left(e_j + p_j + \frac{1}{2}\rho_j v_j^2\right)\right] = H_j + \sum_{k \neq j}^{N} G_{jk} + \alpha_j \rho_j \mathbf{v}_j \cdot \left(\mathbf{E} + \mathbf{v}_j \times \mathbf{B}\right) \tag{2.3}$$

where j refers to the fluid and takes the values $j = 1...N$. ρ_j and p_j are the densities and pressures, $\mathbf{v}_j = (u_{xj}, u_{yj}, u_{zj})$ the velocities, α_j the charge-to-mass ratios and $\hat{I}$ the x-direction unit vector. e_j are the total energies, which are

$$e_j = \rho_j \left(U_j + \frac{1}{2}\mathbf{v}_j^2\right) \tag{2.4}$$

with $U_j = p_j/(\rho_j(\gamma - 1))$ the internal energy per volume per unit mass and γ the ratio of specific heat for the gas. s_{jk}, $\mathbf{f_{jk}}$ and G_{jk} are the mass, momentum and energy transfer rates from fluid j to k, respectively. Finally, H_j are the energy sinks/sources, $\mathbf{E}$ is the electric field and $\mathbf{B}$ is the magnetic field.

The momentum transfer rates take the form

$$\mathbf{f}_{jk} = \rho_j \rho_k \mathbf{K}_{jk}(T_j, T_k, |\mathbf{v}_k - \mathbf{v}_j|)(\mathbf{v}_k - \mathbf{v}_j) \tag{2.5}$$

with $T_{j/k}$ the temperatures of fluids j or k and $\mathbf{K}_{jk}$ the collision coefficient. In the regions of interest, the fractional ionisation is low, hence the mass of the plasma is heavily dominated by the neutrals and only collisions between fluid i and the neutrals are important (with i denoting the charged fluids). The thickness of the shock is a length scale induced by a balance between the $i - n$ (where n denotes the neutral fluid) collisions and the inertia terms. Provided the similarly determined

[1]The model is one-dimensional for computational simplicity. See Chapter 7 for a discussion of higher dimensions.

length scales for the charged fluids, or the Larmor radius of the charged particles, is much smaller than the shock thickness, the inertia and pressure terms of the charged fluids can be considered to be negligible. This reduces the momentum and energy equations for the charged fluids, i, to

$$\alpha_i \rho_i \left(\mathbf{E} + \mathbf{v}_i \times \mathbf{B}\right) + \rho_i \rho_n \mathbf{K}_{in}(\mathbf{v}_n - \mathbf{v}_i) = 0 \tag{2.6}$$

$$H_i + \mathbf{G}_{in} = 0 \tag{2.7}$$

and the source term for the continuity equations are due only to mass transfer to/from the neutrals,

$$\frac{\partial \rho_i}{\partial t} + \frac{\partial}{\partial x}\left(\rho_i u_{xi}\right) = s_{in}, \tag{2.8}$$

where, by global mass conservation, $s_{in} = -s_{ni}$. Dust grains have significantly larger mass than the particles making up the other charged fluids, so their inertia should not be ignored outright. Provided the Larmor radius of the grains is small enough, the grains are well-coupled to the magnetic field lines and their inertia can also be ignored. Also, due to their larger mass they also have a small thermal velocity dispersion in comparison to the drift velocity, so the grain fluids have zero pressure. Additionally, the pressure and inertia terms can be neglected and the fluid equations for the grains look the same as those of the electrons and ions.

The current, $\mathbf{J}$ is given by

$$\mathbf{J} = \sum_{j=1}^{N} \alpha_j \rho_j \mathbf{v}_j \tag{2.9}$$

and charge neutrality means that

$$\sum_{j=1}^{N} \alpha_j \rho_j = 0. \tag{2.10}$$

The use of the current equation and charge neutrality with the reduced momentum equation for the charged fluids means the momentum and energy equations for the neutrals become

$$\frac{\partial \rho_n \mathbf{v}_n}{\partial t} + \frac{\partial}{\partial x}\left(\rho_n u_{xn} \mathbf{v}_n + p_n \hat{I}\right) = \mathbf{J} \times \mathbf{B} \tag{2.11}$$

$$\frac{\partial e_n}{\partial t} + \frac{\partial}{\partial x}\left[u_{xn}\left(e_n + p_n + \frac{1}{2}\rho_n v_n^2\right)\right] = \mathbf{J} \cdot \mathbf{E} + \sum_i H_i. \tag{2.12}$$

The continuity equation for the neutrals remains unchanged since mass transfer occurs with all other fluids,

$$\frac{\partial \rho_n}{\partial t} + \frac{\partial}{\partial x}\left(\rho_n u_{xn}\right) = \sum_i s_{in}. \tag{2.13}$$

The equation for the electric field is given by Ohm's law, formed from the reduced momentum equations and the equation for the current and, by convention, is written as

$$\mathbf{E} = -\mathbf{v} \times \mathbf{B} + r_0 \frac{(\mathbf{J} \cdot \mathbf{B})\mathbf{B}}{B^2} + r_1 \frac{\mathbf{J} \times \mathbf{B}}{B} - r_2 \frac{(\mathbf{J} \times \mathbf{B}) \times \mathbf{B}}{B^2} \tag{2.14}$$

where r_0 is the resistivity along the magnetic field, corresponding to $1/\sigma_0$, r_1 is the Hall resistivity, corresponding to $\sigma_1/(\sigma_1^2 + \sigma_2^2)$, and r_2 is the ambipolar resistivity, corresponding to $\sigma_2/(\sigma_1^2 + \sigma_2^2)$. σ_0, σ_1 and σ_2 are given by

$$\sigma_0 = \frac{1}{B} \sum_i \alpha_i \rho_i \beta_i, \tag{2.15}$$

$$\sigma_1 = \frac{1}{B} \sum_i \frac{\alpha_i \rho_i}{(a + \beta_i^2)}, \tag{2.16}$$

and

$$\sigma_2 = \frac{1}{B} \sum_i \frac{\alpha_i \rho_i \beta_i}{(1 + \beta_i^2)}, \tag{2.17}$$

where β_i is the Hall parameter; the ratio of the gyrofrequency to the frequency of collisions with the neutrals. The Hall parameter can be viewed as a measure of how well the particles are tied to the field. A value of $|\beta_i| \gg 1$ suggests particles which are tightly coupled to field lines, whereas a value of $|\beta_i| \ll 1$ means the particles travel with the neutrals. Clearly, larger grains have Hall parameters which are closer to 1 and the size at which dust grains begin to decouple from the field is $\sim 10^{-5}$ cm (Guillet et al., 2007). The fields are determined by Faraday's induction equation,

$$\frac{\partial B_x}{\partial t} = 0, \quad \frac{\partial B_y}{\partial t} = -\frac{\partial E_z}{\partial x}, \quad \frac{\partial B_z}{\partial t} = \frac{\partial E_y}{\partial x} \tag{2.18}$$

and Ampere's law (without displacement current),

$$\frac{\partial B_y}{\partial x} = J_z, \quad \frac{\partial B_z}{\partial x} = -J_y. \tag{2.19}$$

These two equations, along with the expression for the electric field, give rise to the induction equation

$$\frac{\partial \mathbf{B}}{\partial t} + \frac{\partial \mathbf{M}}{\partial x} = \frac{\partial}{\partial x}\mathbf{R}\frac{\partial \mathbf{B}}{\partial x} \tag{2.20}$$

where $\mathbf{M} = (0, u_x\ B_x - u_y\ B_x, u_x\ B_z - u_z\ B_x)$ is the hyperbolic flux and $\mathbf{R}$ is a resistance matrix which is dependent on the resitivities r_0, r_1 and r_2,

$$\begin{bmatrix} (r_0 - r_2)\frac{B_z^2}{B^2} + r_2 & (r_2 - r_0)\frac{B_y B_z}{B^2} + r_1\frac{B_x}{B} \\ (r_2 - r_0)\frac{B_y B_z}{B^2} - r_1\frac{B_x}{B} & (r_0 - r_2)\frac{B_y^2}{B^2} + r_2 \end{bmatrix}. \tag{2.21}$$

2.2 Numerical model

The neutral equations presented in the previous section, Eq. 2.11 - Eq. 2.13, are solved through use of a conservative 2nd order Godunov scheme as given by Falle (1991, 2003). The neutral fluid equations are of the form

$$\frac{\partial \mathbf{Q}}{\partial t} + \frac{\partial \mathbf{F}}{\partial x} = \mathbf{S} \tag{2.22}$$

where $\mathbf{Q}$ is a vector of the conserved variables, i.e. ρ_n, $\rho_n \mathbf{v}_n$, e_n. $\mathbf{F}$ is a vector of the fluxes and $\mathbf{S}$ is a vector of the source terms, which is dependent on both $\mathbf{Q}$ and a vector $\mathbf{V}$ containing the field and charged fluid variables. These conservative equations are discretised onto a grid as per the finite volume approach, with the solution at time t_n being defined as the cell average inside each cell,

$$\mathbf{Q}_i^n = \frac{1}{\Delta x}\int_{x_{i-1/2}}^{x_{i+1/2}} \mathbf{Q}(t_n, x)\ \mathrm{d}x \tag{2.23}$$

where cell i has boundaries at $x_{i-1/2}$ and $x_{i+1/2}$ with spacing $\Delta x = x_{i+1/2} - x_{i-1/2}$. Integration of Eq. 2.22 leads to the update

$$\mathbf{Q}_i^{n+1} = \mathbf{Q}_i^n + \frac{\Delta t}{\Delta x}\left(\mathbf{F}_{i-1/2}^{n+1/2} - \mathbf{F}_{i+1/2}^{n+1/2}\right) + \Delta t\ \mathbf{S}_i^{n+1/2} \tag{2.24}$$

where Δt is the time-step, $\mathbf{S}_i^{n+1/2}$ is the time-averaged integral of the source term over the cell, and $\mathbf{F}_{i+1/2}^{n+1/2}$ and $\mathbf{F}_{i-1/2}^{n+1/2}$ are the time-averaged fluxes at the cell interfaces. Firstly, approximates to the fluxes and sources are calculated in order to determine the approximate solution at the half-time, $\mathbf{Q}_i^{n+1/2}$. The approach is made second

order in space by constructing a linear function of the primitive variables using the half-time solution. The fluxes are then

$$\mathbf{F}_{i+1/2}^{n+1/2} = \mathbf{F}_*[\mathbf{Q}(\mathbf{P}_L), \mathbf{Q}(\mathbf{P}_R)] \tag{2.25}$$

with $\mathbf{P}_L$ and $\mathbf{P}_R$ the left and right primitive states. The source term is

$$\mathbf{S}_i^{n+1/2} = \mathbf{s}(\mathbf{Q}_i^{n+1/2}, \mathbf{V}_i^{n+1/2}) \tag{2.26}$$

where $\mathbf{V}_i^{n+1/2}$ has yet to be determined.

The magnetic field is advanced to half-time using a first-order scheme according to

$$\begin{aligned} \frac{1}{\Delta t}\left(\mathbf{B}_i^{n+1/2} - \mathbf{B}_i^n\right) + \frac{1}{\Delta x}\left(\mathbf{M}_{i+1/2}^n - \mathbf{M}_{i-1/2}^n\right) \\ = \frac{1}{\Delta x^2}\mathbf{R}_i^n\left(\mathbf{B}_{i+1}^n - 2\mathbf{B}_i^n + \mathbf{B}_{i-1}^n\right), \end{aligned} \tag{2.27}$$

with $\mathbf{R}_i^n = \mathbf{R}(\mathbf{V}_i^n)$, and where the hyperbolic flux is determined by a centered approximation,

$$\mathbf{M}_{i+1/2}^n = \frac{1}{2}\left(\mathbf{M}_{i+1}^n + \mathbf{M}_i^n\right). \tag{2.28}$$

The new magnetic field allows the current to be calculated from a centred approximation to Ampere's law, and the half-time charged fluid densities can be calculated from an explicit upwind approximation to the continuity equations. The current can then be used along with the magnetic field and the neutral half-time state to determine $\mathbf{V}_i^{n+1/2}$ from Equation 2.9 and the reduced energy and momentum equations. $\mathbf{V}_i^{n+1/2}$ is used to calculate $\mathbf{S}_i^{n+1/2}$ so that the full-time neutral solution can be determined. A second-order approximation to the charged fluids' continuity equations can also be used with $\mathbf{V}_i^{n+1/2}$ to advance the charged fluid densities to half-time. The full-time magnetic field is then determined explicitly from the half-time magnetic field solution using

$$\begin{aligned} \frac{1}{\Delta t}\left(\mathbf{B}_i^{n+1} - \mathbf{B}_i^n\right) + \frac{1}{\Delta x}\left(\mathbf{M}_{i+1/2}^{n+1/2} - \mathbf{M}_{i-1/2}^{n+1/2}\right) \\ = \frac{1}{\Delta x^2}\mathbf{R}_i^{n+1/2}\left(\mathbf{B}_{i+1}^{n+1/2} - 2\mathbf{B}_i^{n+1/2} + \mathbf{B}_{i-1}^{n+1/2}\right). \end{aligned} \tag{2.29}$$

The final stage is to advance the charged fluid velocities and temperatures to full-time using the full-time neutral solution, charged fluid densities and magnetic field with the same method as for $\mathbf{V}_i^{n+1/2}$.

When this scheme is advanced explicitly, there is a restriction imposed on the time-step,

$$\Delta t \leq \frac{r_2}{r_1^2 + r_2^2} \Delta x^2 \tag{2.30}$$

so when the Hall resistivity (r_1) becomes significantly larger than the ambipolar diffusion resistivity (r_2) the time-step becomes very small. However, provided the Hall resistivity remains similar to the ambipolar resistivity, as is the case for the simulations in this thesis, the time-step is not severely restricted.

2.3 Chemistry

As a shock front propagates through a molecular cloud the temperature of the gas and charged fluids can be significantly increased from $\sim$ 10 K up to thousands of degrees. However, for a shock to be C-type, the molecular hydrogen must not be entirely dissociated because H_2 provides an important cooling mechanism which, when removed, allows the neutral fluid to heat up. The neutral fluid can then experience a supersonic to subsonic transition, which causes the shock to become J-type. Hence, for a shock to remain C-type the neutral gas temperature must remain below $\sim 10^4$ K which, in turn, allows for a number of chemical reactions to proceed. These reactions cause significant changes to the gas-phase abundances of certain materials and therefore have implications for the gas dynamics and observational signatures. Whilst some studies in the literature include vast chemical networks in their numerical models, for example Flower and Pineau des Forêts (2003) who include around 1000 reactions, this is expensive to do in terms of computing resources. The mulitfluid MHD model presented here therefore solves a relatively modest chemical network based on the most abundant species observed in the regions of interest.

It is assumed that, apart from H_2 molecules, the neutral fluid is initially made up of Mg, O and CO. The ion fluid is assumed to be made up initially of 50% HCO^+ and 50 % Mg^+. In dark clouds ionisation of H_2 occurs via cosmic rays. The ionised hydrogen molecules react with neutral ones to form H_3^+, which in turn produce the ions HCO^+ and H_3O^+ via proton transfer. These molecular ions produce metallic ions, such as Mg^+, due to charge exchange with neutral metal atoms. These metallic atoms are removed by recombination on dust grain surfaces. In addition, the increased temperatures in the shocked gas allow for neutral-neutral chemistry in shocked regions, such as formation of water from O and H_2.

Table 2.1: The chemical reactions included in the computational model, from Van Loo et al. (2013). The reactions labelled with the subscript * are culminations of two reactions (see the main text for details). The rates for reactions 1, 2, 3, 6, 7, 8, 10, 15 and 18 are from the UMIST database for astrochemistry (McElroy et al., 2013) and reactions 5, 12, 13 and 16 are from Pilipp et al. (1990). The reactions 4, 9, 11, 14 and 17 are due to the recombination of ions on grain surfaces, the rates of which are determined by the arrival rate of ions onto grains, Γ_{i_xg}. T_n and T_e are the neutral and electron temperatures, and T_{eff} is the effective temperature, given by Eq. 43 of Flower et al. (1985). Note that reaction 1 has units of s^{-1}.

	Reaction	Rate (cm^3 s^{-1})
1*	$H_2 + CR \rightarrow H_3^+ + e + CR$	1.2×10^{-17} s^{-1}
2	$H_3^+ + CO \rightarrow HCO^+ + H_2$	1.7×10^{-9}
3	$H_3^+ + H_2O \rightarrow H_3O^+ + H_2$	5.9×10^{-9}
4	$H_3^+ + grain^- \rightarrow H_2 + H + grain$	$\Gamma_{H_3^+g}$
5*	$H_3^+ + O \rightarrow H_3O^+$	8.4×10^{-10}
6	$HCO^+ + e \rightarrow H + CO$	$2.76 \times10^{-7}(\frac{T_e}{300})^{-0.69}$
7	$HCO^+ + Mg \rightarrow H + CO + Mg^+$	2.9×10^{-9}
8	$HCO^+ + H_2O \rightarrow H_3O^+ + CO$	2.5×10^{-9}
9	$HCO^+ + grain^- \rightarrow H + CO + grain$	Γ_{HCO^+g}
10	$Mg^+ + e \rightarrow Mg + h\nu$	$2.8 \times10^{-12}(\frac{T_e}{300})^{-0.68}$
11	$Mg^+ + grain^- \rightarrow Mg + grain$	Γ_{Mg^+g}
12	$Mg^+ + H_2 \rightarrow MgH^+ + H$	$3.0\times10^{-10}e^{-27854/T_{eff}}$
13	$MgH^+ + e \rightarrow Mg + H$	$1.1 \times10^{-7}(\frac{T_e}{300})^{-0.5}$
14	$MgH^+ + grain^- \rightarrow Mg + H + grain$	Γ_{MgH^+g}
15	$H_3O^+ + e \rightarrow H_2O + H$	$1.4 \times10^{-7}(\frac{T_e}{300})^{-0.5}$
16	$H_3O^+ + Mg \rightarrow H_2O + Mg^+ + H$	1.8×10^{-9}
17	$H_3O^+ + grain^- \rightarrow H_2O + H + grain$	$\Gamma_{H_3O^+g}$
18*	$O + H_2 \rightarrow H_2O$	$3.14 \times10^{-13}(\frac{T_n}{300})^{2.7}e^{-3150/T_n}$

The full set of reactions which are incorporated in the model are given in Table 2.1 along with their rates. These are the same as those adopted by Van Loo et al. (2013). Reaction 1 describes cosmic ray ionisation of H_2 to form H_3^+, which is actually the cumulation of the following two reactions,

$$H_2 + CR \rightarrow H_2^+ + e + CR$$
$$H_2^+ + H_2 + \rightarrow H_3^+ + H$$

where the rate given is for the first of these reactions, since it is much slower than that of the second. Likewise, reaction 5 is combination of the reactions

$$\begin{aligned} H_3^+ + O &\rightarrow OH^+ + H_2 \\ OH^+ + H_2O &\rightarrow H_3O^+ + O \end{aligned}$$

where the rate given is for the first reaction since it occurs more slowly than the second. Finally, reaction 18 is a cumulation of the set of reactions,

$$\begin{aligned} O + H_2O &\rightarrow OH + H \\ OH + H_2 &\rightarrow H_2O + H \end{aligned}$$

where, again, the rate given is for the first reaction since it occurs much more slowly than that of the second.

Reactions 4, 9, 11, 14 and 17 describe recombination of metallic ions with electrons on the surfaces of dust grains. $\Gamma_{\mathrm{i_xg}}$ is the current of ion species i_x onto grains in fluid g. The rate of formation of neutral species x due to recombination is then the sum over all grain fluids g, $\sum_g \Gamma_{\mathrm{i_xg}} \mathrm{n_g}$, and correspondingly the destruction rate of the ion species undergoing recombination is the negative of this. Expressions for the current of ions onto grains are given in §3.3.

The rate of change of the number densities of particular ion and neutral species are determined by summing the rates of reactions by which they are created or destroyed. In total, 5 ion species and 4 neutral species are followed. The equation rate of change of number densities of each ion species is:

$$\frac{dn_{H_3^+}}{dt} = k_1 n_{H_2} - n_{H_3^+} \left[k_2 n_{CO} + k_3 n_{H_2O} + k_5 n_O + \sum_g \Gamma_{H_3^+ g} n_g \right], \tag{2.31}$$

$$\frac{dn_{HCO^+}}{dt} = k_2 n_{H_3^+} n_{CO} - n_{HCO^+} \left[k_5 n_e + k_7 n_{Mg} + k_8 n_{H_2O} + \sum_g \Gamma_{HCO^+ g} n_g \right], \tag{2.32}$$

$$\frac{dn_{Mg^+}}{dt} = k_7 n_{HCO^+} n_{Mg} + k_{16} n_{H_3O^+} n_{Mg} - n_{Mg^+} \left[k_{10} n_e + k_{12} n_{H_2} + \sum_g \Gamma_{Mg^+ g} n_g \right], \tag{2.33}$$

$$\frac{dn_{H_3O^+}}{dt} = k_8 n_{HCO^+} n_{H_2O} + k_3 n_{H_3^+} n_{H_2O} + k_5 n_{H_3^+} n_O - n_{H_3O^+} \left[k_{15} n_e + k_{16} n_{Mg} + \sum_g \Gamma_{H_3O^+ g} n_g \right], \tag{2.34}$$

$$\frac{dn_{MgH^+}}{dt} = k_{12} n_{Mg^+} n_{H_2O} - n_{MgH^+} \left[k_{13} n_e + \sum_g \Gamma_{MgH^+ g} n_g \right]. \tag{2.35}$$

For the neutral species the rate equations are:

$$\frac{dn_{Mg}}{dt} = k_{10} n_{Mg^+} n_e + k_{13} n_{MgH^+} n_e + \sum_g \Gamma_{Mg^+ g} n_g + \sum_g \Gamma_{MgH^+ g} n_g - n_{Mg} \left[k_7 n_{HCO^+} + k_{16} n_{H_3O^+} \right], \tag{2.36}$$

$$\frac{dn_O}{dt} = -n_O \left[k_5 n_{H_3^+} + k_{18} n_{H_2} \right], \tag{2.37}$$

$$\frac{dn_{H_2O}}{dt} = k_{15} n_{H_3O^+} n_e + k_{16} n_{H_3O^+} n_{Mg} + k_{18} n_O n_{H_2O} + \sum_g \Gamma_{H_3O^+ g} n_g - n_{H_2O} \left[k_3 n_{H_3^+} + k_8 n_{HCO^+} \right]. \tag{2.38}$$

The fourth neutral species which is followed is SiO since, in addition to the reactions in Table 2.1, it is assumed that gas-grain sputtering of grain cores injects Si into the gas phase, where it immediately reacts with oxygen to form SiO (see §2.5.2). Sputtering also releases Mg and O into the neutral gas phase and these rates are added to the necessary total creation/destruction rates above.

The number density of a given species x, n_x, evolves by a rate equation of the form

$$\frac{\partial n_x}{\partial t} + \frac{\partial n_x v_{n,i}}{\partial x} = S_x \tag{2.39}$$

where $v_{n,i}$ is the x-component of the velocity of either the neutrals or the ions depending on the species, and S_x is the creation or destruction rate of the species (Eqs. 2.31 - 2.38).

2.4 Mass, momentum and energy transfer rates

The mass transfer rate per volume between two fluids, j and k, is denoted by s_{jk} in Eq. 2.1. The transfer of mass between the ions/electrons and the neutrals is due to chemical reactions. In particular, cosmic ray ionisation at a rate given in reaction 1 of Table 2.1, electron recombination with Mg^+ as in reaction 10, dissociative recombination of electrons with HCO^+, H_3O^+ and MgH^+ (reactions 6, 13 and 15) and recombination of ions on the surfaces of negatively charged grains (reactions 4, 9, 11, 14 and 17). The contributions to the source terms are calculated by multiplying the rate of creation or destruction per volume of a particular species, as determined by the chemical rate equations, by the mass of that species. Additionally, dust grain sputtering contributes to the grain-neutral mass transfer term, details of which are in § 2.5.2.

We are interested in shocks in molecular clouds, where the medium is weakly-ionised. The mass is dominated by the neutrals and hence in the momentum equations for the charged particles only the collisions with neutrals need to be considered. Eq. 2.5 gives the form of the momentum transfer rates. The collision coefficient between the neutrals, n, and the charged fluid k is K_{nk}, estimates for which are given by Draine et al. (1983). For ion-neutral scattering the collision coefficient is

$$K_{in} = \max[1.9 \times 10^{-9}\mathrm{cm}^3\ \mathrm{s}^{-1}, 1 \times 10^{-15}\mathrm{cm}^2|\vec{v}_n - \vec{v}_i|], \tag{2.40}$$

with $\vec{v}_n$ the neutral velocity and $\vec{v}_i$ the ion velocity. For electron-neutral collisions it is

$$K_{en} = 1 \times 10^{-15}\mathrm{cm}^2 \left((\vec{v}_n - \vec{v}_e)^2 + \frac{128 k_b T_e}{9\pi m_e} \right)^{1/2}, \tag{2.41}$$

with $\vec{v}_e, T_e$ and m_e the electron velocity, temperature and mass, respectively. Finally, for grain-neutral collisions it is

$$K_{gn} = \frac{\pi a^2}{m_n + m_g} \left(\frac{2 k_b T_n}{\pi m_n} \right)^{1/2} \frac{8}{3} \left(1 + \frac{9\pi(\vec{v}_n - \vec{v}_g)^2}{128 k_B T_n} \right)^{1/2}, \tag{2.42}$$

with $\vec{v}_g$, m_g and a the grain velocity, mass and radius, respectively, T_n the neutral temperature and m_n the neutral mass. Typically, relative velocities $\sim v_s/2$, where v_s is the shock velocity, modify the K values appreciably (Draine, 1980).

The energy transfer terms are described by H_j, which is the energy transfer per volume for fluid j due to external energy sources or sinks, and G_{jk} which is the energy transfer per volume between fluids j and k. For the neutrals, the right hand side Eq. 2.12 tells us that the energy transfer terms are given by $\mathbf{J} \cdot \mathbf{E} + \sum_k H_k$, where H_k are the heating and cooling terms of fluid k. For the ion and electron fluids, the reduced energy conservation equations, given by Eq. 2.7, consist of the heating and cooling terms H_j and the transfer rate per volume between the charged fluid and the neutrals, G_{jn}. The expression for G_{jn} is given by Draine (1986),

$$G_{jn} = \frac{\rho_n \rho_j}{(m_n + m_j)} K_{jn} \left(m_j (\mathbf{v}_j - \mathbf{v}_n)^2 + \omega_j k_b (T_n - T_j) \right), \tag{2.43}$$

where ω_j takes a value of 3 for ions and is 4 for electrons.

2.4.1 Heating and cooling

Molecular clouds are well-shielded, so the dominant heating mechanism is cosmic ray ionisation of H_2 molecules and this can be considered to be the only direct heating source of the gas. The heating rate is the product of the cosmic ray ionisation rate and the energy input per ionisation. The contribution to the energy source term of the neutrals, H_n, is (Draine et al., 1983)

$$H_{n,CR} = 1.69 \times 10^{-11} \zeta n_n \tag{2.44}$$

where n_n is the number density of H_2 molecules and $\zeta \sim 10^{-17}\,\mathrm{s}^{-1}$ is the cosmic ray primary ionisation rate.

The post-shock cooling is dominated by H_2 emission. Each electronic state of H_2 has an associated set of rotational-vibrational levels. A H_2 molecule in an excited ro-vibrational state can lose energy via collisional de-excitation or by spontaneous radiative relaxation. Transitions between states adhere to particular selection rules depending on whether they are electric dipole, magnetic dipole, electric quadrupole, etc. Since H_2 is homonuclear and has no overall dipole moment, it has no allowed dipole transitions. However, it does have weak rotational quadrupole transitions

with J = ± 2, where J denotes the vibrational levels. The neutral cooling rate due to these transitions is given by a fit to the temperature and cooling rates given for these transitions in Table 1 of Hartquist et al. (1980),

$$H_{n,H2} = -7.9 \times 10^{-34} n_n T_n^{4.1} \tag{2.45}$$

where T_n is the temperature of the gas. For the densities and velocities appropriate for interstellar C-type shocks this is the primary cooling sources. However, there are other species which make cooling contributions, namely H_2O, CO and O. Unlike H_2, H_2O molecules have a permanent electric dipole, so their allowed transitions give a sizeable contribution to the cooling of the gas. The rate of this is given by Neufeld and Melnick (1987) in the case of a large velocity gradient,

$$H_{n,H_2O} = 2.6 \times 10^{-23} \left(\frac{T_n}{1000K}\right)^{1.95} n_{(o-H_2O)} n_n \left[1 + \left(\frac{\eta}{9 \times 10^4 \left(\frac{T_n}{1000K}\right)^{2.4}}\right)^{\frac{1}{2}}\right]^{-1} \tag{2.46}$$

where $n_{(o-H_2O)}$ is the number density of ortho-water and η is a quantity defined as

$$\eta = n_{(o-H_2O)} \frac{n_n}{10^7 \mathrm{cm}^{-3}} \left(\frac{dv_z/dz}{10^5 \mathrm{kms}^{-1}\mathrm{pc}^{-1}}\right)^{-1} \tag{2.47}$$

where dv_z/d_z is the velocity gradient. H_2O molecules can exist in two particular configurations due to the orientation of their hydrogen molecules; ortho-, and para-. Ortho-H_2O molecules contain hydrogen atoms with symmetrical nuclear spin and para-H_2O molecules have hydrogen atoms with oppostite nuclear spins. This model includes all the levels of the ground vibrational state of ortho-H_2O and assumes the efficiency of para-H_2O is equal to that of ortho-H_2O. In a hot plasma, the abundance of ortho-H_2O is three times that of para-H_2O.

2.5 Dust grain treatment

The dust grains are modelled as spheres, made up of an olivine ($MgFeSiO_4$) core surrounded by a H_2O ice mantle. The dust grains are represented by a number of fluids in which all the dust grains in each fluid have a particular size. All the grains within a fluid are assumed to travel with the same velocity, where the velocity dispersion within a fluid is small compared to the drift velocity. For this reason,

as mentioned previously, the grain states are approximated by the hydrodynamic equations with zero pressure.

2.5.1 Initial grain quantities

The gas-to-dust mass ratio in the ISM is 100:1 (e.g. Knapp and Kerr, 1974; Jura, 1979), therefore the combined mass density of the grain fluids is taken to be equal to 1% of the initial neutral mass density, which in dense clouds ranges from $10^4\ m_H$ g cm^{-3} to $10^6\ m_H$ g cm^{-3} where m_H is the mass of a hydrogen atom. There are N grain fluids, and all the grains in a fluid have a single size. The number densities of grains in each fluid is found by assuming the grains follow an initial MRN distribution, so that $\partial n_g/\partial a \propto a^{-3.5}$ where g denotes a grain fluid. Then $n_g \propto a_g^{-2.5}$. Take $g = 1, 2, ..., N$. Each number density n_g can then be written in terms of n_1 as

$$n_g = n_1 \left(\frac{a_g}{a_1}\right)^{-2.3}. \tag{2.48}$$

Use of $\sum_g \rho_g = 0.01\rho_n$, and the fact that $\rho_g = n_g m_g$ where m_g is the mass of a single grain in fluid g, we can solve for the number density n_1,

$$n_1 = \frac{0.01\rho_n}{\sum_g m_g \left(a_g/a_1\right)^{-2.5}}. \tag{2.49}$$

The grain masses are calculated with the assumption of spherical grains, so that $m_g = 4/3\pi\rho_{ol}a_g^3$ where $\rho_{ol} = 3.3$ g cm^{-3} is the bulk density of olivine. Once n_1 is calculated, the number densities for the remaining grain fluids are determined from Eq. 2.48. The grain number densities are then used to calculate the initial grain mass densities. The initial number density of Si in each grain fluid is calculated simply from finding the number of Si atoms per grain from m_g/m_{ol}, where $m_{ol} = 175\ m_H$ is the mass of an olivine molecule, and multiplying by the number density of grains in the fluid.

The grains are assumed to be coated by an icy H_2O mantle. The grain mantle thickness does not depend on the size of the grain core (Tielens, 2005). The initial total fractional abundance of H_2O ice molecules on the dust grains is $n_{ice}/n_H =$

7.25×10^{-5} (Whittet and Duley, 1991), hence

$$\sum_g \frac{4}{3}\pi\rho_{ice}\left[(a_g+\Delta a)^3 - a_g^3\right] n_g = 7.25\times10^{-5} n_H m_{ice} \tag{2.50}$$

where $\rho_{ice} = 1$ g cm^{-3} is the density of ice and m_{ice} is the mass of a water molecule. The above can be arranged into a polynomial, which can be solved for Δa,

$$\left(\sum_g n_g\right)\Delta a^3 + \left(\sum_g 3a_g n_g\right)\Delta a^2 + \left(\sum_g 3a_g^2 n_g\right)\Delta a - \frac{7.25\times10^{-5} n_H m_{ice}}{4/3\ \pi\rho_{ice}} = 0. \tag{2.51}$$

A typical value for the ice mantle thickness is $\sim$ 175 Å (Tielens, 2005). Finally, once Δa is calculated, the number density of ice in each grain fluid is found from $4\pi\rho_{ice}/(3m_{ice})[(a_g+\Delta a)^3 - a_g^3]n_g$.

2.5.2 Grain sputtering

Gas-grain sputtering is an important destruction mechanism of dust grains in C-type shocks. Due to the fact that the grains carry charge, they are coupled to the magnetic field. Smaller grains are better coupled to the magnetic field than larger grains and hence have a larger relative velocity with the neutrals. In particular, sputtering of grains in shocked layers in molecular outflows is thought to be an important mechanism by which Si is released into the gas phase where it forms SiO. Observations of molecular outflows show that the gas phase fractional abundance of Si is $\sim 10^{-7}$, in comparison to the fractional abundance of $\sim 10^{-12}$ in dark clouds. This makes SiO a good tracer of shocks in the ISM and so it is important to include its production in numerical models of C-type shocks.

The method in which sputtering is included in the computational model is presented by Ashmore (2011) and Van Loo et al. (2013). The rate per volume at which the number density of a species b, n_b, is ejected from a grain of radius a due to sputtering by a projectile neutral particle p is given by Draine and Salpeter (1979),

$$\left.\frac{dn_b}{dt}\right|_{grain} = \pi a^2 n_p \left(\frac{8k_B T_n}{\pi m_p}\right)^{1/2} \frac{1}{s}\int_{x_{th}}^{\infty} \mathrm{d}x\ x^2 \frac{1}{2}\left[e^{-(x-s)^2} - e^{-(x+s)^2}\right]\langle Y(E_p)\rangle_\theta \tag{2.52}$$

where n_p and m_p are the number density and mass of the projectile particle, T_n is the neutral gas temperature, s is related to the grain-neutral relative speed u_{gn} by $s^2 = m_p u_{gn}^2/(2k_B T_n)$, and x is related to the impact energy E_p by $x^2 = E_p/(k_B T_n)$

with x_{th} being the value of x at the threshold energy for sputtering. $\langle Y(E_p)\rangle_\theta$ is the angle-averaged sputtering yield. For low energies, this sputtering yield for the grain mantles can be approximated as twice the yield at normal ($\theta = 0$) incidence, an expression for which is given by Draine and Salpeter (1979)

$$Y(E_p, \theta = 0) = A\frac{(\epsilon - \epsilon_0)^2}{1 + (\epsilon/30)^{4/3}} \tag{2.53}$$

for $\epsilon > \epsilon_0$, where $A \approx 8.3 \times 10^{-4}$ is a constant, $\epsilon = \eta E_p/U_0$, $\epsilon_0 = \max(1, 4\eta)$. U_0 is the binding energy per atom or molecule and $\eta = 4\xi m_p m_t/(m_p + m_t)^2$ with m_t the mass of the target grain and ξ an efficiency factor which for ices is 0.8. x_{th} is calculated from $x_{th} = (\epsilon_0 U_0/(\eta k_b T_n))^{1/2}$. Once the entirety of the grain's icy mantle has been eroded, sputtering of the core can begin. For olivine core sputtering, the yield is given by May et al. (2000),

$$\langle Y(E_p)\rangle_\theta = ke^{-\beta/(E_p - E_{th})} \tag{2.54}$$

with k, β and E_{th} being taken from Table 4 of May et al. (2000). x_{th} can then be directly calculated from the threshold energy, $x_{th} = (E_{th}/(k_B T_n))^{1/2}$.

In order to calculate the sputtering rate per grain the integral in Eq. 2.52 must be evaluated. The function being integrated is

$$f(x) = x^2\left[e^{-(x-s)^2} - e^{-(x+s)^2}\right]. \tag{2.55}$$

$f(x)$ is a sum of two Gaussian functions which, for a particular value of s, comprises for two peaks centred on $\pm\, s$. The negative x solution is unphysical, since there cannot be a negative sputtering rate, so $f(x)$ can be reduced to

$$f(x) = x^2 e^{-(x-s)^2}. \tag{2.56}$$

For the sake of computational efficiency, the limits of the integration need only cover the region where $f(x)$ is sufficiently non-zero. A value of $|x - s| \geq 3$ will give $f(x) \sim 10^{-8}$ (i.e. zero to order of machine precision). Additionally, as we have seen, E_{th} is the minimum required impact energy required for sputtering to occur, which is used to calculate x_{th}. The value of $s \pm 3$ is compared to x_{th} to determine when $f(x)$ is non-zero. If $s + 3 \leq x_{th}$ then the entirety of the curve described by $f(x)$ lies below the threshold impact energy and the sputtering rate is zero. If $s - 3 < x_{th}$ and $s + 3 > x_{th}$ then some portion of $f(x)$ lies below the threshold energy and some

above it, hence the integration limits are x_{th} and $s = 3$. Finally, if $s - 3 \geq x_{th}$ then the entirety of $f(x)$ lies above the threshold and the integration limits are $s - 3$ and $s + 3$.

The integration is calculated numerically using the extended trapezoidal rule (Press et al., 1992)

$$\int_{x_1}^{x_N} f(x)\,\mathrm{d}x = h\left[\frac{1}{2}f_1 + f_2 + f_3 + ... + f_{N-1} + \frac{1}{2}f_N\right] + \mathcal{O}\left(\frac{(b-a)^3 f''}{N^2}\right) \quad (2.57)$$

where N is the number of points between the limits a and b, h is the spacing between two consecutive points and $\mathcal{O}(...)$ is the order of the error of the estimated value. For $N = 1$ the result is $F_1 = \frac{(b-a)}{2}(f(a) + f(b))$, then for each subsequent iteration (i.e. $N = 2, 3, ...$) the accuracy is improved by adding 2^{N-2} points to the interior integration. The error in the estimate is improved by including Simpson's rule, which also improves the efficiency since it requires fewer iterations for the solution to converge. The extended Simpson's rule is

$$\int_{x_1}^{x_N} f(x)\,\mathrm{d}x = h\left[\frac{1}{3}f_1 + \frac{4}{3}f_2 + \frac{2}{3}f_3 + \frac{4}{3}f_4 + ... + \frac{2}{3}f_{N-2} + \frac{4}{3}f_{N-1} + \frac{1}{3}f_N\right] + \mathcal{O}\left(\frac{1}{N^4}\right) \quad (2.58)$$

where the alternation between 2/3, 4/3 continues through the integration. The preferred method for evaluating the above equation is

$$F = \frac{4}{3}F_{2N} - \frac{1}{3}F_N \quad (2.59)$$

where F_N is the result of Eq. 2.57 with N points and F_{2N} is the subsequent calculation made with $2N$ points. The solution is considered to be converged when it is within 1% of the solution from the previous iteration.

Eq. 2.52 can then be used to determine the sputtering rates, and hence the source terms, for the number densities neutral species H_2O, Si, O and Mg. The source terms for the mass densities of the grains are then determined by multiplying the sputtering rates by the corresponding neutral masses and summing over all the species.

3

Modifications and improvements

This chapter describes the initial changes and improvements which were made to the multifluid MHD code. The code has been adapted to follow the change in grain mass due to sputtering, where it had previously been assumed to remain constant, the C- to J-type shock transition is investigated, and corrections are made to the grain charge calculation.

Contents

3.1 Introduction

The numerical multifluid MHD code described in Chapter 2 was used by Van Loo et al. (2009) to carry out time-dependent simulations of C-type shocks, followed by Van Loo et al. (2013) to model the sputtering of dust grains in these shocks. One limitation of that code is that, while it followed the fraction of the mass sputtered from the grains, it did not reduce the grain mass accordingly in the shock dynamics. Here, the method of evolving the dust grain mass is described, and results are given for varying shock velocities and magnetic field orientations.

Investigations are also presented into the C- to J-type shock transition. A shock can only become C-type under particular conditions, namely the plasma in which the shock is propagating must be weakly ionised, the magnetic field must be sufficiently strong and the shock speed must remain below the fast magnetosonic speed of the charged fluids (see §1.2.2.1). Furthermore, the neutral H_2 molecules in the post-shock gas must not become completely dissociated. The velocity at which the transition from C- to J-type occurs is called the critical velocity. According to Draine et al. (1983) (hereafter referred to as DRD), for dense cloud cores ($n_H \geq 10^6$ cm^{-3}) this transition occurs at 44 km s^{-1} and is due to the dissociation of H_2 molecules. This dissociation removes an important coolant from the post-shock gas, which allows the neutrals to heat up; they are no longer supersonic everywhere and the C-type shock solution breaks down. Although the numerical code itself does not account for H_2 dissociation, it would be expected that for shock speeds greater than the critical velocity, the neutral temperature would exceed 4000 K, as this is the temperature at which H_2 is mostly dissociated (Hartquist, 2017). A neutral temperature of 4000 K would then provide a reference point at which the C- to J-type shock transition occurs. However, for all shock speeds initially examined, including those up to 50 km s^{-1}, the results failed to output a high enough neutral temperature to suggest dissociation. In fact, the neutral temperature remained below approximately 2800 K, significantly lower than the expected value. In order to investigate the reasons for this, the cooling mechanisms incorporated into the code were analysed.

Finally, the numerical code included errors in the grain charge calculations, due to the fact that it was assumed that the grain charge is always negative. This is not necessarily the case; electrons can become depleted in the shock, leading to grains becoming neutral, or even having positive charge (Guillet et al., 2011). This is an important implication for the grain dynamics and physical processes. For example, when the grain charge is close to neutral, the grain-neutral velocity becomes small. The sputtering rate is dependent on the speed of grains relative to the neutrals which collide with them, so a reduced velocity will lead to a reduced sputtering rate. Furthermore, the number density was not being updated concurrently with the grain charge, leading to the possibility of the electron density becoming negative and the grain charge having to be reduced post-calculation. Inaccuracies in both the grain charge and electron density propagate through the calculations of the resistivities, and hence the charged fluid velocities. It is therefore important to ensure that they are calculated correctly and accurately.

3.2 Models

The model used throughout this chapter is similar to that of Van Loo et al. (2013), which incorporates five separate fluids; neutrals, electrons, positively-charged ions, large dust grains, and small dust grains. The grains are assumed to be spherical and made up of a silicate core encased by a H_2O ice mantle. The large grains have a radius $a_l = 0.4$ μm and mass $m_l = 8.85 \times 10^{-13}$ g, and small grains have a radius $a_s = 0.04$ μm and mass $m_s = 8.85 \times 10^{-16}$ g. The representative ions are metallic Mg^+ ions, and molecular HCO^+ ions. The dissociative recombination of HCO^+ and electron recombination with Mg^+ is taken into account through the mass transfer terms. Additionally, radiative cooling by O, CO, H_2 and H_2O is included (with rates determined according to the formulae presented in §2.4.1). Ionisation of H_2 occurs at a rate $\chi = 1.2 \times 10^{-17}$ s^{-1}, with the loss of neutrals (and corresponding gain in ions) incorporated into the necessary mass transfer terms. The pre-shock conditions represent those of dark clouds, with densities $n_H = 10^4$ or 10^6 cm^{-3}, where all the hydrogen is in molecular form. The initial abundance of O is 4.25×10^{-4} n_H, of CO is 5×10^{-5} n_H, and of H_2O is zero. The abundances of O and H_2O are updated at each time-step as they are altered by the heating of the gas. The abundance of CO remains constant through the shock. Mg^+ and HCO^+ make up half each of the total ion abundance and takes a mass of 30 m_H where m_H is the mass of a hydrogen atom. Finally, the upstream magnetic field is estimated by $B(\mu G) \sim (n_H(\mathrm{cm}^{-3}))^{-1/2}$.

3.3 Grain charge calculations

The charge on interstellar grains is important for understanding the grain dynamics in shocks. In C-type shocks in molecular clouds the charge on the grains is due to the balance between electron and positive ion attachment to the grain surfaces. The current of particles onto grains depends on the grain-particle relative velocity distributions as well as the densities of the particles, their temperatures and their sticking coefficients (Draine and Sutin, 1987).

In the cold temperatures of dark clouds, dust grains tend to carry a charge of -1e (Havnes et al., 1987). When the average grain charge is $\sim 1e$, the charge distribution must be calculated in order to determine the average charge. Since in interstellar clouds the timescale on which the grain charge fluctuates is small compared with

dynamical timescales, the equilibrium grain charge may be considered. This requires a balance to be made between the current of ions and the current of electrons onto the dust grain surfaces.

The formulation used in the model is that of Havnes et al. (1987), who derived the expressions for these currents. In the original model it was assumed that the grains will have negative charge throughout the shock since electron-grain collisions are usually much more frequent that ion-grain collisions. The method for calculating the grain charges under this assumption is outlined below.

For a grain with average charge Z_g, the current of the ion fluid i with charge Z_i onto the grain, for $Z_g Z_i \leq 0$, is

$$\Gamma_{ig} = \pi a^2 n_i Z_i e \frac{c_i^2}{2v_{ig}} \left\{ \left[1 + 2\left(\frac{v_{ig}}{c_i}\right)^2 - 2Z_i Z_g \xi \right] \cdot \mathrm{erf}\left(\frac{v_{ig}}{c_i}\right) + \frac{2v_{ig}}{c_i\sqrt{\pi}} \exp\left(-\left(\frac{v_{ig}}{c_i}\right)^2\right) \right\} \tag{3.1}$$

where: a is the grain radius; n_i is the number density of ions; e is the charge on an electron; v_{ig} is the drift velocity between the ions and the grains; $c_i = \sqrt{2k_B T/m_i}$ is the most probable speed in the Maxwellian distribution of ions, with k_B the Boltzmann constant, T the gas temperature and m_i the mass of an ion; and $\xi = e^2/(ak_B T)$. For the current of electrons onto grains, $Z_g Z_e > 0$, and the assumption is made that the grain-electron relative velocity is small and the expression for non-shifted Maxwellian functions can be used,

$$\Gamma_{eg} = \pi a^2 n_e Z_e e \sqrt{\frac{8k_B T_e}{\pi m_e}} \exp(-Z_e Z_g \xi) \tag{3.2}$$

where n_e is the number density of electrons and T_e is temperature of the electron fluid. When Z_g is close to 0, the distribution levels are calculated according to

$$\Gamma_{eg}(Z_g) f_{Z_g} + \Gamma_{ig}(Z_g - 1) f_{Z_g - 1} = 0, \tag{3.3}$$

otherwise the currents may be equated,

$$\Gamma_{eg}(Z_g) = \Gamma_{ig}(Z_g). \tag{3.4}$$

The above is a non-linear equation which is solved using an iterative process, such as the Newton-Raphson method (or Halley's method for faster convergence).

However, it is not necessarily the case that the grains remain negatively charged through the shock. For example, Guillet et al. (2011) find that the charge on larger grains can become large and positive when shattering due to grain-grain collisions is included in their model, since the production of many small fragments causes depletion of electrons in the plasma. Additionally, the method involved using fixed values of the ion and electron densities to determine the grain charge, then recalculating the electron density after the grain charge routine according to the charge neutrality condition. Then, if the electron density was found to be negative, the charge on the grains was reduced to ensure that there would always be some population of electrons in the plasma. This was an inaccurate method, contributing to errors both in the grain charge and electron density.

The calculation has been changed to allow the grain charge to become positive, and the density of electrons is changed within the grain charge iteration, meaning that charge neutrality is maintained without allowing the electron density to fall below zero. In practice, this is implemented by first calculating the grain charge distribution around a grain charge $Z_g = 0$. Then, a negative grain charge is assumed, which means Eqs. 3.1 and 3.2 are used. These expressions are equated and constant terms are collected, which gives an expression of the form

$$\alpha - \beta Z_g \xi - \exp[Z_g \xi] = 0 \tag{3.5}$$

where α and β are parameters which depend on the ion and electron densities and temperatures, and ξ is a constant which depends on the temperature and the grain size. It can be shown that a root of this equation only exists if $\alpha < 1$, and the root can be determined by an algorithm such as Halley's method. This is done if the average grain charge from the distribution about zero is less than -1.5e, otherwise the average value is taken from the distribution. If the charge is between -2e and -1.5e then the average of the charge from the distribution and the charge corresponding to the root of Eq. 3.5 is taken as the grain charge.

If $\alpha > 1$, it is possible that the grain charge is positive. In this case, equation 11 of Havnes et al. (1987) should be used for the ion current and equation 12 for the electron current. However, owing to number of error functions and exponentials in equation 11, it is computationally expensive to compute. Therefore the non-shifted expression is used (Eq. 3.2 with the values appropriate for the ions inserted). This simplification is justified by the fact that positive grain charges will be uncommon in the simulations of interest, and are unlikely to be large for the majority of grain

sizes when they do occur [1]. Then, an analogous expression to Eq. 3.5 can be found; $\alpha' + \beta' Z_g \xi' - \exp[-Z_g \xi'] = 0$. Again, if $\alpha' < 1$ then there is a root which can be found and the grain charge is positive. Finally, in the case that both $\alpha > 1$ and $\alpha' > 1$, then the average grain charge is determined from the grain charge distribution. Once the charge has been found for each size of grain, the electron density is updated accordingly. The process is repeated until the electron density converges. Note that there is a minimum possible value for the electron density. This occurs when $\alpha = 1$, which implies that $n_{e,min} \approx (T_i/T_e) n_i$.

A neutral or slightly positive grain charge will have an impact on the dynamics of the grains, since this will result in those grains travelling more closely with the neutral fluid than with the charged particles. There is a reduced collisional cross-section of the neutrals with the charged fluids and the width of the shock profile increases. Another important effect is that the grain-neutral relative speed will be reduced, which in turn will impact the sputter rate.

3.4 Grain mass evolution

One limitation of the computational scheme of Van Loo et al. (2013) was that it followed the amount of sputtered material, but did not change the grain mass, or radius, correspondingly. There are a number of places in the numerical scheme where the grain mass or size is required, such as in the calculations of the resistivities which, in turn, are used to calculate the charged fluid velocities. Additionally, the size of the grains affects the sputtering rate and the current of ions or electrons onto the grain surfaces, which impacts the chemistry. It is therefore important to ensure that the mass (and size) of the grains in a given fluid are updated consistently with the amount of sputtering.

The mass density of grains are governed by the mass conservation equation (Eq. 2.1). The form of this equation used by Van Loo et al. (2013) did not include the source term due to sputtering, so the right-hand side was set to zero. One improvement has been to include sputtering as a source term for the mass density. This allows the mass density of grains in fluid j to evolve over time due to both gas-grain erosion and

[1] Note that Guillet et al. (2011) find that the charge on grains of size 1.6×10^{-5} cm reaches approximately $+150e$ in their simulations of 30 km s^{-1} shocks in a pre-shock medium of density 10^5 cm^{-3}.

advection. The mass of a grain is $m_g = \rho_g / n_g$ where ρ_g is the mass density, and n_g is the number density. Therefore, including an equation for the conservation of number density of grains in the computational method allows straightforward calculation of the mass of a grain in the grain fluid at each time-step in the numerical code. The number density equation is

$$\frac{\partial n_g}{\partial t} + \frac{\partial \left(n_g u_{xg} \right)}{\partial x} = 0. \tag{3.6}$$

The source term on the right-hand side of the equation is zero, since sputtering reduces the mass of the grains whilst conserving the grain numbers (i.e. sputtering is a number-conserving process). The number density of grains is a scalar quantity which is advected across the grid cell at the grain velocity u_{xg}. The mass of a grain in the grain fluid g is then calculated wherever it is required in the code, for example in the determination of the Hall parameter via the charge-to-mass ratio. Note that while there is a current of ions onto grain surfaces, these need not be added to the grain mass since it is assumed that ion attachment leads to recombination with an electron followed by a return to the gas phase (Umebayashi and Nakano, 1980). The mass of electrons which leave the grain surface due to recombination with positively charged ions is negligible.

The radius of a grain in fluid g can be calculated directly from the mass, assuming the grain is spherical and has a constant material density. There is a limitation here in that the core-mantle structure of a grain means that the material density is not actually constant, since the ice mantle will have a lower density than that of the olivine core. This means that there is some error in the grain radius calculation. This could be solved by following the number of ice molecules per grain in each grain fluid. However, the ice mantle is entirely sputtered away for shock speeds $v_s \geq 20$ km s^{-1} (Van Loo et al., 2013) so, for shock speeds above this, it becomes unnecessary to account for the ice mantle in the grain radius. Following the ice molecules per grain would lead to an increase in computational cost, which may not justify the small increase in accuracy for models in which the shock speed is less than 20 km s^{-1}.

To demonstrate the effective implementation of the grain mass evolution method, the results from two different models are presented in the following Section. The first model is for a density of $n_H = 10^4$ cm^{-3} and shock speed $v_s = 16$ km s^{-1}, which allows for comparison with the results of Van Loo et al. (2013). The second is for a

density of $n_H = 10^6$ cm^{-3} and shock speed $v_s = 30$ km s^{-1} and shows how the grain mass changes for a much higher degree of sputtering. Both models are for oblique C-type shocks, with results shown for a number of different angles.

3.4.1 Results and discussion

Figure 3.1 shows the fraction of the grain mass lost for the large and small grain fluids for a shock speed of 16 km s^{-1} and a pre-shock density of 10^4 cm^{-3} where the angle between the magnetic field and the shock propagation direction is $\theta = 30^o, 45^o$, or 60^o. These results are in good agreement with those of Van Loo et al. (2013) (fig. 2 in their paper), although the fraction of ice sputtered for the large and small grains is slightly smaller here for all values of θ. For example, for $\theta = 30^o$, Van Loo et al. (2013) find that the fraction of ice sputtered from the large grains is approximately 0.6 for the small grains and 0.55 for the large grains. In the current model, the fraction of ice sputtered is 0.56 for the small grains and 0.52 for the large grains. There is also agreement that the amount of sputtering is reduced for both sizes of grains as θ increases. This is because for smaller angles between the magnetic field and the direction of propagation of the shock the grains are better coupled to the magnetic field. This causes the grain-neutral velocity to increase and hence increases the sputtering rate.

Fig. 3.1 (j) - (l) shows the fraction of the grains' mass which is removed due to sputtering in the shock. At a shock speed of 16 km s^{-1} no core sputtering occurs, since there is still some amount of ice mantle remaining. This is reflected in the results, where the large grains only experience a small change to their mass. For 30^o, 2.3% of the mass is removed, and for 60^o just 1.4% of the mass is sputtered. Conversely, for the small grains, for $\theta = 30^o$, 22% of the mass is sputtered. The ice mantle makes up a higher proportion of the small grains' initial mass, with about 41% attributed to ice, compared to only about 4.1% for the large grains. This fact, coupled with the knowledge that sputtering is more efficient for smaller grains, explains the larger fractions of the small grain mass which are removed. These values for the change in grain mass correspond well to what is expected from the sputtered ice fractions and suggest that the grain mass evolution is followed accurately in the model.

It is also interesting to see how the grain mass is affected by core sputtering. Fig. 3.2 shows the results for a shock speed $v_s = 30$ km s^{-1} and a pre-shock density of $n_H = 10^6$ cm^{-3}. Fig. 3.2 (d) - (f) shows that both the large and small grains

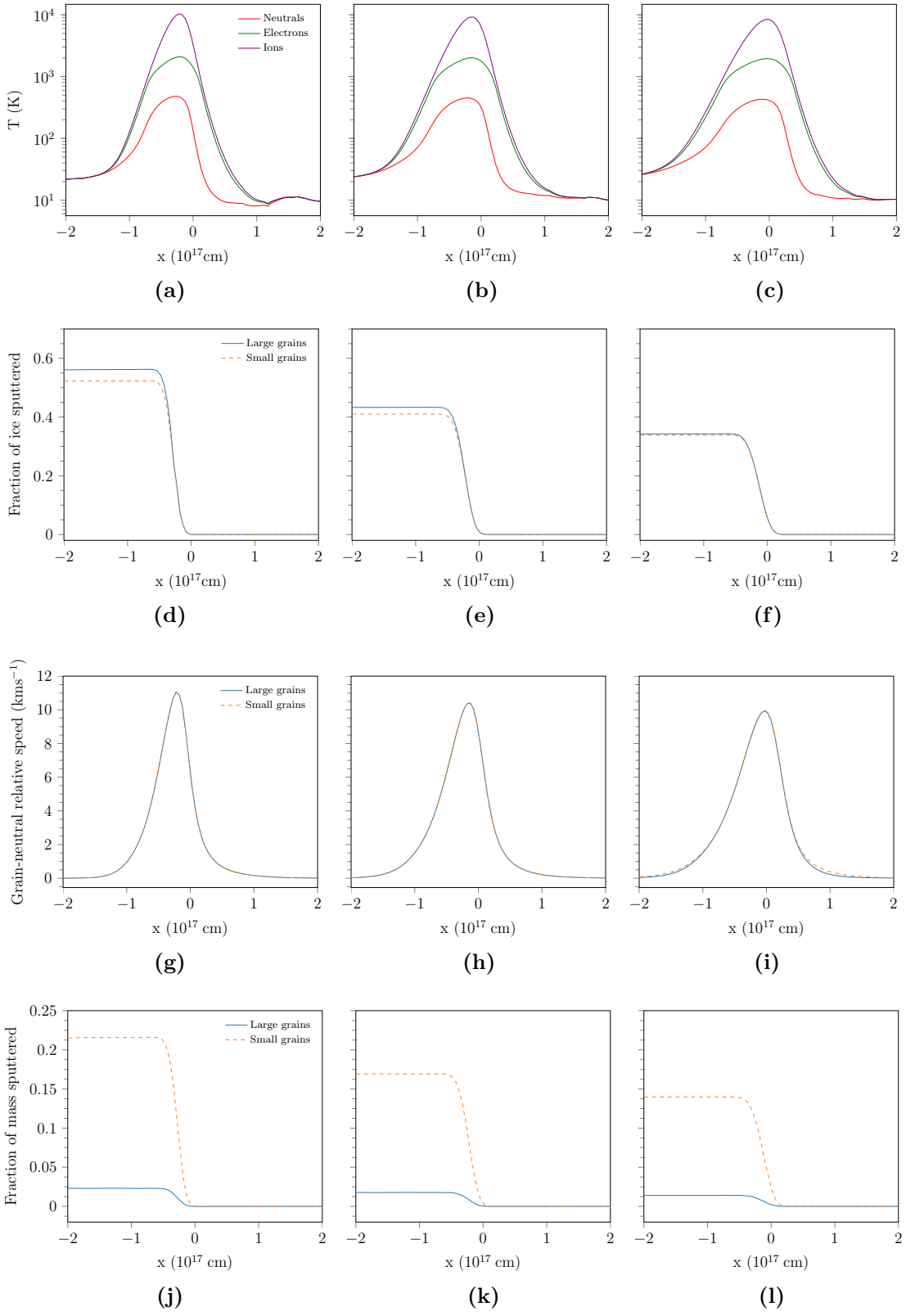

Figure 3.1: Results for a shock speed of 16 km s^{-1} and a pre-shock density of 10^4 cm^{-3}. The top row shows the temperatures for the neutrals (red), electrons (green) and ions (purple). The second row shows the fraction of ice sputtered from the large (blue) and small (orange dashed) grains. The third row shows the grain-neutral velocity for large and small grains, and the final row shows the fraction of the mass sputtered from large and small grains. The left column is for a magnetic field angle of 30^o, the middle column is for 45^o and the right column is for 60^o.

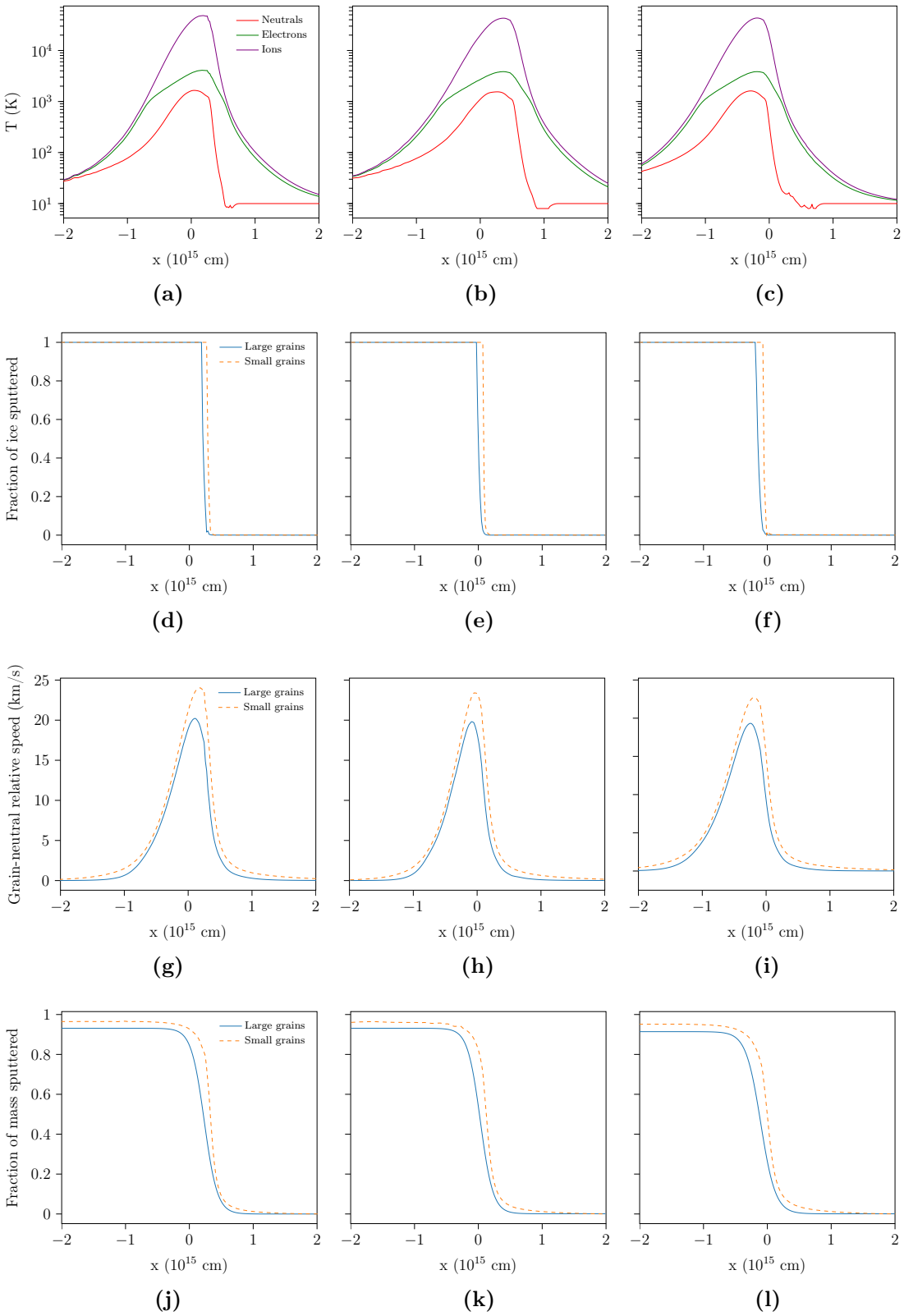

Figure 3.2: Results for a shock speed of 30 km s^{-1} and density of 10^6 cm^{-3}. The top row shows the temperatures for the neutrals (red), electrons (green) and ions (purple). The second row shows the fraction of ice sputtered from the large (blue) and small (orange dashed) grains. The third row shows the grain-neutral velocity for large and small grains, and the final row shows the fraction of the mass sputtered from large and small grains. The left column is for a magnetic field angle of 30^o, the middle column is for 45^o and the right column is for 60^o.

have their ice mantles completely destroyed by sputtering for all angles θ. The ice sputtering is more efficient for the small grains than the large grains, and results in the mantle being removed from the small grains slightly earlier in the shock than for the large grains. There is a much clearer difference in the grain-neutral velocity in comparison to the lower velocity and density model. Fig. 3.2 (j) - (l) shows the fraction of the total grain mass which has been sputtered. Close to 100% of the mass is eroded for both the small and large grains. The difference in the proportions of the grain masses which are initially made up of ice means that, although a greater fraction of the overall mass of the small grains has been sputtered than the large grains, this actually corresponds to a smaller fraction of the core being sputtered. For example, for an angle of $\theta = 30^o$, 96.5% of the small grain mass has been removed compared to 93.1% of the large grain mass. Taking into account the fraction of the mass which consists of the ice mantle, this means that 55.3% of the core of the small grains has been sputtered compared to 89.1% of the large grain core.

Two distinct models have been presented here, one for a shock speed of 16 km s^{-1} and density of 10^4 cm^{-3}, the other for a shock speed of 30 km s^{-1} and density of 10^6 cm^{-3}. For the first model only a small amount of sputtering occurs, and the ice mantle is not fully eroded for either size of grain. The fraction of the total mass sputtered corresponds well to the fraction of ice sputtered from the grains and indicates that the changes to the code to allow the evolution of the grain masses to be tracked has been implemented correctly. The second model demonstrates that the entire ice mantle is removed by sputtering for both the large and small grains, allowing core sputtering to proceed. Although a larger fraction of the total grain mass of the small grains is removed than that of the large grains, the values show that this corresponds to the fact that a larger portion of the core mass has been sputtered for the large grains than the small grains. This is because a significantly higher percentage of the initial small grain mass is made up of ice in comparison to the large grains.

3.5 C- to J-type shock transitions

Shocks in molecular clouds are likely to be C-type, in part due to the effective radiative cooling which takes places in these regions (Draine, 2011). In particular, an important coolant is H_2, the cooling rate of which is given by a fit to the temperature

and cooling rates given for the appropriate ro-vibrational transitions (Hartquist et al., 1980). There are two limiting velocities when it comes to a shock remaining C-type. One is the fast magnetosonic speed, which must be greater than the shock speed in order for the charged fluids to propagate ahead of the shock and form the magnetic precursor essential for C-type shock formation. The other is the speed at which H_2 is fully dissociated. It is this transition which is explored here.

3.5.1 H_2 DISSOCIATION

Dissociation of H_2 molecules removes an important coolant from the gas, resulting in a significant increase in the maximum neutral temperature. This causes a sonic point in the flow and the shock becomes J-type. For high enough shock speeds H_2 is destroyed by collisional dissociation. The critical shock speed associated with such dissociation depends on the pre-shock density n_H, magnetic field B_0 and fractional ionisation χ. The dissociation energy of H_2 is 4.48 eV, roughly corresponding to a neutral temperature $T_n \gtrsim 6000$ K for high densities. For non-magnetised shocks, the critical shock speed for dissociation can be approximated by setting $\mu\, v_s^2 \geq 4.48$ eV, which gives $v_s \geq 21$ km s^{-1} (Hartquist, 2017). A similar critical speed is obtained by Kwan (e.g. 1977), who find that for densities $n_H \gtrsim 10^2$ cm^{-3}, non-magnetic, single-fluid shocks cause complete destruction of H_2 for $v_s \gtrsim 24$ km s^{-1}. However, the presence of a magnetic field significantly increases this critical speed, with Draine et al. (1983) finding negligible dissociation for their 25 km s^{-1} models, and determining critical speeds of $49 \leq v_{crit} \leq 40$ km s^{-1} for densities $10^4 \leq n_H \leq 10^6$ cm^{-3}. The work by Le Bourlot et al. (2002) includes a more comprehensive dissociation rate for H_2 in their shock models, and found a significantly higher value for the critical speed of $v_{crit} \simeq 70$ km s^{-1} for a pre-shock density of $n_H = 10^4$ cm^{-3}, allowing a maximum neutral temperature of $T_n \approx 12000$ K for a shock velocity just below v_{crit}. However, for a pre-shock density of $n_H = 10^6$ cm^{-3} they found a critical velocity $v_{crit} \simeq 31$ km s^{-1}, allowing neutral temperatures up to $T_n \approx 5000$ K.

The numerical code described in Chapter 2 does not include H_2 dissociation, since the rates at which dissociation occurs in the C-type shocks of interest are negligible. However, it is expected that, for models with shock speeds close to or exceeding the critical velocity for dissociation, the maximum neutral temperature in the shock front would reach values above which it is known that H_2 is fully dissociated. The work by DRD analyses the maximum neutral temperature as a function of shock speed for different pre-shock densities. For $n_H = 10^6$ cm^{-3}, H_2 dissociation occurs

at a shock velocity of 44 km s^{-1}, corresponding to a maximum neutral temperature of $T_n \approx 4000$ K. The numerical model used in this thesis adopts similar cooling rates to those used in the model of DRD. Therefore, for a comparable set of pre-shock conditions, it is assumed that the critical velocity could be estimated by monitoring the maximum neutral temperature achieved in the shock front and, in particular, determining the shock speed for which the neutral temperature exceeds 4000 K. However, for a density of $n_H = 10^4$ cm^{-3} DRD find that C-type shock solution is limited by 'self-ionisation', meaning the fractional ionisation is changed by an amount large enough such that the change to the force per volume on the gas is more than 10% in the hottest part of the shock. This occurs at a shock speed of 49 km s^{-1} and corresponds to a maximum neutral gas temperature of approximately 3100 K.

However, it was found that for all shock speeds tested (up to 50 km s^{-1}), the neutral temperature did not reach 4000 K for $n_H = 10^6$ cm^{-3} or 3100 K for $n_H = 10^4$ cm^{-3}. This prompted an investigation into the cooling rates in an attempt to address why the maximum neutral temperature was remaining relatively low. The gas temperature profile is indicative of the shock structure, so inaccuracies in the cooling rates could have significant effects on the both the shock dynamics and the chemistry. This is therefore an important issue to resolve in order to ensure the validity of our model.

3.5.2 Results and discussion

Figure 3.3 shows the maximum neutral and electron temperatures as a function of shock speed. The plots are for pre-shock densities of 10^4 cm^{-3} and 10^6 cm^{-3} and compare the results to those of DRD. The results show that the same trends as DRD are followed for the maximum temperatures, particularly for the electron temperature. For $n_H = 10^4$ cm^{-3}, despite increasing with shock speed, the maximum neutral temperature of the model is consistently a factor of ~ 2 smaller than the results of DRD. For $n_H = 10^6$ cm^{-3} the difference in maximum neutral temperatures is not as clear. However, for $v_s \gtrsim 25$ km s^{-1} the current results and those of DRD begin to diverge. Importantly, for DRD the maximum neutral temperature at $v_s = 44$ km s^{-1} just exceeds 4000 K, at which point all the H_2 molecules are dissociated and the C-type shock solution no longer exists. In contrast, the current model does not see the neutral temperature exceeding 4000 K, even for a shock speed of 50 km s^{-1}. It is sensible to conclude that there is a problem with the

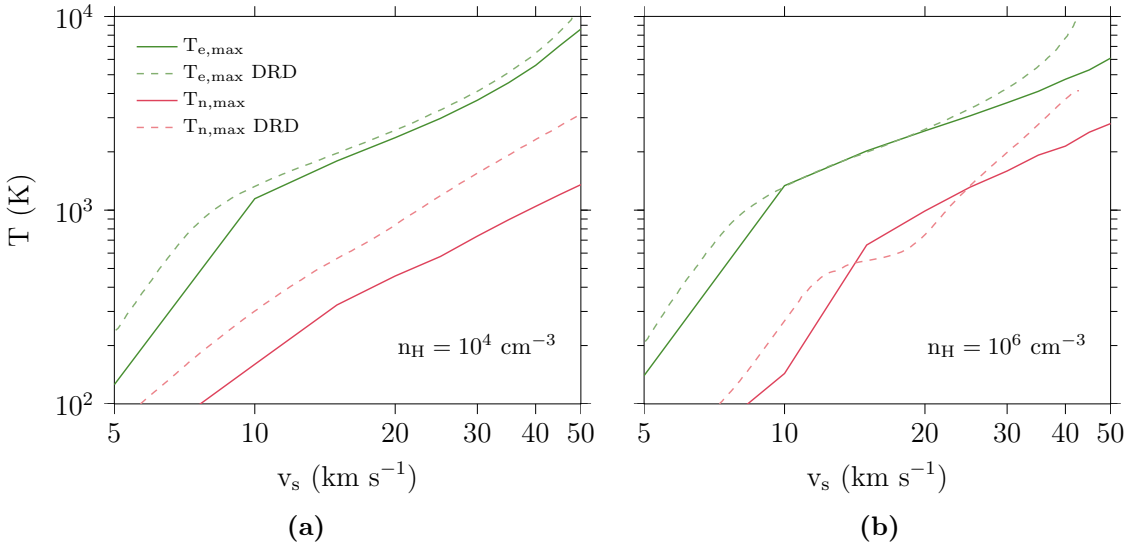

Figure 3.3: Maximum neutral (pink) and electron (green) temperatures as a function of shock speed. The dashed lines, labelled 'DRD', are the results from Draine et al. (1983). (a) is for a pre-shock density of 10^4 cm^{-3} and (b) is for a pre-shock density of 10^6 cm^{-3}.

computational model which causes the maximum neutral and electron temperatures to be suppressed at higher shock speeds. The cooling rates included in the model govern the neutral and electron temperatures, so these rates were investigated to confirm that they were not the cause of this temperature discrepancy.

To compare with the results of DRD, each of the cooling rates is plotted as a function of the shock velocity. DRD use the fraction of the total power radiated by the cooling mechanism, so here the peak of each cooling mechanism has been integrated at each velocity and then calculated as a fraction of the total cooling. The results are shown in Fig. 3.4 for the current model along with the results from DRD. Note that the model by DRD also includes cooling by OH molecules, but this has been left out of Figs. 3.4 (b) and (d) for clarity. For both 10^4 cm^{-3} and 10^6 cm^{-3} the cooling is dominated by H_2 and H_2O at high shock speeds ($v_s \gtrsim 20$ km s^{-1}). The fractional cooling rates appear to follow a similar trend to those of DRD for $n_H = 10^4$ cm^{-3} and for shock speeds upwards of approximately 10 km s^{-1}. However, the region where 10 km s^{-1} $< v_s <$ 20 km s^{-1} shows a significant difference between the amounts of H_2O cooling. Additionally, whilst there is a large discrepancy between the amounts of H_2 cooling at small shock speeds, at large shock speeds the fractions of H_2 cooling are in good agreement, contributing to the cooling by a fraction of approximately 0.79.

To confirm the effect of the H_2 cooling, the model was run with this mechanism

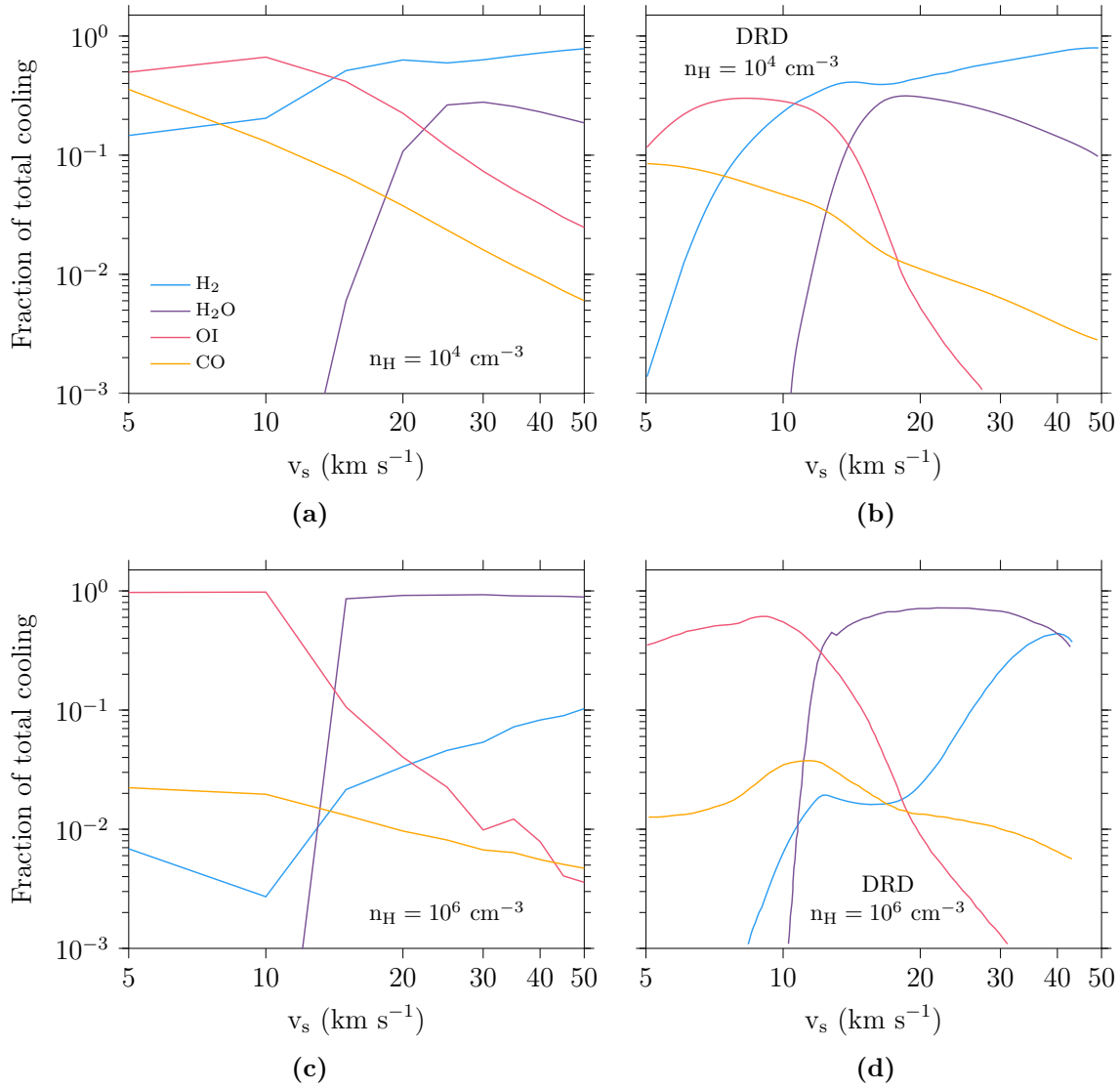

Figure 3.4: The contributions of different cooling mechanisms to the total cooling. (a) and (b) are for a pre-shock density of 10^4 cm^{-3}, (c) and (d) are for a pre-shock density of 10^6 cm^{-3}. (b) and (d) are the results from Draine et al. (1983) (labelled 'DRD').

'switched off'. Fig. 3.5 shows the results of this for both pre-shock densities. It is clear that for $n_H = 10^6$ cm^{-3} neglecting the contribution of H_2 cooling has no effect on the maximum electron temperature, and only a mild effect on the neutral temperature, causing it to increase by a factor of 1.17. To understand why this is the case, it is useful to think about which processes dominate the cooling at which shock velocities. For velocities above about 11 km s^{-1} the dominant cooling mechanism is that of H_2O. Therefore, removing the H_2 cooling has little effect on the neutral temperature at these speeds. However, for a density of $n_H = 10^4$ cm^{-3}, it is H_2 cooling which contributes the most for shock speeds above 11 km s^{-1} and hence there is a more significant increase in the neutral temperature when the H_2 cooling

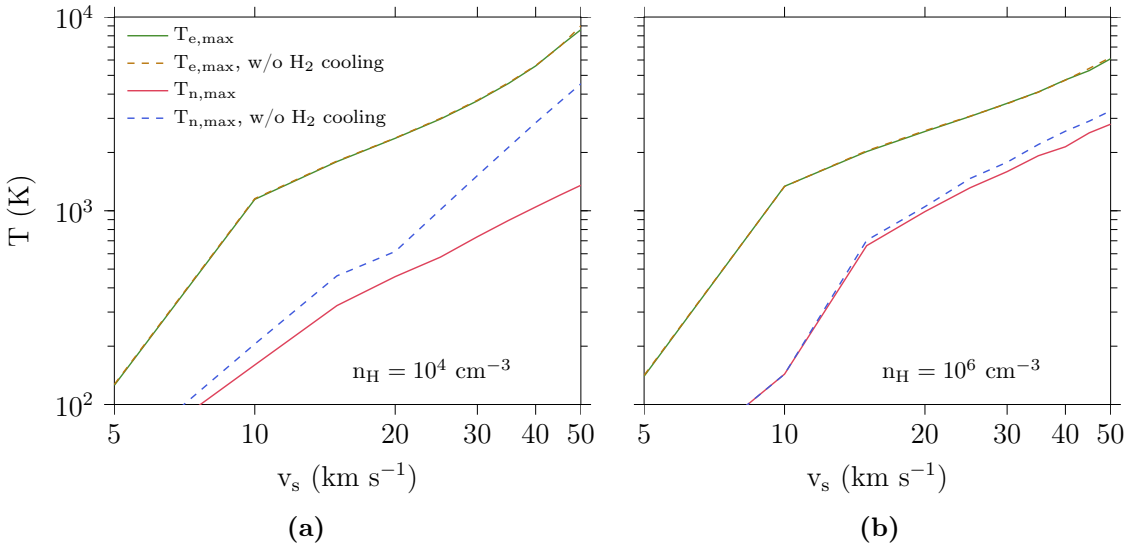

Figure 3.5: Maximum neutral and electron temperatures as a function of shock speed with (neutral; solid pink, electron; solid green) and without (neutral; dashed blue, electron; dashed brown) the inclusion of H_2 cooling. (a) is for a pre-shock density of 10^4 cm^{-3} and (b) is for a pre-shock density of 10^6 cm^{-3}.

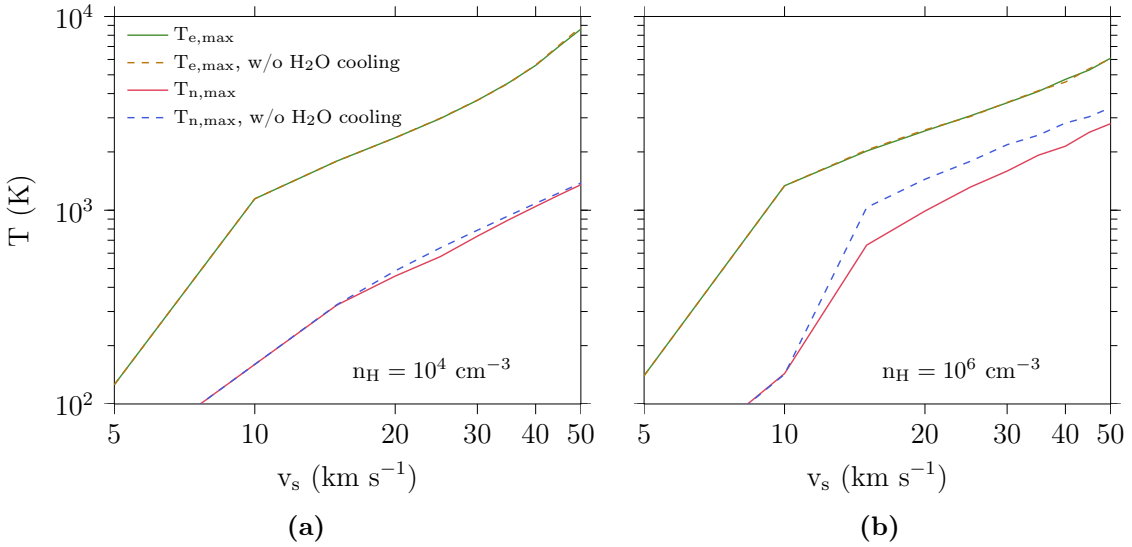

Figure 3.6: Maximum neutral and electron temperatures as a function of shock speed with (neutral; solid pink, electron; solid green) and without (neutral; dashed blue, electron; dashed brown) H_2O cooling. (a) is for a pre-shock density of 10^4 cm^{-3} and (b) is for a pre-shock density of 10^6 cm^{-3}.

is removed. In this case the neutral temperature at $v_s = 50$ km s^{-1} is increased by a factor of 3.33, and the neutral temperature does exceed the value of 3100 K indicative of a C-to-J-type shock transition. Overall, the modest changes to the neutral temperature for the high density model do not suggest an overestimation of the H_2 cooling as the reason for the neutral temperature discrepancy.

Fig. 3.6 shows the maximum neutral and electron temperatures as a function of shock speed for both densities, with and without H_2O cooling. These results show that, conversely to switching off H_2 cooling, switching off the H_2O cooling has a more significant effect on the temperature of the neutrals in the 10^6 cm^{-3} model than those in the 10^4 cm^{-3} model. H_2O molecules have a permanent electric dipole, so their permitted transitions allow a sizeable contribution to the overall cooling of the gas. However, as with the H_2 cooling, the rise in neutral temperature when the cooling is switched off is not large enough to suggest that the cooling rate is being overestimated.

It is clear that the cooling mechanisms which dominate at high shock speeds are not the cause of the suppression of the neutral gas temperature at these speeds; there must be some other effect at play. The cause could be the cumulative effect of certain approximations and inaccuracies in the numerical code. For example, one simplification that had been applied to the calculation of the cooling rates in the numerical code was to use approximations for the number densities of O and H_2O. These have now been updated to be the actual values as determined from the sputtering and chemistry. Additionally, the ion density should be fixed to be the sum of the densities of the separate ion species, but this was not being enforced in the code. These corrections were made and the models re-run.

Fig. 3.7 shows the maximum neutral and electron temperatures as a function of the shock velocity in comparison to DRD's results after these amendments have been made. In particular, for a density of 10^6 cm^{-3} the maximum neutral temperature now follows that of DRD much more closely than previously (Fig. 3.3). The neutral temperature now reaches approximately 3900 K, significantly closer to the 4000 K which indicates H_2 dissociation. There is still some discrepancy in the temperatures for the 10^4 cm^{-3} model. At 50 km s^{-1}, the maximum neutral temperature is slightly over 1400 K. This corresponds to a temperature increase of about 100 K compared to the previous model. So, while there has been some improvement in the temperature, it does not reach the expected $\sim$ 3100 K temperature of DRD's model. However, DRD attribute the break down of the C-type shock solution for

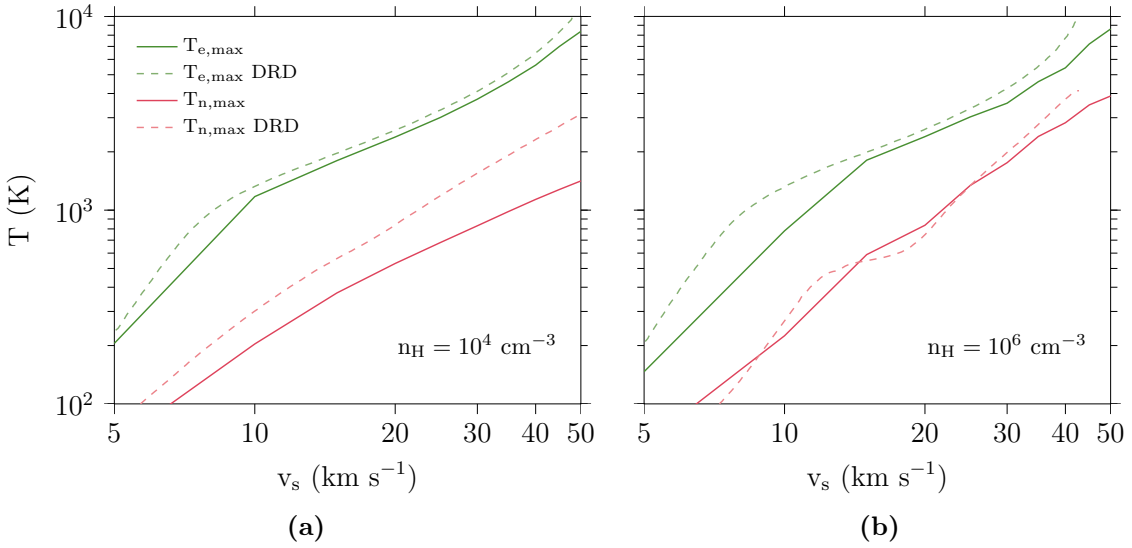

Figure 3.7: Maximum neutral (pink) and electron (green) temperatures as a function of shock speed. The dashed lines, labelled 'DRD', are the results from Draine et al. (1983). (a) is for a pre-shock density of 10^4 cm^{-3} and (b) is for a pre-shock density of 10^6 cm^{-3}.

10^4 cm^{-3} to 'self-ionisation', where the fractional ionisation is assumed to remain constant through the computation of their shock results, and then the change in fractional ionisation is determined afterwards. This change is determined from the rates due to processes such as electron impact excitation, photoionisation of trace metal atoms by UV radiation, ion-neutral and neutral-neutral collisions. Furthermore, DRD include grain mantle sputtering in the their model, which could impact the neutral temperature since it reduces the size of the grains and therefore affects how well coupled the grains are to the magnetic field.

In this section, the cause of the suppressed neutral temperature has been investigated. The switching-off of H_2 or H_2O cooling does not lead to such an increase in the temperature as to suggest that those cooling rates are being overestimated. What did have an effect was seemingly minor corrections, namely using calculated values of the O and H_2O number densities in the cooling rate calculations, and fixing the ion density to be the sum of the densities of the individual ion species. These corrections improve the accuracy of the cooling rate calculations and the chemistry, in turn affecting the neutral gas temperature. In particular, for the 10^6 cm^{-3} model, this gave good agreement with the results of DRD. While there remains some discrepancy in the neutral temperatures for the 10^4 cm^{-3} models, it is important to keep in mind the differences between the model presented here and that of DRD. The addition of grain processing in DRD's models, along with their method of calculating

the change in fractional ionisation could both play a part in causing the continuing difference in temperature for this model.

3.6 Conclusions

The numerical model for simulating C-type shocks in the interstellar medium described in Chapter 2 is the same as that used by Van Loo et al. (2009, 2013). There were a number of incorrect assumptions to be addressed and alterations to be made to this code in order to improve the accuracy of the results. Firstly, the grain charge calculation was corrected to allow for grains to become positively charged and so that the electron density is updated within the charge iteration. This fixed a problem in which the electron density could become negative. It is important to accurately determine the average charge on the grains, since it can have a significant effect on the shock dynamics. In fact, a neutral grain (or grain with small charge) will travel with the neutral fluid, affecting the shock width, temperature of the gas and rates of dust grain destruction. It is therefore important to follow the grain charges correctly, particularly due to the impact that this will have when exploring the evolution of the grain-size distribution in subsequent chapters.

Secondly, one drawback of the original model was that the grain masses were not being updated as they were changed by sputtering. The grain model was that of spherical grains made up of a silicate core encased by an icy mantle layer. The grains undergo sputtering in the shock due to impacts with neutral particles. Sputtering first erodes the mantle, and then, once the mantle has been fully sputtered, begins to erode the core. Despite this material being lost from the grains, the masses were not updated accordingly. The grain masses are used in the calculation of the Hall parameters (in the form of the charge-to-mass ratio), and the grain radii are used in the grain charge calculations. This therefore impacts the values of the resistivities and, hence, the fluid velocities, so it is important to track the grain masses accurately through the shock. The original model contained a mass conservation equation for each grain fluid. This was expanded to also include a continuity equation for the number density of the grains. Sputtering is a number-conserving process, hence alters the grain mass whilst conserving the grain numbers. This means that the mass of a single grain in the fluid can be calculated wherever required in the code according to $m_g = \rho_g / n_g$.

Results were shown for two sets of initial conditions; (1) $n_H = 10^4$ cm^{-3}, $v_s = 16$ km s^{-1} and (2) $n_H = 10^6$ cm^{-3}, $v_s = 30$ km s^{-1}. In the first model the shock speed was low enough that only about half of the ice mantle is sputtered from the grains, with the smaller grains experiencing slightly more sputtering than the larger grains. Due to the fact that the ice mantle makes up a larger fraction of the initial mass of the smaller grains, the smaller grains experienced a significantly greater fraction of their total mass removed by sputtering. However, the amount of mass removed was as expected given the fraction of ice removed and shows that the mass evolution of the grains is followed accurately in the code. In the second model the entire ice mantle was removed for both sizes of grains. For the small grains this represents 41% of the total initial mass, but for the large grains corresponds to to just 4.1% of the total initial mass. Therefore, although a greater portion of the overall small grain mass is eroded by sputtering, this was due to the large proportion of ice which needed to be removed, and actually a smaller fraction of the core was sputtered for the small grains compared to the large grains.

Finally, there was an issue with the maximum neutral temperature being reached in the higher-velocity shock models. DRD show that the there is a breakdown in the C-type shock solutions for perpendicular models which occurs at a maximum neutral temperature of approximately 4000 K. For a pre-shock density of 10^6 cm^{-3}, this transition from C-type to J-type shocks is a result of the total dissociation of H_2 molecules in the neutral fluid. This removes an important cooling mechanism from the gas, in turn causing the neutral fluid to become subsonic and hence the shock is no longer C-type. For a pre-shock density of 10^4 cm^{-3} the transition occurs due to a large change in the ionisation fraction. DRD refer to this as 'self-ionisation' and it suggests that the fractional ionisation changes to such a degree that the force per volume on the neutral fluid is altered by more than 10% in the hottest region of the shock. The current model showed that the maximum neutral temperature did not reach the expected 4000 K for shock speeds up to 50 km s^{-1}. Therefore the critical speed for the transition from C-to-J-type could not be determined, and suggested some error in the numerical code. Analysis of the cooling rates used in the code determined that these were not the cause of the low gas temperature. The problem was instead solved by replacing calculated average values of the number densities of O and H_2O with the actual values as updated by chemistry and sputtering at each time-step, which yielded maximum gas temperatures comparable to what is expected.

4

Grain-size distribution functions

This chapter presents work published by Sumpter and Van Loo (2020) and details a numerical approach for accurately evolving dust grain-size distributions in simulations where the dust undergoes physical processes, whilst maintaining a low computational cost. The method is tested against other methods that are used in the literature.

Contents

4.1 Introduction

The importance of dust in the ISM was highlighted in §1.3. A commonly accepted model for the size distribution of dust grains in the ISM is the MRN power-law distribution,

$$\frac{\mathrm{d}n(a)}{\mathrm{d}a} \propto a^{-3.5} \tag{4.1}$$

where a is the grain radius and $\mathrm{d}n(a)/\mathrm{d}a \times \mathrm{d}a$ is the number density of grains with radii in the range $[a, a + \mathrm{d}a]$ (Mathis et al., 1977). This model comes from fits to the Milky Way extinction curve, and assumes a mixture of silicate and graphite grains with sizes from $a = 5 \times 10^{-7}$ cm to $a = 3 \times 10^{-5}$ cm. This distribution is subject to local variations due to physical processes. For example, dust is thought to be produced in the upper atmospheres of Asymptotic Giant Branch (AGB) stars

(Maercker et al., 2018), experience growth in molecular clouds (Jones and Williams, 1985; Liffman and Clayton, 1989; Ossenkopf, 1993; Inoue, 2003; Ormel et al., 2009; Asano et al., 2013; Ysard et al., 2016; Jones et al., 2017), and be destroyed in interstellar shocks (Tielens et al., 1994; Jones et al., 1996; Flower and Pineau des Forêts, 2003; Guillet et al., 2007, 2009; Hirashita and Yan, 2009; Guillet et al., 2011; Anderl et al., 2013; Van Loo et al., 2013). Dust growth and destruction mechanisms can be broadly categorised into number-conserving and mass-conserving processes. Coagulation of dust grains and grain-grain shattering are both examples of mass-conserving processes, since the total number of grains in the distribution will change, but the total mass remains constant. Conversely, number-conserving processes, such as gas-grain sputtering and mantle accretion, conserve the total number of grains in the distribution but alter the total mass. These grain processes affect the overall grain-size distribution and therefore can have significant effects on the dynamics of e.g. the ISM and protoplanetary disks. For example, in the outflows of young stellar objects (YSOs) dust grains are important charge and current carriers and so determine the structure of C-type shocks (Van Loo et al., 2009), while in protoplanetary disks, different dust grain sizes influence the growth and structure of the magnetorotational instability (Salmeron and Wardle, 2008). Furthermore, in quiescent dark clouds silicon is adsorbed onto dust grains, but SiO is detected in the clumpy structure of YSO outflows due to shock-induced sputtering and vaporisation which release silicon into the gas phase (e.g. Martín-Pintado et al., 1992; Mikami et al., 1992). It is therefore important to accurately follow the evolution of the dust grain-size distribution to model both the dynamics and the emission signatures.

In §2.5 the treatment of the dust grains in the numerical formulation was described. The dust grain-size distribution is emulated through use of a large and small dust grain fluid, where all the grains in each fluid are of equal size. This is a simple approach which has been used in previous studies (e.g. Draine et al., 1983; Van Loo et al., 2013; Hirashita, 2015). Whilst this is a sufficient approximation for number-conserving processes, it becomes unsuitable for mass-conserving ones. Grain-grain collisions in C-type shocks arise due to the relative velocity which exists between grains of different sizes. The Hall parameter is the ratio of the gas-grain collision frequency to the gyrofrequency and is dependent on the charge-to-mass ratio of the grains. Therefore, larger grains tend to have smaller Hall parameters, so are less tightly coupled to the magnetic field, than smaller grains, which have larger Hall parameters and tend to travel with the electron and ion fluids. In order to capture

this variation in velocity, as well as the distribution of fragments which are produced in grain-grain collisions, the full grain-size distribution must be modelled.

A more rigorous approach is to follow the grain distribution using a discrete grain-size distribution. Then, the distribution can be updated by redistributing the grains across the bins in a way appropriate to capture the modelled grain process (e.g. Mizuno et al., 1988; Liffman and Clayton, 1989; Jones et al., 1994, 1996; McKinnon et al., 2018). Most of these studies focus on coagulation and shattering, i.e. the mass-conserving processes, so the models follow the total dust mass and not the total number of grains. To model the number-conserving processes of sputtering and accretion, McKinnon et al. (2018) (hereafter McK18) modified the discrete distribution approach by using a piecewise-linear discretisation inside each size bin in order to conserve both the mass and number of grains. McK18 show that this technique is second-order accurate in the number of grains. However, to achieve an accuracy $\sim \mathcal{O}(1\%)$ in both mass and number conservation, it is necessary to use about 50-100 bins. Including such a scheme into a numerical hydrodynamics (HD) or MHD code therefore significantly increases the computational cost.

This chapter presents an alternative approach to the discretisation within a size bin in order to minimise the numerical cost whilst maintaining high accuracy. As the typical observed dust distribution follows a power law (the MRN distribution) this alternative approach adopts a power-law discretisation. Section 4.2 outlines the method describing the calculation of the power law parameters (a coefficient and an index), and the redistribution of the dust grains for both number-conserving and mass-conserving processes. In Section 4.3 the method is applied to a number of test problems and the results are discussed. Finally, Section 4.4 gives the conclusions.

4.2 Numerical method for the evolution of grain distributions

Here, the numerical methods to evolve a power-law grain-size distribution are presented. First, the construction of a piecewise power-law distribution and the formulation of the power-law coefficients and indices are considered. Since the tests in §4.3 compare the power-law method to piecewise-linear and piecewise-constant

discretisations, these formulations are also presented. Finally, the routines to redistribute the mass and number density of grains across the size bins are discussed for grain processes that conserve the total grain numbers or total grain mass.

4.2.1 Discrete power-law distribution

Dust grains are usually irregular in shape (e.g. Draine, 2003), but for the purposes of this thesis it is assumed that they are spherical. This significantly simplifies the treatment of the dust grains as the grain distribution depends only on the grain radius a. Furthermore, it is assumed that the grain radii are limited to the range $[a_{\rm min}, a_{\rm max}]$. This range is then divided up logarithmically with a spacing determined by

$$\Delta a = \frac{\log(a_{\rm max}/a_{\rm min})}{N} \tag{4.2}$$

where N is the number of bins. This means that the edges of any bin i are given by

$$\begin{aligned} a_i &= a_{\rm min} {\rm e}^{i\Delta a} \\ a_{i+1} &= a_{\rm min} {\rm e}^{(i+1)\Delta a} \end{aligned} \tag{4.3}$$

where $i = 0,\ 1,\ ...,\ N-1$. The differential grain-size number density distribution in bin i has a power-law shape,

$$\left.\frac{\partial n(a,t)}{\partial a}\right|_i = A_i a^{-\alpha_i} \tag{4.4}$$

where $\partial n(a,t)/\partial a \times {\rm d}a$ is the number density of grains in a size interval $[a, a+{\rm d}a]$ at time t. Note that as grain processes change the distribution function, the power-law coefficient A_i and index α_i are implicitly time-dependent.

To determine the power-law coefficient and index, the grains' bin-averaged number density, $n(t)$, and mass density, $\rho(t)$, are used. $n(t)$ and $\rho(t)$ are followed according to the redistribution routine described in §4.2.2. The bin-averaged number density of grains in bin i at time t is given by the integral

$$n_i(t) = \int_{a_i}^{a_{i+1}} \left.\frac{\partial n(a,t)}{\partial a}\right|_i {\rm d}a = \begin{cases} \frac{A_i}{1-\alpha_i}\left(a_{i+1}^{1-\alpha_i} - a_i^{1-\alpha_i}\right) & \alpha_i \neq 1 \\ \\ A_i \log\left(a_{i+1}/a_i\right) & \alpha_i = 1 \end{cases} . \tag{4.5}$$

It is convenient to rewrite this expression through use of the bin edges in Eq. 4.3 as

$$n_i(t) = A_i \; a_{i+1/2}^{1-\alpha_i} \; \Delta a \; \mathcal{F}\left((1-\alpha_i)\frac{\Delta a}{2}\right), \tag{4.6}$$

where $\mathcal{F}(x) = \sinh(x)/x$ (since the exponentials can be rewritten in terms of the sinh() function) and applies to all values of α_i, and $a_{i+1/2} = a_{\min} \exp[(i+1/2)\Delta a]$. However, this does not, by itself, uniquely determine A_i and α_i. Therefore, a second expression is required and is provided by the grains' bin-averaged mass density

$$\rho_i(t) = \int_{a_i}^{a_{i+1}} m(a) \left.\frac{\partial n(a,t)}{\partial a}\right|_i \mathrm{d}a \tag{4.7}$$

where

$$m(a) = \frac{4}{3}\pi\rho_g a^3 \tag{4.8}$$

is the grain mass with ρ_g the density of the grain material. In a similar way as for Eq. 4.6, the expression for ρ_i can be rewritten as

$$\rho_i(t) = \frac{4}{3}\pi\rho_g \; A_i \; a_{i+1/2}^{4-\alpha_i} \; \Delta a \; \mathcal{F}\left((4-\alpha_i)\frac{\Delta a}{2}\right). \tag{4.9}$$

Combination of Eqs. 4.6 and 4.9, and use of the fact that the average grain mass in bin i is $m_i = \rho_i/n_i$, an expression can be derived which is dependent only on the power-law index α_i. This expression is

$$\frac{m_i}{m(a_{i+1/2})} \; \mathcal{F}\left((1-\alpha_i)\frac{\Delta a}{2}\right) - \mathcal{F}\left((4-\alpha_i)\frac{\Delta a}{2}\right) = 0 \tag{4.10}$$

and needs to be solved numerically using a root-finding algorithm, such as the Newton-Raphson method. As $\mathcal{F}$ in Eq. 4.10 is a monotonic function, only a few iterations are needed to find the solution, especially if the initial guess is close to the root. Once α_i is determined, the value of A_i can be calculated directly from Eq. 4.6 or Eq. 4.9.

The power-law description can be compared to methods previously used in the literature, such as piecewise-constant and piecewise-linear ones. The piecewise-constant discretisation takes on a constant value for the distribution in bin i according to

$$\left.\frac{\partial n(a,t)}{\partial a}\right|_i = \frac{n_i}{(a_{i+1} - a_i)}, \tag{4.11}$$

where here the constant reflects the total number density of grains in the bin. Alternatively, it could be chosen that the distribution constant reflects the mass density ρ_i in the bin. A clear disadvantage of this method is that it only accurately describes either the number density or mass density, but not both. The piecewise-linear method of McK18 fixes this by assuming a linear distribution around the bin's midpoint $a_{c,i} = (a_i + a_{i+1})/2$,

$$\left.\frac{\partial n(a,t)}{\partial a}\right|_i = \frac{n_i}{(a_{i+1} - a_i)} + s_i(t)(a - a_{c,i}), \tag{4.12}$$

where the slope $s_i(t)$ is chosen so that the mass density in the bin is equal to ρ_i. Note, however, that the linear distribution can become negative and non-physical if the slope is too steep. This is remedied by imposing a slope limiter ensuring positivity of the distribution function and conserving the grain mass density (described in Section 3.2.1 of McK18). Unfortunately, this also implies that the grain numbers within the bin are not conserved. The piecewise-constant and piecewise-linear methods can be considered to be first and second-order approximations to the power-law, respectively (see Appendix A). The accuracy depends on the bin size and on the distribution that needs to be modelled. For example, if the distribution is flat within the bin, all three methods give identical results since $s_i = 0$ in the piecewise-linear approach and $\alpha_i = 0$ in the power-law method so these reduce to the piecewise-constant distribution (Eq. 4.11).

In the description of each method it has been implicitly assumed that the grain distribution fills an entire bin. This does not necessarily need to be true, especially near the limits of the distribution $r_{\min}$ and $r_{\max}$ (where $a_{\min} \leq r_{\min} < r_{\max} \leq a_{\max}$). Then it is possible that the distribution is skewed towards one of the bin edges. In the piecewise-linear method of McK18, this causes the distribution function to become negative within the bin and slope limiting is required. Conversely, the power-law method always guarantees positivity. However, a skewed distribution produces a large power-law index resulting, numerically, in a floating point error. To take into account the possibility that bin i is only partially populated, alternative bin limits are set according to $a_i^* = \max(a_i, r_{\min})$ and $a_{i+1}^* = \min(a_{i+1}, r_{\max})$. Furthermore, it is necessary to take $\Delta a^* = \log(a_{i+1}^*/a_i^*)$ and $a_{i+1/2}^* = a_i^* \exp[\Delta a^*/2]$ to determine A_i and α_i. This small modifications avoids floating point errors and conserves both grain mass and number densities. This also means that the bins need not be restricted to a uniform logarithmic widths, but can be randomly sized.

While using Δa^* in the root-finding algorithm for Eq. 4.10 improves the conservation properties of the distribution function, it also highlights a concern when Δa^* becomes small, i.e. the root-finding algorithm is either unable to find a unique solution for α_i, or unable to find a solution at all. This is due to the shape of the function $\mathcal{F}(x)$. For small values of x, and thus Δa^*, the function reduces to $\mathcal{F}(x) \approx 1 + x^2/3$ and is numerically a constant for $x < 1.5 \times 10^{-3}$ (as the second term falls below the machine precision of 10^{-7}). Given that Δa^* is of the same order as x, we are limited to using the root-finding algorithm for values of $\Delta a^* > 5 \times 10^{-3}$. For values below this limit, a piecewise-constant approach is adopted, so $\alpha_i = 0$.

4.2.2 Redistribution of grain numbers and mass

The evolution of an advected dust grain-size distribution can be expressed as (Tsai and Mathews, 1995)

$$\frac{\partial}{\partial t}\left(\frac{\partial n(a,t)}{\partial a}\right) + \nabla \cdot \left(\frac{\partial n(a,t)}{\partial a}\,\mathbf{v}\right) = -\frac{\partial}{\partial a}\left(\frac{\partial n(a,t)}{\partial a}\frac{\mathrm{d}a}{\mathrm{d}t}\right) + S(a,t) \tag{4.13}$$

where $\mathrm{d}a/\mathrm{d}t$ is the rate of change of grain radius and $S(a,t)$ is the source/sink of grains. Note that if the terms on the right-hand side are equal to zero, this just represents changes in the distribution due to advection. Therefore, physical processes that affect the grain-size distribution are described by the terms on the right-hand side of Eq. 4.13. The first term represents processes that increase of decrease the grain radius and conserve the total grain numbers (e.g. sputtering and mantle accretion), while production and destruction processes are included in the second term. Of the latter processes, the focus is only on the ones that preserve mass (e.g. shattering and coagulation) as other processes, like supernova dust production, are straightforward to implement. In the following, sputtering and shattering are used to illustrate the methods for the grain distribution evolution, since they are relevant to C-type shocks.

4.2.2.1 Number conserving processes

In the ISM, the impact of neutral particles and ions on dust grains releases, or sputters, grain material such as Si, Mg and O, at a rate given by (Tielens et al., 1994)

$$\frac{\mathrm{d}N_s}{\mathrm{d}t} = 2\pi a^2 n_p u_p Y_s(u_p) \tag{4.14}$$

where N_s is the number of sputtered particles of species s, n_p is the number density of the projectile impact particles, u_p is the relative speed between the impacting particles and the grains and Y_s is the sputtering yield for species s integrated over all impact angles and evaluated for an impact speed of u_p. The rate of change of grain radius due to sputtering can be determined using the mass of the sputtered species m_s and is given by

$$\frac{\mathrm{d}a}{\mathrm{d}t} = -\sum_{s,p} \frac{m_s n_p}{2\rho_g}\, u_p Y_s(u_p). \tag{4.15}$$

Note that $\mathrm{d}a/\mathrm{d}t$ does not explicitly depend on the grain radius, but it does have a weak dependence through the sputtering yield. This is because the relative speed between impinging neutral or ion species and the grains is grain-radius dependent (e.g. Van Loo et al., 2009) and, for small grains, the projectile particle may be able to pass through the grain, therefore reducing the sputtering yield at these sizes (Bocchio et al., 2014).

When $\mathrm{d}a/\mathrm{d}t$ (or $\dot{a}$) is a constant, the time evolution of the grain distribution simply reduces to

$$\frac{\partial n(a, t+\Delta t)}{\partial a} = \frac{\partial n(a - \dot{a}\Delta t, t)}{\partial a} \tag{4.16}$$

and it is possible to split the effect of number-conserving processes from Eq. 4.13. The number density distribution at time $t + \Delta t$ for bin i is then

$$\begin{aligned} n_i(t+\Delta t) &= \int_{a_i}^{a_{i+1}} \left.\frac{\partial n(a, t+\Delta t)}{\partial a}\right|_i \mathrm{d}a \\ &= \sum_{j=0}^{N-1} \int_{a_i^j}^{a_{i+1}^{j+1}} \left.\frac{\partial n(a - \dot{a}\Delta t, t)}{\partial a}\right|_j \mathrm{d}a, \end{aligned} \tag{4.17}$$

where $a_i^j = \max[a_i, a_j + \dot{a}\Delta t]$ and $a_{i+1}^{j+1} = \min[a_{i+1}, a_{j+1} + \dot{a}\Delta t]$. Therefore, to determine the evolved number density in bin i it is only necessary to determine from which bin j the dust grains now residing in bin i came from. This can be done by calculating the position of the edges of bin j at time $t+\Delta t$, i.e. $[a_j + \dot{a}\Delta t, a_{j+1} + \dot{a}\Delta t]$, and establishing which bins overlap with bin i. The contribution to the number density is then worked out analytically using A_j and α_j describing the power-law distribution in bin j at time t. Similarly, the mass density of grains in bin i can be

updated using

$$\begin{aligned}\rho_i(t+\Delta t) &= \int_{a_i}^{a_{i+1}} m(a)\ \left.\frac{\partial n(a,t+\Delta t)}{\partial a}\right|_i \mathrm{d}a \\ &= \sum_{j=0}^{N-1} \int_{a_i^j}^{a_{i+1}^{j+1}} m(a)\ \left.\frac{\partial n(a-\dot{a}\Delta t,t)}{\partial a}\right|_j \mathrm{d}a.\end{aligned} \tag{4.18}$$

The updated $n_i(t+\Delta t)$ and $\rho_i(t+\Delta t)$ values can be used to solve for the power-law coefficient A_i and index α_i at time $t+\Delta t$, which in turn are used to find the discrete distribution function $\partial n(a,t+\Delta t)/\partial a|_i$.

4.2.2.2 Mass-conserving processes

In contrast to sputtering, shattering due to grain-grain collisions conserves the total mass density of the grain distribution but not the total number density. Above a threshold impact velocity some volume fraction of the grains involved will fragment into smaller dust grains, which themselves follow a power-law size distribution according to (Jones et al., 1996)

$$\frac{\partial N_{frag}}{\partial a} \propto a^{-3.3} \tag{4.19}$$

where N_{frag} is the number of fragments. The evolution of the grain distribution is then described as (e.g. Jones et al., 1994)

$$\begin{aligned}S(a,t) = &-\frac{\partial n}{\partial a}\int_{a_{\min}}^{a_{\max}} \mathrm{d}a_1 \frac{\partial n}{\partial a_1}\sigma(a,a_1) \\ &+\frac{1}{2}\int_{a_{\min}}^{a_{\max}} \mathrm{d}a_1 \frac{\partial n}{\partial a_1} \times \int_{a_{\min}}^{a_{\max}} \mathrm{d}a_2 \frac{\partial n}{\partial a_2}\sigma(a_1,a_2)\frac{\partial N_{frag}}{\partial a}(a,a_1,a_2),\end{aligned} \tag{4.20}$$

where $\sigma(a_1,a_2) = \pi(a_1+a_2)^2 v_r(a_1,a_2)$ when multiplied by the grain number density gives the collision frequency between grains of size a_1 and a_2 if the relative velocity, $v_r(a_1,a_2)$, is above the threshold value for shattering, and is equal to zero otherwise. $\partial N_{frag}(a,a_1,a_2)/\partial a \times \mathrm{d}a$ is the number of grains with radii in the range $[a, a+\mathrm{d}a]$ produced by interactions of grains with radius a_1 and a_2. In Eq. 4.20 the first term describes the removal of dust grains from the interval and the second term gives the

contribution due to fragmentation, and requires integration over the entire grain-size distribution.

For the purpose of evolving a discrete distribution, Eq. 4.20 needs to be integrated across the different bins. Hence, the change in number density as a function of time for bin i is given by

$$S_i(t) = \int_{a_i}^{a_{i+1}} \mathrm{d}a \; S(a,t)$$

$$\begin{aligned} &= -\sum_{j=0}^{N-1} \pi v_r(\langle a\rangle_i, \langle a\rangle_j) n_i n_j \left\{\langle a^2\rangle_i + 2\langle a\rangle_i\langle a\rangle_j + \langle a^2\rangle_j\right\} \\ &\quad + \frac{1}{2}\sum_{j=0}^{N-1}\sum_{k=0}^{N-1} \pi v_r(\langle a\rangle_j, \langle a\rangle_k) n_j n_k N_{frag,i}^{j,k} \left\{\langle a^2\rangle_j + 2\langle a\rangle_j\langle a\rangle_k + \langle a^2\rangle_k\right\}, \end{aligned} \tag{4.21}$$

where

$$\langle a^l\rangle_i = \frac{1}{n_i}\int_{a_i}^{a_{i+1}} \mathrm{d}a \; a^l \; \frac{\partial n}{\partial a}, \tag{4.22}$$

where l is an integer, and

$$N_{frag,i}^{j,k} = \int_{a_i}^{a_{i+1}} \mathrm{d}a \frac{\partial N_{frag}}{\partial a}(a, \langle a\rangle_j, \langle a\rangle_k) \tag{4.23}$$

is the number of fragments with sizes in the range $[a_i, a_{i+1}]$ due to fragmentation by collisions of grains with bins j and k. Here, it has been assumed that the distribution of grain fragments is the same for all grains in bins j and k, i.e. $\partial N_{frag}/\partial a(a, a_1, a_2) = \partial N_{frag}/\partial a(a, \langle a\rangle_j, \langle a\rangle_k)$. If the analytic form of the size distribution of fragments and its dependence on the projectile and target radii are known, a more accurate version of Eq. 4.21 can be derived. Furthermore, it is presumed that all grains in a size bin have the same velocity, therefore the relative velocity between two bins is also constant. Use of Eq. 4.21 means the number density in bin i at time $t + \Delta t$ is then

$$n_i(t + \Delta t) = n_i(t) + S_i(t)\Delta t. \tag{4.24}$$

Likewise, the mass density can be updated using

$$\rho_i(t + \Delta t) = \rho_i(t) + S_i^{'}(t)\Delta t, \tag{4.25}$$

where $S_i'(t)$ is derived by multiplying Eq. 4.20 with $m(a)$ and then discretising the integrals. This gives

$$\begin{aligned} S_i'(t) = &- \frac{4}{3}\pi\rho_g\langle a^3\rangle_i \sum_{j=0}^{N-1} \pi v_r(\langle a\rangle_i, \langle a\rangle_j) n_i n_j \left\{\langle a^2\rangle_i + 2\langle a\rangle_i\langle a\rangle_j + \langle a^2\rangle_j\right\} \\ &+ \frac{1}{2}\sum_{j=0}^{N-1}\sum_{k=0}^{N-1} \pi v_r(\langle a\rangle_j, \langle a\rangle_k) n_j n_k m_{frag,i}^{j,k} \left\{\langle a^2\rangle_j + 2\langle a\rangle_j\langle a\rangle_k + \langle a^2\rangle_k\right\} \end{aligned} \tag{4.26}$$

where $m_{frag,i}^{j,k}$ is the mass transferred to bin i due to collisions between grains in bins j and k and is given by

$$m_{frag,i}^{j,k} = \int_{a_i}^{a_{i+1}} \mathrm{d}a\; m(a)\; \frac{\partial N_{frag}}{\partial a}(a, \langle a\rangle_j, \langle a\rangle_k). \tag{4.27}$$

This means that the radius of the fragmented grains is not taken into account, but only an appropriate mass for all grains within a bin is assumed. This assumption must also be reflected in the mass-loss term, i.e. the first term on the left-hand side of Eq. 4.26, as otherwise a systematic discrepancy arises between the mass-loss due to fragmentation and the redistributed mass across the distribution. Again, such simplifications are not required when the analytic expressions for the fragment distribution in terms of the radii of colliding grains is known. Eqs. 4.21 and 4.26 are analogous to the expressions of other authors who have used either a piecewise-constant or piecewise-linear description for the discrete distribution function (e.g. Mizuno et al., 1988; Jones et al., 1994, 1996; Hirashita and Yan, 2009, McK18).

4.3 Tests and results

To test the power-law description of the grain distribution, the methods of §4.2 are applied to the test problems outlined in McK18. As these tests have analytical solutions, this allows a direct comparison with both the piecewise-constant and piecewise-linear methods studied in McK18. Note that these tests do not necessarily represent physical or realistic situations.

4.3.1 Sputtering of a boxcar distribution

Here, the convergence of the error in the total grain mass density is tested depending on the number of size bins used. McK18 show that the piecewise-linear method exhibits a $1/N^2$ scaling of the convergence and, thus, second-order behaviour. This is an improvement on the piecewise-constant method which is only first-order.

The initial distribution is taken to be a boxcar function[1]

$$\frac{\partial n}{\partial a} = \begin{cases} 1 \text{ cm}^{-4} \text{ if } a_L \leq a \leq a_R \\ 0 \text{ cm}^{-4} \text{ otherwise,} \end{cases} \tag{4.28}$$

where $[a_L, a_R] = [a_{\min}(a_{\max}/a_{\min})^{3/8}, a_{\min}(a_{\max}/a_{\min})^{1/2}]$, $a_{\min} = 1 \times 10^{-7}$ cm and $a_{\max} = 1 \times 10^{-4}$ cm. Contrary to McK18, who adopt a grain growth rate, here a constant grain sputtering rate of $\dot{a} = -2.4 \times 10^{-7}$ cm Gyr^{-1} is applied for a time of $t = 5$ Gyr in 100 equal time steps. A constant sputtering rate is used to ensure that the test is analogous to that of McK18. In reality, the sputtering rate is size-dependent via the sputtering yield (e.g. Bocchio et al., 2014). Grains which are sputtered to a size smaller than $a_{\min}$ are assumed to be too small to participate in further sputtering and are removed from the distribution. Since sputtering only affects the grain mass (and not the number of grains), the final distribution is still a boxcar function, but is shifted to be between the limits $[a_L + \dot{a}t, a_R + \dot{a}t]$.

Fig. 4.1 shows the fractional error in the total grain mass density as a function of the number of bins (from $N = 8$ to $N = 2048$) for the piecewise-constant, piecewise-linear and power-law methods. Both the piecewise-constant and linear methods show their expected first- and second-order dependence, respectively, on bin size, and the latter method outperforms the former. However, the power-law method surpasses both of these with a fractional error below 0.1% for all numbers of bins. Especially for a small number of bins the power-law method is more than four orders of magnitude better than the other two methods. The linear method only achieves this accuracy for $N = 512$ and the piecewise-constant method for $N = 2048$.

It is pertinent to understand where these differences in the fractional error between the methods come from. In principle, all of the methods should describe the distribution equally well as, for example, the piecewise-linear should reduce to the piecewise-constant method (see §A). Furthermore, for the power-law method, the power-law

[1]Note that the units for $\partial n/\partial a$ (Eq. 4.28, for example) are perhaps more clearly written as cm^{-3} cm^{-1}, but are given as cm^{-4} throughout this thesis for brevity.

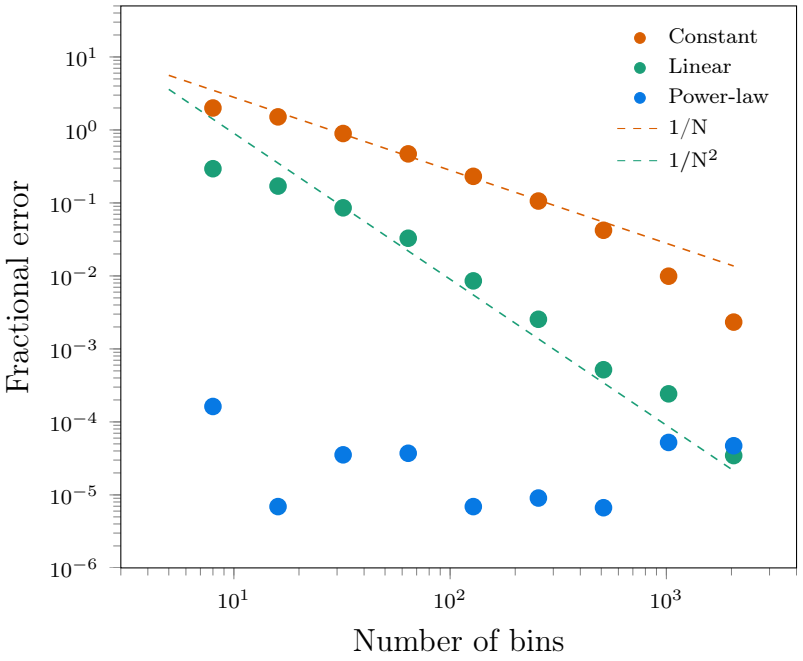

Figure 4.1: Fractional error in the total grain mass density as functions of the number of bins, N, for an initial boxcar distribution affected by sputtering. The circles show the results for the power-law (blue), piecewise-linear (green) and piecewise-constant (red). The dashed lines show a $1/N$ scaling (red) and $1/N^2$ scaling (green).

index is set to $\alpha_i = 0$ for $N = 2048$ as the root-finding algorithm breaks down (see §4.2.1). This implies that it also reduces to the piecewise-constant method, yet it produces a result that is nearly two orders of magnitude better than the piecewise-constant method. The only difference is the treatment of the distribution edges. As the distribution evolves due to sputtering, it moves across the bins, but does not necessarily continue to cover and entire bin at the distribution limits. However, the piecewise-constant method dictates that the grains are uniformly distributed in a bin and, likewise, the linear method uses slope-limiting to distribute the grains across an entire bin. This causes the discrete distribution to be smeared out at its edges, as seen in fig. 4.2. Only the power-law method follows the distribution edges and takes them into account when determining the distribution function inside the bin. Modification of the piecewise-constant and linear methods leads to an increased accuracy, with the relative errors in the mass density of below 10^{-4} for all bin sizes. Note that the treatment of the distribution edges in the power-law method also produces the variations seen in the relative error as a function of the bin number.

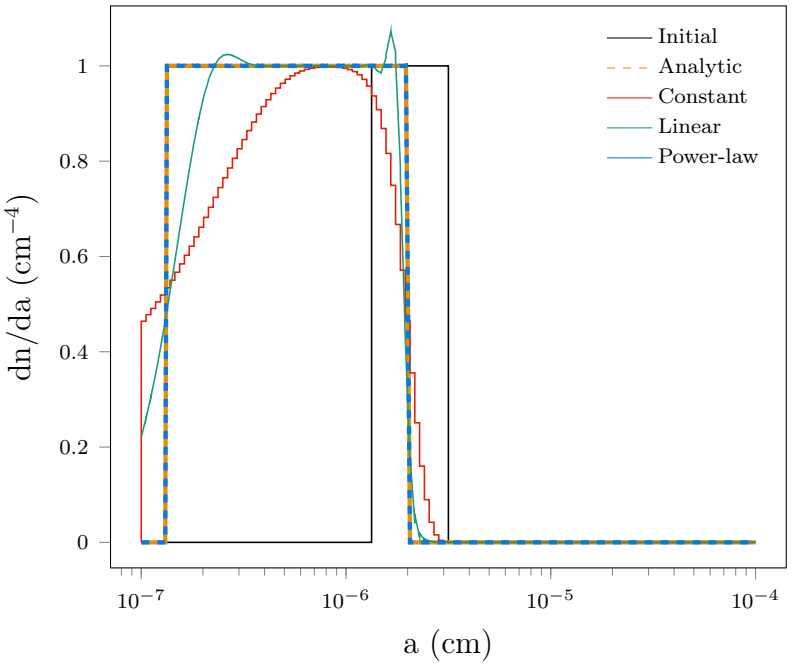

Figure 4.2: Initial boxcar distribution (solid black line) with $N = 128$ evolved by the application of a sputtering rate of $\dot{a} = -2.7\times10^{-7}$ cm Gyr^{-1} for 5 Gyr using the piecewise-constant (red), piecewise-linear (green) and power-law (blue) methods, and compared to the analytic solution (orange dashed).

4.3.2 Sputtering of an MRN distribution

Whilst the boxcar distribution of the previous section shows that it is important to carefully treat the edges of the distribution, it is not representative of realistic grain-size distributions. In the ISM, the size distribution for silicate and carbon grains is given by a power-law (Mathis et al., 1977). Therefore, in this test, the three methods are tested on their ability to follow the evolution of a power-law distribution affected by sputtering.

Each bin is initialised between $[a_{\rm min}, a_{\rm max}]$ with the number and mass densities calculated using $\partial n(a)/\partial a|_i = a^{-3.5}$. The same $a_{\rm min}$, $a_{\rm max}$, sputtering rate and evolution time are used as for the boxcar test in the previous section. While the errors occurring at the distribution edges have been minimised here by completely filling the full grain-size range, the piecewise-constant and linear methods have been further modified to track the distribution limits as was already done for the power-law method. As a result, the distribution is not affected by the issues arising when the edge of the distribution falls inside a bin, as in the boxcar test, and all the differences are due to the ability of each method to describe the underlying grain-size distribution.

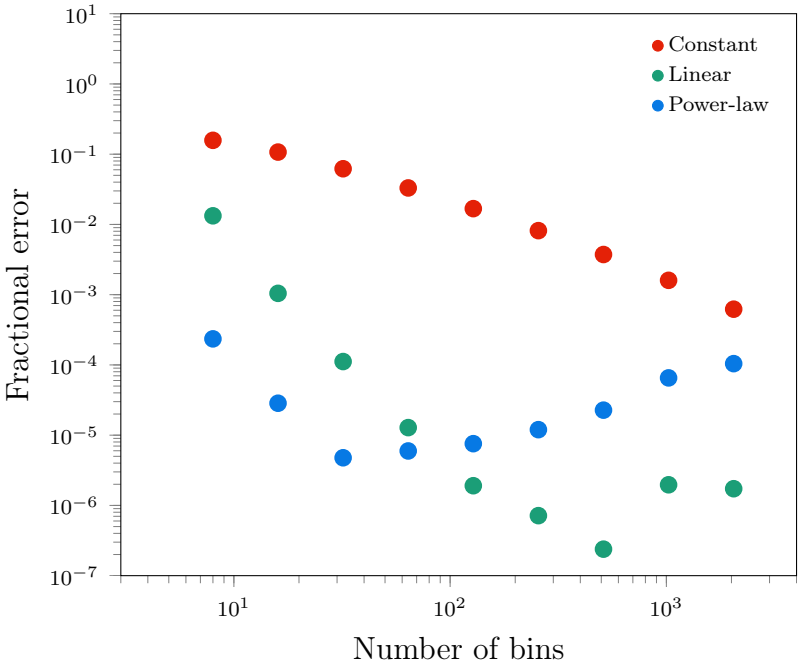

Figure 4.3: Fractional error of the numerical grain mass density as a function of the number of bins N for an initial MRN distribution affected by sputtering. The circles show the results for the power-law (blue), modified piecewise-linear (green) and modified piecewise-constant (red) methods.

Fig. 4.3 shows the fractional error in the total grain mass density at the final time for the different methods. While, for the boxcar distribution, the modified piecewise-constant and linear methods have relative errors of the order 10^{-5} for all bin sizes, this is no longer the case. Especially, the modified piecewise-constant method shows linear behaviour in the fractional error with large errors for small numbers of bins, i.e. $> 10\%$ for $N \leq 32$. The modified piecewise-linear method is significantly better, but still performs poorly for small numbers of bins, i.e. $N < 16$. Only the power-law method consistently produces errors smaller than 10^{-3} for all numbers of bins. However, note that, for large values of N, the modified piecewise-linear method is better than the power-law method as the latter reduces to the modified piecewise-constant method when the bin size becomes very small (see §4.2.1).

The discrete distribution function for the evolved MRN distribution is shown in Fig. 4.4 for $N = 8$ and $N = 128$. From the figure it is clear that the power-law method describes the power-law distribution very well. The modified linear method does capture the analytic solution at small grain radii, but is less accurate at large radii where slope-limiting needs to be applied. However, the modified linear method is always better than the modified constant one when describing a power-law distribution and, as N increases, the modified linear method converges to the

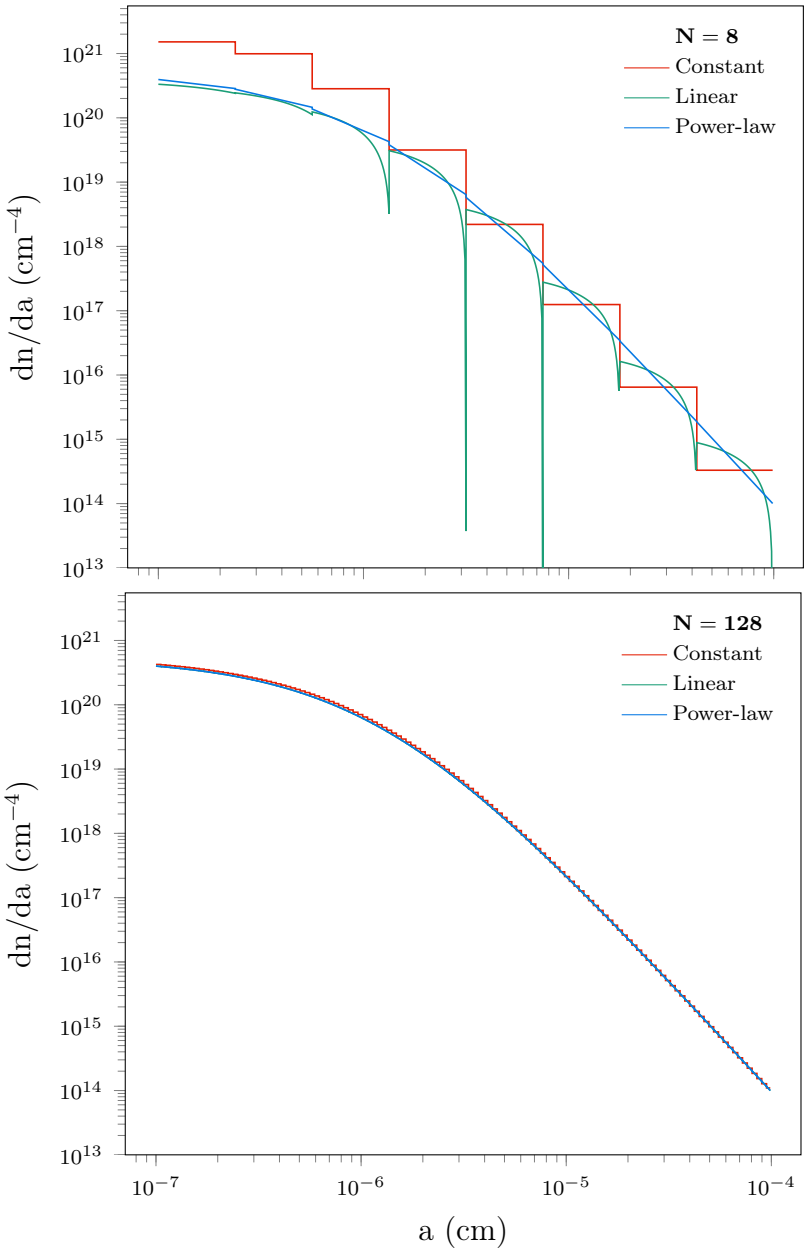

Figure 4.4: MRN distribution evolved by the application of a sputtering rate of $\dot{a} = -2.4\times10^{-7}$ cm Gyr^{-1} for 5 Gyr using the modified piecewise-constant (red) and piecewise-linear (green) methods and the power-law method (blue). These are compared to the analytic distribution (orange dashed) for $N = 8$ (top) and $N = 128$ (bottom).

power-law method. Eventually, the modified piecewise-constant method will also converge but only at much larger values of N. This is expected as a power-law distribution can be approximated to second order as

$$\left.\frac{\partial n(a)}{\partial a}\right|_i = A_i a_0^{-\alpha_i} - \alpha_i A_i a_0^{-\alpha_i - 1}(a - a_0), \tag{4.29}$$

where a_0 is a grain size in the interval $[a_i, a_{i+1}]$. The piecewise-linear and piecewise-constant discretisations are expressed similarly and therefore eventually converge as the bin size decreases (i.e. as N increases). Note that the convergence is faster for shallower power laws. Although all the methods are able to conserve the total grain

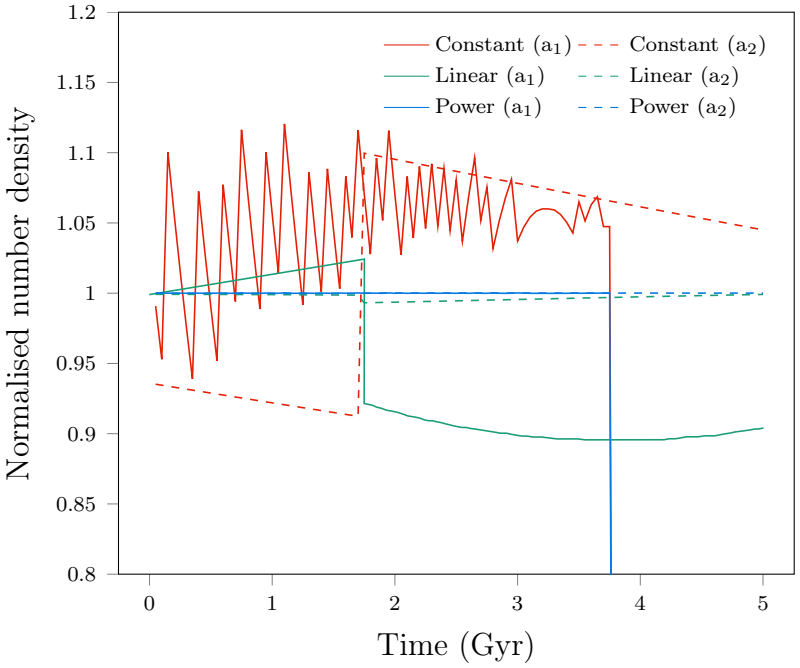

Figure 4.5: Evolution of the number density as a function of time for grains with an initial radius of $a_1 = 1 \times 10^{-6}$ cm (solid) and $a_2 = 5 \times 10^{-5}$ cm (dashed) for the modified piecewise-constant (red), modified piecewise-linear (green) and power-law (blue) methods with $N = 128$. The number densities are normalised to the analytic values.

mass density and reproduce the final distribution to a high degree for $N = 128$ (see Figs. 4.3 and 4.4), it is also useful to evaluate the distribution function at specific grain radii. For processes such as sputtering, as the grains shrink, the number of grains doesn't change. Fig. 4.5 shows the grain number normalised to their initial value for grains with an initial radius of 1×10^{-6} cm or 5×10^{-5} cm for the three methods over a time range of 5 Gyr. While the power-law method maintains a constant grain number for both grain radii, the modified piecewise-constant and linear methods show errors of the order of $10 - 15\%$. These errors do not remain constant but vary significantly over time with large discontinuities when the grains move from one bin to another. Note that the 1×10^{-6} cm grains move through many more bins that the 5×10^{-5} cm ones before they reach the lower limit of the distribution, $a_{\min}$, and are removed from the model around 3.8 Gyr. Thus, the power-law model not only preserves global properties of the distribution, but also the inter-bin characteristics, unlike the modified piecewise-constant and linear methods.

4.3.3 Grain shattering

The previous tests dealt with grain sputtering, a process that conserves the total number density of grains in the distribution while the total mass density of grains in the distribution changes. Here, grain shattering is examined, in which the total mass density of grains is conserved but the number density of grains is altered significantly due to the production of many small fragments. When two grains of differing sizes, and different velocities, collide at a relative velocity exceeding a threshold value, some portion of the grains are fragmented. These smaller fragments can themselves be treated as spherical grains that follow a power-law grain-size distribution.

Here, the same shattering test as in McK18 is presented. Only the collisions between large grains ($\geq 1 \times 10^{-5}$ cm) cause fragmentation, with both grains completely destroyed. For simplicity, the fragments are distributed across the full size range $[a_{\min}, a_{\max}]$, where $a_{\min} = 1 \times 10^{-7}$ cm and $a_{\max} = 1 \times 10^{-4}$ cm, following a distribution $\propto a^{-3.3}$. Note that, since fragments can be larger than the grains from which they came, this model can be thought of as allowing some degree of grain growth in addition to shattering. The collision velocity between grains is set to 3 km s^{-1}. With these assumptions, the distribution of fragments is

$$\frac{\partial N_{frag}}{\partial a}(a, a_1, a_2) = 0.7 \frac{(a_1^3 + a_2^3)}{(a_{\max}^{0.7} - a_{\min}^{0.7})} \; a^{-3.3}, \tag{4.30}$$

which results in

$$N_{frag,i}^{j,k} = \frac{0.7}{2.3} \left(\langle a^3 \rangle_j + \langle a^3 \rangle_k \right) \; \frac{\left(a_i^{-2.3} - a_{i+1}^{-2.3} \right)}{(a_{\max}^{0.7} - a_{\min}^{0.7})}, \tag{4.31}$$

and

$$m_{frag,i}^{j,k} = \left(\langle m \rangle_j + \langle m \rangle_k \right) \; \frac{\left(a_{i+1}^{0.7} - a_i^{0.7} \right)}{(a_{\max}^{0.7} - a_{\min}^{0.7})}, \tag{4.32}$$

where $\langle m \rangle = 4/3 \; \pi \rho_g \langle a^3 \rangle$. Eq. 4.32 is the same as in McK18 (their eq. 63) and, to compare results, this expression is also used for this test. However, as the fragment size distribution, Eq. 4.30, has a simple analytic expression, it is possible to derive more accurate, exact versions for Eqs. 4.21 and 4.26. Whilst these expressions aren't used to determine the results, they are used to produce quasi-analytic solutions (using $N = 256$ bins) and to evaluate the approximations made in $N_{frag,i}^{j,k}$ and $m_{frag,i}^{j,k}$. To differentiate between the two power-law methods, the former will be referred to as the default method, and the latter will be referred to as the exact method. The same initial conditions are used as in the shattering test by McK18,

that is, a lognormal distribution represented by a piecewise discrete distribution over $N = 8$ bins and the assumption that only the largest grains contribute to the shattering as $v_r(a_i, a_j) = 3$ km s^{-1} if $a_i \geq 1 \times 10^{-5}$ cm and $a_j \geq 1 \times 10^{-5}$ cm and is equal to zero otherwise. Fig. 4.6 shows the grain distribution due to shattering for a time of 150 Myr. At this time a reasonable amount of large grains have been shattered so that, while the initial distribution is only slightly modified at the large radius end of the distribution, the small grains follow the $a^{-3.3}$ power law distribution resulting from the fragmentation. The piecewise-linear method of McK18 describes this distribution reasonably well, especially if the distribution is evaluated at the geometric midpoints of the bins. Furthermore, quantitatively, the piecewise-linear routine produces a relative error in the total number density of about 10%, and conserves the total mass density exactly. However, a closer inspection of the distribution shows that it is not adequately described, particularly at the bin edges. This is due to the slope limiting which needed to be performed at the small grain sizes ($< 1 \times 10^{-5}$ cm) in order to ensure positivity of the distribution (whilst conserving mass). At the same time, it can be seen that the distribution of the large grains remains uniform within the bin (that is, a slope of zero). This is because, in the method of McK18, the average grain size does not change if a bin loses mass, only when it gains mass. While it is not a significant problem for this specific test, where shattering is treated alone, reproducing the distribution shape becomes important when number-conserving processes are considered simultaneously with mass-conserving ones.

The power-law method does describe the grain distribution across the full range of grain sizes more accurately with only minor deviations from the analytic solution at the larger grain sizes. The exact method performs slightly better than the default one in reproducing the analytic solution. Both methods have a relative error below machine precision for the mass density, and below 2% for the number density. Although the exact method does describe the distribution better than the default method, the errors are similar since a discrete distribution with $N = 8$ bins cannot adequately model the break in the analytic distribution at $a = 1 \times 10^{-5}$ cm. This break does not coincide with a bin edge, but instead falls in the middle of a bin. The benefits of the exact method become clear if we check the relative error in the number density in each bin. The total number density is dominated by a single bin; the bin with the smallest radius. Therefore, errors at the larger grain radii are not quantified by the relative error in the total grain number density. In the bin with the largest radii, the relative error is below 0.1% for the exact method, 8% for the

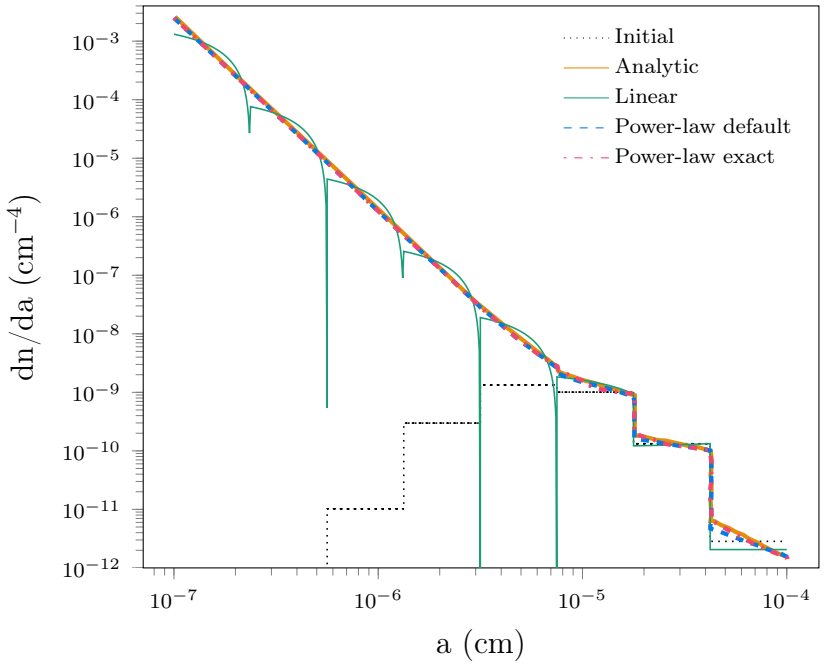

Figure 4.6: Distribution of grains due to shattering after 150 Myr for the piecewise-linear method (green) and the power-law method. The dashed blue line uses the default method with an approximated mass deposited in a bin, while the dotted red line uses the exact method using an exact mass calculation. The quasi-analytic solution is given by the yellow solid line and the initial distribution by the dotted black line.

default method, and reaches 25% for the linear method. The accuracy at which the exact power-law method can reproduce the distribution in a bin reflects in improved performance at longer evolution times. If the shattering test is run over a longer time period, for example up to $t = 1$ Gyr, the relative error in the total number density increases to $\approx 10\%$ for the default method, but only to $\approx 5\%$ for the exact method. Thus, it is crucial that the shattering integrals include as much information as possible to minimise the effect of error on the redistribution of fragments across the grain sizes, especially if modelling both mass- and number-conserving processes.

4.3.4 Combined sputtering and shattering

While §4.3.2 and §4.3.3 show that the power-law method performs well for number-conserving and mass conserving processes individually, these processes often arise simultaneously. There, here the combined effect of sputtering and shattering of grains on a initial MRN distribution is studied.

In this test the dust grain evolution is modelled as it occurs within a C-type shock from moving through a medium of $n_H = 10^6$ cm^{-3} with a dust-to-gas mass ratio of 0.01. In this situation, the dynamics of the grains is determined by the balance of

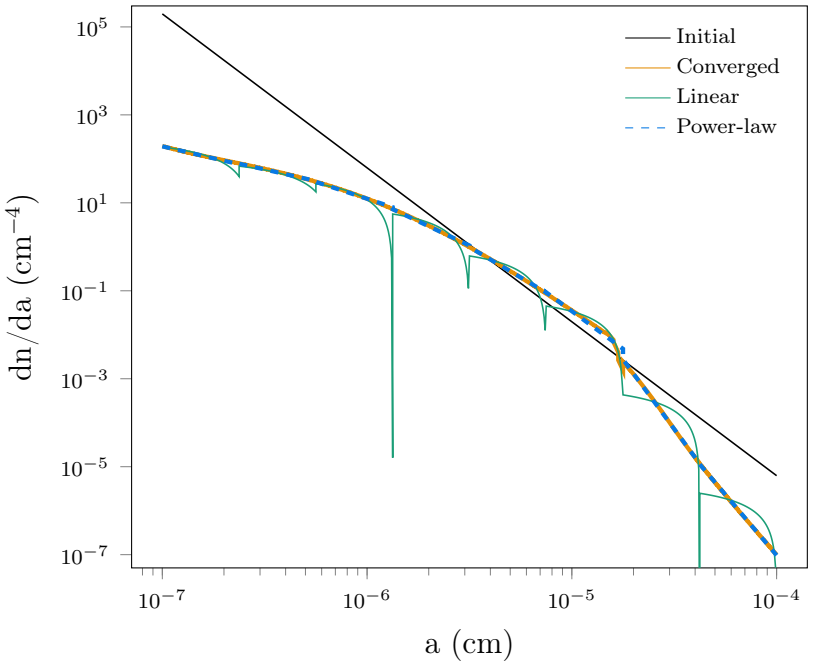

Figure 4.7: Final distribution after sputtering and shattering are applied in combination for a time of 10^6 s, with a sputtering rate of -10^{-12} cm s^{-1}, for the piecewise-linear (green) and power-law (blue) methods ($N = 8$). The initial MRN distribution is shown in black and the converged solution in dashed yellow ($N = 256$).

Lorentz forces and collision forces with neutral particles. This results in an effective velocity difference between small grains that are coupled to the magnetic field and move with the ions and electrons, and the large grains moving with speeds close to that of the neutrals. Guillet et al. (2007) show that the grain radius at which this transition occurs is between $\sim 7.5 \times 10^{-6}$ cm and 2.5×10^{-5} cm depending on the density of the gas. Here it is assumed that such a discontinuous transition exists at

$$a_t = a_{\rm min} \left(\frac{a_{\rm max}}{a_{\rm min}} \right)^{3/4} = 1.78 \times 10^{-5} \text{ cm}, \tag{4.33}$$

where $a_{\rm min}$ and $a_{\rm max}$ are the same distribution limits as used in all previous tests, and that the velocity difference is 15 km s^{-1}. Hence, only the small grains, those with sizes $a < a_t$, will experience non-thermal sputtering due to neutral species, while shattering is due to collisions of small grains with large grains. For simplicity, the same shattering procedure is applied as in §4.3.3, that is both grains completely shatter and the fragments are distributed across the full range of grain radii. Use of Eq. 4.15 allows an estimation of the rate at which the grain radius decreases, i.e.

[2]Note that this transition will always be at a bin edge.

$da/dt \approx -10^{-12}$ cm s^{-1}. The distribution is evolved for a time of 10^6 s.[3] As there is no analytic solution for this problem, the results are assessed using the converged solution for the distribution function as the bin number increases. It is found that both the linear and the power-law methods converge to the same solution.

Fig. 4.7 shows the grain distribution for the piecewise-linear and power-law methods using $N = 8$ bins. Comparing the results to the initial MRN distribution, it is found that sputtering changes the slope of the distribution towards the small grains, while shattering changes it for the large grains, an effect previously noted by Bocchio et al. (e.g. 2014, 2016); Kirchschlager et al. (e.g. 2019). Both the power-law and piecewise-linear methods are close to the converged distribution function, although the linear method is affected by slope-limiting to ensure positivity of the distribution function. Slope limiting conserves mass, but not numbers, which is reflected in the error relative to the converged solution. The linear method has a relative error in the total mass density of only 2%, but has an error of 7% in the total number density. In comparison, both relative errors are below 1%, even for $N = 8$ bins. However, it should be noted that the linear method does converge quickly, and achieves this same accuracy for $N = 32$ bins.

The results of this test depend on the relative strength of the sputtering and shattering. Therefore, as the linear and power-law methods perform differently for number-conserving and mass-conserving processes, a test is also performed for a sputtering rates which are an order of magnitude larger and smaller. Fig. 4.8 shows the grain distributions for these two additional models. For the higher sputtering rate, the evolution of the distribution is dominated by sputtering. The sputtering removes more small grains from the distribution in comparison to the model with the default rate. Hence, less projectiles are available to shatter the larger grains and, consequently, the distribution function at large grain radii does not evolve at the same rate. Both the piecewise-linear and power-law methods with $N = 8$ bins are close to the converged solution, with the relative error in the total mass density about 2% for the linear method and 0.1% for the power-law method. However, the error in the total number density is up to 20% for the linear method, while it is less than 1% for the power-law method. The linear method achieves the same performance as the power-law method for $N = 64$ bins. For the lower sputtering rate, the evolution is mainly due to shattering and the number of large grains in the distribution

[3]This timescale differs from the previous tests due to the more 'realistic' distribution coefficient which is used here in order to better represent the conditions in which C-type shocks occur.

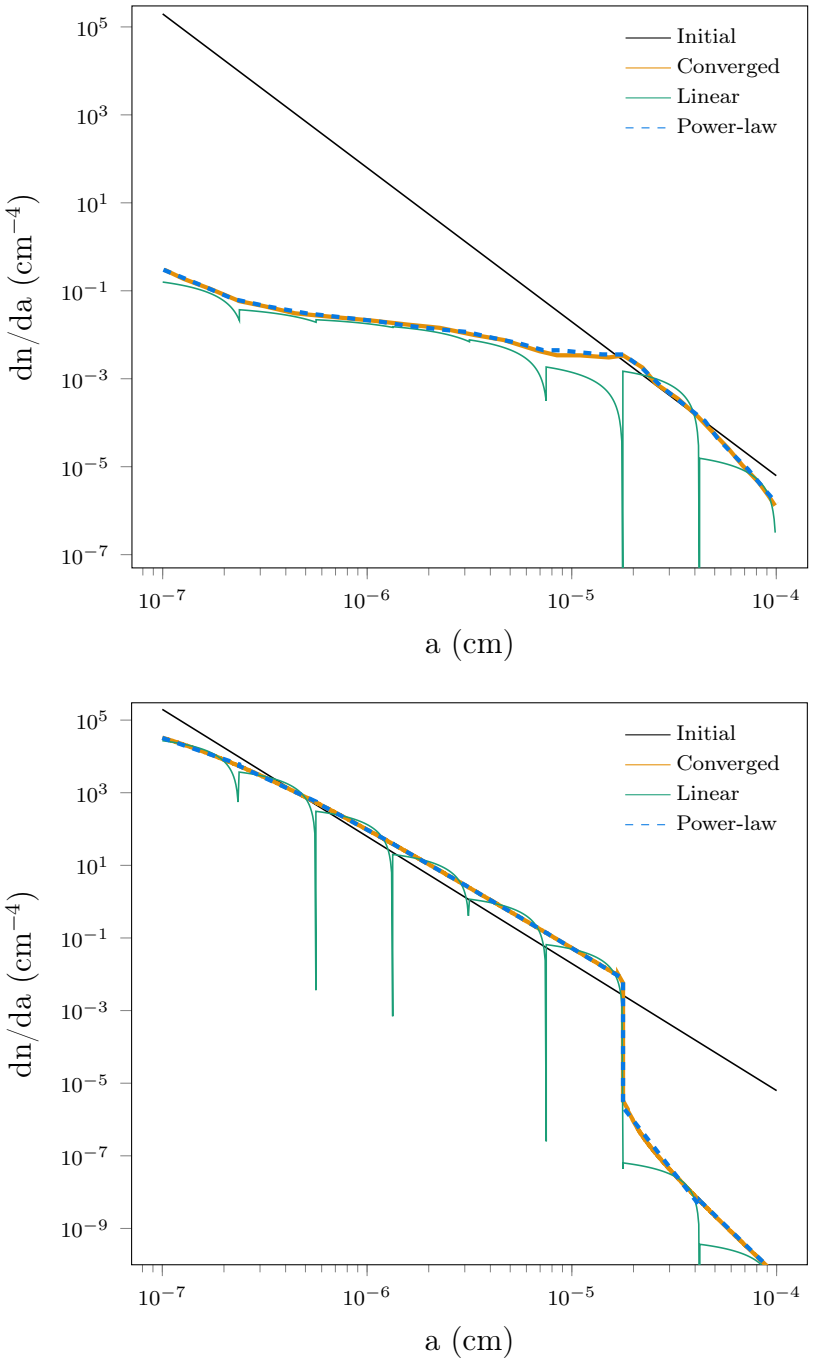

Figure 4.8: Same as Fig. 4.7 but with a sputtering rate of -10^{-11} cm s^{-1} (top) and -10^{-13} cm s^{-1} (bottom).

drops significantly. Sputtering does not remove as many grains at the small radii, so more projectile grains are available to collide with the large grains and shatter them. Again, both methods reproduce the converged solution very well, a fact revealed in the relative errors. The relative error in the total grain number density for the linear method (which is always the largest error) is only 3%.

This test shows that the power-law method maintains its high level of accuracy for

$N = 8$ bins, even when combining number-conserving and mass-conserving processes. To achieve the same level with the piecewise-linear method, one must model the distribution with more bins, i.e. $N > 32$. Additionally, as with the previous tests, the power-law method is also able to produce the correct shape of the final distribution with only $N = 8$ bins, something which the linear method has been unable to achieve across all tests. This further enforces the usefulness of the power-law method for following the evolution of a grain-size distribution when limited computational resources are required or necessary.

4.4 Discussion and conclusions

In this chapter, a numerical method has been presented which follows the evolution of a grain-size distribution undergoing processes which either conserve the total grain mass or total grain numbers. Guided by observations of typical ISM dust distributions, this method uses a power-law prescription to specify the distribution within a bin. Using the number and mass densities of grains within a bin, the coefficient and index of the power law can be uniquely determined. The grain size limits of the distribution are also explicitly tracked. Furthermore, the methods to evolve the discrete power-law distribution due to number- or mass-conserving processes are described, and illustrated with gas-grain sputtering and grain-grain shattering. The power-law method is complementary to the methods employing either a discrete piecewise-constant or piecewise-linear distribution (e.g. Mizuno et al., 1988; Jones et al., 1996; McKinnon et al., 2018).

The tests performed here show that the power-law method significantly outperforms both the piecewise-constant and linear methods for following the evolution of the distribution function, especially when the distribution is covered by a small number of bins. The main reason is, of course, that the discrete power-law method is naturally suited to modelling a continuous power-law distribution of the type which often occurs in the ISM. The linear and constant methods only provide a second and first order approximation, respectively. In part, it is also because in the power-law method the limits of the distribution are followed and taken into account when deriving the distribution properties. This is important when considering number-conserving processes and the full allowed radius range for a bin is not filled. For

these processes, both the piecewise-constant and linear methods then diffuse the distribution limits. Implementation of the same technique as in the power-law method allows the relative errors to be reduced in the other two methods.

The power-law method is more effective for treating mass-conserving processes than the other methods, with the best results occurring when more information of the physical processes (in this case shattering) is included when evaluating the integrals. All methods conserve the mass to machine accuracy, but the number density of the grains is better reproduced with the power-law method. While uncertainties are expected when modelling physical processes, it is best to avoid numerically induced ones. As mass- and number-conserving processes are often modelled together, the combined sputtering and shattering test demonstrated that the power-law method provides the best results, especially for small bin numbers (that is, $N = 8$). For larger bin numbers both the power-law and piecewise-linear methods produce similar results.

The aim of this work is to provide an efficient numerical method that describes the evolution of a dust grain-size distribution due to advection and grain physics accurately in large-scale simulations. To avoid a large demand in numerical resources, it is beneficial to cover the grain distribution with as few bins as possible. As the power-law method produces small errors even for $N = 8$ bins, it is perfect to include this approach in a numerical MHD code. One drawback is that operations such as pow(), log() and sinh() are considerably more CPU expensive than linear operations. This is especially important when finding the root of Eq. 4.10. Using standard algorithms, the power-law method using $N = 8$ is only as fast as the linear method with $N = 128$. However, one can use alternative algorithms and approximations for these operations so that the CPU cost of the power-law method is only 1.5 times that of the piecewise-linear method for the same number of bins. Thus, the power-law method not only provides a more accurate, but also a viable, alternative to the piecewise-linear method. A different approach would be to use a lookup table for values of the power-law index, which has the potential to provide greater efficiency and avoid numerical errors which occur during the iteration.

5

Sputtering of a power-law grain-size distribution in oblique C-type shocks

This chapter presents the method of implementation of the routines detailed in Chapter 4. The implementation of an initial MRN grain-size distribution is tested through simulations which both neglect and include sputtering, with the intention of demonstrating how many size bins are required to accurately evolve the distribution in oblique C-type shocks.

Contents

5.1 Introduction

There have been a number of approaches to modelling the sputtering of dust grains in C-type shocks (see Fig. 1.6 for a diagram of the expected structure of a C-type shock). However, these models often consist of single-sized grains (e.g. Van Loo et al., 2013; Nesterenok, 2018). Studies that choose to incorporate a grain-size distribution tend to follow a piecewise-constant approach (e.g. Guillet et al., 2011), which can cause inaccuracies when modelling a power-law such as the MRN distribution (Chapter 4 and Sumpter and Van Loo (2020)). Furthermore, there have been limited investigations into sputtering in oblique shocks. The work by Van Loo

et al. (2013) showed that the degree of sputtering is enhanced in oblique shocks for a given shock speed, which may be important in explaining the increased elemental abundances observed in shocked regions of molecular clouds.

The model by Van Loo et al. (2013) and Ashmore (2011) was improved upon, as described in Chapter 3, by allowing the mass of individually-sized grains to be updated according to destruction by sputtering. Then, Chapter 4 introduced a method for evolving a grain-size distribution as it changes due to number-conserving and mass-conserving processes. Here, the implementation of this method into the multifluid MHD code is described. The implementation is tested through simulations in which gas-grain sputtering is neglected, so the distribution is evolved due to advection only, and the results are compared to those for multiple single-sized grains. Results are then presented for the effect of sputtering on the grain-size distribution in C-type shocks, with the aim of determining the number of size bins required to accurately model this destructive grain process.

5.2 Implementation

To incorporate the grain-size distribution into the multifluid MHD numerical scheme described in Chapter 2, and which was improved upon in Chapter 3, modifications must be made to the equations for the grain fluids. The dynamical equations for each (pressureless) grain fluid are the continuity equations and the reduced momentum equation,

$$\begin{aligned} &\frac{\partial n}{\partial t} + \nabla \cdot (n\mathbf{v}) = S_{sputt}(a,t), \\ &\frac{\partial \rho}{\partial t} + \nabla \cdot (\rho\mathbf{v}) = S'_{sputt}(a,t), \\ &\alpha\rho\left(\mathbf{E} + \mathbf{v} \times \mathbf{B}\right) + \rho\rho_n K_{gn}(\mathbf{v}_n - \mathbf{v}) = 0, \end{aligned} \tag{5.1}$$

where n and ρ are the number and mass densities of grains, $\mathbf{v}$ is the grain velocity, and α is the grain charge-to-mass ratio. ρ_n and $\mathbf{v}_n$ are the mass density and velocity of the neutral particles, $\mathbf{E}$ and $\mathbf{B}$ are the electric and magnetic fields of the medium, and $S_{sputt}(a,t)$ and $S'_{sputt}(a,t)$ are the source terms due to sputtering, which depend on the grain size a and time t. Lastly, K_{gn} is the collision coefficient between the grains and the neutrals, given by (Draine, 1980)

$$K_{gn} = \frac{8}{3}\frac{\pi a^2}{m_n + m}\left(\frac{2k_B T_n}{\pi m_n}\right)^{1/2}\left(1 + \frac{9\pi(\mathbf{v}_n - \mathbf{v})^2}{128\ k_B T_n}\right)^{1/2} \tag{5.2}$$

with T_n the temperature of the gas, and m_n and m the mass of a neutral particle and mass of a single grain, respectively. In the dense, molecular regions of interest, the medium is modelled as a weakly-ionised plasma, so the collision frequency between grains and charged particles is negligible and only grain-neutral collisions need to be considered. To incorporate the grain-size distribution, n becomes $\partial n/\partial a \times \mathrm{d}a$, and ρ becomes $m(a)\ \partial n/\partial a \times \mathrm{d}a$. The governing equations are found through integration of the above equations over the range of radii for a given bin. For bin i the equations become

$$\begin{aligned} &\frac{\partial n_i}{\partial t} + \nabla \cdot (n_i \mathbf{v}) = S_{i,sputt}, \\ &\frac{\partial \rho_i}{\partial t} + \nabla \cdot (\rho_i \mathbf{v}) = S'_{i,sputt}, \\ &\langle Z \rangle_i e n_i \left(\mathbf{E} + \mathbf{v}_i \times \mathbf{B}\right) + n_i \rho_n K^*_{gn} (\mathbf{v}_n - \mathbf{v}_i) = 0, \end{aligned} \tag{5.3}$$

where $S_{i,sputt}$ and $S'_{i,sputt}$ are the sputtering losses in bin i, and $\langle Z \rangle_i e$ is the average grain charge. K^*_{gn} is the mean specific collision coefficient between neutrals and grains in bin i, given by

$$K^*_{gn} = \frac{8}{3}\pi \langle a^2 \rangle_i \left(\frac{2 k_B T_n}{\pi m_n}\right)^{1/2} \left(1 + \frac{9\pi (\mathbf{v}_n - \mathbf{v}_i)^2}{128\ k_B T_n}.\right)^{1/2} \tag{5.4}$$

In the derivation of these expressions, the only assumption to be made is that all the grains within a bin have the same velocity ($\mathbf{v}_i$). From the reduced momentum equation, it is clear that the grain velocity depends on the grain radius through the Hall parameter, which is the ratio of the gas-grain collision frequency to the gyrofrequency, $\beta = ZeB/(m\rho_n K_{gn}) \propto a^{-1}$. For small Hall parameters, i.e. when $|\beta| < 0.1$, the grains move with the neutrals, while, for $|\beta| > 2$ they move with the electrons and ions. Thus, there is only a small range of β values, or grain radius, for which grains have a velocity in between these limits. Only in the bin where this transition occurs will some error in the dynamics be expected. To incorporate the process of sputtering into the MHD code, the routines described in §4.2 are used, where sputtering is included as a source function during the advection update.

5.2.1 Tests

The implementation of the grain-size distributions method into the MHD code is tested, and the results compared to that of single-sized fluids. A sample shock of speed $v_s = 25$ km s^{-1} and angle between the direction of magnetic field and the direction of propagation of the shock of $\theta = 45^o$. The pre-shock density is $n_H =$

10^4 cm^{-3} or $n_H = 10^6$ cm^{-3}. The tests were carried out for C-type shocks without dust grain processing, so the grain-size distribution is only affected by advection.

5.2.1.1 Single-sized grains

Here the initialisation of multiple single-sized grain fluids is described. For N single-sized fluids, it is assumed that the mass density of grains represented by each fluid is equivalent to what it would be for N size bins used to model an MRN distribution, i.e. for fluid i

$$\rho_i = \frac{4}{3}\pi\rho_0 \; A_0 \frac{\left(a_{i+1}^{4-\alpha_0} - a_i^{4-\alpha_0}\right)}{4-\alpha_0} \tag{5.5}$$

where $\alpha_0 = 3.5$, and $\sum_i \rho_i = 0.01\rho_n$. The grains in fluid i take an initial representative size,

$$\langle a \rangle_i = \frac{\int_{a_i}^{a_{i+1}} \; a \; A_0 \; a^{-\alpha_0} \; \mathrm{d}a}{\int_{a_i}^{a_{i+1}} \; A_0 \; a^{-\alpha_0} \; \mathrm{d}a}. \tag{5.6}$$

The mass of a grain in fluid i is calculated from

$$m_i = \frac{4}{3}\pi\rho_0\langle a \rangle_i^3 \tag{5.7}$$

and the number density is determined according to $\rho_i = m_i n_i$. This means that, relative to an equivalent number of bins covering the distribution, the number density of grains in the single-sized fluids contains some error. For example, for 8 single-sized fluids, the error in the total number of grains compared with 8 size bins is approximately 7%.

In a sense, the single-sized grains method can be thought of as a Langrangian approach since the size of individual grains is tracked, whereas the distributions method is an Eulerian approach where the grains are shifted between bins according to their new size at each time step.

5.2.1.2 Results and discussion

The number of grain bins (for the power-law approach) or grain fluids (for the single-sized grain approach) was varied from 1 to 16 to determine the effect that this has on the shock dynamics, and to see how well the grain-size distribution is modelled. From here on, 'fluids' refers to the models where grains are described by single-sized fluids, and 'bins' refers to the models where an initial MRN grain-size distribution is discretised into a number of size bins.

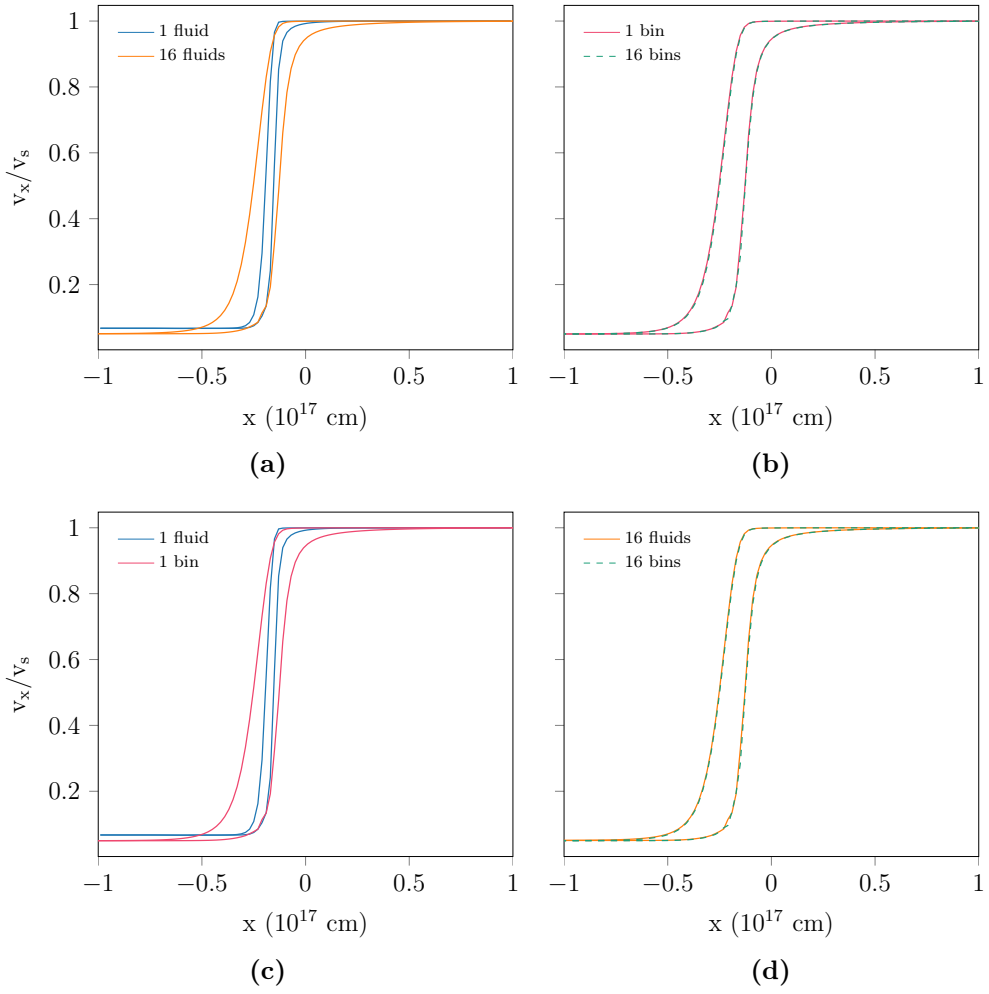

Figure 5.1: Shock profiles for a pre-shock density of 10^4 cm^{-3}. The profile is made up of the normalised x-velocities of the neutral fluid and the ion fluid. (a) compares the profile obtained using 1 single-sized fluid (blue) with that for 16 single-sized fluids (orange). (b) compares the profile obtained using 1 bin (red) with 16 bins (green dashed) for a power-law discretisation. (c) compares the profile for 1 single-sized fluid with the profile for 1 bin. Finally, (d) compares with profile for 16 single-sized fluids with 16 bins.

Fig. 5.1 shows the shock profiles for 1 grain bin or fluid vs 16 grain bins or fluids. The shock profile can be characterised by its width, which is calculated from the points at which the neutral temperature is 100 K as per Anderl et al. (2013). It can be seen from (a) that the shock profile is much narrower for 1 fluid than for 16 fluids, whereas there is little discernible difference at all between the profiles for 1 bin compared with 16 bins (plot (b)). This is demonstrated more clearly in Fig. 5.2, where plot (a) shows that the width is almost constant for all numbers of bins. In contrast, the width is much narrower for 1 fluid than for 1 bin, with a fractional error of about 0.89. There is convergence towards the result of 16 bins as more single-sized fluids are used, with a fractional error of about 0.1 for 4 fluids, 0.05 for 8 fluids and of less than 0.02 for 16 fluids. Plot (b) shows the dependence of the maximum neutral

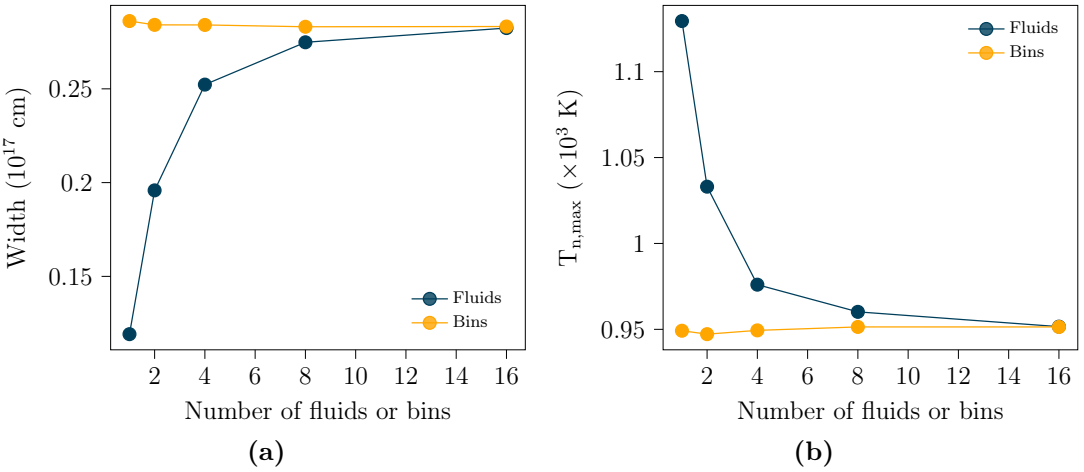

Figure 5.2: (a) shows the shock width as measured at a neutral temperature of T_n = 100 K for a pre-shock density of $n_H = 10^4$ cm^{-3} vs the number of bins (orange) or fluids (blue) used. (b) shows the maximum neutral temperature as a function of the number of bins or fluids.

temperature on the number of fluids or bins, with hotter temperatures corresponding to thinner shocks because there is a narrower radiating layer. Since the power-law discretisation describes the distribution in each bin as itself a power law, the initial MRN size distribution can be just as accurately represented with 1 bin as with 16 bins. On the other hand, using just one fluid of single-sized grains does a poor job of modelling the MRN distribution. The representative average radius of a grain is heavily skewed towards the small end of the distribution as there are many more small grains than large grains. This results in the grains being modelled by 1 grain fluid having a size of 8.32×10^{-7} cm and mass of 7.95×10^{-22} g. The small size and mass of the grains in the fluid result in the grains having a large Hall parameter, and therefore being well-coupled to the magnetic field. The number density of grains in the one grain fluid is 2.1×10^{-3} cm^{-3}, more than seven times that for 1 bin. The large number of small grains, all having a large Hall parameter, increases the cross-section for collisions between the grains and the neutral particles; neutrals are better coupled to the field and the shock structure becomes thinner than if the full range of grain sizes was being adequately represented.

Fig. 5.3 compares the shock profiles for bins and single-sized fluids for a higher pre-shock gas density of $n_H = 10^6$ cm^{-3}. Fig. 5.4 (a) shows the dependence of the shock width on the number of bins or fluids, and 5.4 (b) shows how the maximum neutral temperature changes with the number of bins or fluids. A similar trend is shown for the widths to that of the $n_H = 10^4$ cm^{-3} model, although there is some change in the width from 1 bin to 2 or more bins. The width of the shock when 1

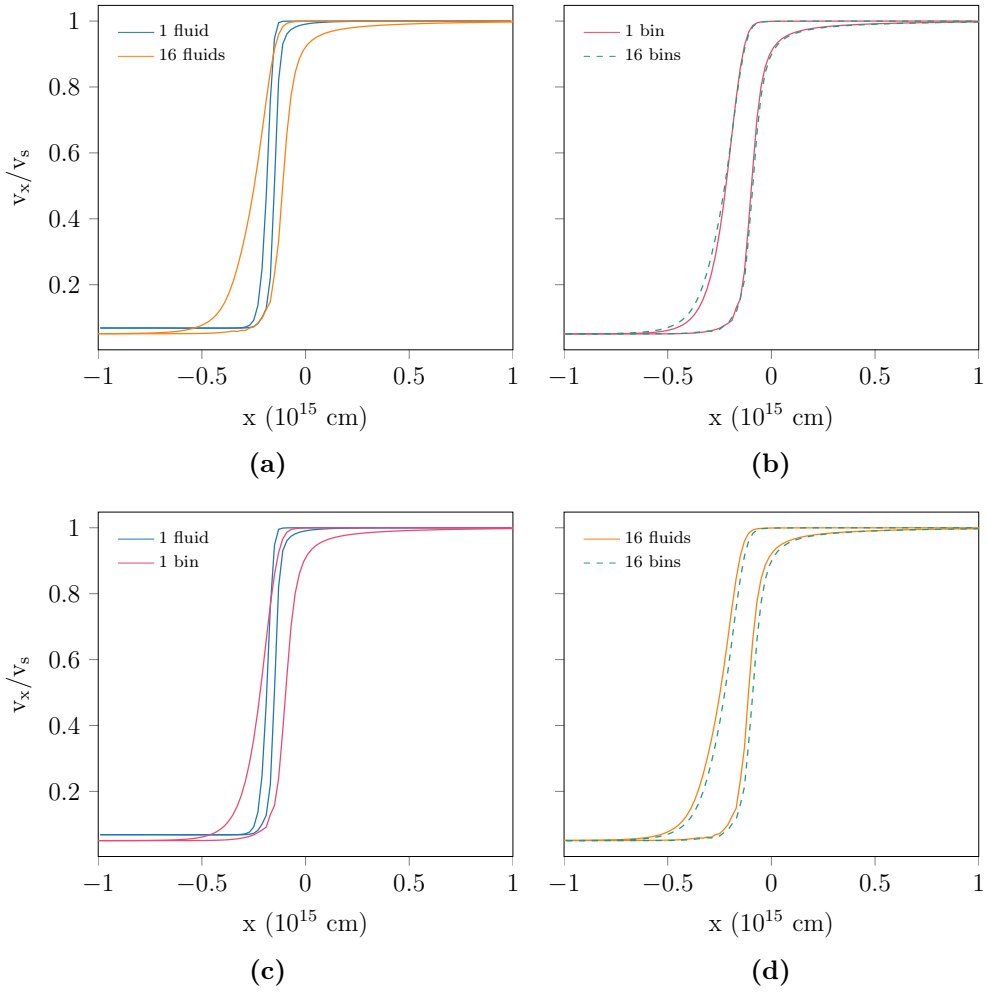

Figure 5.3: Shock profiles for a pre-shock density of 10^6 cm^{-3}. (a) compares the profile obtained using 1 single-sized fluid (blue) with that for 16 single-sized fluids (orange). (b) compares the profile obtained using 1 bin (red) with 16 bins (green dashed) for a power-law discretisation. (c) compares the profile for 1 single-sized fluid with the profile for 1 bin. Finally, (d) compares with profile for 16 single-sized fluids with 16 bins.

single-sized fluid is used is much narrower than that of 1 bin, with a fractional error in the width for 1 fluid as compared to 1 bin of approximately 0.95.[1] However, as for the 10^4 cm^{-3} model, convergence in the widths occurs as the number of fluids is increased and for 16 fluids the fractional error is just 0.015.

There is an overall difference in the shock width of approximately 2 orders of magnitude between the 10^4 cm^{-3} models and the 10^6 cm^{-3} models, an effect explained by Ashmore (2011) and Van Loo et al. (2009). For the lower density models most of the charge is carried by the electrons. In this case it is the ion-neutral collision frequency which determines the shock width; the grains do not carry significant enough charge

[1]Note that in the calculation of the fractional error, the result for the bins is taken to be the 'correct' value.

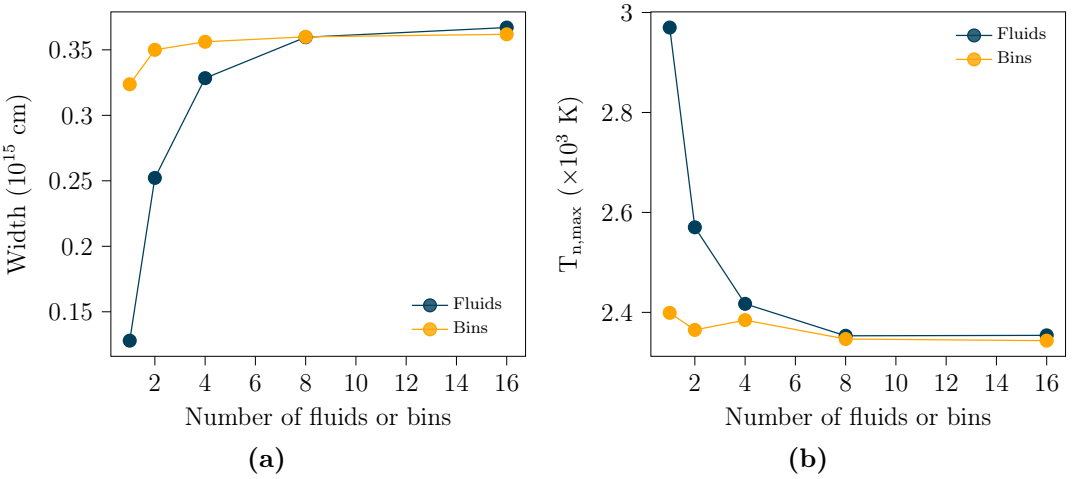

Figure 5.4: (a) shows the shock width as measured at a neutral temperature of T_n = 100 K for a pre-shock density of $n_H = 10^6$ cm^{-3} vs the number of bins (orange) or fluids (blue) used. (b) shows the maximum neutral temperature as a function of the number of bins or fluids.

to affect the shock width. In the higher density models, the grains carry a greater proportion of the overall charge density. The shock width is then determined by grain-neutral collisions. Therefore, for the 10^6 cm^{-3} models, the shock width depends on the number of grains which are well-coupled to the magnetic field. Smaller grains are better coupled to the magnetic field, hence have a larger Hall parameter due to their smaller collision frequency with the neutrals. When 2 grain bins are used to model the distribution, the grains in the larger size bin are skewed towards the lower size limit of the bin. The effect of large grains moving with the neutrals is not properly captured and the abundance of small grains results in a thinner shock than when more bins are used. This is seen in 5.4 (a), where we see a smaller width for 1 bin than for greater numbers of bins.

The difference between the higher and lower density models is further seen in Fig 5.5, which shows the normal velocities of the neutrals, ions, and grains in the largest and smallest size bins or fluids normalised to the shock velocity. The larger grains show a peak in the profile just into the downstream region of the shock. This corresponds to where the grains shift from moving with the charged particles to moving with the neutrals. It can also be seen that the peaks for 2 fluids and 2 bins are of different height, varying by almost a factor of 2. In contrast, the peaks are of equal height for 16 fluids and 16 bins, consistent with the convergence of the shock widths seen in Fig. 5.4.

The reason for the peaks in the normal velocity of the large grains is seen in Fig. 5.6,

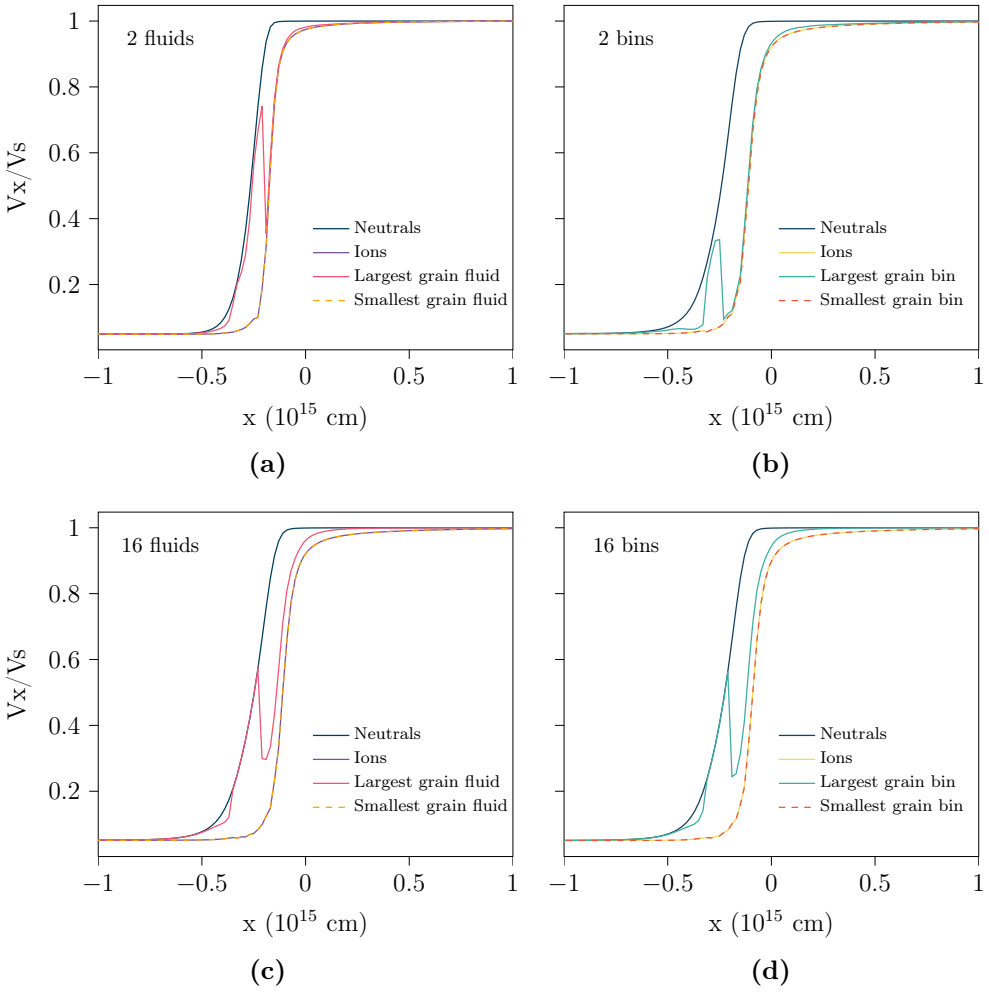

Figure 5.5: Normal velocities normalised to the shock speed for the neutrals, ions, and largest and smallest grain bins or fluids for (a) 2 fluids, (b) 2 bins, (c) 16 fluids, and (d) 16 bins. The pre-shock density is 10^6 cm^{-3}.

which shows the absolute value of the Hall parameter of the largest and smallest grains through the shock, and Fig. 5.7 which shows the grain charge. At the point in the shock corresponding to the normal velocity peak, there is a significant decrease in the magnitude of the grain charge; it becomes very close to zero and the grains become neutral. The Hall parameter sees a corresponding drop in magnitude, falling to values close to 1, consistent with the grains no longer being well coupled to the magnetic field and instead travelling with the neutrals. The impact of this is seen in the grain-neutral relative velocity, shown in Fig. 5.8. There is a dip in the profiles where the drift velocity falls close to zero. The profiles converge for single-sized fluids and bins as more fluids are used. The sputtering rate is dependent on the grain-neutral relative velocity, so this effect could have consequences for the amount of sputtering which is seen at higher densities. Furthermore, since this effect only

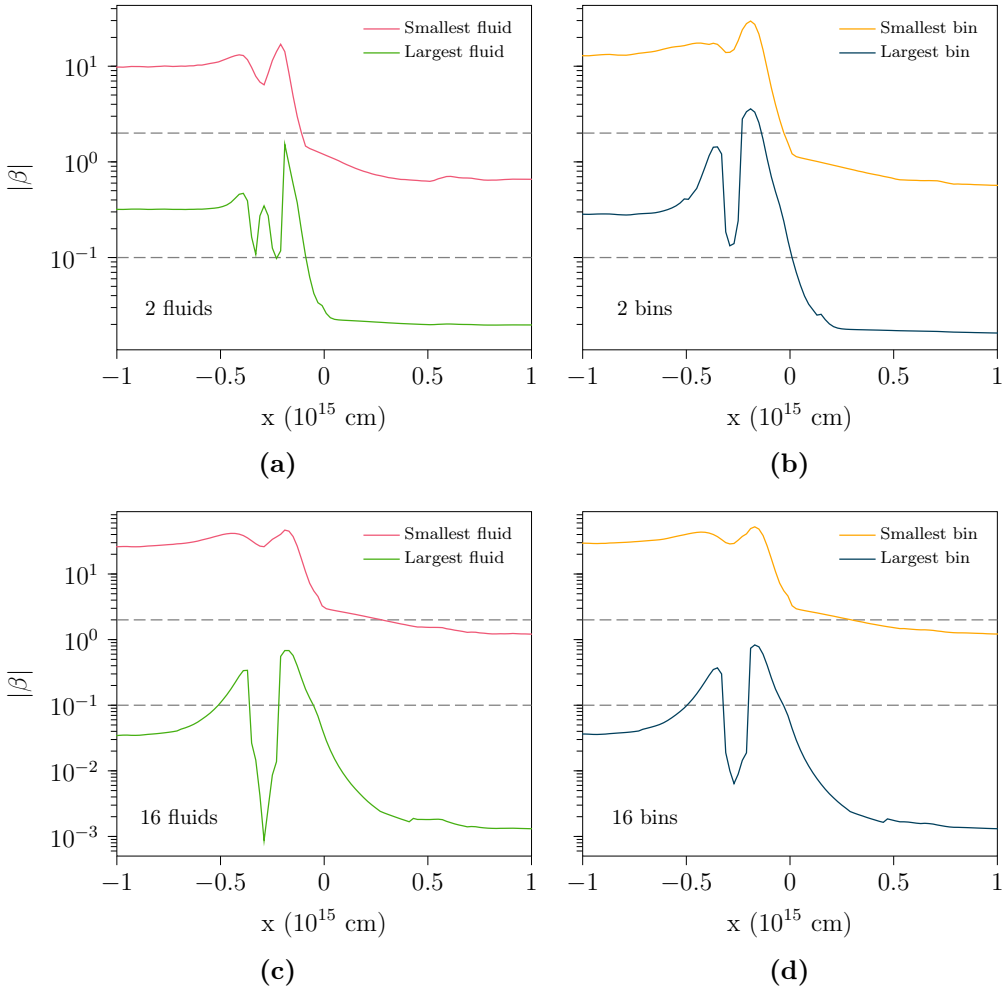

Figure 5.6: The absolute value of the Hall parameter β of the smallest and largest grain size fluids or bins for (a) 2 fluids, (b) 2 bins, (c) 16 fluids and (d) 16 bins. All are for a pre-shock density of 10^6 cm^{-3}.The grey dashed lines on each plot mark $|\beta| = 2$, where values of $|\beta|$ larger than this indicate that the grains are moving with the charged particles, and $|\beta| = 0.1$, where values of $|\beta|$ smaller than this indicate that the grains are moving with the neutrals.

occurs for grains at the larger end of the size distribution, it cannot be captured when only one grain fluid or bin is used.

The results shown here demonstrate that the grain-size distribution method has been implemented correctly, since the single-sized fluids results converge to the results for the size bins. The importance of using a distribution of grain sizes is demonstrated, with single-sized fluids only accurately achieving the same shock profile as the distribution for upwards of about 8 fluids. In contrast, for the 10^4 cm^{-3} model, only 1 size bin is required to accurately model the size distribution and model the shock dynamics. However, for the 10^6 cm^{-3} model an additional effect comes into play.

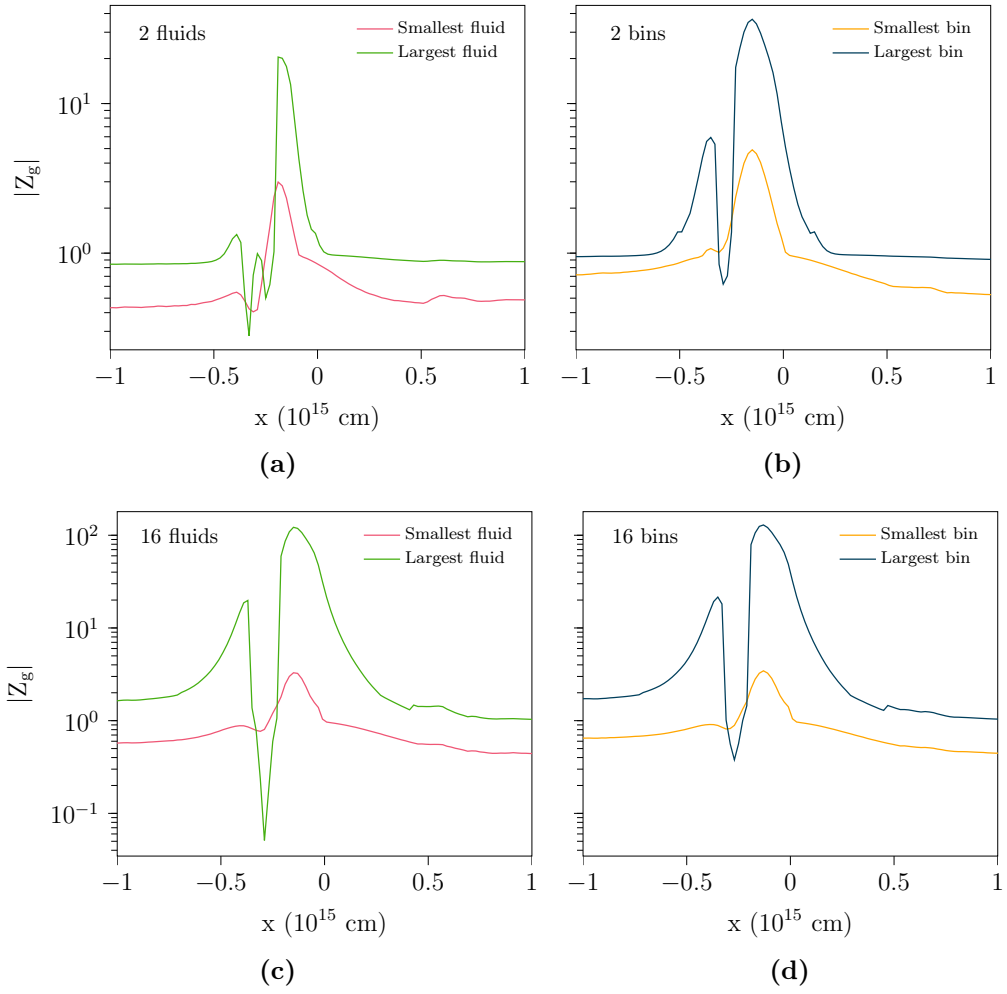

Figure 5.7: The absolute value of the number of charges per grain Z_g for the smallest and largest grain size fluids or bins for (a) 2 fluids, (b) 2 bins, (c) 16 fluids and (d) 16 bins. All are for a pre-shock density of 10^6 cm^{-3}.

The larger grains in the distribution become neutral in the shock, causing a reduction in the Hall parameter due to the increased grain-neutral collision frequency, and a drop in the grain-neutral relative velocity. This then requires at least 2 size bins to model the distribution.

5.3 Sputtering

In this section the effect of sputtering on an initial MRN distribution is explored. In §5.2.1 it was demonstrated that for advection-only models, only 2 size bins are necessary to correctly simulate the shock dynamics. However, this is unlikely to be the case when the size of the grains is altered by sputtering. The only assumption made

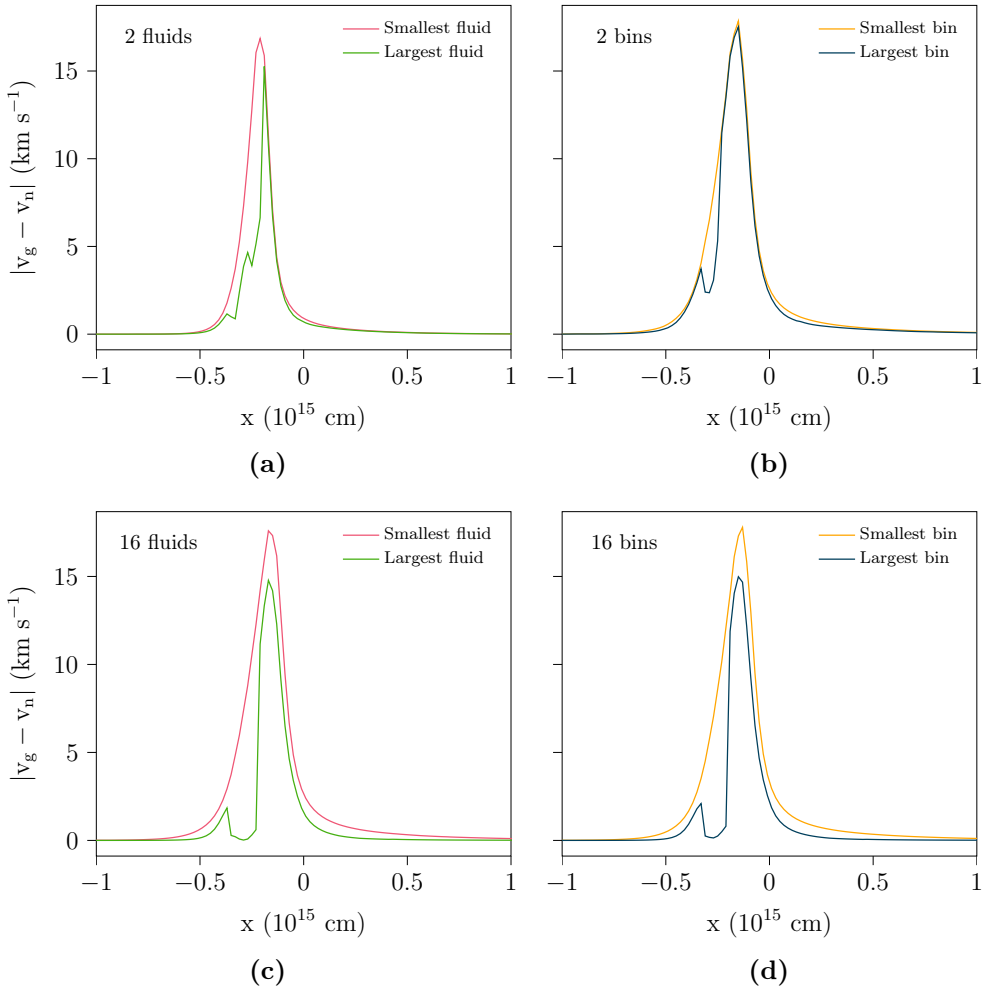

Figure 5.8: The grain-neutral relative velocity for the smallest and largest grain size fluids or bins for (a) 2 fluids, (b) 2 bins, (c) 16 fluids and (d) 16 bins. All are for a pre-shock density of 10^6 cm^{-3}.

in the implementation of the distributions method was that all the grains within a bin travel with the same velocity. Given that the sputtering rate is dependent on the grain-neutral relative velocity, there will be some error incurred due to the fact the constant velocity assumption necessitates that the sputtering rate within a bin is also constant.

To calculate the sputtering rate in each bin, some modifications must be made to the method described in §2.5.2. For the redistribution method presented in §4.2.2, the rate of change of radius of grains in bin i due to sputtering needs to be calculated. For the single-sized grain fluid models, the sputtering rate is calculated as a change in mass density per time (Eq. 2.52 multiplied by the corresponding neutral masses, m_b and summed over all species b), which must now become a change in radius per time. Given that sputtering is a number-conserving process, the rate of change of

grain mass density can be written

$$\frac{d\rho}{dt} = n\frac{dm}{dt} \tag{5.8}$$

where m is the mass of a spherical grain such that

$$\frac{dm}{dt} = 4\pi\rho_0 a^2 \frac{da}{dt} \tag{5.9}$$

hence the rate of change of radius in bin i is

$$\left.\frac{da}{dt}\right|_i = -\sum_{p,b} \frac{m_b}{4\rho_0} n_p \left(\frac{8k_B T_n}{\pi m_n}\right)^{1/2} \frac{1}{s} \int_{x_{th}}^{\infty} \mathrm{d}x\ x^2 \frac{1}{2} e^{-(x-s)^2} \langle Y(E_p)\rangle_\theta \tag{5.10}$$

where the summation is over all the combinations of projectile species p and sputtered species b, and $x^2 = E_p/(k_B T_n)$ where E_p is the impact energy (see §2.5.2 Eq. 2.52 for a full description of the terms present in Eq. 5.10). Note that this is not dependent explicitly on the grain size, only implicitly via the grain-neutral velocity, since the parameter s is given by $s^2 = m_p u_{in}^2/(2k_B T_n)$ where u_{in} is the relative velocity between the neutrals and the grains in bin i. Given that the velocity is assumed to be the same for all grains in a bin, this relative velocity is also constant in each bin.

Once the rate of change of radius has been determined for each bin, the grains are redistributed according to the routine described in §4.2.2. The source terms for sputtering are calculated from the number and mass densities before the update, at time t, and the values after redistribution, at time $t + \Delta t$.

In the results that follow, a representative 'standard' shock model is adopted. This is a shock with speed 40 km s^{-1} through a medium of density $n_H = 10^6$ cm^{-3}. The shock propagates in the x-direction, and the magnetic field initially lies in the x-y plane and makes an angle of $\theta = 45^o$ with the shock propagation direction. The grains are modelled by an initial MRN distribution of grain cores (without ice mantles) from $a_{\min} = 5 \times 10^{-7}$ cm to $a_{\max} = 3 \times 10^{-5}$ cm. The lack of ice mantle is justified by the fact that shock speeds above about 30 km s^{-1} are required for core sputtering to commence, and the ice mantle is likely to be fully eroded for shock speeds of 20 km s^{-1} (Van Loo et al., 2013). Discussion of the inclusion of ice mantles in a grain-size distribution undergoing physical processes is provided in Chapter 7.

The results by Van Loo et al. (2013) (fig. 3 and table 3) show that the amount of Si removed from grain cores by sputtering is small for shock speeds within the critical velocity for C-type shocks. The aim here is to demonstrate the effectiveness of the method of including sputtering of a grain-size distribution into a self-consistent multifluid MHD code and, since no mechanisms of C-type shock break-down are present, it is possible to take shock speeds above the critical speed in order to obtain larger degrees of sputtering. From Van Loo et al. (2013) it would be expected that the fraction of Si removed from grains in this shock be $\sim 10^{-2}$. However, this is for two single-sized grain fluids, so in the following section the effect of using increasing numbers of single-sized fluids is examined and compared to the results for increasing numbers of size bins used in the discretisation of an initial MRN grain-size distribution.

5.3.1 Results and discussion

Results were obtained for the standard shock model, with the inclusion of dust grain sputtering, for 2, 4, 8, 16 and 32 single-sized fluids and distribution size bins. Fig. 5.9 shows the shock profiles for different numbers of bins and fluids, and Fig. 5.10 shows the shock width as a function of the number of single-sized fluids and the number of size bins. Note that there are some wiggles in the velocity profiles in the region where the ion fluid reaches its downstream velocity, which is due to numerical fluctuations in the iteration which determines the charged fluid velocities. As for the advection-only models, there is little variation in the width when modelling a size distribution for different numbers of bins. The shock is slightly narrower for 2 and 4 bins, with the width converging for 8 bins or more. The difference between the width for 2 bins and 32 bins is approximately 9%, 4 bins is 5% and for 8 bins is 1.5%. There is a much stronger dependence of shock width on the number of single-sized fluids, and more fluids are required to achieve a converged result. The fractional difference between 2 fluids and 32 fluids is 44%, for 4 fluids is 18%, for 8 bins is 5% and for 16 bins is less than 1%. Additionally, the widths for the distributions model converge to a different value than that of the single-sized fluids model. The shock width is determined by the grain-neutral drag (Van Loo et al., 2009), and therefore the grains' Hall parameter. Fig. 5.11 shows the maximum magnitude of the Hall parameter β as a function of grain size when 32 fluids or bins are used. Particularly for smaller grains, the Hall parameter is larger for the distribution than for the

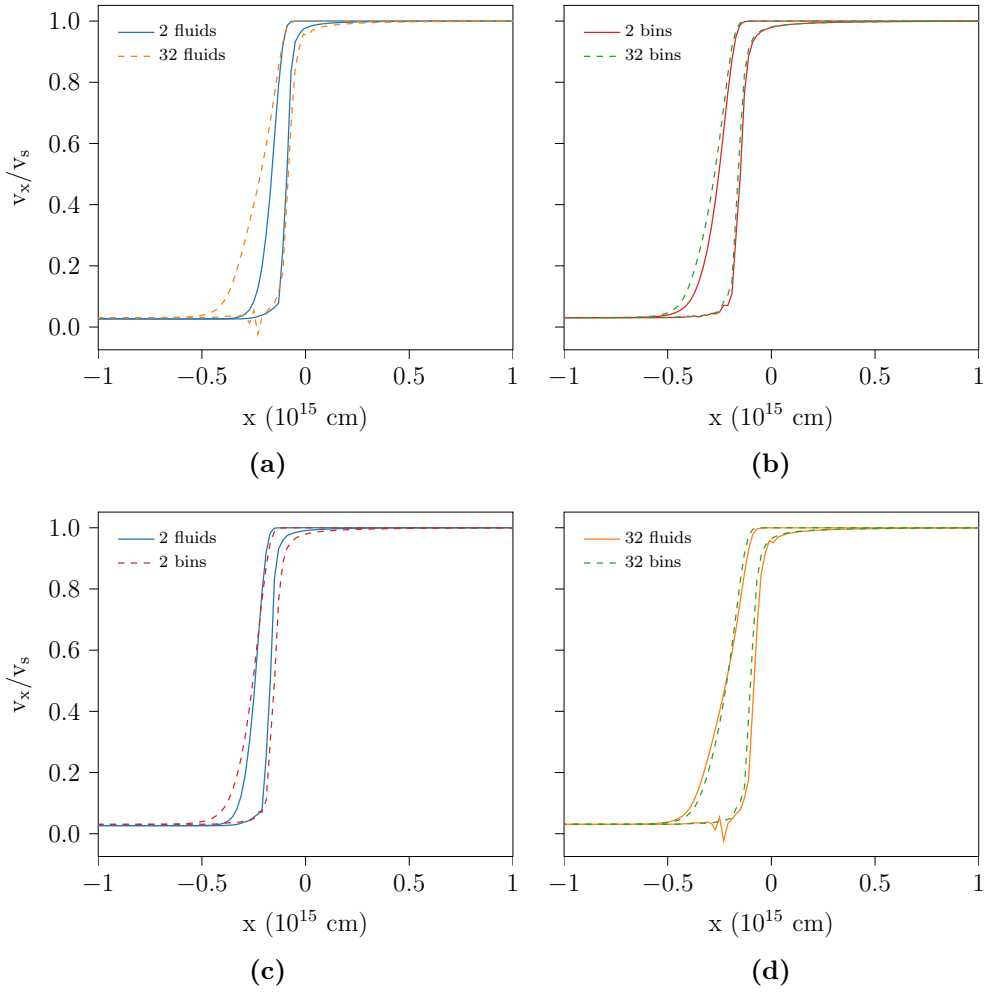

Figure 5.9: Profiles for a 40 km s^{-1} shock through a medium of density 10^6 cm^{-3} where the magnetic field makes an angle of 45^o with the direction of propagation of the shock. Profiles are compared for 2 fluids (blue), 32 fluids (orange), 2 bins (red) and 32 bins (green).

single-sized fluids. This difference in the Hall parameters indicates a difference in the grain-neutral collision frequencies and therefore the shock widths.

Fig. 5.12 shows the fraction of Si removed from the grain cores by sputtering. The study by Van Loo et al. (2013) finds that the total fraction of Si removed from grains for a 40 km s^{-1} shock is 3.78×10^{-2} when 2 single-sized grain fluids are used. There is agreement in the results presented here, as the fraction of Si removed for 2 single-sized fluids is 3.98×10^{-2}. However, Fig. 5.12 shows that the degree of sputtering decreases as more fluids or bins are used. The fraction of Si lost appears to converge to a value of approximately 2.5×10^{-2}. The value when 2 size bins are used is over double this value, at 5.3×10^{-2}. This can be understood by analysing the sputter rate as a function of the grain size. Figure 5.13 compares the sputter

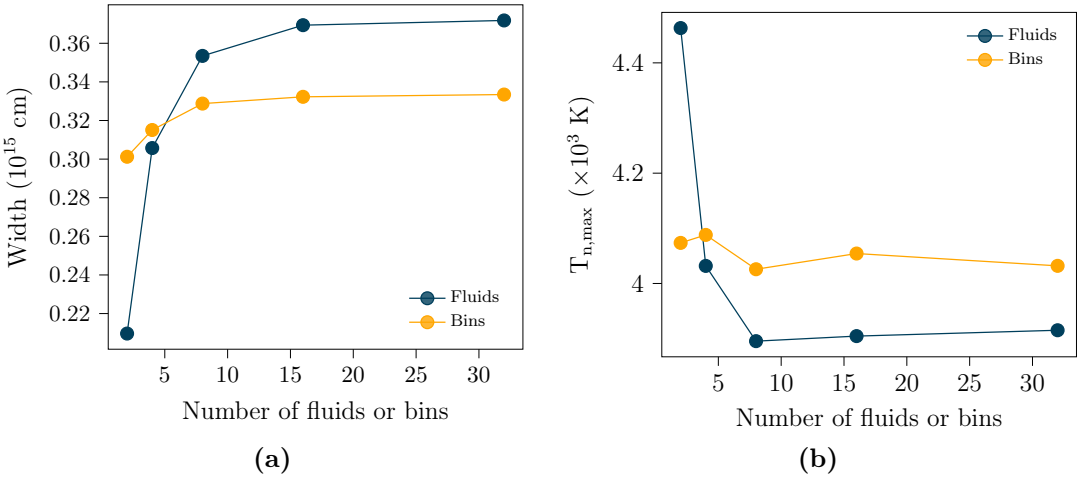

Figure 5.10: (a) shows the shock width as measured at a neutral temperature of T_n = 100 K vs the number of bins (orange) or fluids (blue) used. (b) shows the maximum neutral temperature as a function of the number of bins or fluids.

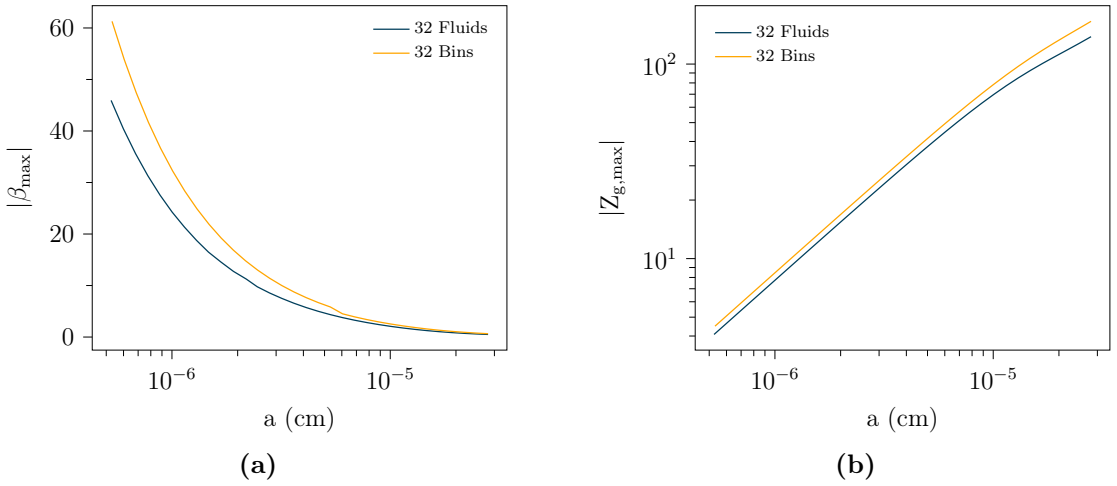

Figure 5.11: (a) is the magnitude of the maximum Hall parameter vs the size of grains for 32 single-sized fluids (blue) and 32 size bins (orange). (b) is the magnitude of the maximum number of charges on the grain surfaces as a function of grain size for 32 single-sized fluids or size bins.

rate da/dt as a function of grain size for 2, 8 and 32 bins and fluids. When only a small number of size bins are used, the constant sputter rate across each bin leads to an overestimation of the overall removal of Si, since there is a broad range of sizes being described by each bin. The constant grain-neutral relative speed in the bin becomes skewed towards that of the smaller grains (since there are many more of them), and is therefore larger than what it would be for larger grains if more bins are used.

There is not such an obvious convergence for the single-sized fluids, although for more than 4 fluids, the result is approximately 2.0×10^{-2}. When 2 bins or fluids

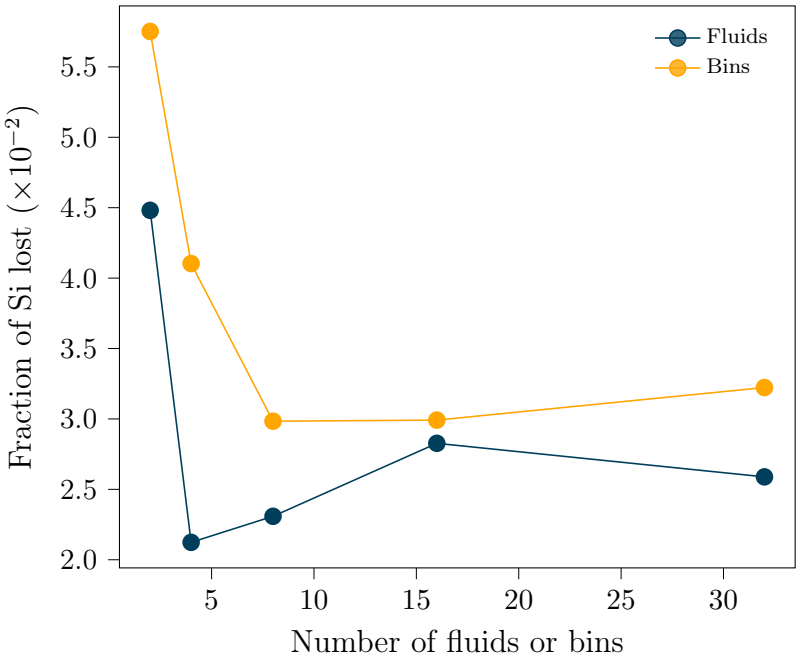

Figure 5.12: Fraction of Si released from grain cores as a function of the number of size bins (orange) or single-sized fluids (blue).

are used (top plot in Fig. 5.13), while the rate is similar for the smaller size fluid or bins, the rates differ by more than 5 orders of magnitude for the larger size fluid and bin. For the distribution, the sputter rates are comparable for each bin, which is not the case for the single-sized fluids and demonstrates that the fact that the large grains move with the neutrals is not captured when 2 bins are used. This explains why the fraction of Si sputtered from grains for 2 bins is larger than that for 2 fluids. The results converge as more bins and fluids are used, with the sputter rate for the largest grains being considerably less than for the rest of the grains in the distribution due to the smaller Hall parameter of the large grains. The results for 8 bins are comparable to those for 32 bins, in keeping with the similar fractions of Si released from grains seen for these models. The sputter rates converge to slightly different values for bins and fluids, with the rate being larger for bins than for fluids at all grain sizes, demonstrating the impact that using a size distribution instead of single-sized fluids has on the sputtering of the grains. It can be concluded that for accurate results, in terms of the shock width and the degree of sputtering, at least 8 size bins are required to model number-conserving changes to the distribution.

Figure 5.14 shows the downstream size distributions of the grains when different numbers of bins are used. The distributions are compared for those with and without sputtering applied. As expected, all numbers of bins show a deviation from the initial distributions, particularly for smaller grains. This is because as the smaller grains

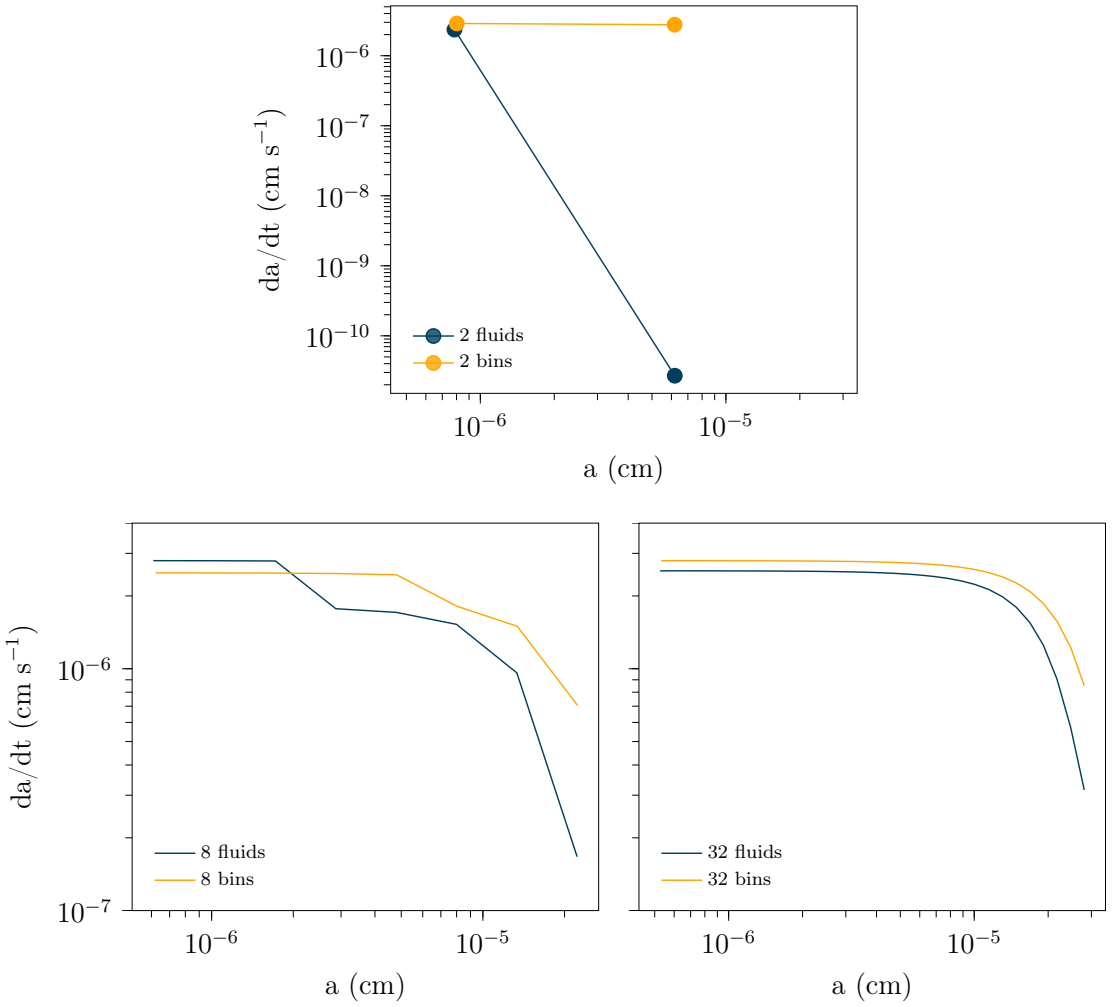

Figure 5.13: Comparison of sputter rate vs grain size for 2, 8 and 32 bins (orange) and fluids (blue).

are sputtered to sizes below $a_{\min}$, they are removed from the distribution, resulting in a reduction in the number of grains at these sizes. For all numbers of bins the total number density of grains is reduced by approximately 14%. The result for 2 bins (top left of Fig 5.14) confirms the overestimation of the amount of Si released from grains due to sputtering, since each bin covers a broad range of sizes. Therefore, there is a relatively significant reduction in the number of grains for sizes from 5×10^{-7} cm to 3.9×10^{-6} cm, confirming that, when destructive processes are included in the model, 2 bins are not sufficient to accurately model the evolution of the distribution. The result for 4 bins (top right) also shows inaccuracies, particularly in the calculations of the power-law indices. This is likely due to an accumulation of small errors when shifting the grains between bins. For 8, 16 and 32 bins, the distributions appear to be similar, in agreement with the convergence of the fraction of Si released from grains.

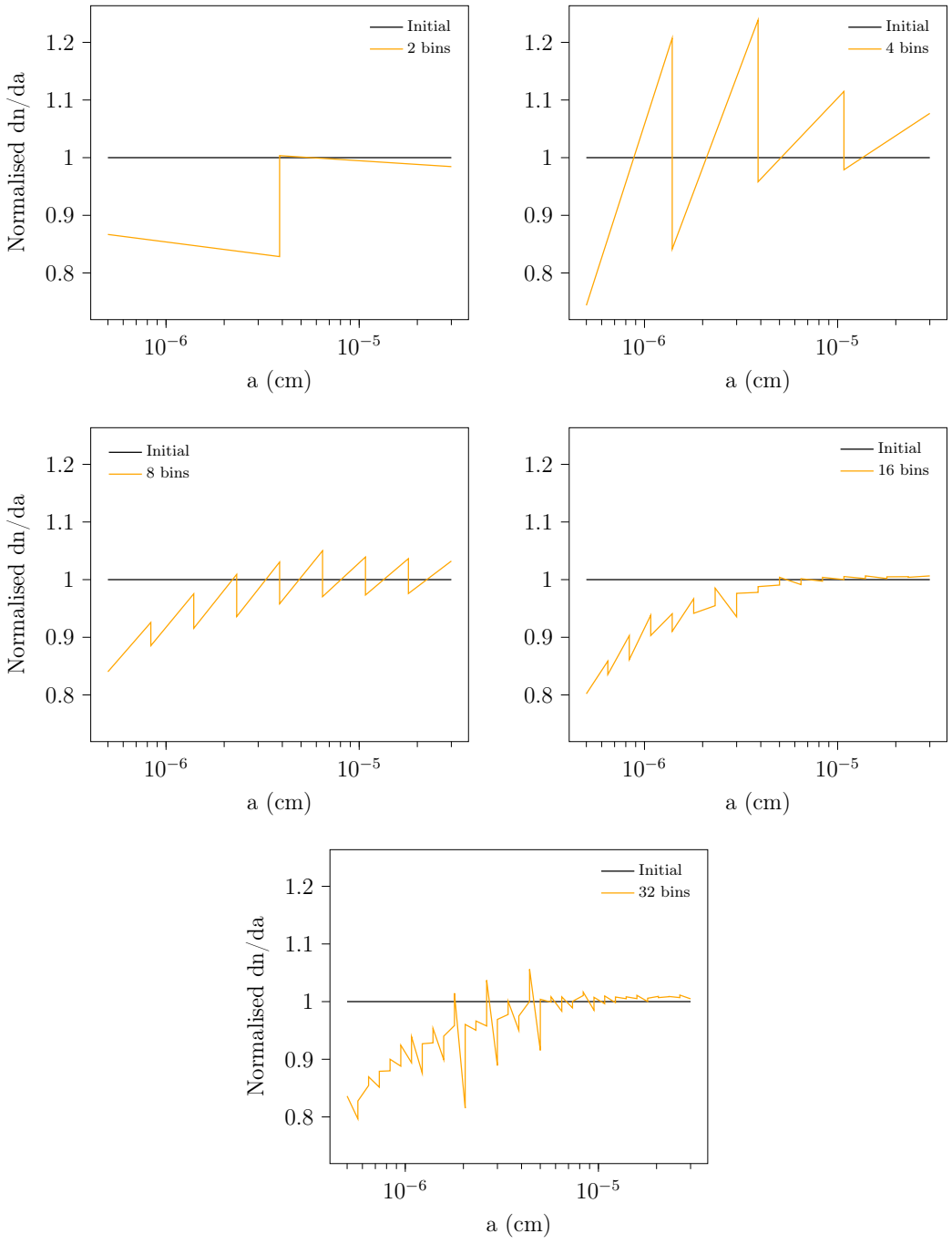

Figure 5.14: Downstream distribution function normalised to the initial distribution for different numbers of bins for a shock speed of 40 km s^{-1}, pre-shock density of 10^6 cm^{-3} and magnetic field angle of 45^o. The black line for each plot shows the result without sputtering, and the orange line shows the distribution after sputtering.

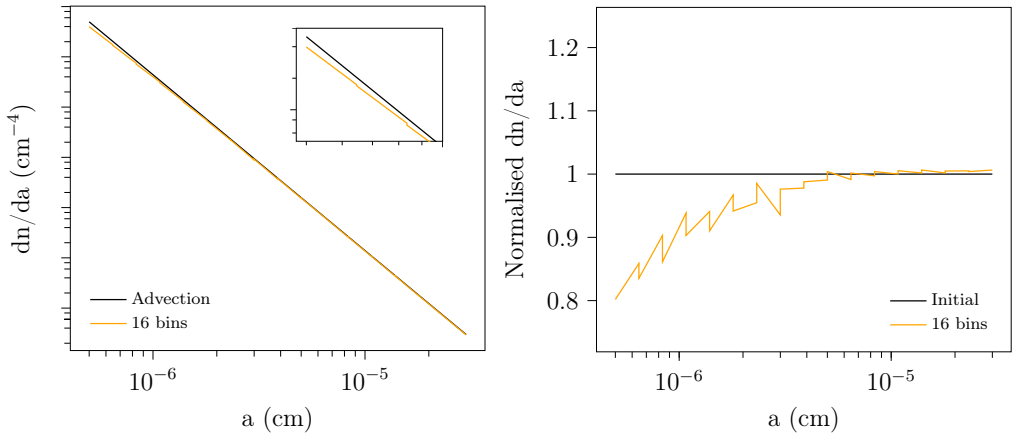

Figure 5.15: Downstream distribution function with sputtering (orange) compared to without (black) for 16 bins. (a) shows the result when the actual distribution values are plotted. The inset plot is provided to show more clearly the deviation occurring in the distribution at small grain sizes. This covers the size range $5 \times 10^{-7} - 1 \times 10^{-6}$ cm and dn/da values from $5 \times 10^{3} - 6 \times 10^{4}$ cm^{-4}. (b) shows the result when the distribution is normalised to the initial distribution. Results are for a shock speed of 40 km s^{-1}, pre-shock density of 10^{6} cm^{-3} and magnetic field angle of 45^{o}.

Figure 5.15 compares the downstream grain-size distribution for 16 bins when (a) the actual distribution values are used and (b) the distribution is normalised to the initial distribution. This highlights that the change to the power-law distribution shape by sputtering is quite small, and mainly deviates from the initial distribution at the small sizes. When the distribution is normalised, small errors in the power-law index seem large but, as the convergences of both the shock widths and the fraction of Si removed from the grains show, these errors are not large enough to be detrimental to the shock calculations for ≥ 8 bins.

5.4 Conclusions

The implementation of grain-size distributions has been investigated. The shock widths as a function of number of bins or single-sized fluids are presented in §5.2 and show that an MRN distribution can be accurately modelled using two size bins, when physical grain processes are neglected and the size distribution evolves due to advection only. The shock width for single-sized fluids converges to that of the bins as the number of fluids is increased, with an error between the shock widths for bins and fluids of under 2% when 16 fluids are used. This is further seen in the shock profiles, where the shape of the shock profile for the single-sized fluids converges to that of the size bins as more fluids are used. The Hall parameters of the grains

offers an explanation as to why there is a discrepancy in the shock widths for small numbers of single-sized fluids. A large Hall parameter indicates that the grains are less well-coupled to the neutrals than a Hall parameter that is close to 1. When 2 fluids are used, both fluids have relatively small maximum Hall parameters, which points to the fact that the grains have a larger collision frequency with the neutrals and results in a thinner shock. As more fluids are used, there is a wider spread in collision frequencies and the larger grains don't have such an influential effect in decreasing the thickness of the shock; the thickness converges to that which results from using size bins.

Following the results showing correct implementation of the grain-size distribution, the sputtering method described in §2.5.2 was modified and used to obtain results for a 40 km s^{-1} shock propagating through a medium of density 10^6 cm^{-3} where the magnetic field is at an angle of 45^o to the direction of propagation for varying numbers of size bins and single-sized fluids. Similarly to the advection-only results, there was very little variation in the shock width as the number of bins was increased, with the value of the shock width converging for 8 bins or more. Conversely, there is a strong dependence of the shock width on the number of fluids, with reasonable convergence for 16 fluids or more. The fraction of Si removed from grains by sputtering showed agreement with the results of Van Loo et al. (2013). Again, for size bins convergence was achieved for 8 or more bins, with the fraction being overestimated when fewer bins were used. Convergence didn't appear so concretely for single-sized fluids, and showed values smaller than for the equivalent number of bins. The reason for this becomes clear when looking the sputter rate as a function of grain size. For 2 bins or fluids the sputter rates deviated significantly for the larger grains, with the rate being much larger when using bins. The shape of the curve appeared similar for 8 bins and 32 bins, explaining the convergence of the fraction of Si removed from grains.

The evolved grain-size distributions for different numbers of bins were compared with and without sputtering. All showed an appreciable reduction in the number of small grains, as these grains are sputtered to sizes beyond the lower limit of the distribution and removed from the distribution. However, for 2 bins the overall distribution could not be modelled as accurately as for larger numbers of bins since each bin covers a broad range of sizes. In the larger size bin, the power law distribution means that the grains are heavily skewed towards the small end of the bin and the assumption that the velocity, and therefore the sputter rate, is constant within a bin means

that the amount of sputtering is overestimated. The larger grains in the bin move with the neutrals (i.e. with the species that cause sputtering), but this cannot be captured properly when 2 bins are used. For 4 bins, the distribution showed errors at the edges of the bins, possibly due to errors occurring the redistribution of the grains after sputtering. The distribution is modelled well for 8 bins or more.

The aim of this chapter has been to provide confidence that the distributions method described in Chapter 4 is implemented correctly, as well as to investigate how many size bins are required to accurately evolve the grain-size distribution due to sputtering, and to explore the differences which arise when using a size distribution in comparison to single-sized fluids. It is sensible to conclude from the sputter results that at least 8 size bins must be used to model such number-conserving processes. Furthermore, discrepancies between the convergence fluids and bins, for example for the fraction of Si lost from grains and the sputter rates, show that using a grain-size distribution does impact the effect of sputtering, which in turn will affect the abundance of gas-phase Si resulting from the shock.

6

Grain-grain collisions in C-type shocks

This chapter describes a routine to determine the source terms for the grain mass and number densities due to grain-grain collisions. This formulation is more accurate than others in the literature. The implementation of the routine is tested to determine the effect of the number of bins on the shock dynamics and shape of the grain-size distribution. Results are provided for C-type shocks where both sputtering and grain-grain collisions alter the grain-size distribution for different shock velocities and pre-shock gas densities.

Contents

6.1 Introduction

Studies have shown that single-sized grain fluids may be sufficient for modelling C-type shocks in which the grains are disrupted by number-conserving processes such as sputtering (e.g. Draine et al., 1983; Caselli et al., 1997; Jiménez-Serra et al., 2008; Van Loo et al., 2013). However, for processes such as shattering this is no longer feasible due to the distribution of fragments which result from grain-grain collisions (Jones et al., 1996). Therefore, to update the code to include a more

comprehensive treatment of physical grain processes, the implementation of a grain-size distribution is necessary. To this end, Chapter 5 saw the implementation and testing of a discretised power-law grain-size distribution undergoing sputtering in our time-dependent, multifluid MHD code for C-type shock simulations. The next stage is the formulation and implementation of a method which evolves the grain-size distribution due to grain-grain collisions. The effect of sputtering and grain-grain collisions on the size distribution and the abundance of gas phase SiO can then be analysed.

In the literature, studies which include grain-grain collisions tend to follow the formulation introduced by Tielens et al. (1994) and Jones et al. (1996) (e.g. Hirashita and Yan, 2009; Guillet et al., 2011; Asano et al., 2013). When two grains collide, strong shock waves propagate through the grains and cause the grain material to compress to high pressures. When these pressures exceed the strength of the material, some portion of the grains shatter into a number of fragments. Additionally, some portion of the grain material may pass directly into the gas phase via vaporisation when the energy transferred to the grain by the collision exceeds the threshold value. It is possible that vaporisation is the dominant cause of Si being released from grains in shocks at high ($> 10^4$ cm^{-3}) densities (Caselli et al., 1997; Guillet et al., 2011).

The analytic formulation developed by Tielens et al. (1994) allows the volumes of vaporised and shattered material to be estimated. It was determined by Jones et al. (1996) that the fragments resulting from a collision can be modelled with a power-law size distribution which scales as $a^{-3.3}$, where a is the radius of a fragment. Furthermore, Jones et al. (1996) found that the maximum possible fragment size depends on the collision velocity, such that larger collision velocities result in larger maximum fragment sizes, up to the point at which the grain is completely destroyed.

The shattered and vaporised fractions of a grain involved in a collision are used along with the fragment size distribution to determine the rate at which grains are added or removed to size bins in a discretised grain-size distribution. If the sum of the vaporised and shattered fractions is less than 1, there will be a portion of the grain remaining after the collision which must be transferred to the appropriate size bin. Other studies to investigate grain-grain shattering take the remaining target grain to have an average size (e.g. Jones et al., 1996; Hirashita and Yan, 2009; Guillet et al., 2011). In this case all the grains in the target bin are then re-binned into the

size bin corresponding to the average size of the target. Unless using large numbers of bins, this will inevitably lead to errors in the size distribution.

Furthermore, these studies use average values in the fragment distribution. However, use of certain approximations allows analytic expressions to be devised which take into account the distribution of the grains undergoing fragmentation when calculating the fragment distribution. This means the only assumptions we need to make are that the grain velocity and the fractions of the grain mass shattered or vaporised are constant within a bin. The routine for grain-grain shattering and vaporisation is presented in Section 6.2. Section 6.4 then analyses the implementation of this routine. Furthermore, the grain-size distribution is evolved due to both grain-grain collisions and gas-grain sputtering, and the contributions of each process to the gas phase SiO is investigated for different shock velocities and pre-shock densities. Finally, Section 6.5 provides conclusions.

6.2 Grain-grain collisions routine

The fragmentation routine described in §4.2.2.2 follows the method presented by McKinnon et al. (2018) in that it assumes that the entirety of both grains involved in a collision are fully fragmented. This assumption removes the need to deal with any grain remnants. However, particularly for large grains (the targets), only a small portion of the grain may be fragmented in a collision with a smaller grain (the projectile). In the literature, the remnants are re-binned according to their average size (e.g. Jones et al., 1996; Hirashita and Yan, 2009; Guillet et al., 2011). A more accurate approach is to determine the size distribution of the grain remnants and re-bin them by shifting them into the corresponding bins in a similar way as to for number-conserving processes (see §4.2.2.1). Additionally, vaporisation occurs for collisions in which the relative velocity exceeds 19 km s^{-1} (Tielens et al., 1994). This threshold velocity is higher than that of shattering (2.7 km s^{-1}) so vaporisation is always accompanied by shattering. The impact of vaporisation is to reduce the size of the grain remnants, but this doesn't change the method by which the remnants are redistributed.

In §4.2.2.2 the source terms due to shattering were introduced. They are repeated here with the second term of each equation written in terms of target grains of size

a_T which reside in bin j, and projectile grains of size a_P which reside in bin k,

$$S(a,t) = -\frac{\partial n}{\partial a}\int_{a_{\min}}^{a_{\max}} \mathrm{d}a_1 \frac{\partial n}{\partial a_1}\pi v_r(a,a_1)\,(a+a_1)^2 + \frac{1}{2}\sum_{k=0}^{N-1}\sum_{j=0}^{N-1}\int_{a_k}^{a_{k+1}}\mathrm{d}a_P\frac{\partial n}{\partial a_P} \tag{6.1}$$

$$\times \int_{a_j}^{a_{j+1}}\mathrm{d}a_T\frac{\partial n}{\partial a_T}\pi v_r(a_P,a_T)\,(a_P+a_T)^2\,\frac{\partial N_{frag}}{\partial a}(a,a_T,a_P),$$

and

$$S'(a,t) = -m(a)\frac{\partial n}{\partial a}\int_{a_{\min}}^{a_{\max}} \mathrm{d}a_1 \frac{\partial n}{\partial a_1}\pi v_r(a,a_1)\,(a+a_1)^2 + \frac{1}{2}\sum_{k=0}^{N-1}\sum_{j=0}^{N-1}\int_{a_k}^{a_{k+1}}\mathrm{d}a_P\frac{\partial n}{\partial a_P} \tag{6.2}$$

$$\times \int_{a_j}^{a_{j+1}}\mathrm{d}a_T\frac{\partial n}{\partial a_T}\pi v_r(a_P,a_T)\,(a_P+a_T)^2\,m(a)\frac{\partial N_{frag}}{\partial a}(a,a_P,a_T),$$

where N is the number of bins and $m(a) = (4/3)\pi\ \rho_0\ a^3$ is the mass of a spherical grain with radius a and density ρ_0, and $v_r(a_P,a_T)$ is the relative velocity between grains of size a_T and a_P. The rate of grain numbers or mass per volume added to or taken away from bin i are then found by integrating $S(a,t)$ or $S'(a,t)$ with respect to a over the appropriate limits.

The first term in Eqs. 6.1 and 6.2, which represents the rate of mass and numbers of grains lost from bin i, remains the same as described in §4.2.2.2 when integrated and discretised. However, the second term in these equations, which represents the rate at which grain numbers and mass are gained, must be changed. The method used by Hirashita and Yan (2009) and Guillet et al. (2011) essentially takes the number of fragments from the target bin j entering bin i due to a collision between grains in bins j and k to be $N_{frag,i}^{j,k} + 1$ and the mass to be $m_{frag,i}^{j,k} + m_{rem,T}$, where $m_{rem,T}$ is the average mass of the target grain remnant, provided the average target remnant grain size lies between the limits of bin i. When this is integrated, it adds the entire number of grains which were in the target bin into bin i. An alternative approach is to include the distribution of target grain remnants and add them to the appropriate size bins. One assumption which is still made, however, is that the fraction of target or projectile mass which is shattered or vaporised is the same for all grains within a bin. In reality there will be some size-dependence, although the variation is likely to be small. These fractions are determined using the method

described in section 3.3 of Tielens et al. (1994) for the target and projectile grains. Note that vaporisation takes precedence over shattering (Jones et al., 1996), so the vaporised fraction F_{vap} is calculated first, then the shattered fraction F_{sh} takes the final value $\min[F_{sh}, 1 - F_{vap}]$ to ensure that $F_{sh} + F_{vap} \leq 1$.

The distribution of grains resulting from a collision between a target grain and projectile grain is then a combination of the fragments and the remnants,

$$\begin{aligned}\frac{\partial N_{frag,T}}{\partial a} = \; & C_{f,T}\; a^{-3.3} + C_{R,T}\; \delta\left(a - (1 - F_{sh,T} - F_{vap,T})^{1/3}\; a_T\right) \\ & + C_{f,P}\; a^{-3.3} + C_{R,P}\; \delta\left(a - (1 - F_{sh,P} - F_{vap,P})^{1/3}\; a_P\right)\end{aligned} \tag{6.3}$$

where T denotes targets and P denotes projectiles. $C_{f,T/P}\; a^{-3.3}$ is the fragment distribution as given by Jones et al. (1996), which has limits $a_{f,T/P\,\min} = 5.0 \times 10^{-8}$ cm and $a_{f,T/P\,\max} = (0.0204\;\; \min[F_{sh,T/P}, 0.5])^{1/3}\; a_{T/P}$ (Jones et al., 1996; Guillet et al., 2011) since if the fraction of mass which is shattered is larger than 0.5 then it is assumed that the entire grain fragments. $C_{R,T/P}\; \delta(a-(1-F_{sh,T/P}-F_{vap,P/T})^{1/3} a_{T/P})$ is the remnant distribution, where $F_{sh,T/P}$ is the fraction of the target or projectile which is shattered, and $F_{vap,T/P}$ is the fraction of the target or projectile which is vaporised. From here on, the target grains will be used to demonstrate the method. The procedure is the same for the projectile grains.

The pre-factor $C_{f,T}$ in the fragment distribution must be calculated. To do this, we introduce a variable $\beta_T = (0.0204\;\; \min[F_{sh,T}, 0.5])^{1/3}$ in the expression for the maximum fragment size,

$$a_{f,T\,\max} = \beta_T a_T, \tag{6.4}$$

and equate the integral of $m(a) C_{f,T}\; a^{-3.3}$ between the fragment distribution limits with the mass of the target grain which is shattered,

$$\int_{a_{f,T\,\min}}^{a_{f,T\,\max}} \mathrm{d}a\; \frac{4\pi\rho_0}{3}\; a^3\; C_{f,T}\; a^{-3.3} = F_{sh,T}\; a_T^3\; \frac{4\pi\rho_0}{3}. \tag{6.5}$$

Evaluation of the integral gives

$$C_{f,T} = \frac{0.7\; F_{sh,T}\; a_T^3}{(\beta_T\; a_T)^{0.7} - a_{f,T\,\min}^{0.7}}. \tag{6.6}$$

In the source terms, this must be integrated with respect to a_T if we are to include the distribution of the maximum target fragment sizes. Clearly this is not straightforward to evaluate. However, it is found that the above expression can be

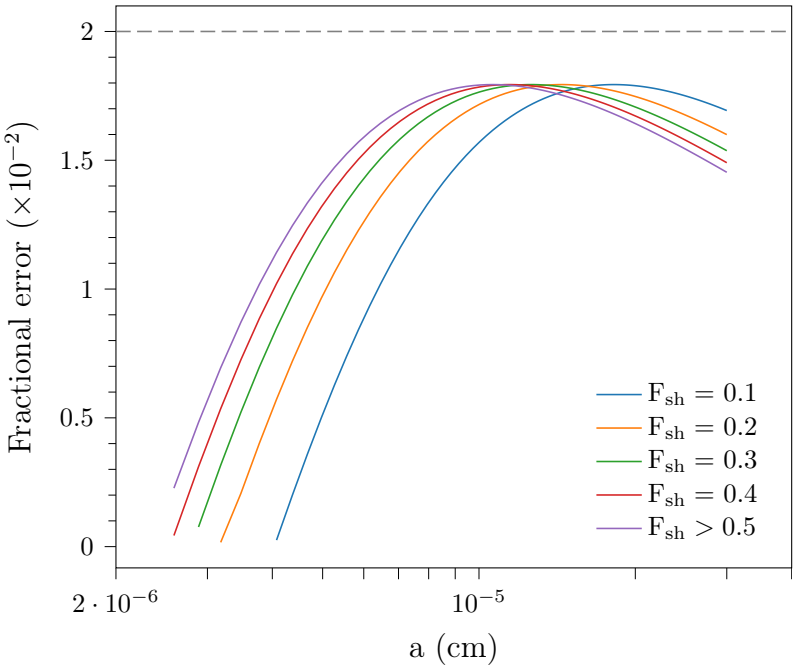

Figure 6.1: Fractional error between the actual and approximated values of C_f across the full range of grain sizes in the grain-size distribution for which $\beta a > a_{\rm min}$ (see the main text for a definition of β) for different values of the shattered mass fraction F_{sh}. The grey dashed line shows an error of 2%.

approximated by

$$C_{f,T} \approx 0.7 \; F_{sh,T} \; \beta_T^{-0.7} \; a_T^{2.3} \left(1 + 2.5 \; \frac{a_{f,T\,\rm min}}{\beta_T \; a_T} \right). \tag{6.7}$$

This need only be calculated when $\beta_T \; a_T \geq a_{\rm min}$ where $a_{\rm min}$ is the minimum size limit of the distribution (otherwise all the fragments are smaller than the lower limit of the grain-size distribution and are removed from the distribution). For all values of $F_{sh,T}$, this approximation is within 2% of the true value. This is shown in Fig. 6.1, where the fractional error between the approximate and actual value is plotted against the grain sizes for which $\beta_T a > a_{\rm min}$, for increasing values of $F_{sh,T}$. Note that values of $F_{sh,T} > 0.5$ are set to 1 since it is assumed in this case that catastrophic destruction occurs and the entire grain breaks up into fragments. This approximation allows an analytic expression to be formed for the source terms.

The constant in front of the δ-function is $C_{R,T} = 1$. Then the contribution to the number density source term, from bins j and k, becomes

$$S(a,t) += \frac{1}{2}\int_{a_k}^{a_{k+1}} \mathrm{d}a_P \frac{\partial n}{\partial a_P} \int_{a_j}^{a_{j+1}} \mathrm{d}a_T \frac{\partial n}{\partial a_T} \pi \left(a_P^2 + a_T^2\right) v_r(a_P, a_T) \times \left[A_T\ a_T^{2.3}\left(1 + B_T\ a_T^{-1}\right) a^{-3.3} + \delta\left(a - \gamma_T a_T\right)\right] \tag{6.8}$$

where $\gamma_T = (1 - F_{sh,T} - F_{vap,T})^{1/3}$, and the constants in Eq. 6.7 have been absorbed into the new variables A_T and B_T. Similarly the contribution to the mass density source term is

$$S'(a,t) += \frac{1}{2}\int_{a_k}^{a_{k+1}} \mathrm{d}a_P \frac{\partial n}{\partial a_P} \int_{a_j}^{a_{j+1}} \mathrm{d}a_T \frac{\partial n}{\partial a_T} \pi \left(a_P^2 + a_T^2\right) v_r(a_P, a_T) \times \left[A_T\ a_T^{2.3}\left(1 + B_T\ a_T^{-1}\right) a^{-3.3} + \delta\left(a - \gamma_T a_T\right)\right] m(a). \tag{6.9}$$

These expressions can be divided into two parts; the contribution of the fragments and the contribution of the remnants. We examine these parts separately in what follows.

6.2.1 Fragments

Here we address the contribution of the fragments to the source terms. First consider the case where $a < \beta_T\ a_{T,\mathrm{min}}$, which says that the grains in bin i lie below the largest fragment size from the smallest sized target grains. The contribution to the number density source term is the integral $\mathcal{I}_n$,

$$\mathcal{I}_n = \pi v_r(a_P, a_T) A_T \int_{a_k}^{a_{k+1}} \mathrm{d}a_P \frac{\partial n}{\partial a_P} \times \int_{a_j}^{a_{j+1}} \mathrm{d}a_T \frac{\partial n}{\partial a_T} \left(a_T + a_P\right)^2 a_T^{2.3} \left[1 + B_T\ a_T^{-1}\right] a^{-3.3}. \tag{6.10}$$

After evaluation of the integrals this is

$$\mathcal{I}_n = \pi v_r(a_P, a_T) A_T \; n_j \; n_k \left\{ \langle a^{4.3} \rangle_j + 2\langle a^{3.3} \rangle_j \langle a \rangle_k + \langle a^{2.3} \rangle_j \langle a^2 \rangle_k \right. \\ \left. + B_T \left(\langle a^{3.3} \rangle_j + 2\langle a^{2.3} \rangle_j \langle a \rangle_k + \langle a^{1.3} \rangle_j \langle a^2 \rangle_k \right) \right\} a^{-3.3}, \tag{6.11}$$

where $\langle a^l \rangle$ is the moment of order l, calculated according to Eq. 4.22. For the mass density the integral $\mathcal{I}_\rho$ is equivalent to $m(a)\mathcal{I}_n$. The rate at which the number or mass density of fragments are added to bin i is then determined by integration of $\mathcal{I}_n$ or $\mathcal{I}_\rho$ with respect to a from a_i to $\min[a_{i+1}, \beta_T \; a_j]$.

Next, we consider the case where $\beta_T \; a_j < a < \beta_T \; a_{j+1}$, which says that the grains in bin i are larger than the largest fragment size from the smallest target grains, but smaller than the largest fragment size from the largest target grains. Then the integral for the number density is,

$$\mathcal{II}_n = \pi v_r(a_P, a_T) A_T \int_{a_k}^{a_{k+1}} \mathrm{d}a_P \frac{\partial n}{\partial a_P} \\ \times \int_{a/\beta_T}^{a_{j+1}} \mathrm{d}a_T \frac{\partial n}{\partial a_T} \left(a_T + a_P\right)^2 a_T^{2.3} \left[1 + B_T \; a_T^{-1}\right] a^{-3.3} \tag{6.12}$$

where the difference between this and Eq. 6.10 is that the lower limit in the integration over a_T is a/β_T rather than a_j. The result after integration is

$$\mathcal{II}_n = \pi v_r(a_P, a_T) A_T \; n_k \left\{ \frac{a_{j+1}^{5.3-\alpha_j} - (a/\beta_T)^{5.3\alpha_j}}{5.3 - \alpha_j} + 2\langle a \rangle_k \frac{a_{j+1}^{4.3-\alpha_j} - (a/\beta_T)^{4.3-\alpha_j}}{4.3 - \alpha_j} \right. \\ + \langle a^2 \rangle_k \frac{a_{j+1}^{3.3-\alpha_j} - (a/\beta_T)^{3.3-\alpha_j}}{3.3 - \alpha_j} + B_T \left[\frac{a_{j+1}^{4.3-\alpha_j} - (a/\beta_T)^{4.3-\alpha_j}}{4.3 - \alpha_j} \right. \\ \left. \left. + 2\langle a \rangle_k \frac{a_{j+1}^{3.3-\alpha_j} - (a/\beta_T)^{3.3-\alpha_j}}{3.3 - \alpha_j} + \langle a^2 \rangle_k \frac{a_{j+1}^{2.3-\alpha_j} - (a/\beta_T)^{2.3-\alpha_j}}{2.3 - \alpha_j} \right] \right\} a^{-3.3}. \tag{6.13}$$

Again, for the mass density the integral is $\mathcal{II}_\rho = m(a)\mathcal{II}_n$. The contribution of fragments to bin i is found through integration of $\mathcal{II}_n$ or $\mathcal{II}_\rho$ with respect to a from $\max[a_i, \beta_T \; a_j]$ to $\min[a_{i+1}, \beta_T \; a_{j+1}]$.

The final case of fragments to consider is when $a > \beta_T a_{j+1}$. In this case there is no contribution to bin i as the lower limit of bin i is larger than the largest target fragment size.

6.2.2 Remaining grains

Now we examine the contribution of remnant grains to bin i. If $a_j \leq a/\gamma_T \leq a_{j+1}$ then some remaining target grains have sizes between the limits of bin i after shattering. The contribution to the number density source term is found via the integral,

$$\mathcal{I}_{R,n} = \pi v_r(a_P, a_T) \int_{a_k}^{a_{k+1}} \mathrm{d}a_P \frac{\partial n}{\partial a_P} \times \int_{a_j}^{a_{j+1}} \mathrm{d}a_T \frac{\partial n}{\partial a_T} \left(a_T + a_P\right)^2 \delta(a - \gamma_T\ a_T). \tag{6.14}$$

Evaluation of the above yields

$$\mathcal{I}_{R,n} = \pi v_r(a_P, a_T)\ n_{0,j} \left(\frac{a}{\gamma_T}\right)^{-\alpha_j} \left[\left(\frac{a}{\gamma_T}\right)^2 n_k + 2\left(\frac{a}{\gamma_T}\right) n_k \langle a\rangle_k + n_k \langle a^2\rangle_k\right]. \tag{6.15}$$

The contribution to the mass density source term is

$$\mathcal{I}_{R,\rho} = \frac{4}{3}\pi\rho_0\ \pi v_r(a_P, a_T)\ n_{0,j}\ \frac{a^{3-\alpha_j}}{\gamma_T^{-\alpha_j}} \left[\left(\frac{a}{\gamma_T}\right)^2 n_k + 2\left(\frac{a}{\gamma_T}\right) n_k \langle a\rangle_k + n_k \langle a^2\rangle_k\right]. \tag{6.16}$$

To find the contribution of remnant grains to bin i, Eq. 6.15 or 6.16 is integrated with respect to a from $\max[a_i, \gamma_T a_j]$ to $\min[a_{i+1}, \gamma_T\ a_{j+1}]$. If a/γ_T does not lie in the region $[a_j, a_{j+1}]$ then $\mathcal{I}_{R,n} = \mathcal{I}_{R,\rho} = 0$ and there are no target remnants added to the source terms for bin i.

6.2.3 SiO emission by vaporisation

Vaporisation directly releases SiO into the gas phase. The fraction of a grain's mass which is vaporised, F_{vap}, is calculated in the same way as that of shattering, but with the appropriate values for the threshold velocity and pressure. The source term

for the production of SiO due to vaporisation is

$$S_{sio} = \frac{1}{2}\int_{a_k}^{a_{k+1}} \mathrm{d}a_P \frac{\partial n}{\partial a_P} \int_{a_j}^{a_{j+1}} \mathrm{d}a_T \frac{\partial n}{\partial a_T} \pi \left(a_P + a_T\right)^2 v_r \left(a_P, a_T\right) N_{si} \tag{6.17}$$

where N_{si} is the number of Si atoms released by vaporisation,

$$N_{si} = \frac{4}{3}\pi\rho_0 \frac{(F_{vap,P}\ a_P^3 + F_{vap,T}\ a_T^3)}{m_{ol}} \tag{6.18}$$

and $m_{ol} = 172\ m_H$ is the mass of an olivine molecule. The total rate per volume of SiO released is then obtained through the summation over all values of j and k. After evaluation of the integrals the source term is

$$S_{sio} = \frac{1}{2}\frac{4\pi\rho_0}{3m_{ol}} \sum_{k=0}^{N-1}\sum_{j=0}^{N-1} v_r\left(\langle a\rangle_j, \langle a\rangle_k\right) n_j n_k \left\{F_{vap,P}\left[\langle a^5\rangle_k + 2\langle a^4\rangle_k\langle a\rangle_j + \langle a^3\rangle_k\langle a^2\rangle_j\right]\right.$$
$$\left. + F_{vap,T}\left[\langle a^2\rangle_k\langle a^3\rangle_j + 2\langle a\rangle_k\langle a^4\rangle_j + \langle a^5\rangle_k\right]\right\}. \tag{6.19}$$

When sputtering is also included, this rate is added to that which is calculated for sputtering to determine the total rate of production of gas phase SiO at each time step.

6.2.4 A note on computational considerations

There are some implications to consider when implementing the method described in this section into a numerical code. For example, Eq. 6.13 requires the calculation of $a_{j+1}^{5.3-\alpha_j}$ and, given that $a_{j+1} \sim 10^{-6}$, when the magnitude of α_j is large this can produce exceedingly small numbers (e.g. $\sim 10^{-60}$). However, this can be mitigated through use of the fact that $a_{j+1} = a_j \exp[da]$ where $da = \log(a_{j+1}/a_j)$. The use of sensible choices of calculation can therefore both avoid floating point errors, and reduce the computational cost.

6.3 Models

In this chapter, the 'standard' oblique model we use has a shock speed $v_s = 40$ km s^{-1}, magnetic field angle $\theta = 45^o$, and pre-shock gas density $n_H = 10^5$ cm^{-3}. This differs

from the pre-shock density of 10^6 cm^{-3} used for the standard shock model in Chapter 5 in order for us to be able to compare our results with Guillet et al. (2011), who do not run simulations for the higher density as their steady-state solution is unable to converge. This standard model is used to test the implementation of the grain-grain collisions routine. The aim of this testing is to determine the number of bins required to accurately model grain-grain collisions.

Following the testing of the implementation of the shattering routine, results are given for a combination of sputtering and grain-grain collisions for the standard shock model, as well as for shock speeds of 30 km s^{-1} and 50 km s^{-1} to show the effect that shock speed has on the evolution of the grain-size distribution. Results are also given for the fraction of Si removed from the grains for combined shattering and sputtering, and these are compared with results for sputtering only. Finally, results are also given for a density of 10^6 cm^{-3} at two shock velocities; 30 km s^{-1} and 40 km s^{-1}.

For all models the grains are assumed to follow an MRN distribution, with an upper size limit of $a_{\rm max} = 3 \times 10^{-5}$ cm and a lower size limit of $a_{\rm min} = 5 \times 10^{-7}$ cm. The distribution is discretised into N size bins according the method described in §4.2.1.

6.4 Results and discussion

6.4.1 Implementation

The implementation of the grain-grain collisions routine has been tested for 8, 16 and 32 size bins. Grain-grain collisions depend on the relative velocity between the projectile and target grains, thus to accurately capture the effect that grain-grain collisions have on the grain-size distribution enough bins must be used in order that the assumption that the velocity of all grains within a bin is constant does not have a detrimental effect on the collision rates. It was shown in Chapter 5 that 8 bins are required to accurately model changes to the grain-size distribution by sputtering, therefore 8 bins is the minimum number of bins used here. Figure 6.2 (a) compares the shock profiles for 8 and 32 bins for the 'standard' model described in §6.3. The profiles appear very similar, and Fig. 6.2 (b), which displays the shock width (as measured at the points where the neutral gas temperature is 100 K) as function of the number of bins, confirms that this is the case. There is an error of just 0.2%

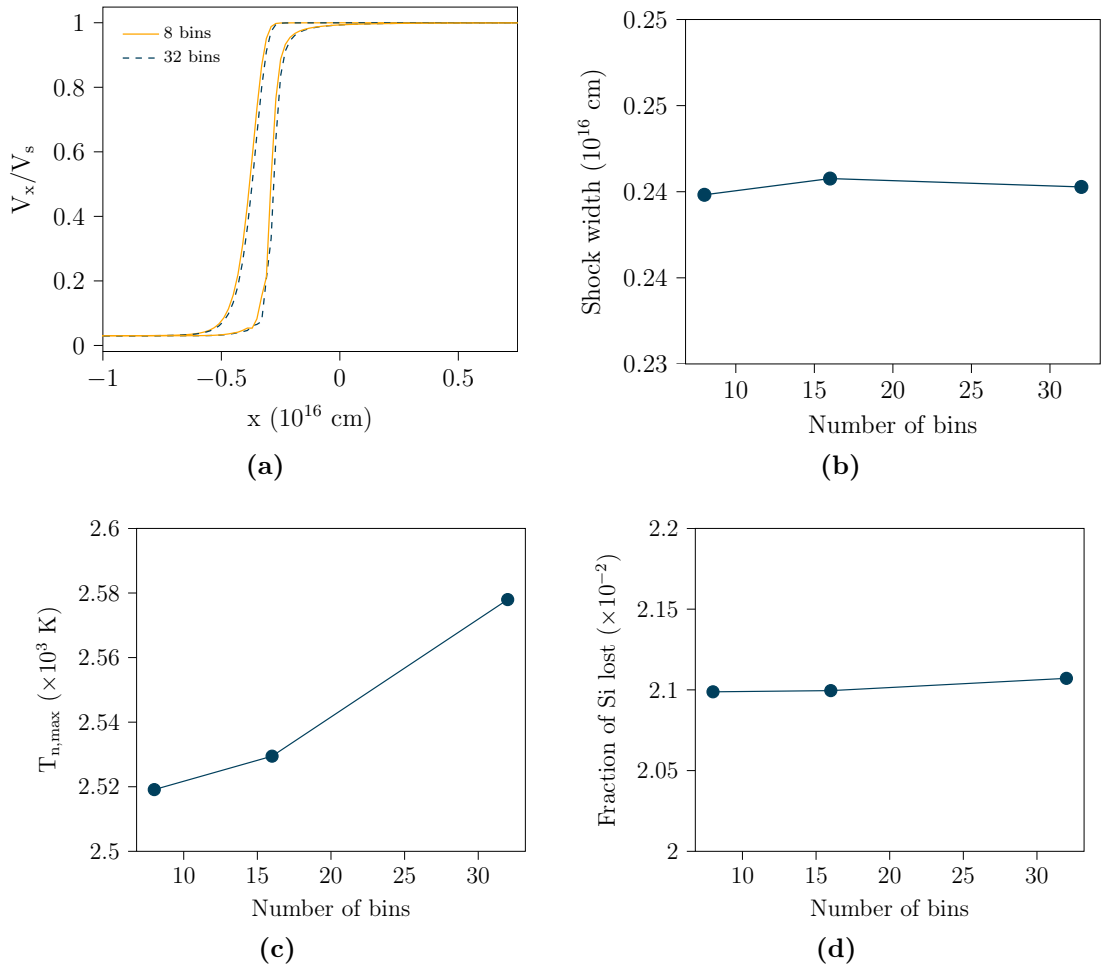

Figure 6.2: (a) Profiles for 8 bins and 32 bins for a 40 km s^{-1} shock through a medium of density 10^5 cm^{-3} where the magnetic field makes an angle of 45^o with the direction of propagation of the shock. (b) shows the shock width, (c) shows the maximum neutral temperature, and (d) shows the fraction of Si lost from the grains, all as a function of the number of bins.

between the widths for 8 and 32 bins. Fig. 6.2 (c) shows the maximum neutral temperature as a function of the number of bins. Although there is clearly some variation here, the error between 8 bins and 32 bins is 2.3%. Finally, Fig. 6.2 (d) shows the fraction of Si removed from the grains as a function of the number of bins. Again there is very little variation, with an error between 8 bins and 32 bins of 0.4%. Overall it can be concluded that use of more than 8 bins does not have any significant impact on the shock dynamics and structure.

A further consideration to be made is the impact of the number of bins on the shape of the grain-size distribution in the downstream region of the shock. Fig. 6.3 shows the downstream distributions when sputtering and grain-grain collisions are applied when (a) 8 bins, (b) 16 bins and (c) 32 bins are used. Fig. 6.3 (d) compares compares

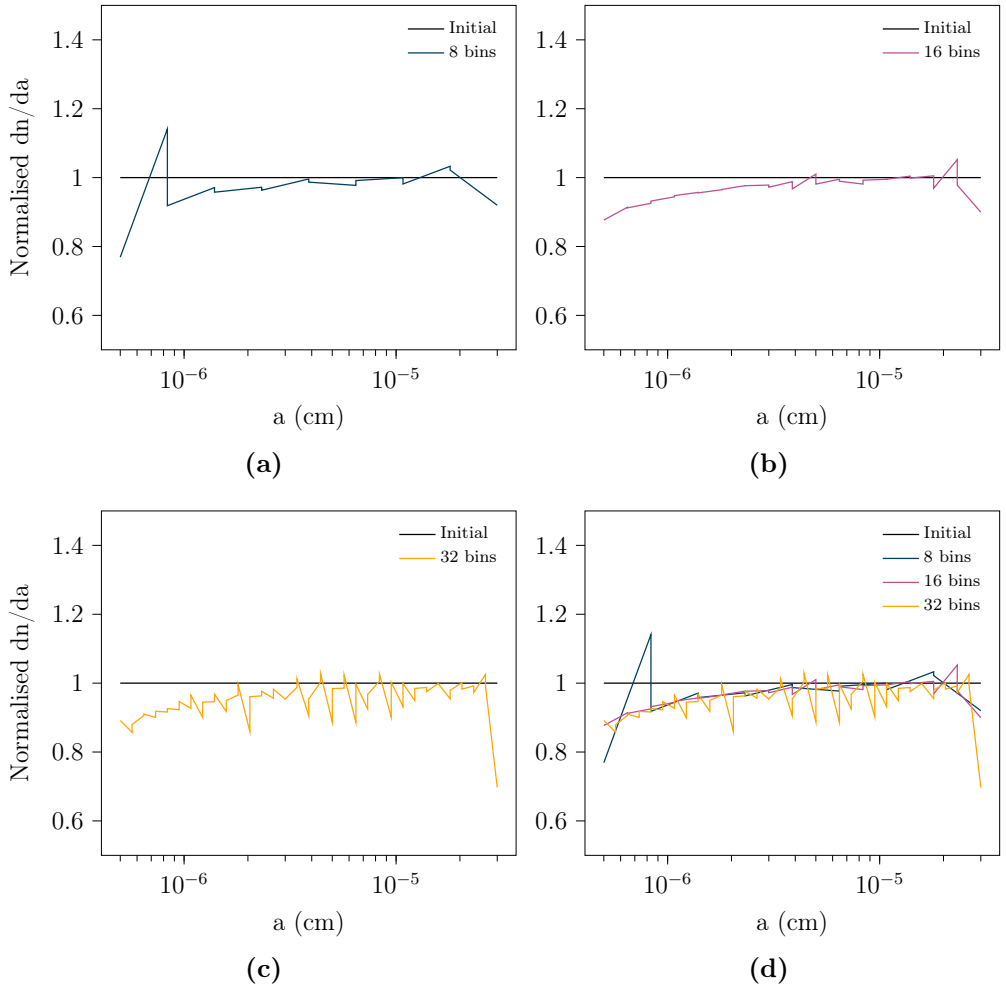

Figure 6.3: Downstream grain-size distribution normalised to the initial distribution for the standard shock model for (a) 8 bins, (b) 16 bins, and (c) 32 bins. (d) compares the distributions for 8, 16 and 32 bins.

all 3 distributions. The effect on the distribution is a reduction in the number of grains at either end of the distribution. This because small grains undergo efficient sputtering, which reduces their size until they are smaller than the lower limit of the distribution and removed. Additionally, for a pre-shock density of 10^5 cm^{-3} the relative velocity is only sufficient for disruption between the grains at the extreme ends of the distribution. Fig. 6.3 (a) shows that there is some inaccuracy for the smallest size bin, likely because many of the fragments resulting from grain-grain collisions end up in this bin and there are not enough bins for this to be captured properly. In contrast, the distribution appears much smoother than the small end of the distribution for 16 bins. The distribution for 32 bins looks much rougher than that for 16 or 8 bins. While this may seem counter-intuitive, the cause for this is likely to be the smaller bin widths which can cause issues in the root-finding algorithm for the bin power-law index; the smaller the bin width the less able it is to

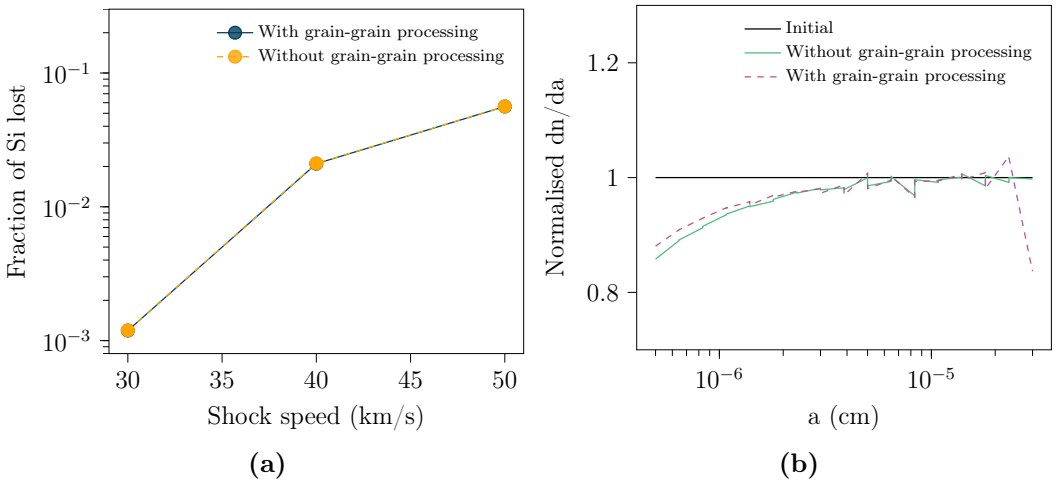

Figure 6.4: (a) Comparison the fraction of Si lost from the grains as a function of shock speed with (dark blue) and without (yellow) grain-grain processing, and (b) comparison of the normalised downstream grain-size distribution with and without grain-grain processing for a shock speed of 40 km s^{-1}. The pre-shock gas density is $n_H = 10^5$ cm^{-3} and the magnetic field angle is $\theta = 45^o$.

find a unique solution. It should also be noted that because the distributions have been normalised to the initial distribution, and the changes are slight, small errors in the power-law index can cause the distribution to appear rough (see Fig. 5.15 for a comparison of actual and normalised distributions). These small differences in the grain-size distribution do not cause any discernible difference in the shape of the shock, or the fraction of Si released from the grains.

6.4.2 Grain processing in shocks

The previous section showed that the use of 8 size bins is sufficient to model the grain-size distribution as it evolves in C-type shocks due to sputtering and grain-grain collisions. However, the shape of the grain-size distribution is best captured when 16 size bins are used. Therefore, 16 size bins have been used here to show the effect that the shock velocity has on the fraction of Si which is released from grains due to processing in shocks.

Fig. 6.4 (a) shows the fraction of Si released from the grains as function of shock speed for a pre-shock density of 10^5 cm^{-3}. There is almost no difference at all between the fraction of Si released with and without grain-grain processing (the error is $\sim 0.1\%$). Fig. 6.4 (a) compares the downstream distributions with and without grain-grain processing. There is only a small difference in the distributions at the small grain sizes, with the effect of the grain-grain collisions being to slightly

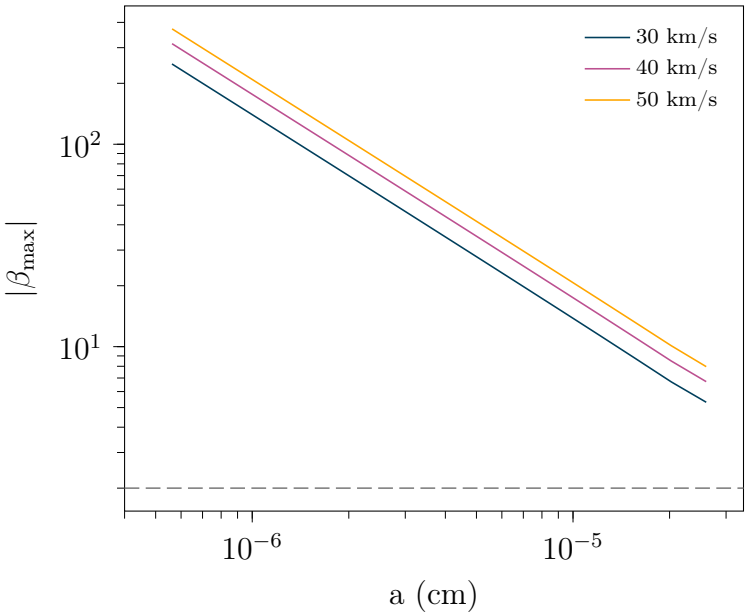

Figure 6.5: The magnitude of the maximum Hall parameter $|\beta_{\max}|$ as a function of grain size for shock speeds of 30 km s^{-1} (dark blue), 40 km s^{-1} (pink) and 50 km s^{-1} (yellow). The pre-shock density is 10^5 cm^{-3}, the magnetic field angle is $\theta = 45^o$ and the grain-size distribution is modelled using 16 bins. The grey dashed line indicates a value of $|\beta| = 2$.

increase the number of grains at these sizes due to the production of fragments. However, this doesn't seem to translate into a significant difference in the fraction of Si released by sputtering. Furthermore, the grain-grain relative speeds are never sufficient to cause vaporisation, which has a threshold velocity of 19 km s^{-1}. For example, the maximum relative speed between the bin containing the smallest grains and the bin containing the largest grains is approximately 4 km s^{-1}, regardless of the shock speed. Figure 6.5 shows why this is the case. This plot shows the magnitude of the maximum grain Hall parameter as a function of the grain size for different shock speeds, with the value $|\beta| = 2$ marked with a grey, dashed line. A value of $|\beta| \gg 2$ indicates that the grains are well-coupled to the magnetic field. Since even the largest grains in the distribution have $|\beta| > 5$, all the grains are coupled to the magnetic field and the relative grain-grain velocities remain small.

These results are in contrast to those of Guillet et al. (2011) who find that vaporisation dominates over sputtering for a density of 10^5 cm^{-3}. However, in comparing results it is important to note the differences between our models. One such important difference is that Guillet et al. (2011) include a number of initially empty bins from 5×10^{-8} cm to 1×10^{-6} cm which become filled by fragments when shattering occurs between larger grains. Shattering is a self-enhancing process, in which the production of small fragments then provides an abundance of grains which are then

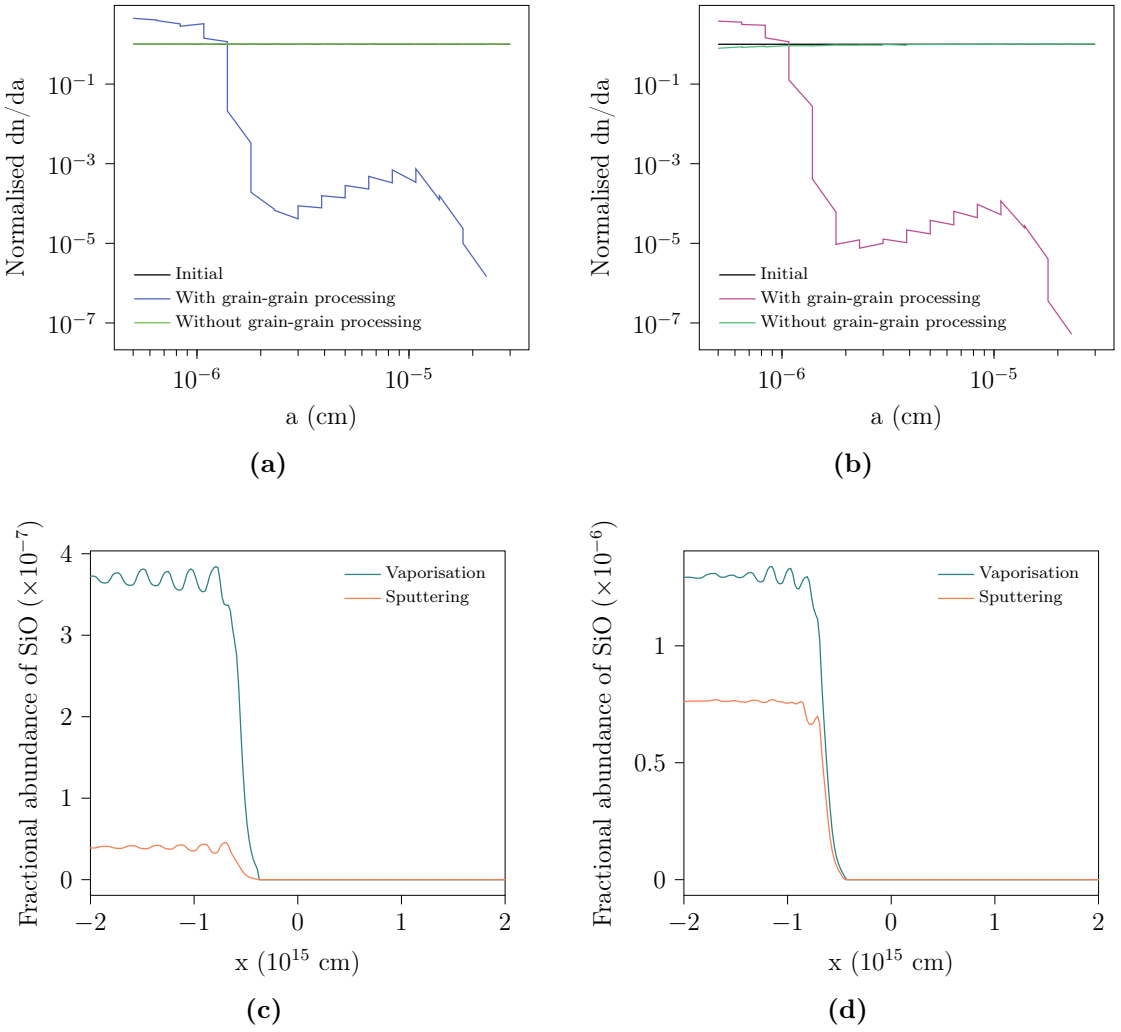

Figure 6.6: Comparison of the downstream grain-size distributions for (a) a 30 km s^{-1} shock with (purple) and without (dark green) grain-grain processing and (b) a 40 km s^{-1} shock with (pink) and without (light green) grain-grain processing. The bottom plots show the fractional abundance of gas phase SiO produced by sputtering (orange) and vaporisation (teal) for (c) 30 km s^{-1} and (d) 40 km s^{-1}. Results are for a pre-shock gas density of $n_H = 10^6$ cm^{-3} and magnetic field angle $\theta = 45^o$.

able to collide with the larger grains, thereby producing even more small fragments, and so on. The optimum ratio of grain sizes for fragmentation is ~ 10 (Jones et al., 1996), so these very small grains could therefore have a large impact on both the evolution of the distribution and the fraction of Si released from the grains.

Guillet et al. (2011) do not run simulations for densities higher than 10^5 cm^{-3} because their steady-state shock code was not able to converge at these densities due to the strong feedback of shattering in the shock. However, since we do not see such a significant effect of shattering at 10^5 cm^{-3}, this feedback is not an issue for a higher density of 10^6 cm^{-3}.

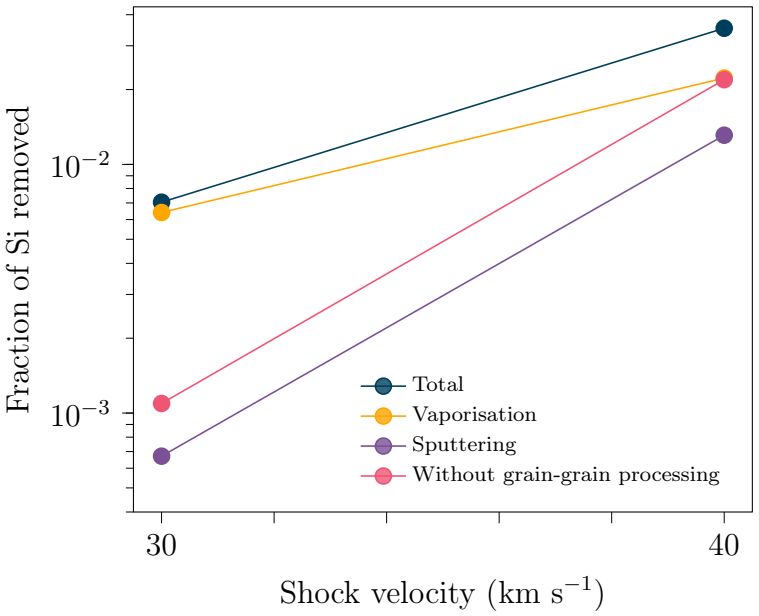

Figure 6.7: Fraction of Si removed from the grains as a function of shock velocity for a density of $n_H = 10^6$ cm^{-3} and a magnetic field angle $\theta = 45^o$. The total fraction of Si removed (dark blue) is compared to the fraction removed by sputtering vaporisation (yellow) and sputtering (purple), and also compared to the result without grain-grain processing (pink).

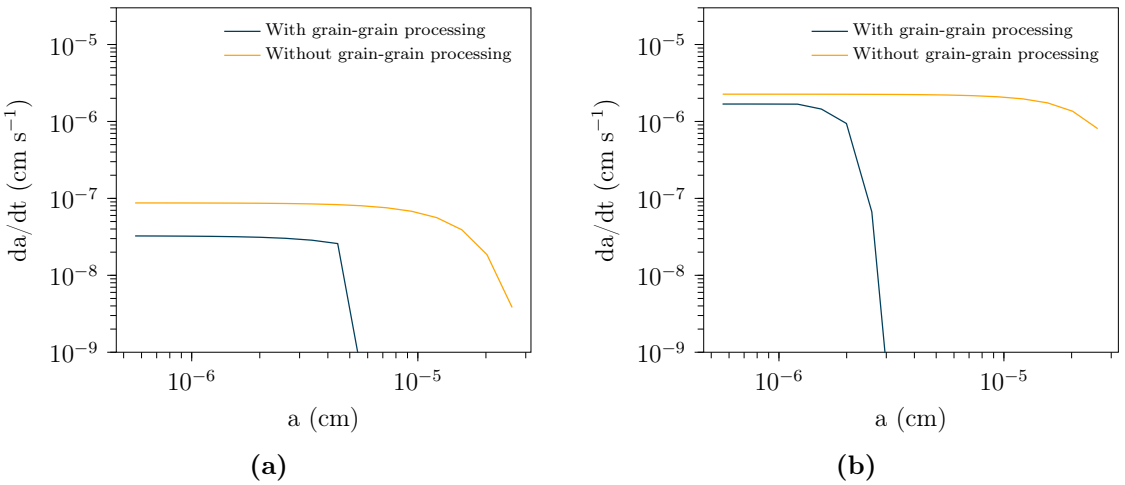

Figure 6.8: Comparison of the maximum sputter rate in the shock as a function of grain size with (dark blue) and without (yellow) grain-grain processing for (a) a shock velocity of 30 km s^{-1} and (b) a shock velocity of 40 km s^{-1}. Both plots are for a pre-shock density of 10^6 cm^{-3} and a magnetic field angle of 45^o.

Figure 6.6 (a) shows the downstream grain-size distribution for a 40 km s^{-1} shock through a gas of density 10^6 cm^3 with and without grain-grain processing. It is clear that for this higher density model there is a much more significant impact of grain-grain collisions on the grain-size distribution in comparison to the 10^5 cm^{-3} models. There is a large increase in the number of small grains, and a large decrease in the number of large grains. Furthermore, as shown in Fig. 6.6 (b), for this higher density not only does vaporisation occur, but it contributes more than sputtering to the overall gas phase SiO produced by the shock. Note that the fluctuations seen in the SiO abundances are a consequence of small numerical variations.

Figure 6.7 shows the fraction of Si removed from the grains for the 2 shock velocities. The total fraction of Si removed is compared to the fractions removed by vaporisation and by sputtering, as well as these being compared with the result without grain-grain processing. For both velocities, the fraction of Si removed by vaporisation exceeds that of sputtering. For example, for 40 km s^{-1} the fraction of Si removed from the grains by vaporisation is 0.022 compared to fraction of 0.013 removed by sputtering. Furthermore, Fig. 6.7 shows that the fraction of Si removed from the grains by sputtering when grain-grain collisions are neglected is greater than with grain-grain collisions. For example, for 30 km s^{-1} the fraction of Si removed by sputtering without grain-grain processing is 1.1×10^{-3}, compared to 6.7×10^{-4} with grain-grain processing. Guillet et al. (2011) find that grain-grain collisions enhance the amount of Si removed from the grains by sputtering, which is not the case here. However, this could be an impact of the higher density model we have used, or because the lower size limit of the distribution we use, $a_{\rm min} = 50$ Å , is larger than their value of 5 Å. The large reduction in grains above a size of approximately 1×10^{-6} cm appears to negatively impact the amount of sputtering to a higher degree than the increase in small grains enhances sputtering. However, we do see that vaporisation is more prominent than sputtering, a fact in agreement with Guillet et al. (2011), albeit for different pre-shock densities.

The cause of the reduced sputtering contribution when grain-grain collisions are included is illustrated in Fig. 6.8, which shows the sputter rate as a function of grain size for (a) 30 km s^{-1} and (b) 40 km s^{-1}, both with and without grain-grain processing. Both shock speeds see a significant drop-off in the sputter rate for larger grains. The size of grains corresponding to this drop-off is approximately 5×10^{-6} cm for 30 km s^{-1}, and is about 2×10^{-6} cm for 40 km s^{-1}. The sputtering rate functions without grain-grain processing show that the rate is approximately constant up to

grain sizes of the order 10^{-5} cm (since this is the size at which the grains become less well-coupled to the magnetic field and hence the grain-neutral relative velocity reduces). Therefore, the huge reduction in the number of grains with sizes between the drop-off and 10^{-5} cm removes otherwise significant contributors to the gas phase SiO.

The dramatic changes to the grain-size distribution by grain-grain collisions has an effect on the shock structure. For both shock speeds analysed, the shocks when grain-grain processing is applied are narrower than those without grain-grain processing by approximately 30%. There is a corresponding increase in the maximum neutral temperature (an increase of 7% of 30 km s^{-1} and 9% for 40 km s^{-1}) due to the reduced radiating layer. The reason for this narrowing of the shocks is the number of grains produced by shattering. The total number of grains in the distribution in the downstream region of the shock is larger for the shocks in which there are grain-grain collisions by a factor of 3. We see from the distributions that the number of large grains is greatly reduced, hence there is significant increase in the number of small grains. These small grains are tightly coupled to the magnetic field and, since the shock width is determined by grain-neutral collisions, this results in thinner shocks.

6.5 Conclusions

Our time-dependent multifluid MHD model has been modified to include grain-grain collisions which disrupt a grain-size distribution function modelled using a number of size bins. Expressions for the source terms for the number and mass densities of grains have been formulated in a more accurate way than has been seen before in the literature. In particular, the fragments and remnants which result from a grain-grain collision are distributed into the appropriate size bins without the need for using average values. In order to achieve an analytical formulation, it is necessary to make an approximation to the pre-factor in the fragment distribution. However, the error in this approximation is less than 2% for all grain sizes and shattered mass fractions. The only other approximations to be made are that the velocity in a bin is constant for all grains in that bin, and that the fraction of the grain mass shattered or vaporised is also constant within a bin.

The implementation of the grain-grain collisions routine was tested for a 40 km s^{-1} shock through a medium of density 10^5 cm^{-3} using 8, 16 and 32 size bins to model the grain-size distribution. It was found that the shock widths, and fraction of Si released from the grains due to sputtering and grain-grain collisions was unaffected by an increasing number of bins. However, the shape of the downstream distribution appeared smoothest for 16 size bins. This is because for 8 bins the distribution at small grain sizes, which is altered due to competition between the destruction due to sputtering and the production of fragments from collisions, cannot be well-captured. Additionally, for 32 bins there appear to be errors in the calculation of the power-law index, which could be a result of the smaller bin widths; the smaller the width the more difficult it is for the root-finding algorithm to find a unique solution. However, for our 10^5 cm^{-3} models the effect of shattering is slight, and small errors in the power-law index can appear to cause quite large deviations in the shape of the distribution, but these don't negatively impact the accuracy of the determination of the fraction of Si released from the grains. Therefore, it can be concluded that 8 bins is sufficient to model C-type shocks in which sputtering and grain-grain collisions occur but, for the sake of accurate visualisation of the evolution of the distribution, 16 bins may be preferable.

Results are provided for a number of shock velocities for a gas density of 10^5 cm^{-3}. However, it has been shown that at this density the grain-grain relative velocities are never sufficient for vaporisation to occur. Additionally, the impact of shattering is not great enough to produce a discernible difference in the fraction of Si removed from the grains in comparison the same models without grain-grain processing. This is contrast to the results of Guillet et al. (2011) who find that that vaporisation dominates over sputtering for all shock speeds at this density. However, it is important to acknowledge the differences in our models when drawing comparison. One potentially significant difference is that Guillet et al. (2011) extend the lower limit of the grain-size distribution down to 5 Å , where these initially empty bins are filled by fragments as shattering proceeds. The possibility of extending the distribution in a similar way is addressed in Chapter 7.

Results are further provided for a higher density of 10^6 cm^{-3}. At this density, the relative velocity between large grains and small grains is sufficient for vaporisation to occur and it is found that this is the dominant source of gas phase SiO at velocities of 30 and 40 km s^{-1}. Furthermore there is a much more dramatic effect on the shape of the grain-size distribution in comparison to the 10^5 cm^{-3} models. Although it is

difficult to compare with Guillet et al. (2011) as they don't give results for higher density models, an interesting difference is that Guillet et al. (2011) find that the contribution of sputtering to the removal of Si from the grains is enhanced by grain-grain collisions. In contrast, we find that the inclusion of grain-grain collisions reduces the effect of sputtering. Analysis of the maximum sputtering rates as a function of grain size through the shock show that the huge loss in numbers of grains above a size of $\sim 10^{-6}$ cm causes a correspondingly large reduction in the sputtering rates. The impact of the grain-grain collisions is therefore to heavily reduce the number of otherwise significant contributors to sputtering, and this is shown in the reduction in the fraction of Si released from grains by sputtering when grain-grain collisions are included. Furthermore, grain-grain collisions cause shocks which are approximately 30% narrower at this density, due to the huge increase in small grains which are well-coupled to the magnetic field.

Overall we find that while there is some difference in the shape of the evolved grain-size distribution for a pre-shock density of 10^5 cm^{-3} when grain-grain processing is included compared to sputtering alone, this doesn't translate into a difference in the gas phase SiO produced by dust grain disruption. However, for a higher density of 10^6 cm^{-3} the changes to the distribution are much more significant. Vaporisation then dominates over sputtering for the production of SiO for both shock velocities examined. Furthermore, the huge reduction in the number of larger grains in the distribution causes a reduction in the amount of Si released from the grains by sputtering in comparison to the case without grain-grain collisions. While there is a reduction in the number of large grains, there is an increase in the number of small grains, which has the effect of causing shocks which are thinner, and in which the maximum neutral temperature is greater.

7

Conclusions

This chapter provides the overarching conclusions for the work presented in this thesis. Suggestions for further work are discussed, with a focus on the inclusion of icy mantles on grains in a size distribution which undergoes physical processes, and the possibility of extending the grain-size distribution down to smaller radii.

Contents

7.1 Concluding remarks

The aim of this thesis has been to extend the treatment of dust grains in the model used by Van Loo et al. (2013) and Ashmore (2011) to simulate oblique C-type shocks. The ability of such numerical models to accurately evolve dust grain distributions is important, since the release of elements such as Si from dust grain cores provide a means of explaining the enhanced abundances of molecules like SiO observed in shock regions of dense molecular clouds. Additionally, changes to the dust grain-size distribution have implications for the shock structure and dynamics which, in turn, impact the chemistry of the region. Therefore, it is important that we are able to properly simulate the physics of dust grains in shocks, so that we are able to better understand the conditions of these dense clouds where stars are born.

Chapter 2 describes the original time-dependent, multifluid MHD model as used by Van Loo et al. (2013) and Ashmore (2011). This model self-consistently solves the shock and grain dynamics along with a limited chemical network. Grains are

included as a number of single-sized grain fluids, where the grains are modelled as spherical silicate cores covered by an icy mantle layer. The grains are able to undergo gas-grain sputtering, which releases grain material into the gas phase. Firstly, some improvements and adjustments were made to this model, as discussed in Chapter 3. Importantly, while the grains in the original model were able to lose material due to sputtering, the changes to the grain size and mass that this caused were not tracked. The size of the grains is used in the calculations for the collision coefficients and, at high densities ($> 10^4$ cm^{-3}), the shock structure is determined by grain-neutral drag, hence it is important to be able to determine the collision coefficients accurately. To address this, a conservation equation for the number density of grains was introduced. Since the mass density of grains is already tracked through the shock, the addition of the number density means that the mass (and therefore size) of the grains can be calculated wherever required in the code.

A further issue with the original model is that the maximum neutral temperatures reached in the shock were lower than expected. The critical velocity for C-type shocks, which describes the threshold shock velocity for which the C-type shock breaks down, is a result of the dissociation of H_2 molecules. The dissociation of H_2 removes an important coolant from the gas, which allows the neutral gas to heat up; the fluid becomes subsonic and the shock is no longer C-type. Dissociation occurs at temperatures of about 4000 K. So, despite the fact that the model does not account for dissociation, a gas temperature of 4000 K would provide an indicator for the transition of the shock from C- to J-type. However, such high neutral temperatures were not being seen, even for a shock velocity of 50 km s^{-1} (which should exceed the critical velocity). After investigations into the cooling mechanisms used the code found no cause for error, it was concluded that the cause of the reduced gas temperature was approximations which were made for the number densities of O and H_2O. These were replaced with the values which are updated at each time step in the code due to chemistry and sputtering, solving the issue of the reduced maximum gas temperature.

The final problem to be addressed in Chapter 3 was the grain charge calculation. In the original model, the grain charges were not able to become positive. While it is true that the grains are expected to carry negative charge in molecular clouds since the rate of grain-electron collisions is greater than the rate at which grains collide with positively-charged ions, this is not necessarily the case in the shock. The grain charge calculation was therefore modified to account for both positive

and negative charges. Furthermore, the electron density is now updated in the grain charge iteration, which solved a problem in which the electron density could become negative. The grain charge is an important factor in determining how well coupled the grains are to the magnetic field. This, in turn, affects the grain-neutral collision rate, which determines the shock width at high densities, and impacts the sputtering rate of the grains. It is therefore important to ensure that the grain charges are calculated correctly.

Following the improvements to the numerical code, Chapter 4 described a novel method for discretising and evolving grain-size distributions. While the use of multiple single-sized grain fluids works well for number-conserving processes such as sputtering, processes which alter the number of grains require the use of a grain-size distribution. We are interested in modelling grain-grain collisions, which involves two processes; shattering and vaporisation. Although vaporisation is a number-conserving process, so could be modelled in much the same way as sputtering, the fragmentation of grains, which always accompanies vaporisation, produces grain fragments which themselves follow a size distribution. It is generally accepted that grains in the ISM follow a power law with respect to their radius a, such as the MRN distribution which is proportional to $a^{-3.5}$.

Our approach uses a power-law discretisation to model the distribution, as opposed to piecewise-constant or piecewise-linear ones which have been used in the literature. In this approach, the distribution is discretised into a number of size bins, where the distribution in each bin is described as a power law characterised by its power-law index. The number and mass densities of the grains, which are tracked for each bin, are evolved due to physical processes. These values are then used at each time-step to uniquely determine the power-law index in each bin, thus the overall grain-size distribution can be produced at any point in the shock. A number of numerical tests were carried out where it was shown that this method outperforms piecewise-constant and -linear approaches, particularly for a small number of bins, in terms of both number- and mass-conserving processes. While the use of a small number of bins is desirable, since it limits the computational cost of large-scale simulations, finding the power-law index requires the use of a root-finding algorithm, which has the potential to be CPU expensive due to mathematical operations such as pow(), log() and sinh(). However, appropriate approximations can be made which avoid the use of too many of these operations, which allow this method to become a viable alternative to piecewise-constant and -linear ones.

Chapter 5 describes the implementation of this distributions method into the modified MHD code. This required a number of changes to the equations for the grains fluids. In particular, average quantities are used for the grain charge and collision coefficients, since it is assumed that the grain velocity is constant within a bin. This is a valid assumption, as there is only a narrow range of grain radii for which the grains move between travelling with the charged particles and moving with the neutrals. Provided enough bins are used to model the distribution, this should not cause significant errors in the dynamics.

The implementation was tested through the comparison of results for different numbers of multiple single-sized grains fluids and for corresponding numbers of size bins when modelling the grain-size distribution. In these tests, physical processes were neglected, so that the grain sizes or size distribution were evolved by advection only. The shock structure can be characterised by its width, and it was shown that for pre-shock densities of 10^4 cm^{-3} and 10^6 cm^{-3} the shock width converges for just 2 size bins. In contrast, 16 single-sized fluids are required for the same degree of convergence. This is because, when few single-sized fluids are used, the grains end up being modelled by a large number of small grains. These grains are all well-coupled to the magnetic field; there is a large grain-neutral collision frequency and the shock is thinner than when the larger grains are accounted for through the use of more single-sized fluids. In contrast, since the distributions method models the distribution in each bin as a power-law itself, the effect of the large grains can be captured with just a small number of bins.

Further to the testing of the implementation, Chapter 5 provided results for standard shock model simulations where sputtering is applied to the grain-size distribution. Through analysis of the downstream grain-size distributions and fraction of Si removed from the grains, it was shown that 8 or more bins are required to accurately evolve the distribution due to sputtering. This is due to the dependence of the sputtering rates on the grain size. All the grains up to a size of $\sim 10^{-5}$ cm travel with a similar velocity; that of the charged particles. Therefore, they also all experience the same sputter rate. For sizes above this, the sputter rate begins to fall, since the grains move from travelling with the charged particles to travelling with the neutrals within the shock. This variation in the sputter rate requires a sufficient number of bins in order to be captured effectively. The impact of sputtering on the shape of the size distribution was shown to be relatively mild. Since sputtering is more efficient for small grain sizes, the result is a reduction in the number of grains

at the small end of the distribution as they are reduced in size to below the lower limit and removed from the distribution. The shape is best captured for 8 or more size bins, an observation which is confirmed by the convergence in the calculated fraction of Si which is removed from the grains which occurs for ≥ 8 bins.

Chapter 6 describes the formulation and implementation of a routine for grain-grain collisions into the MHD model. A result of the structure of C-type shocks is that dust grains travel with different velocities depending on how well coupled they are to the magnetic field. It is therefore thought that, in addition to the sputtering caused by gas-grain sputtering, the production of SiO in shocked molecular regions is due to destruction in grain-grain collisions. For relative velocities above 19 km s^{-1}, SiO is released directly into the gas phase by vaporisation. Shattering, which occurs in collisions faster than 2.7 km s^{-1} for silicate grains, alters the grain-size distribution. This impacts the amount of Si which is released by sputtering. In the literature, models which include grain-grain collisions tend to use average values in both the calculation of the fragment distribution and the re-distribution of grain remnants. Analytic expressions for the sources of grain numbers and mass in each bin as a result of grain-grain collisions are developed which account for the distributions of the fragments and remnants in a more accurate way. In doing so, the only assumptions to be made are that the velocity of the grains is constant in bin, and that the fraction of the grain mass which is disrupted by collisions is the same for all grains in a bin.

The implementation of the grain-grain collisions routine is tested through simulations of a standard shock in which both sputtering and grain-grain collisions are applied for increasing numbers of size bins. Since it was determined in Chapter 5 that 8 size bins are required to accurately model the shock when grains undergo sputtering, 8 was taken as the minimum number of bins. It was shown that the shock structure was unaffected by increasing the number of bins, and the fraction of Si released from the grains showed little variation, too. The main difference came from the shape of the downstream distribution functions, with 16 bins proving to show a smoother function than both 8 and 32 bins. The effect of grain-grain collisions is to reduce the number of large grains and increase the number of small grains. However, this effect was shown to be small for the standard model with density 10^5 cm^{-3}. The grain-grain relative velocities were too small for vaporisation to proceed, and the shattering only slightly increased the number of small grains in comparison to models without grain-grain processing. As a result, the shape of the distributions, when normalised to the initial distribution, appeared to be rough.

Since the changes were small anyway, small errors in the calculation of the power-law indices appeared to be significant in the shape of the distribution. When each bin covers a smaller range of sizes, as is the case of 32 bins compared to 8 and 16, it is more difficult for the root-finding algorithm to determine a unique solution for the power-law index, which could be the cause of the rougher distribution seen for 32 bins.

Results were then compared for 3 shock velocities at a density of 10^5 cm^{-3}. Vaporisation is unable to proceed at this density, as the grain-grain collision velocities are always below the relevant threshold. This is in contrast to the results of Guillet et al. (2011) who find that vaporisation dominates over sputtering for all velocities at this density. However, this may be explained by the differences between our models, an important one being that Guillet et al. (2011) follow grain fragments down to smaller grain sizes (5 Å compared to 50 Å). For a higher density of 10^6 cm^{-3}, we find that grain-grain collisions cause significant alterations to the grain size distribution. Additionally, grain-grain velocities are high enough for vaporisation to occur at this density, and dominates over sputtering for the 2 velocities analysed (30 km s^{-1} and 40 km s^{-1}). When grain-grain processing is included, the fraction of Si released from the grains is increased by a factor of 7 for 30 km s^{-1} and a factor of almost 2 for 40 km s^{-1}. The fraction of Si released by sputtering is reduced by the effect of grain-grain collisions on the size distribution. The decrease in the number of large grains causes a drop-off in the sputter rate for sizes above $\sim 10^{-5}$ cm, and therefore there is a reduction in the amount of Si released. Furthermore, the production of a large number of small grains by shattering means the total number density of grains in the downstream distribution is increased by a factor of about 3 in comparison to the models without grain-grain processing. These small grains are well-coupled to the magnetic field so there is an increase in the grain-neutral collision rate. Given that the shock width is determined by the grain-neutral drag at this density, the shock becomes narrower and there is a corresponding increase in the maximum gas temperature.

The progression of the original multifluid MHD model through this thesis has allowed physical grain processes occurring in C-type shocks to be simulated in a more accurate way than has been seen previously in the literature. The development of a new approach for modelling grain-size distributions, which works particularly well for power-law distributions, allows the evolution of grain sizes to be followed in a way

that is both accurate and computationally viable. An improved routine for calculating changes to the numbers and mass of grains due to grain-grain collisions means that the grain-size distribution can be evolved using just a few necessary assumptions. Grain-grain collisions may be necessary to explain the enhanced abundances of SiO observed in shocked regions of molecular clouds (Caselli et al., 1997), and our simulations have shown that for a density of 10^6 cm^{-3}, the amount of Si released from grains is increased by grain-grain processing.

7.2 Future work

The work presented in this thesis goes some way towards expanding the dust grain physics included in a time-dependent multifluid MHD code which models C-type shocks in molecular clouds. However, there remain a number of limitations which are open to improvement in future work. Possibilities for such work included here are the inclusion of grain mantles, and the extension of the grain-size distribution down to smaller sizes.

7.2.1 Ice mantles

The model used in Chapter 3 (which was first used by Van Loo et al. (2013) and Ashmore (2011)) included ice mantles on multiple single-size grains. These mantles were assumed to consist of H_2O, although features in the Milky Way extinction curve indicate that grain mantles in the ISM also consist of species such as CO_2, CO, NH_3 and CH_4. Whilst the inclusion of mantles is mostly straightforward to do when single-sized grains are used and the only dust grain processes being modelled are number-conserving ones, it becomes a more complex task when modelling grains with a distribution of sizes, and when processes which alter the overall number of grains in the distribution (such as shattering) are involved.

The initial mantle thickness which grows on dust grains in molecular clouds is independent of the core grain size; all grains have the same thickness of mantle (Tielens, 2005). For example, Guillet et al. (2007) find an ice mantle ~ 150 Å thick. This mantle thickness can be determined for grains in a size distribution as follows. The total mass density of material making up the ice mantles is ρ_m, and the volume of ice on a grain of core size a and with mantle thickness Δa is $(a + \Delta a)^3 - a^3$. The

integral of the mass of the mantle on a grain multiplied by the distribution function over the entire distribution is equated with the total mass density of grain material,

$$\int_{a_{\min}}^{a_{\max}} \frac{4}{3}\pi\rho_{ice}\left((a+\Delta a)^3 - a^3\right)\frac{\partial n}{\partial a}\,\mathrm{d}a = \rho_m \tag{7.1}$$

where $a_{\min}$ and $a_{\max}$ are the minimum and maximum core radii in the distribution, respectively, ρ_{ice} is the density of the mantle material, and $\partial n/\partial a$ is the core size distribution. Given the definitions of the moments of the distribution $\langle a^l \rangle$ (see Eq. 4.22) the above expression is found to be cubic in Δa,

$$n(\Delta a)^3 + 3n\langle a\rangle(\Delta a)^2 + 3n\langle a^2\rangle\Delta a - \frac{3\rho_m}{4\pi\rho_{ice}} = 0 \tag{7.2}$$

where n is the number density of grains. Eq. 7.2 is solved for the unique, real value of Δa.

This method can be used to determine the initial mantle thickness of ice which covers all the grains in the distribution. If the distribution is discretised into bins according to the core grain sizes, as described in Chapter 4, then the addition of the mantle may take the total grain size outside of the size limits of the bin. However, the addition of a mantle doesn't affect the number density so the only change to the calculations in the code is that $a + \Delta a$ is used as the grain size wherever it is required in the code.

Guillet et al. (2007) find that all the grains travel with the ions, even at higher densities, because small grains, which are well-coupled to the magnetic field throughout the shock, dominate the gas-grain coupling. They are therefore able to justify the fact that they assume that the mantle thickness remains independent of the core size through the shock. Whilst we agree that this is the case for a pre-shock gas density of 10^4 cm^{-3}, we find that for 10^6 cm^{-3} the largest grains deviate from the ion and electron motion in the shock, and instead move with the neutrals.

In the case of sputtering, since we assume that the sputter rate da/dt is constant for all grains inside a bin, it can be assumed that all the grains within a bin carry the same mantle thickness at each time step in the simulation. The source term for the loss of ice mantle mass density due to sputtering can be calculated for each bin, then the mantle thickness can be determined in each bin i by solving Eq. 7.2 with the appropriate number density and moments. One factor which must be taken into

consideration is the fact that da/dt differs between bins, due to the different grain-neutral relative velocities. This variation is demonstrated in Fig. 5.13, where the grains in the largest size bin experience a sputter rate which differs from that of the grains in the smallest bin by a factor of 3. Therefore, we cannot necessarily expect all the grains in the distribution to lose their mantles at the same time. Core sputtering only proceeds once the entirety of the ice mantle has been eroded. It is a sensible choice, then, to only allow core sputtering (and therefore the grain redistribution) to occur once the grains in all bins have completely lost their mantles.

It is a more complex task to continue tracking ice mantles when grain-grain collisions are included. As noted by Guillet et al. (2009), it is difficult to incorporate the effect on the ice mantle when shattering and vaporisation occur since it means the history of each colliding grain must be tracked. Guillet et al. (2011) address this problem by assuming that all grains of a particular size have a mantle of the same thickness, and the mantle is reduced only by sputtering (i.e. shattering and vaporisation do not alter the mantle). Although this is a limitation, it is perhaps the most reasonable course to take, since tracking the mantle history of the grains is likely to be computationally expensive.

7.2.2 Extending the grain-size distribution

The method of Guillet et al. (2007, 2009, 2011) differs from the method presented in Chapter 6 for grain-grain collisions in that their model takes an initial MRN distribution of 'large' grains from $a_{\rm min} = 100$ Å to $a_{\rm max} = 3000$ Å. Then, a number of empty bins are added from 5 Å to 100 Å which become filled by fragments as the large grains collide with each other and shatter. In contrast, our model covers the initial grain-size range $a_{\rm min} = 50$ Å to $a_{\rm max} = 3000$ Å and, while we assume that the fragments produced in any collision have a minimum size of 5 Å, we remove any grains smaller than $a_{\rm min}$ from the distribution. One issue faced in extending the grain-size distribution to smaller sizes is that the approximation to the pre-factor in the fragment distribution (see Fig. 6.1) is only within an error of 2% for sizes down to 50 Å. For a minimum grain size of 10 Å, the approximation is accurate to within 15 %, but for sizes below this the error in the approximation grows rapidly. In particular, to go down to 5 Å increases the error to above 70% at the small end of the distribution when the fraction of a grain which is shattered is about 0.2. It is therefore unfeasible to use this approximation if the distribution is extended down to these small sizes. Additionally, the validity of these modelling techniques must be

brought into question when representing grains on such small scales ($\lesssim 5$ Å), since the macroscopic physics used to describe the destruction of dust grains in shocks may no longer hold.

We saw in Chapter 6 that the production of many small grain fragments by grain-grain collisions reduced the shock width and increased the gas temperature. It is reasonable to assume that this effect is enhanced if even smaller grain sizes are accounted for. It is therefore worth investigating further whether the grain-size distribution can be extended in a way that continues to allow the use of the more accurate method for re-binning fragments.

7.2.3 Further possibilities

Simulations of C-type shocks in molecular clouds are an active area of research. It seems that there is a trade-off between the size of the chemical network, the accuracy with which the dust grain distribution is evolved, and the order of dimensionality of the simulations. Currently, a computationally efficient model is necessary due to restrictions on resources. As computing power continues to improve, these restrictions may not play such an important role. While this thesis has played some part in extending a self-consistent, time-dependent 1-D model to include accurate dust grain physics, there are continued improvements which can be made. The ideas mentioned so far in this section, i.e. including ice mantles and extending the distribution down to smaller sizes to better capture the effect of small fragments produced by shattering, are the logical next steps.

Beyond this, another possibility for improving the model is the inclusion of dust grain inertia, which is currently neglected in many models featuring dust grains. For the time-dependent model developed by Falle (2003) this simplification was justified by assuming that the grain mass density is small compared to that of the gas. This allows the momentum equation for the grains to be reduced in the same way as those of the ions and electrons. However, though it's true that the grain mass density is small compared with the neutral gas, it can be large with respect to that of the ions. In this case, grain inertia may effect the dynamics (Shull and Draine, 1987). Additionally, if the grain inertia contributes to the calculation of the pre-shock fast magnetosonic speed it is significantly reduced, meaning a magnetic precursor, necessary for the formation of a C-type shock, may not be obtained in the ion fluid for shock speeds greater than about 20 km s^{-1} (Draine and McKee,

1993). However, the fact that a grain-size distribution exists in molecular clouds means that not all grains are necessarily well-coupled to the magnetic field and the effect on the creation of a magnetic precursor may not be significant. Grain inertia has been included in the transverse steady-state models of Guillet et al. (2007) and Flower and Pineau des Forêts (2003), and in the time-dependent models of Ciolek et al. (2004) and Ciolek and Roberge (2002), where investigations were carried out into the critical velocity for the transition for C- to J-type shocks. There is more work to be done on the effect of including the dust grain inertia into time-dependent oblique shock models.

A further consideration to make could be the shape of interstellar dust grains. The vast majority of studies to include dust grains assume that the grains are homogeneous spheres (e.g. Pilipp et al., 1990; Pilipp and Hartquist, 1994; May et al., 2000; Field et al., 2004; Wardle, 1998; Hirashita and Yan, 2009; Guillet et al., 2009; Van Loo et al., 2009; Guillet et al., 2011; Van Loo et al., 2013; Anderl et al., 2013). In reality, dust grains are irregularly-shaped (e.g. Draine, 2003). The shape of a dust grain will impact its optical properties, and therefore influence the structure of its absorption and emission spectra. It was shown by Min et al. (2007) that non-spherical grain shapes (specifically, porous Gaussian Random Field particles) are able to accurately fit the interstellar extinction curve for silicate grains. As yet, it seems that the topic of modelling the destruction of irregularly-shaped dust grains in shocks has yet to be tackled, and could prove to be an interesting direction for future research.

Finally, most models in the literature solve the fluid equations for the simplified geometry of a 1-D planar shock (Flower and Pineau des Forêts, 2003; Guillet et al., 2007; Van Loo et al., 2009). However, observations of protostellar outflows suggest that shocks in these regions have a bow-shape morphology (Bally, 2016). Models such as that by Gustafsson et al. (2010) have built up 3-D bow shock structures from 1-D planar shock models. By projecting their models to create H_2 emission maps they were able to compare directly to observations in a more accurate way than was previously possible. However, there is much scope remaining for the development of self-consistent 3-D shock models, and these are likely to be an area of future research.

Bibliography

Anderl, S., V. Guillet, G. Pineau des Forêts, and D. R. Flower

2013. Shocks in dense clouds IV. Effects of grain-grain processing on molecular line emission. *A&A*, 556:A69–A95.

Arce, H. G., D. Mardones, S. A. Corder, G. Garay, A. Noriega-Crespo, and A. C. Raga

2013. ALMA observations of the HH 46/47 molecular outflow. *ApJ*, 774:39–53.

Arce, H. G. and A. I. Sargent

2006. The evolution of outflow-envelope interactions in low-mass protostars. *ApJ*, 646:1070–1085.

Arendt, R. G., E. Dwek, W. P. Blair, P. Ghavamian, U. Hwang, K. S. Long, R. Petre, J. Rho, and F. Winkler

2010. Spitzer observations of dust destruction in the Puppis A supernova remnant. *ApJ*, 725:585–597.

Asano, R. S., T. T. Takeuchi, H. Hirashita, and T. Nozawa

2013. What determines the grain size distribution in galaxies? *MNRAS*, 432:637–652.

Ashmore, I.

2011. *Time dependent multifluid magnetohydrodynamic models of C-type shocks in weakly ionized, dusty media*. PhD thesis, University of Leeds.

Bachiller, R.

1996. Bipolar molecular outflows from young stars and protostars. *ARA&A*, 34:111–154.

Bally, J.

2016. Protostellar outflows. *ARA&A*, 54:491–528.

Bally, J., J. Walawedner, and B. Reipurth

2012. Deep imaging surveys of star-forming clouds. V. New Herbig-Haro shocks and giant outflows in Taurus. *ApJ*, 144:143–150.

Banerjee, R., R. S. Klessen, and C. Fendt

2007. Can protostellar jets drive supersonic turbulence in molecular clouds? *ApJ*, 668:1028–1041.

Bernstein, R. A., W. L. Freedman, and B. F. Madore
2002. The first detections of the extragalactic background light at 3000, 5500, and 8000 Å. III. Cosmological implications. *ApJ*, 571:107–128.

Bhat, C. L., M. R. Issa, B. P. Houston, C. J. Mayer, and A. W. Wolfendale
1985. Cosmic γ rays and the mass of gas in the galaxy. *Nature*, 314:511–515.

Binney, J. and S. Tremaine
2008. *Galactic Dynamics: Second Edition*, 2 edition. Princeton, NJ USA: Princeton University Press.

Birnstiel, T., C. P. Dullemond, and F. Brauer
2010. Gas- and dust evolution in protoplanetary disks. *A&A*, 513:1–21.

Blandford, R. D. and D. G. Payne
1982. Hydromagnetic flows from accretion discs and the production of radio jets. *MNRAS*, 199:883–903.

Bocchio, M., A. P. Jones, and J. D. Slavin
2014. A re-evaluation of dust processing in supernova shock waves. *A&A*, 570:A32–A49.

Bocchio, M., S. Marassi, R. Schneider, S. Bianchi, M. Limongi, and A. Chieffi
2016. Dust grains from the heart of supernovae. *A&A*, 587:A157–A171.

Bodenheimer, P.
1978. Evolution of rotating interstellar clouds. III. On the formation of multiple star systems. *ApJ*, 224:488–496.

Boyd, T. J. M. and J. J. Sanderson
2003. *The physics of plasmas*. Cambridge University Press.

Cantó, J., A. C. Raga, and D. A. Williams
2008. The intersection of a YSO outflow with the surrounding molecular cloud core. *Revista Mexicana de Astronomía y Astrofísica*, 44:293–300.

Caratti o Garatti, A., B. Stecklum, R. Garcia Lopez, J. Eislöffel, T. P. Ray, A. Saan, R. Cesaroni, C. M. Walmsley, R. D. Oudmaijer, W. J. de Wit, L. Moscadelli, J. Greiner, A. Krabbe, C. Fischer, R. Klein, and J. M. Ibañez
2017. Disk-mediated accretion burst in a high-mass young stellar object. *Nature Physics*, 13:276–279.

Caselli, P., T. W. Hartquist, and O. Havnes
1997. Grain-grain collisions and sputtering in oblique C-type shocks. *A&A*, 322:296–301.

Chapman, J. F. and M. Wardle

2006. Dust grain dynamics in C-type shock waves in molecular clouds. *MNRAS*, 371:513–529.

Ciolek, G. and W. Roberge

2002. Time-dependent, multifluid, magnetohydrodynamic shock waves with grain dynamics I. Formulation and numerical tests. *ApJ*, 567:947–961.

Ciolek, G. E., W. G. Roberge, and T. C. Mouschovias

2004. Multifluid, magnetohydrodynamic shock waves with grain dynamics. II. Dust and the critical speed for C shocks. *ApJ*, 610:781–800.

Claussen, M. J., H. A. Wootten, C. L. Brogan, K. B. Marvel, and R. S. Furuya

2005. Probing jet and disk winds toward low-mass protostars. In *Future Directions in High Resolution Astronomy: the* 10^{th} *Anniversary of the VBLA*, J. D. Romney and M. J. Reid, eds., volume 340, Pp. 324–328. ASP conference series.

Combes, F.

1991. Distribution of CO in the Milky Way. *ARA&A*, 29:195–237.

Cowie, L. L.

1978. Refractory grain destruction in low-velocity shocks. *ApJ*, 225:887–892.

Cunningham, A. J., M. R. Krumholz, C. F. McKee, and R. I. Klein

2018. The effects of magnetic fields and protostellar feedback on low-mass cluster formation. *MNRAS*, 476:771–792.

Dale, J. E. and I. A. Bonnell

2008. The effect of stellar winds on the formation of a protocluster. *MNRAS*, 391:2–13.

Dame, T. M., D. Hartmann, and P. Thaddeus

2001. The Milky Way in molecular clouds: A new complete CO survey. *ApJ*, 547:792–813.

Draine, B. T.

1980. Interstellar shock waves with magnetic precursors. *ApJ*, 241:1021–1038.

Draine, B. T.

1986. Multicomponent, reacting MHD flows. *MNRAS*, 220:133–148.

Draine, B. T.

1989. On the interpretation of the λ 2175 Å feature. In *Interstellar dust: Proceedings of the* 135^{th} *symposium of the International Astronomical Union*, L. J. Allamandola and A. G. G. M. Tielens, eds., Pp. 313–327. Kluwer Academic Publishers, Dordrecht.

Draine, B. T.
2003. Interstellar dust grains. *ARA&A*, 41:241–289.

Draine, B. T.
2004. Astrophysics of dust in cold clouds. In *The Cold Universe, Saas-Fee Advanced Course 32 2002*, D. Pfenniger and Y. Revaz, eds., chapter 3, Pp. 213–304. Springer-Verlag Berlin Heidelberg.

Draine, B. T.
2011. *Shock waves*, chapter 36, Pp. 396–411. Princeton University Press.

Draine, B. T. and C. F. McKee
1993. Theory of interstellar shocks. *ARA&A*, 31:373–432.

Draine, B. T., W. T. Roberge, and A. Dalgarno
1983. Magnetohydrodynamic shock waves in molecular clouds. *ApJ*, 264:485–507. (DRD).

Draine, B. T. and E. E. Salpeter
1979. On the physics of dust grains in hot gas. *ApJ*, 231:77–94.

Draine, B. T. and B. Sutin
1987. Collisional charging of interstellar grains. *ApJ*, 320:803–817.

Falle, S. A. E. G.
1991. Self-similar jets. *MNRAS*, 250:581–596.

Falle, S. A. E. G.
2003. A numerical scheme for multifluid magnetohydrodynamics. *MNRAS*, 344:1210–1218.

Federrath, C., J. M. Rathbone, S. N. Longmore, M. D. Kruijssen, J. Bally, Y. Contreras, R. M. Crocker, G. Garay, J. M. Jackson, L. Testi, and A. J. Walsh
2016. The link between turbulence, magnetic fields, filaments, and star formation in the central molecular zone cloud G0.253+0.016. *A&A*, 832.

Ferreira, J., C. Dougados, and S. Cabrit
2006. Which jet launching mechanism(s) in T Tauri stars? *A&A*, 453:785–796.

Field, D., P. W. May, G. Pineau des Forêts, and D. R. Flower
2004. Sputtering of the refractory cores of interstellar grains. *MNRAS*, 285:839–846.

Field, G. B., J. D. G. Rather, and P. A. Aannestad
1968. Hydrodynamic shock waves and their infrared emission in HI regions. *ApJ*, 151:953–975.

Flower, D. and G. Pineau des Forêts

2003. The influence of grains on the propagation and structure of C-type shock waves in interstellar molecular clouds. *MNRAS*, 343:390–400.

Flower, D. R. and P. des Forêts

1994. Grain-mantle erosion in magnetohydrodynamic shocks. *MNRAS*, 268:724–732.

Flower, D. R. and P. des Forêts

1995. Non-thermal sputtering of interstellar grains in magnetohydrodynamic shocks. *MNRAS*, 275:1049–1056.

Flower, D. R., P. des Forêts, D. Field, and P. W. May

1996. The structure of MHD shocks in molecular outflows: grain sputtering and SiO formation. *MNRAS*, 280:447–457.

Flower, D. R., G. Pineau des Forêts, and T. W. Hartquist

1985. Theoretical studies of interstellar molecular shocks I. General formulation and effects of the ion-molecule chemistry. *MNRAS*, 216:775–794.

Frank, A., T. P. Ray, S. Cabrit, P. Hartigan, H. G. Arce, F. Bacciotti, J. Bally, M. Benisty, J. Eislöffel, M. Güdel, S. Lebedev, B. Nisini, and A. Raga

2014. Morphological evolution of bipolar outflows from young stellar objects. In *Protostars and Planets VI*, H. Beuther, R. S. Klessen, C. P. Dullemond, and T. Henning, eds., volume 914, Pp. 427–442. University of Arizona Press.

Guillet, V., A. P. Jones, and P. des Forêts

2009. Shocks in dense clouds II. Dust destruction and SiO formation in J shocks. *A&A*, 497:145–153.

Guillet, V., G. Pineau des Forêts, and A. P. Jones

2007. Shocks in dense clouds I. Dust dynamics. *A&A*, 476:263–277.

Guillet, V., G. Pineau des Forêts, and A. P. Jones

2011. Shocks in dense clouds III. Dust processing and feedback effects in C-type shocks. *A&A*, 527:A123–A133.

Gustafsson, M., T. Ravkilde, L. E. Kristensen, S. Cabrit, D. Field, and G. Pineau des Forêts

2010. 3D model of bow shocks. *A&A*, 513:A5–A27.

Haro, G.

1952. Herbig's nebulous objects near NGC 1999. *ApJ*, 115:572.

Haro, G.

1953. Hα emission stars and peculiar objects in the Orion nebula. *ApJ*, 117:73.

Hartmann, L. and J. R. Stauffer

1989. Additional measurements of pre-main-sequence stellar rotation. *AJ*, 97:873–880.

Hartquist, T. W.

2017. *Shocks and turbulence and their effects on chemistry*, chapter 2, Pp. 21–62. The Royal Society of Chemistry.

Hartquist, T. W., A. Dalgarno, and M. Oppenheimer

1980. Molecular diagnostics of interstellar shocks. *ApJ*, 236:182–188.

Havnes, O., T. W. Hartquist, and W. Pilipp

1987. The effects of dust on the ionization structures and dynamics in magnetised clouds. In *Physical Processes in Interstellar Clouds; Proceedings of the NATO Advanced Study Institute*, G. E. Morfill and M. Scholer, eds., Pp. 389–482. D. Reidel Publishing Co.

Herbig, G. H.

1950. The spectrum of the nebulosity surrounding T Tauri. *ApJ*, 111:11.

Herbig, G. H.

1951. The spectra of two nebulous objects near NGC 1999. *ApJ*, 113:697–699.

Hirashita, H.

2015. Two-size approximation: a simple way of treating the evolution of grain size distribution in galaxies. *MNRAS*, 447:2937–2950.

Hirashita, H. and H. Yan

2009. Shattering and coagulation of dust grains in interstellar turbulence. *MNRAS*, 394:1061–1074.

Hsieh, T.-H., S.-P. Lai, and A. Belloche

2017. Widening of protostellar outflows: an infrared outflow survey in low-luminosity objects. *ApJ*, 153:173–185.

Inoue, A. K.

2003. Evolution of dust-to-metal ratio in galaxies. *PASJ*, 55:901–909.

Jeans, J. H.

1902. On the stability of a spherical nebula. *Philosophical transactions of the Royal Society of London*, 199:1–53.

Jiménez-Serra, I., P. Caselli, J. Martín-Pintado, and T. W. Hartquist
2008. Parametrization of C-shocks. Evolution of the sputtering of grains. *A&A*, 482:549–559.

Jones, A. P., M. Köhler, N. Ysard, M. Bocchio, and Verstraete
2017. The global dust modelling framework THEMIS. *A&A*, 602:A46–A55.

Jones, A. P., A. G. G. M. Tielens, and D. J. Hollenbach
1996. Grain shattering in shocks: the interstellar grain size distribution. *ApJ*, 469:740–764.

Jones, A. P., A. G. G. M. Tielens, D. J. Hollenbach, and C. F. McKee
1994. Grain destruction in shocks in the interstellar medium. *ApJ*, 433:797–810.

Jones, A. P. and D. A. Williams
1985. Time-dependent sticking coefficients and mantle growth on interstellar grains. *MNRAS*, 217:413–421.

Jura, M.
1976. Calcium abundance variations in diffuse interstellar clouds. *ApJ*, 206:691–698.

Jura, M.
1979. Dust-to-gas ratio in disk galaxies. *ApJ*, 229:485–488.

Kirchschlager, F., F. D. Schmidt, M. J. Barlow, E. L. Fogerty, A. Bevan, and F. D. Priestley
2019. Dust survival rates in clumps passing through the Cas A reverse shock I. Results for a range of clump densities. *MNRAS*, 489:4465–4496.

Knapp, G. R. and F. J. Kerr
1974. The galactic gas-to-dust ratio from observations of eighty-one globular clusters. *A&A*, 35:361–379.

Königl, A. and R. E. Pudritz
2000. Disk winds and accretion-outflow connection. In Mannings et al. (2000), Pp. 759–791.

Kuiper, R., N. J. Turner, and H. W. Yorke
2000. Efficiencies of low-mass star and star cluster formation. *ApJ*, 832.

Kulsrud, R. M.
2009. *Plasma physics for astrophysics*. Princeton University Press.

Kwan, J.
1977. On the molecular hydrogen emission at the Orion nebula. *ApJ*, 216:713–723.

Lada, C. J.

1987. Star formation: from OB associations to protostars. In *IAU Symposium, Vol. 115*, P. 1.

Lada, C. J.

2005. Star formation in the galaxy: an observational overview. *Progress of Theoretical Physics Supplements*, 158.

Larson, R. B.

2003. The physics of star formation. *Reports on Progress in Physics*, 66:1651–1697.

Le Bourlot, J., G. Pineau des Forêts, D. R. Flower, and S. Cabrit

2002. New determinations of the critical velocities of C-type shock waves in dense molecular clouds: application to the outflow source in Orion. *MNRAS*, 332:985–993.

Lee, C.-F.

2020. Molecular jets from low-mass young protostellar objects. *The Astronomy and Astrophysics Review*, 28.

Lee, C.-F., R. Rao, T.-C. Ching, S.-P. Lai, N. Hirano, P. T. P. Ho, and H.-C. H

2014. Magnetic field structure in the flattened envelope and jet in the young protostellar system HH 211. *ApJ*, 797:L9.

Liffman, K. and D. D. Clayton

1989. Stochastic evolution of refractory interstellar dust during the chemical evolution of a two-phase interstellar medium. *ApJ*, 340:853–868.

Machida, M. N. and T. Matsumoto

2011. The origin and formation of the circumstellar disc. *MNRAS*, 413:2767–2784.

Maercker, M., T. Khouri, E. De Beck, M. Brunner, M. Mecina, and O. Jaldehag

2018. Properties of dust in the detached shells around U Antilae DR Serpentis, and V644 Scorpii. *A&A*, 620:A106–A115.

Mannings, V., A. P. Boss, and S. S. Russell, eds.

2000. *Protostars and Planets IV*. University of Arizona Press.

Martín-Pintado, J., R. Bachiller, and A. Fuente

1992. SiO emission as a tracer of shocked gas in molecular outflows. *A&A*, 254:315–326.

Mathis, J. S., W. Rumpl, and K. H. Nordsieck

1977. The size distribution of interstellar grains. *ApJ*, 217:425–433.

Matzner, C. D. and C. F. McKee

2000. Efficiencies of low-mass star and star cluster formation. *ApJ*, 545:364–378.

May, P. W., G. Pineau des Forêts, D. R. Flower, D. Field, N. L. Allan, and J. A. Purton
2000. Sputtering of grains in C-type shocks. *MNRAS*, 318:809–816.

McElroy, D., C. Walsh, A. J. Markwick, M. A. Cordiner, K. Smith, and T. J. Millar
2013. The UMIST database for astrochemistry 2012. *A&A*, 550:A36.

McKee, C. F., D. J. Hollenbach, C. G. Seab, and A. G. G. M. Tielens
1987. The structure of time-dependent interstellar shocks and grain destruction in the interstellar medium. *ApJ*, 318:674–701.

McKee, C. F. and J. P. Williams
1997. The luminosity function of OB associations in the galaxy. *ApJ*, 476:144–165.

McKinnon, R., M. Vogelsberger, P. Torrey, F. Marinacci, and R. Kannan
2018. Simulating galactic dust grain evolution on a moving mesh. *MNRAS*, 478:2851–2886. (McK18).

Mikami, H., T. Umemoto, S. Yamamoto, and S. Saito
1992. Detection of SiO emission in the L1157 dark cloud. *ApJ*, 392:L87–L90.

Min, M., L. B. F. M. Waters, A. de Koter, J. W. Hovenier, L. P. Keller, and F. Markwick-Kemper
2007. The shape and composition of interstellar silicate grains. *A&A*, 462:667–676.

Mizuno, H., W. J. Markiewicz, and H. J. Völk
1988. Grain growth in turbulent protoplanetary accretion disks. *A&A*, 195:183–192.

Mouschovias, T. C. and E. V. Paleologou
1980. Magnetic braking of an aligned rotator during star formation: an exact, time-dependent solution. *ApJ*, 237:877–899.

Mullan, D. J.
1971. The structure of transverse hydromagnetic shocks in regions of low ionisation. *MNRAS*, 153:145–170.

Nesterenok, A. V.
2018. Chemical evolution of the gas in C-type shocks in dark clouds. *Ap&SS*, 363:151–176.

Neufeld, D. A. and G. J. Melnick
1987. H_2 line emission from shocked gas. *ApJ*, 322:266–274.

Offner, S. S. R. and H. G. Arce
2014. Investigations of protostellar outflow launching and gas entrainment: hydrodynamic simulations and molecular emission. *ApJ*, 784.

Ormel, C. W., D. Paszun, C. Dominik, and A. G. G. M. Tielens
2009. Dust coagulation and fragmentation in molecular clouds I. How collisions between dust aggregates alter the dust size distribution. *A&A*, 502:845–869.

Ossenkopf, V.
1993. Dust coagulation in dense molecular clouds: the formation of fluffy aggregates. *A&A*, 280:617–646.

Pilipp, W. and T. W. Hartquist
1994. Grain dynamics in weakly ionized clouds II. Magnetic field rotation in oblique shocks. *MNRAS*, 267:801–810.

Pilipp, W., T. W. Hartquist, and O. Havnes
1990. Grain dynamics in weakly ionized clouds I. A one fluid treatment of grain dynamics. *MNRAS*, 243:685–691.

Podio, L., C. Codella, F. Gueth, S. Cabrit, A. Maury, B. Tabone, C. Lefèvre, S. Anderl, P. Andre, A. Belloche, S. Bontemps, P. Hennebelle, B. Lefloch, S. Maret, and L. Testi
2016. First image of the L1157 molecular jet by the CALYPSO IRAM-PdBI survey. *A&A*, 593:L4.

Podio, L., S. Medves, F. Bacciotti, J. Eislöffel, and T. Ray
2009. Physical structure and dust reprocessing in a sample of HH jets. *A&A*, 506:779–788.

Press, W. H., S. A. Teukolsky, W. T. Vetterling, and B. P. Flannery
1992. *Numerical recipes in C: The art of scientific computing*, 2 edition. New York: Cambridge University Press.

Pudritz, R. E. and C. A. Norman
1983. Centrifugally driven winds from contracting molecular disks. *ApJ*, 274:677–697.

Pudritz, R. E. and T. P. Ray
2019. The role of magnetic fields in protostellar outflows and star formation. *Frontiers in Astronomy and Space Sciences*, 6.

Pudritz, R. E., C. D. Wilson, J. E. Carlstrom, O. P. Lay, R. E. Hills, and D. Ward-Thompson
1996. Accretion disks around class 0 protostars: the case of VLA 1623. *ApJ*, 470:L123–L126.

Raga, A. C., P. F. Velázquez, J. Cantó, and E. Masciadri
2002. The time-dependent ejection velocity histories of HH 34 and H 111. *A&A*, 395:647–656.

Ray, T.

2007a. *The first three million years*, Pp. 3–19. Springer.

Ray, T. P.

2007b. The generation of jets from young stars: an observational perspective. In *Star-Disk Interaction in Young Stars*, J. Bouvier and I. Appenzeller, eds., Pp. 183–194. Proceedings of the International Astronomical union, IAU symposium.

Reipurth, B.

1999. ViXieR online data catalog. *General Catalogue of Herbig-Haro Objects*.

Reipurth, B. and J. Bally

2001. Herbig-Haro flows: probes of early stellar evolution. *ARA&A*, 39:403–455.

Richer, J. S., D. S. Shepherd, S. Cabrit, R. Bachiller, and E. Churchwell

2000. Molecular outflows from young stellar objects. In Mannings et al. (2000), Pp. 427–442.

Salmeron, R. and M. Wardle

2008. Magnetorotational instability in protoplanetary discs: the effect of dust grains. *MNRAS*, 388:1223–1238.

Schilke, P., C. M. Walmsley, G. Pineau des Forêts, and D. R. Flower

1997. SiO production in interstellar shocks. *A&A*, 321:293–304.

Schnack, D. D.

2009. *Lectures in Magnetohydrodynamics: with an appendix on extended MHD*. Berlin Heidelberg: Springer.

Seab, C. G. and M. J. Shull

1983. Shock processing of interstellar grains. *ApJ*, 275:652–660.

Seale, J. P. and L. W. Looney

2008. Morphological evolution of bipolar outflows from young stellar objects. *ApJ*, 675:427–442.

Shu, F., J. Najita, E. Ostriker, and F. Wilkin

1994. Magnetocentrifugally driven flows from young stars and disks. I. A generalized model. *ApJ*, 429:781–796.

Shu, F. H., J. R. Najita, H. Shang, and Z. Li

2000. X-winds theory and observations. In Mannings et al. (2000), Pp. 789–813.

Shull, J. M.

1977. Grain disruption in interstellar hydromagnetic shocks. *ApJ*, 215:805–811.

Shull, J. M.

1978. Disruption and sputtering of grains in intermediated-velocity interstellar clouds. *ApJ*, 226:858–862.

Shull, M. J. and B. T. Draine

1987. The physics of interstellar shock waves. In *Interstellar Processes. Astrophysics and Space Science Library (A Series of Books on the Recent Developments of Space Science and of General Geophysics and Astrophysics Published in Connection with the Journal Space Science Reviews)*, D. J. Hollenbach and H. A. Thronson Jr., eds., Pp. 283–319. Springer, Dordrecht.

Snell, R. L., R. B. Loren, and R. L. Plambeck

1980. Observations of CO in L1551: evidence for stellar wind driven shocks. *ApJ*, 239:L17–L22.

Stahler, S. W.

1983. The birthline for low-mass stars. *ApJ*, 274:822–829.

Stahler, S. W. and F. Palla

2004. *The formation of stars*. Germany: WILEY-VCH Verlag GmbH & Co. KGaA.

Steinicke, W.

2016. William Herschel's 'Hole in the Sky' and the discovery of dark nebulae. *Journal of Astronomical History and Heritage*, 19:305–326.

Stepnik, B., A. Abergel, J. P. Bernard, F. Boulanger, L. Cambrésy, M. Giard, A. P. Jones, G. Lagache, J. M. Lamarre, C. Meny, F. Pajot, F. Le Peintre, I. Ristorcelli, G. Serra, and J. P. Torre

2003. Evolution of dust properties in an interstellar filament. *A&A*, 398:551–563.

Sumpter, R. and S. Van Loo

2020. Evolving grain-size distributions embedded in gas flows. *MNRAS*, 494:2147–2157.

Tafalla, M. and R. Bachiller

2011. Molecules in bipolar outflows. In *The Molecular Universe IAU Symposium*, J. Cernicharo and R. Bachiller, eds., volume 280, Pp. 88–102.

Tielens, A. G. G. M.

2005. *The physics and chemistry of the interstellar medium*. Cambridge University Press.

Tielens, A. G. G. M., C. F. McKee, C. G. Seab, and D. J. Hollenbach

1994. The physics of grain-grain collisions and gas-grain sputtering in interstellar shocks. *ApJ*, 431:321–340.

Tsai, J. C. and W. G. Mathews
1995. Interstellar grains in elliptical galaxies: grain evolution. *ApJ*, 448:84–97.

Umebayashi, T. and T. Nakano
1980. Recombination of ions and electrons on grains and the ionization degree in dense interstellar clouds. *PASJ*, 32:405–421.

Van Loo, S., I. Ashmore, P. Caselli, S. A. E. G. Falle, and T. W. Hartquist
2009. Time-dependent simulations of steady C-type shocks. *MNRAS*, 395:319–327.

Van Loo, S., I. Ashmore, P. Caselli, S. A. E. G. Falle, and T. W. Hartquist
2013. Sputtering in oblique C-type shocks. *MNRAS*, 428:381–388.

Wardle, M.
1998. Dust grains and the structure of steady C-type magnetohydrodynamic shock waves in molecular clouds. *MNRAS*, 298:507–524.

Wardle, M. and B. T. Draine
1987. Oblique magnetohydrodynamic shock waves in molecular clouds. *ApJ*, 321:321–333.

Whelan, E. T., T. P. Ray, F. Bacciotti, A. Natta, L. Testi, and S. Randich
2005. A resolved outflow of matter from a brown dwarf. *Nature*, 435:652–654.

Whittet, D. C. B. and W. W. Duley
1991. Carbon monoxide frosts in the interstellar medium. *A&ARv*, 2:167–189.

Whittet, D. C. B., C. A. Poteet, J. E. Chiar, L. Pagani, V. M. Bajaj, D. Horne, S. S. Shenoy, and A. J. Adamson
2013. Ice and dust in the prestellar dark cloud Lynds 183: preplanetary matter at the lowest temperatures. *ApJ*, 774:1–14.

Williams, D. A. and C. Cecchi-Pestellini
2019. *Dust in galaxies*. UK: Royal Society of Chemistry.

Williams, D. A., T. W. Hartquist, J. M. C. Rawlings, C. Cecchi-Pestellini, and S. Viti
2017. *Dynamical Astrochemistry*. The Royal Society of Chemistry.

Wu, Y., Y. Wei, Y. Shi, W. Yu, S. Qin, and M. Huang
2004. A study of high velocity molecular outflows with an up-to-date sample. *A&A*, 426:503–515.

Ysard, N., M. Köhler, A. Jones, E. Dartois, M. Godard, and L. Gavilan
2016. Mantle formation, coagulation, and the origin of cloud/core shine II. Comparison with observations. *A&A*, 588:A44–A54.

Zhang, Y., H. G. Arce, D. Mardones, S. Cabrit, M. M. Dunham, G. Garay, A. Noriega-Crespo, S. S. R. Offner, R. A. C., and S. A. Corder
2019. An episodic wide-angle outflow in HH 46/47. *ApJ*, 883:1–11.

Zhang, Y., H. G. Arce, D. Mardones, S. Cabrit, M. M. Dunham, G. Garay, A. Noriega-Crespo, S. S. R. Offner, A. C. Raga, and S. A. Corder
2016. ALMA cycle 1 observations of the HH 46/47 molecular outflow: structure, entrainment, and core impact. *ApJ*, 832.

Appendices

A Discrete linear and constant distributions

The power-law discretisation for a grain-size distribution is given by (Eq. 4.4)

$$\left.\frac{\partial n(a,t)}{\partial a}\right|_i = A_i a^{-\alpha_i}. \tag{3}$$

This equation can be linearised about the midpoint of bin i, $a_{c,i}$, to give the piecewise-linear distribution,

$$\left.\frac{\partial n(a,t)}{\partial a}\right|_i = \frac{n_i(t)}{(a_{i+1}-a_i)} + s_i(t)\,(a - a_{c,i})\,, \tag{4}$$

where $s_i(t)$ is the slope of the linear function and the number density of grains in bin i is equal to the value at the bin's midpoint. A piecewise-constant discretisation takes a constant value for the distribution in bin i according to

$$\left.\frac{\partial n(a,t)}{\partial a}\right|_i = \frac{n_i(t)}{(a_{i+1}-a_i)}. \tag{5}$$

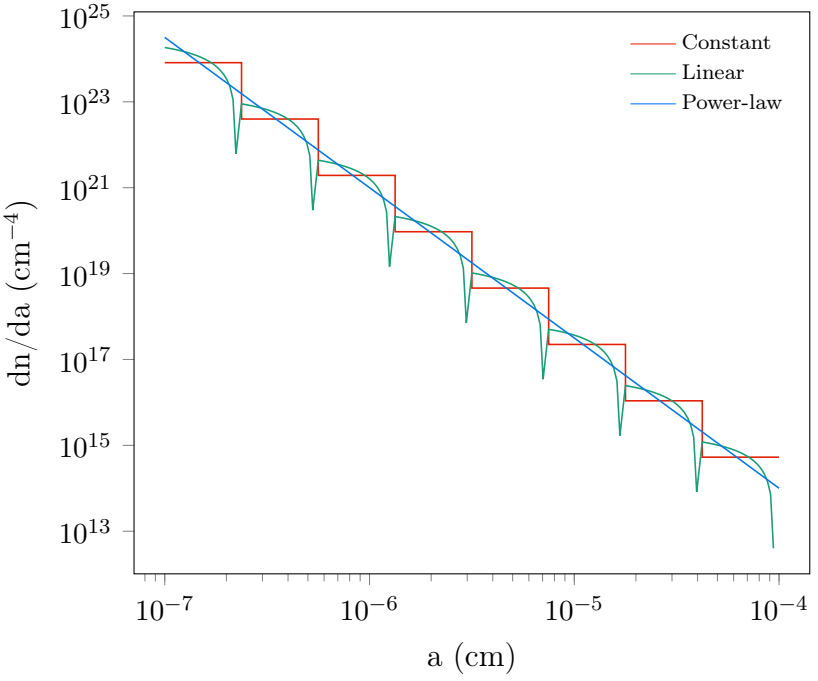

Figure A.1: Comparison of power-law (blue), piecewise-linear (green) and piecewise-constant (red) approximations to an MRN grain-size distribution using $N = 8$ bins.

The piecewise-constant and linear methods are first- and second-order approximations to the power law, respectively. If the slope in a bin is zero (as is the case for the

boxcar function in §4.3.1) then the index $\alpha_i = 0$ and the power-law distribution in the bin reduces to A_i, which is a constant (first-order). Likewise, the piecewise-linear distribution in the bin will have a slope $s_i(t) = 0$, so also reduces to first-order. Fig. A.1 shows how an MRN distribution is described by power-law, piecewise-linear and piecewise-constant discretisations for 8 size bins. The steepness of the slope in the linear function means that the distribution falls below zero at the right edges of the bins, hence the slope limiting routine (described in section 3.2.1 of McK18) is necessary when using the linear approach. Obviously, a power-law (such as MRN) will always be best described by a power-law discretisation. Many bins are required to accurately model a power-law using a linear distribution, while even more are necessary for a piecewise-constant approach.